Ultrafast Transient Absorption Studies of Environment Influence on the Photolysis of B_{12} Complexes and the Subsequent Recombination and Escape of Caged Radicals

by

Andrew B. Stickrath

A dissertation submitted in partial fulfillment
of the requirements of the degree of
Doctor of Philosophy
(Applied Physics)
in the University of Michigan
2008

Doctoral Committee:

Professor Roseanne J. Sension, Chair
Professor Philip H. Bucksbaum
Professor Theodore B. Norris
Professor Duncan G. Steel
Associate Professor Eitan Geva

To my Parents

Acknowledgements

I have been very fortunate to work with Professor Roseanne Sension. Prof. Sension is a fantastic scientist and teacher; and hopefully I have learned from her model. Moreover, she has encouraged and developed the members of her research group into excellent scientists as well. Without such support, I don't think that I would have successfully completed graduate school. Thank you, Roseanne.

I would also like to thank the members of my doctoral committee, who agreed to meet on late notice! Prof. Philip Bucksbaum and his group have been an enriching relationship. A great deal of the experimental apparatus described in this thesis was constructed with the help of Prof. Theodore Norris' ultrafast optics course. I would like to thank Prof. Eitan Geva for the recommendations for future analysis. Prof. Duncan Steel went out of his way to offer personal assistance during a very difficult time; and I thank him for that.

Many people have contributed directly to work presented in this thesis. In particular, the experiments in Chapter 3 were done with Ahmasi Harris and Beth Carroll. Ahmasi taught me a great deal as well about the optics setup used for these experiments. Aaron Rury succeeded in the difficult task of synthesizing ethyl- and propylcobalamin. Anne Vasquez contributed significantly to this feat as well. This synthesis was important to for my research; and I want to thank both of them for their help. Crystal Fox and Prof. Neil Marsh provided the protein samples (they provided many samples before we finally

got the experiment right!). Cassey Tang also helped to collect the escape and recombination data presented in Chapter 4.

Prof. Kenneth Spears has been a great source for optics advice. Prof. Penner-Hahn suggested the use of sucrose solutions and offered (along with Prof. Sension) me the opportunity to work on the x-ray experiments described in Chapter 5. Jack Novodoff kept the building running so that we were able to keep the experiments running. The Applied Physics office has been a great help over the years; I especially would like to thank program director Prof. Bradford Orr. I am still indebted to my undergraduate advisor, Prof. Kenneth Singer who introduced me to the world of optics and scientific research in general. He is also a great scientist and teacher. Professors Jian Xu and Oksana Ostroverkhova both took a considerable amount of their time to teach me as they were finishing up there own graduate studies. I now know how much of a sacrifice that was.

I appreciate very much that I have not simply had colleagues in the Sension group, but great friends: Michael Orozco, Ahmasi Harris, Cassey Tang, Aaron Rury, Beth Carroll, Andre Florean, Anne Vasquez, and Jian Peng, as well as honorary members Will Lai and Joe Gallegos (who helped me repair anything broken). Those who suffered through my defense practice (and didn't have to) definitely are owed thanks: Danica Forguch, Kaitlin McLoughlin, Dan Devries, Ozgun Suzer, and Brandon Lucas. Many thanks are also owed to my many friends outside the lab.

Most importantly, I want to thank Mom, Dad, Michael, David, Amy, Jackson and Gracie: my family. They are what makes all of the hard work worthwhile. My extended family has also been an important part of my life, and I would especially like to acknowledge Grandma Bettie, Grandma George, Amy and Peter.

I can’t begin to describe how much I owe to my parents, what a wonderful life and all the opportunities they’ve given me. My parents have sacrificed for, supported, encouraged, and demanded a lot of my brothers and I our entire lives; there is no other way I would be in the position to submit this thesis. Thank you Mom and Dad!

Table of Contents

List of Figures

Figures:

List of Tables

Tables:

List of Appendices

Appendices:

Abstract

Femtosecond to nanosecond transient absorption experiments were performed on a series of B_{12} complexes to assess the influence of the solvent environment on the excited state electronic structure and resulting dynamics. A series of alkylcobalamins (adenosyl-, ethyl, methyl, and propylcobalamin), all of which are known to undergo cobalt-carbon bond homolysis in response to excitation at 400nm were studied in a variety of surroundings. Measurements on adenosylcobalamin (coenzyme B_{12}) bound to glutamate mutase demonstrate a metal-to-ligand-charge-transfer (MLCT) state en route to bond homolysis, supported by protein influence on the excited state electronic structure. This charge transfer intermediate, which is similar to that reported in the literature for methylcobalamin, is not observed for free adenosylcobalamin. Measurements on methylcobalamin probe solvent influence on the MLCT state and characterize it by a large charge density transfer. This result is in contrast to studies on cyanocobalamin, which is not observed to undergo homolysis, where the solvent dependent lifetime of an intermediate ligand-to-metal-charge-transfer (LMCT) state is characterized by a modest transfer of charge density. Such a LMCT intermediate is observed for adenosylcobalamin in water leading to bond homolysis. The protein has greatly altered the photochemical pathway to homolysis, which is expected to be representative of influence on thermolysis.

Upon homolysis the photoinduced alkyl and cob(II)alamin radicals may recombine or escape the solvent cage to form solvent separated radical pairs which do not recombine in the bulk by the 9ns time limit of these experiments. Recombination can be monitored directly via the oxidation state of the cobalt atom. The neutral alkyl radical is a paradigm for small particle escape and diffusive motion in a liquid. The escape behavior is similar for adenosyl, ethyl, and propyl radicals indicating that hydrogen bonding with the solvent is not a major influence. The methyl radical appears to dissociate from the cobalamin with excess kinetic energy. Preliminary analysis is presented suggesting the escape is not adequately modeled by the steady state diffusive hydrodynamic theory. To explain the discrepancy of escape in different environments an outline of planned analysis is presented.

Chapter 1

Introduction

Vitamin B_{12}, B_{12} cofactors (Figure 1.1), and cofactor analogues, like other transition metal complexes, exhibit rich colors due to their low-lying valence electronic transitions. Beyond the inherent beauty, the photochemistry and photophysics responsible for cofactor pigmentation is also a probe into the inner workings of the complex. Absorption and emission can be used to study the underlying electronic structure which gives rise to these spectra. As well, the key event for the participation of B_{12} cofactors in enzyme mediated catalysis is the thermally induced cleavage of the cobalt – carbon (Co-C) bond. The cleavage of the active bond may also be induced by a photon, resulting in photolysis. Changes in the electronic structure as well as conformational changes of the molecule occur on very fast time scales (femtosecond to picosecond). The time resolved techniques of ultrafast optics are then uniquely suited to the study of the cobalamins, whereby the active Co-C bond may be cleaved and the resulting chemistry and physics monitored on a fast time scale in both free and protein bound environments during and following bond cleavage.

Observation of the photochemistry and photobiology of B_{12} complexes has helped to elucidate some aspects of the Co-C bond reactivity and ultimately the question of organic radical generation for enzyme mediated catalysis. Even beyond these specific, biologically important questions, the B_{12} coenzymes may also serve as a paradigm system

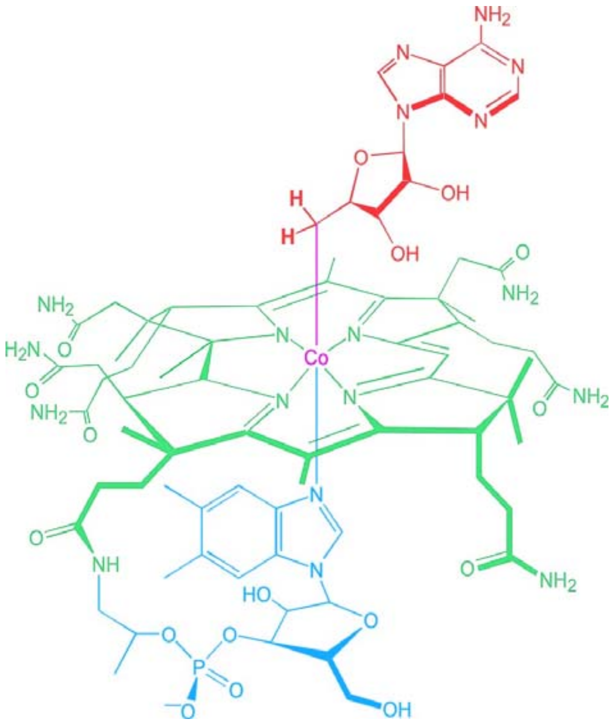

Figure 1.1. Free adenosylcobalamin. The corrin ring and side groups are colored green, the dimethylbenzimidazole and other pendants in blue and the adenosyl in red. The functional group in red may also be a methyl, cyano, or aquo group (ethyl- and propylcobalamin were synthesized). This is just s schematic cartoon and does not indicate the geometry of the corrin ring. Figure modified from Reference [1].

for the general model of bond breaking reactions involving small particle diffusion in the condensed phase environment [2]. In the studies reported in this work we have probed the influence of environment on the electronic structure of cobalamins in solution and bound to the protein glutamate mutase with the collaboration of the B_{12} photophysics (Chapter 3). We have also used the photolysis and geminate recombination of alkylcobalamins to investigate diffusive cage escape of small radicals in solution (Chapter 4), though analysis is ongoing and only preliminary results are presented on this topic.

1.1 B_{12}: An Introduction

B_{12} cofactors participate in a variety of isomerases and methyltransferase enzyme mediated catalysis reactions in nature. In mammals, which are unable to synthesize vitamins, only two enzymes are known to be dependent on B_{12} cofactors. Methionine synthase utilizes heterolytic bond cleavage of methylcobalamin to produce methionine, an essential amino acid from homocysteine and release tetrahydrofolate [3].

Methylmalonyl-CoA mutase produces succinyl-CoA from methylmalonyl-CoA with the aid of free radical production via the homolytic bond cleavage of the Co-C bond of adenosylcobalamin [3]. This reaction is important for both energy production and the synthesis of hemoglobin. A specific adenosylcobalamin dependent protein, glutamate mutase, similar in structure and function to methylmalonyl-CoA mutase will be considered in Chapter 3. Glutamate mutase is a well characterized protein which will help illustrate how enzymes can use organic free radicals to facilitate a carbon skeletal rearrangement reaction, effectively isomerizing about a carbon-carbon bond.

Control of the bond cleavage to form different oxidation states of the cobalamin, though widely studied, remains an open question. The interaction and metabolic pathways associated with the biologic function of B_{12} cofactors also remain at the center of intense interdisciplinary study. The form of B_{12} typically used for fortification in the food supply is cyanocobalamin despite the fact this form is not the one used by the body. Mammals can readily convert cyanocobalamin to either adenosylcobalamin or methylcobalamin. Cyanocobalamin is used in the food industry due to its stability [4]. The name “Vitamin B_{12}” often refers to cyanocobalamin and is the convention adopted in this work.

B_{12} complexes consist of a central cobalt atom ligated to five nitrogen atoms and one carbon atom in an octahedral arrangement (shown for the case of adenosylcobalamin in Figure 1.1; and shown for the isolated cobalamin in Figure 1.3). Four of the nitrogen atoms are in one plane and part of a corrin ring structure. The fifth nitrogen is ligated in the lower axial position and may be from an associated (pendant) dimethlybenzimidazole, or in the case of bonding to proteins, may be supplied by a histidine residue of the protein (where the dimethlybenzimidazole has been displaced, Figure 1.2). Below physiological pH dimethylbenzimidazole may become protonated leaving the cobalamin in the base-off configuration. At the pH values for experiments considered here the cobalamin is expected to be base-on [5].

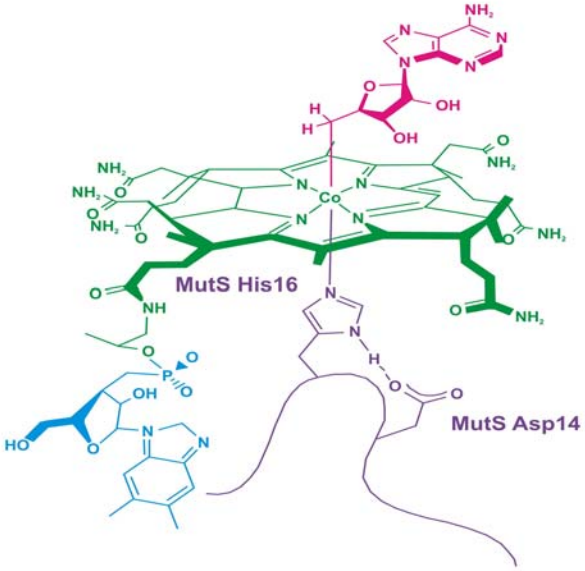

Figure 1.2. Adenosylcobalamin with lower axial nitrogen bond supplied by a histidine residue of glutamate mutase. Figure reproduced from Reference [6].

The upper axial, active bond is to a carbon atom, which can be one of several functional groups or synthetically prepared groups. The biologically relevant forms for human physiology are adenosylcobalamin (coenzyme B_{12} -- where the carbon is supplied by 5-deoxyadenosyl), methylcobalamin (methyl), and cyanocobalamin (vitamin B_{12} -- cyanide). Two synthesized alkylcobalamins were also studied in the course of this work: ethylcobalamin (carbon atom in the Co-C is supplied by an ethyl) and n-propylcobalamin (n-propyl).

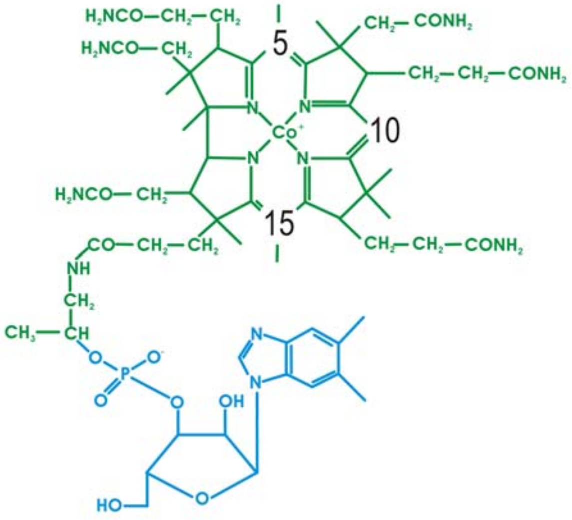

Figure 1.3. Cobalamin looking "downward" along the upper axial direction. The corrin ring structure and side chains are identified by green, and the dimethylbenzimidazole by blue. Both the upper and lower axial ligands are not bonded in this figure.

The conjugated structure and associated electron mobility of the corrin ring, which is similar in structure to the more familiar porphyrin (but likely not as flexible [7]), is the basis for the much of the electronic spectrum of alkyl and nonalkylcobalamins. There are fourteen π electrons associated with the 13 atoms of the corrin ring itself [8]. In fact studies of metal free corrinoids and of corrinoids with different substitution metals besides cobalt exhibit similar absorption spectra to the coblamin arrangment. In general, the substitution of a coordinating metal atom in the ring induces "surprisingly little effect" [8] on the spectrum. Fortunately, especially in the instance of alkylcobalamins, the absorption spectrum is modified characteristically by the axial ligation as a function of the ligand σ-donor strength, and more subtlety so by environment [8]. A review of the literature for each of the alkylcobalamins studied as well as for cyanocobalamin follows.

The steady state absorption spectra of vitamin B_{12}, B_{12} cofactors, and synthetic analogues are characteristic of both axial ligation and environment [6]. The spectra are especially indicative of the oxidation state of the cobalt atom, which is related to axial ligation and the details of bond cleavage between the Co-C bond. Steady-state absorption spectra for a variety of oxidation states are shown in Figure 1.4A [6]. Figure 1.4B contrasts the much more subtle influence on the spectrum due to environment and functional group (for two alkyl functional groups, adenosyl and methyl).

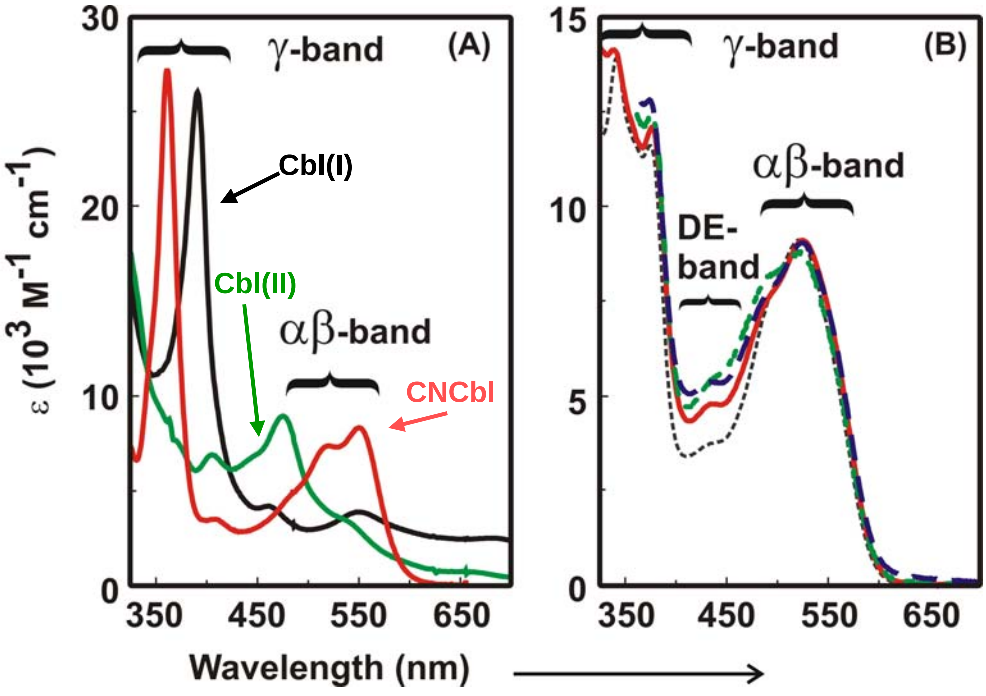

Figure 1.4. The steady-state absorption spectrum is characteristic of (A) cobalt oxidation state and (B) environment. In box A cob(I)alamin is in black, cob(II)alamin in green, and cyanocobalamin (Co^{3+}) in red. In box B the spectra of adenosylcobalamin are shown in water (red), ethylene glycol (green dash), and protein (blue dash) environments. Methylcobalamin in water is also plotted (grey dash). Figure reproduced from Reference [6].

When the cobalt atom is octahedrally bonded as shown in Figures 1.1 and 1.2, it assumes a 3+ oxidation state, with an absorption spectrum similar to the red trace (cyanocobalamin) in Figure 1.4A, and each trace for adenosylcobalamin and methylcobalamin in Figure 1.4B. If the Co-C bond cleavage proceeds via homolysis one electron each will be retained by the cobalamin and functional group resulting in two free radicals. The cobalt atom assumes a 2+ oxidation state, with the unpaired electron in the d_{z^2} orbital [5]. There are two options for heterolytic bond cleavage. Both electrons may be retained by either the cobalamin or the functional group. For methyltransferase mediated reactions the heterolytic cleavage results in cob(I)alamin, with both electrons remaining on the cobalamin.

When a molecule is placed into an electronic excited state a number of reaction pathways not energetically favorable for the ground state may become available for evolution from the excited state [9]. The energy of visible and ultraviolet photons falls in the correct regime to induce such transitions making this spectrum an invaluable tool for the study of excited state dynamics, as well as a nearly innumerable host of other physical phenomena.

For the experiments presented in this work, the specific choice of optical probe was ultrafast transient absorption spectroscopy [10]. The experimental details along with some theoretical background will be discussed in Chapter 2. It is well established that introducing enough energy via a photon to an alkylcobalamin results in homolytic cleavage of the Co-C bond [11-13], with varying quantum yield. Aside from the innate interest and significance inherent in the photochemical behavior, photolytically induced bond homolysis may be a model for aspects of bond homolysis during enzyme mediated catalysis reactions, and give some insight into why cleavage is directed heterolytically in methylcobalamin dependent proteins but homolytically in adenosylcobalamin dependent enzymes.

The spectroscopic signature of the radical pairs produced following thermal homolysis (cob(II)alamin in Figure 1.4) is identical to that observed following the photolysis generated radical pairs. Photolysis directed research holds several advantages over thermolysis studies. Exciting with a photon allows for experiments in the more restricted protein environment, where the high temperatures and long times involved would result in denaturing of the protein [14]. A protein environment photolysis study is presented in Chapter 3. Thermolysis studies cannot provide the time resolved information made possible by the introduction of short pulses. Considerable work has been done towards characterizing the photolysis of B_{12} compounds [11, 12, 15-18]. Only recently, however, has much of that work been done with femtosecond precision [6, 13, 19-26]. A brief review of the literature on photophysics of the B_{12} compounds used for this work follows.

1.2 Photophysics Tour d'Horizon

Photolysis of alkycobalamins (including adenosylcobalamin, ethylcobalamin, methylcobalamin, and propylcobalamin) proceeds via homolytic cleavage of the Co-C bond with varying quantum yield, and excited state dynamics. Excitation of nonalkylcobalamins, such as cyanocobalamin and hydroxocobalamin, does not induce bond cleavage but instead is followed by internal conversion to the ground state on picosecond timescales. The existing literature on the excited state dynamics of each of these compounds will be considered. The wavelength used for excitation in all experiments conducted for this work was the readily available second harmonic of titanium sapphire near 400nm. The dynamics reviewed below are considered in regards to excitation wavelength beyond 400nm.

1.2.1 Alkylcobalamins

1.2.1.1 Adenosylcobalamin

Adenosylcobalamin excited at 400nm in free aqueous solution first undergoes subpicosecond internal conversion to the low lying S_1 excited state (first singlet state). The pathway to bond homolysis proceeds via a spectroscopically identifiable intermediate characteristic of a weakened trans-axial nitrogen bond (towards base off configuration) [13, 24-26]. The dynamics are not observed to exhibit wavelength dependence between excitation at 400nm and 530nm [13]. Experiments with an excitation wavelength of 355nm are in general agreement, but are limited by nanosecond resolutions [17]. The radical pair, adenosyl and cob(II)alamin, is photolytically generated with a thermal energy near that of its surroundings [22], and may then either recombine or diffuse from each other to form a solvent separated radical pair. Bulk recombination will not occur on the timescales (9ns) of the experiments performed in this thesis [27]. The spectrum indicative of a radical pair (cob(II)alamin) arises in ≤ 100ps, following the intermediate arising at ≤ 14ps [25, 26]. At room temperature the quantum yield for the formation of solvent separated radical pairs is ~20-24% [17, 18, 24].

Identical experiments probing the dynamics of adenosylcobalamin in ethylene glycol [25] found bond homolysis on a timescale of ≤ 28ps, without an identifiable intermediate as seen in water. The quantum yield for formation of solvent separated radical pairs is reduced from that observed in water to ~8% in ethylene glycol. The intrinsic rate for geminate recombination is largely independent of the environment, while the effective rate is influenced by the solvent viscosity [25].

1.2.1.2 Ethylcobalamin, Methylcobalamin, and Propylcobalamin

The three alkylcobalamins, ethyl-, methyl-, and propylcobalamin have been grouped together due to the similarity of the functional groups and due to similarities in the observed dynamics. Transient absorption studies on ethylcobalamin and propylcobalamin return nearly identical dynamics [2]. Excitation at 400nm results predominantly in direct homolysis. Further spectral evolution may represent some subpicosecond internal conversion to the S_1 excited state with a spectrum characteristic of a nonalkylcob(III)alamin type state, or vibrational relaxation of the corrin ring [2, 21]. Decay of the excited state via bond homolysis with near unit quantum efficiency (or vibrational relaxation) follows on a time of 30ps (water) to 100ps (ethylene glycol). Excitation at 520nm shows similar but delayed dynamics. Quantum yields for solvent separated radical pairs at room temperature for ethylcobalamin are: ~61-62% in water; and ~21% in ethylene glycol, regardless of excitation wavelength. For propylcobalamin quantum yields are: ~43% in water; and ~13% in ethylene glycol [2, 14, 26]. The propylcobalamin geometry is that of n-propylcobalamin where the Co-C bond occurs along one end of the propyl molecule.

Although the methyl radical is very similar to ethyl and propyl radicals the photoinduced dynamics of methylcobalamin are more complicated. Excitation at 400nm results in a one to three ratio of subpicosecond partitioning between prompt bond homolysis and subpicosecond internal conversion to the S_1 excited as for the ethyl- and propylcobalamin. However, the intermediate lifetime is lengthened for methylcobalamin due to the decreased σ-donating character of the methyl radical. The nonalkylcob(III)alamin type intermediate spectrum, like that observed in ethyl- and propylcobalamin, is characteristic of a metal-to-ligand charge transfer (MLCT) state, which is destabilized by the donating ability of the ligand [26].

The intermediate decays on a nanosecond timescale with ~85% returning to the ground state and ~15% of the population undergoing homolysis. The radical pairs produced from the intermediate decay, like those produced following prompt homolysis may recombine or form solvent separated radical pairs. Overall (prompt homolysis and homolysis ocurring along the intermediate pathway) quantum yield for the formation of solvent separated radical pairs at room temperature are: ~80% [26] in water and ~74% in ethylene glycol [2]. The room temperature quantum yields for the formation of solvent separated radical pairs are much larger for methylcobalamin than for any of the other alkylcobalamins studied. These suggest excess kinetic energy of the methyl radical following homolysis and aiding solvent cage escape, and have in part inspired the experiments of Chapter 4 designed to look at the cage escape for the photolytically generated radicals [6].

The kinetic data for methylcobalamin in water following excitation at 520nm and 530nm did not demonstrate any evidence of *prompt* bond cleavage. Instead, the MLCT transfer state described for excitation at 400nm is the only observed photoproduct on picosecond timescales. The intermediate charge transfer state than decays similarly (via bond homolysis) as for the case of 400nm. Since solvent separated radical pairs result only from decay of the intermediate, the quantum yield is reduced to ~14% [13]. The smaller yield may indicate that the methyl radicals formed by homolysis of the intermediate state do not have the excess kinetic energy acquired by those radicals formed via prompt homolysis following excitation.

1.2.2 Nonalkylcobalamins

1.2.2.1 Cyanocobalamin

Transient absorption studies on cyanocobalamin have not seen evidence of bond cleavage. Instead a subpicosecond ground state bleach is followed by a clean ~ 6.7ps decay at room temperature in aqueous solution. The dynamics were observed to be largely insensitive to environment and excitation wavelength (400nm and 520nm) [23]. The decay to ground state ranges from the 6.7ps in water to ~18.5ps in 2-Propanol; however, comparison of intermediate lifetime in a range of solvents showed only an inverse dependence on the solvent dielectric constant and no dependence on the viscosity [23]. The short-lived intermediate following excitation is characteristic of a ligand-to-metal charge transfer (LMCT) state [23], as opposed to the MLCT state observed in the simple alkylcobalamins, ethyl-, methyl-, and propylcobalamin. The dynamics for cyanocobalamin are similar to those observed for other nonalkylcobalamins including hydroxocobalamin. In the course of the experiments presented in this thesis, hydroxocobalamin transient absorption scans were collected which are very similar to those reported for cyanocobalamin. Kinetic traces are shown for hydroxocobalamin following 400nm excitation, for two probe wavelengths. Only the decay times differ substantially from the cyanocobalamin kinetic traces reported.

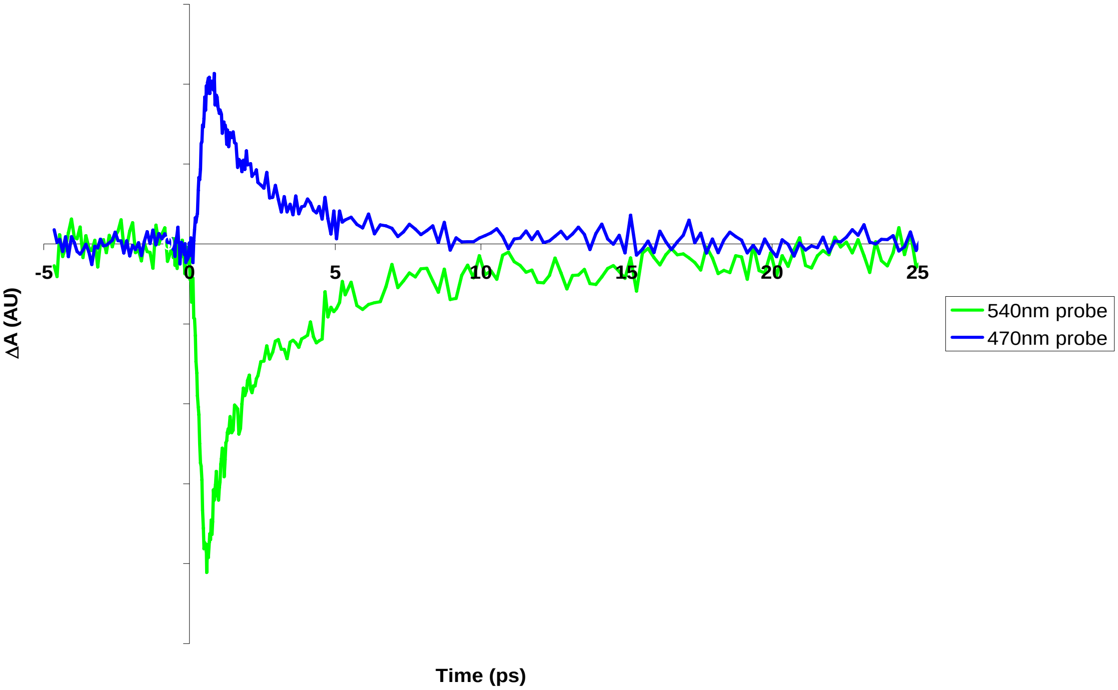

Figure 1.5. Kinetics of the nonalkylcobalamin, hydroxocobalamin, following excitation at 400nm. Probe wavelengths are 540nm and 470nm as indicated in the Figure.

1.3 Thesis Outline

Beginning from the body of knowledge briefly outlined in Section 1.2, several experiments have been carried out. Transient absorption pump-probe measurements, which are outlined in Chapter 2 along with other relevant experimental information, were performed on adenosylcobalamin bound to the protein glutamate mutase. These experiments are a direct extension of those described in free solution above, but provide critical insight into the protein environment and the validity of photolysis as a model for radical generation in biological systems. The protein bound experiments are described in Chapter 3. Also described in Chapter 3 is the extension of the transient absorption studies on adenosylcobalamin, cyanocobalamin, and methylcobalamin to a systematic variation in solvent environment through the use of temperature variation.

Chapter 4 describes a series of measurements in solvent mixtures building upon the suggestive behavior of cage escape briefly noted above in reference to the quantum yield for solvent separated radical pairs. With this data in mind a series of experiments were performed to systematically study the photolysis and geminate recombination of adenosylcobalamin and methylcobalamin in different solvent environments (mixtures of water and ethylene glycol, and sucrose solutions) and to include the synthetic alkylcobalamins ethyl- and propylcobalamin to investigate the cage escape. The choice of these new alkylcobalamins is particularly well suited for the goal of cage escape, as it introduces the parameter of radical size, while the homolysis kinetics are nearly identical. An analysis considering standard hydrodynamic diffusion is applied to the cage escape data, with a further kinetic approach outlined.

Chapter 5 suggests several immediate and long term directions for this research and provides a brief summary of the results and questions arising from the experiments in Chapters 3 and 4. Of particular note to experimenters continuing this work or making use of the experimental methods described in Chapter 2 is that a great deal of effort has been directed towards suggesting possible improvements on the experimental apparatus.

1.4 Bibliography

1. Marsh, E.N.G. and Drennan, C.L., *Adenosylcobalamin-dependent isomerases: new insights into structure and mechanism.* Current Opinion in Chemical Biology, 2001. **5**(5): p. 499-505.

2. Sension, R.J., Harris, D.A., and Cole, A.G., *Time-Resolved Spectroscopic Studies of B_{12} Coenzymes: A Comparison of the Influence of Solvent on the Primary Photolysis Mechanism and Geminate Recombination of Methyl-, Ethyl-, n-Propyl-, and 5'-Deoxyadenosylcobalamin.* Journal of Physical Chemistry B, 2005. **109**: p. 21954-21962.

3. Banerjee, R., *The Yin-Yang of cobalamin biochemistry.* Chemistry & Biology, 1997. **4**(3): p. 175-186.

4. Victor, H., *Vitamin B-12: plant sources, requirements, and assay.* Am. J. Clin. Nutr., 1988. **48**: p. 852-858.

5. Banerjee, R., *B-12 trafficking in mammals: A case for coenzyme escort service.* Acs Chemical Biology, 2006. **1**(3): p. 149-159.

6. Sension, R.J., Harris, D.A., Stickrath, A., Cole, A.G., Fox, C.C., and Marsh, E.N.G., *Time-Resolved Measurements of the Photolysis and Recombination of Adenosylcobalamin Bound to Glutamate Mutase.* Journal of Physical Chemistry B, 2005. **109**(38): p. 18146-18152.

7. Geno, M.K. and Halpern, J., *Why Does Nature Not Use the Porphyrin Ligand in Vitamin-B12.* Journal of the American Chemical Society, 1987. **109**(4): p. 1238-1240.

8. Pratt, J.M., *The Roles of Co, Corrin, and Protein. II. Electronic Spectra and Structure of the Corrin Ligand: Molecular Machinary of the Protein*, in *Chemistry and Biochemistry of B_{12}*, R. Banerjee, Editor. 1999, John Wiley & Sons, Inc.: New York.

9. Coyle, J.D., *Introduction to Organic Photochemistry*. 1986, Chichester: John Wiley & Sons Ltd.

10. Anfinrud, P.A., Johnson, C.K., Sension, R., and Hochstrasser, R.M., *Ultrafast Spectroscopic Techniques*, in *Applied Laser Spectroscopy, Techniques, Instrumentation and Applications*, D.L. Andrews, Editor. 1992, VCH Publishing: New York, New York.

11. Gerards, L.E.H., Bulthuis, H., Bolster, M.W.G.d., and Balt, S., *A study of the cage mechanism for the homolytic cleavage of the cobalt-carbon bond in coenzyme*

B12 by varying the solvent viscosity. Inorganica Chimica Acta, 1991. **190**(1): p. 47-53.

12. Koenig, T.W., Hay, B.P., and Finke, R.G., *Cage effects in organotransition metal chemistry: Their importance in the kinetic estimation of bond dissociation energies in solution.* Polyhedron, 1988. **7**(16-17): p. 1499-1516.

13. Shiang, J.J., Walker II, L.A., Anderson, N.A., Cole, A.G., and Sension, R.J., *Time-Resolved Spectroscopic Studies of B12 Coenzymes: The Photolysis of Methylcobalamin Is Wavelength Dependent.* Journal of Physical Chemistry B, 1999. **103**: p. 10532-10539.

14. Cole, A., *Ultrafast Transient Absorption Studies of Coenzyme B12 Analogs and Derivatives: Biological Activity of Alkylcobalamins*, in *Chemistry*. 2003, University of Michigan: Ann Arbor, Michigan.

15. Pratt, J.M. and Whitear, B.R.D., *Photolysis of Methylcobalamin.* Journal of the Chemical Society a -Inorganic Physical Theoretical, 1971(2): p. 252-&.

16. Taylor, R.T., Smucker, L., Hanna, M.L., and Gill, J., *Aerobic photoiysis of alkylcobalamins: Quantum yields and light-action spectra.* Archives of Biochemistry and Biophysics, 1973. **156**(2): p. 521-533.

17. Chen, E. and Chance, M.R., *Nanosecond transient absorption spectroscopy of coenzyme B12. Quantum yields and spectral dynamics.* Journal of Biological Chemistry, 1990. **265**: p. 12987-12994.

18. Chen, E. and Chance, M.R., *Continuous- Wave Quantum Yields of Various Cobalamins Are Influenced by Competition between Geminate Recombination and Cage Escape?* Biochemistry, 1993. **32**: p. 1480-1487.

19. Walker II, L.A., Jarrett, J.T., Anderson, N.A., Pullen, S.H., Matthews, R.G., and Sension, R.J., *Time-Resolved Spectroscopic Studies of B12 Coenzymes: The Identification of a Metastable Cob(III)alamin Photoproduct in the Photolysis of Methylcobalamin.* Journal of the American Chemical Society, 1998. **120**: p. 3597-3603.

20. Stickrath, A.B., Harris, D.A., and Sension, R.J. *Ultrafast Studies of the Electronic Structure and Dynamics of B12 Cofactors*. in *Femtochemistry VII: Fundamental Ultrafast Processes in Chemistry, Physics, and Biology*. 2005. Washington D.C.: Elsevier.

21. Harris, D.A., Stickrath, A.B., Carroll, E.C., and Sension, R.J., *Influence of environment on the electronic structure of Cob(III)alamins: Time-resolved absorption studies of the S-1 state spectrum and dynamics.* Journal of the American Chemical Society, 2007. **129**(24): p. 7578-7585.

22. Sension, R.J., Harris, D.A., and Cole, A.G., *Time-resolved spectroscopic studies of B-12 coenzymes: Comparison of the influence of solvent on the primary photolysis mechanism and geminate recombination of methyl-, ethyl-, n-propyl-, and 5 '-deoxyadenosylcobalamin.* Journal of Physical Chemistry B, 2005. **109**(46): p. 21954-21962.

23. Shiang, J.J., Cole, A.G., Sension, R.J., Hang, K., Weng, Y., Trommel, J.S., Marzilli, L.G., and Lian, T., *Ultrafast Excited-State Dynamics in Vitamin B12 and Related Cob(III)alamins.* Journal of the American Chemical Society, 2006. **128**: p. 801-808.

24. Walker II, L.A., Shiang, J.J., Anderson, N.A., Pullen, S.H., and Sension, R.J., *Time-Resolved Spectroscopic Studies of B12 Coenzymes: The Photolysis and Geminate Recombination of Adenosylcobalamin.* Journal of the American Chemical Society, 1998. **120**: p. 7286-7292.

25. Yoder, L.M., Cole, A.G., Walker II, L.A., and Sension, R.J., *Time-Resolved Spectroscopic Studies of B12 Coenzymes: Influence of Solvent on the Photolysis of Adenosylcobalamin.* Journal of Physical Chemistry B, 2001. **105**(48): p. 12180-12188.

26. Cole, A.G., Yoder, L.M., Shiang, J.J., Anderson, N.A., Walker II, L.A., Banaszak Holl, M.M., and Sension, R.J., *Time-Resolved Spectroscopic Studies of B12 Coenzymes: A Comparison of the Primary Photolysis Mechanism in Methyl-, Ethyl-, n-Propyl-, and 5'-Deoxyadenosylcobalamin.* Journal of the American Chemical Society, 2002. **124**: p. 434-441.

27. Rice, S.A., *Diffusion-Limited Reactions*. Comprehensive Chemical Kinetics, ed. C.H. Bamford, C.F.H. Tipper, and R.G. Compton. Vol. 25. 1985, Amsterdam, The Netherlands: Elsevier.

Chapter 2

Experimental Methods

The research described in this dissertation involves a diverse and highly interdisciplinary range of both basic and applied research. The common theme allowing participation in such a varied range of research has been the use of light as a fantastic tool to probe the inner workings of material systems ranging from semiconductors to, more importantly for this work, molecules. Accordingly, this chapter will largely be an introduction to the ultrafast laser system and related optical techniques which made the detection of the microscopic and "fast" events associated with alkylcobalamin excitation, bond cleavage, and ultimately radical escape possible.

Some of the techniques and apparatus central to the studies reported here might properly be considered old hat, as they have been reviewed in many places [1-4]. Even so, particular attention and considerable time has been devoted to improving upon and optimizing the already top rate designs. A further review is therefore warranted, with special emphasis on those topics where improvements can be suggested. As well, it is hoped that some of the calculations and suggestions for further improvements will prove useful for future students, especially in relation to optical compression efficiency.

2.1 Introduction to Experiment Principles

The primary technique upon which this thesis rests is transient absorption spectroscopy. Although now a "routine" pump-probe experimental approach, transient absorption spectroscopy still can give great insight into a myriad of physical systems. In the case of these experiments, the constructed apparatus provides a direct temporally resolved probe of the recombination and cage escape of an alkyl radical and a cob(II)alamin radical produced by photolysis. There are several unique features of the implemented setup which move the conducted experiments out the realm of "routine." Although there are some fundamental limitations inherent in the technique, as practiced here these are rarely reached and the limitations are simply those defined by the input optical pulse temporal profile.

When light is incident on some medium (alkylcobalamin dissolved in water and ethylene glycol for instance), the intensity decay via absorption can be described by the Beer-Lambert law:

$$\log\frac{I}{I_0} = \log T = -\varepsilon[J]l = -A\,. \tag{2.1}$$

I_0 is the intensity of the incident light and I the intensity after traversing a distance l through the assumed isotropic medium. The ratio of I to I_0, T, is known as the transmittance. The product $A = -\varepsilon[J]l$ is the sample absorbance (optical density), with ε the species (J) specific molar absorption coefficient (extinction coefficient), and $[J]$ the concentration of the absorbing species. Although empirically derived, the Beer-Lambert law can be given a strong physical motivation. Following Atkins [5], when light of intensity I traverses an isotropic medium, a decrease in intensity, $-dI$, can be expected over a slice of medium, *dx*. The decrease should also be proportional to the concentration of the absorbing species [*J*]. With κ as the proportionality constant:

$$dI = -\kappa [J] I dx , \tag{2.2}$$

which can be rearranged to give

$$\frac{dI}{I} = -\kappa [J] dx . \tag{2.3}$$

Continuing with Atkins, since Equations 2.2 and 2.3 apply for each successive "slice" of medium through which the light propagates, the next step is to integrate over the total distance *l*, assuming an initial intensity I_0 (Equation 2.4):

$$\int_{I_0}^{I} \frac{dI}{I} = -\kappa \int_0^l [J] dx , \tag{2.4}$$

which when integrated gives

$$\ln \frac{I}{I_0} = -\kappa [J] l . \tag{2.5}$$

Converting to the base 10 logarithm and setting the proportionality factor $\kappa = \varepsilon \ln(10)$ results in Equation 2.1.

The light exiting (depending on the experiment, it may be simply weakened in intensity, scattered, frequency converted, etc.; the Beer-Lambert law, however, describes only absorption) the sample then provides a probe of the medium. In the simplest case, the steady state absorption spectrum obtained in this way can provide a fingerprint of the absorbing species and concentration, as well as limited information about the excited state near the ground state equilibrium geometry. Such a scheme is basically the one employed here, with the introduction of "ultrafast" temporal identification of the absorbing species (the oxidation state of the cobalt atom in cobalamin).

By introducing short (~100fs) pulses, the material response to an excitation can be temporally resolved; and in this way the excited state evolution may be probed in regions away from the ground state equilibrium geometry. An initial excitation pulse first puts the system into some excited state or begins a photoinduced chemical process such as a bond breaking as is observed for the alkycobalamins. A second probe pulse then follows at some variable delay to determine the evolution of the sample response to the initial excitation. For femtosecond time scale resolution the delay between the pump and probe pulse is achieved through the use of a mechanical delay line (i.e. a moving stage) as depicted schematically in Figure 2.1.

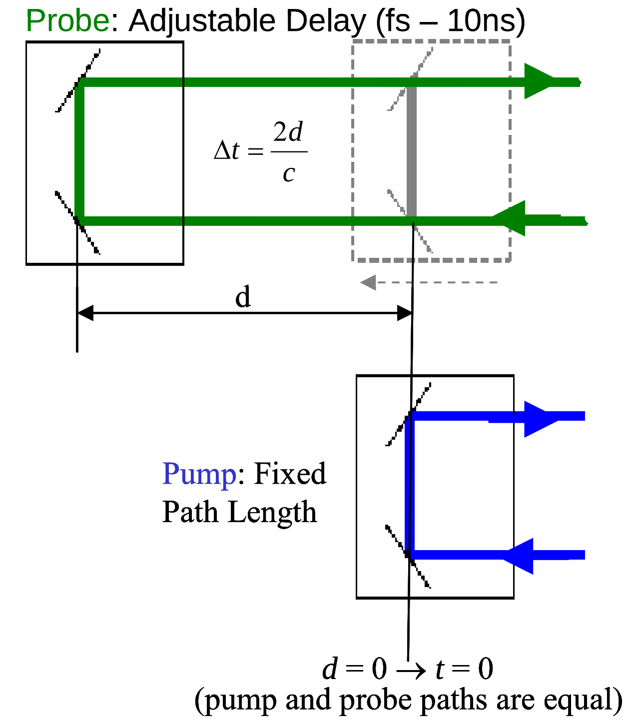

Figure 2.1. Optical path length delay for fine temporal resolution.

In the example of Figure 2.1 the pump beam traverses a fixed path while the probe traverses a variable delay. When the probe path length is the same as the pump's, the two pulses reach the sample at the same time (denoted as $d = 0$ in Figure 2.1). As the probe path is increased through variable stage steps, the resulting response can be observed on a femtosecond timescale. The stage used was able to take steps as small as one micron in length. The smallest time step available then was $\Delta t = 2d/c = 6.67$fs, which is much shorter than the duration of the input pulses. The 1.5m stage length allowed a total delay of $3\text{m}/c = 10$ns. If the probe path length is made shorter than the pump length (negative times), a baseline reading can be established. Through this simple exploitation of the speed of light, the oxidation state of the cobalamin cobalt atom, and consequently the escape and recombination of photolysis induced radical pairs, can be monitored on a femtosecond timescale out to times as long as ten nanoseconds. This idea is at the heart of the data described in Chapters 3 and 4. Although the principle may be simple, the practical details of implementing the method move these experiments beyond the realm of turn crank data collection. Traces collected following this prescription are called kinetic traces. It is also convenient to collect data for a broad spectrum at a particular delay and construct the difference spectrum (as is done in Chapter 3); and depending on the sample and experimental parameters, temporal and spectral data may be collected simultaneously.

Table 2.1 lists the variable time steps typically used for these kinetic traces. Smaller steps are taken at early times to capture all of the dynamics possible with the given probe and pump pulse temporal resolution (described below). However, due to the long time (10ns) nature of these scans, it is not feasible to take such small steps (~100s fs) at longer times where there is no fast dynamic information to be studied. The introduction of variable steps is also necessary for some samples due to the short useable life of the sample (typically due to the large quantum yield from photolysis and thermolysis buildup in n-propyl- and ethylcobalamin samples). With the ten different step size regions chosen, a single kinetic trace with 500-1000 shots per time position, required ~11-12 minutes. Each sample in a particular environment and at a specific temperature was averaged at minimum over four scans to ensure stage alignment. Times longer than this began to show product buildup in the sample volume (as evidenced in the kinetic traces and in steady state spectra). Sometimes more scans were necessary to achieve a suitable signal to noise ratio. These scans were completed with fresh sample for those alkylcobalamins showing product accumulation.

Table 2.1. Variable time steps for kinetic transient absorption scans.

Time Region (ps)	Step Size (fs)
-10 – 5	10
5 – 10	20
10 – 20	50
20 – 50	100
50 – 100	200
100 – 200	500
200 – 500	1000
500 – 1000	2000
1000 – 2000	5000
2000 - 9000	10000

The transient absorption principles describe above require the introduction of an ultrashort laser pulse of an appropriate wavelength to match the electronic absorption spectrum (Figure 2.2) of the alkylcobalamins and probe the cobalt oxidation state. A second pulse is also necessary to precipitate homolytic bond cleavage, producing a radical pair (cob(II)alamin and alkyl radical). The short pulse is produced in a Kerr lens modelocked (KLM) Titanium:Sapphire laser, which is amplified in a Titanium:Sapphire multipass amplifier, chirped pulse amplification (CPA) scheme. This laser, described briefly below, reliably produces pulses of approximately 60fs, centered near 800nm. Examination of Figure 2.2, which shows the steady state absorption spectrum for alkylcobalamins and a cobalamin radical following homolytic bond cleavage, demonstrates that this wavelength is not ideal. Therefore several nonlinear optical techniques are utilized to produce pulses centered at the desired wavelength for pump and probe. These techniques are also described below. More detail concerning the choice of pump and probe wavelength can be found in Chapters 1 and 3.

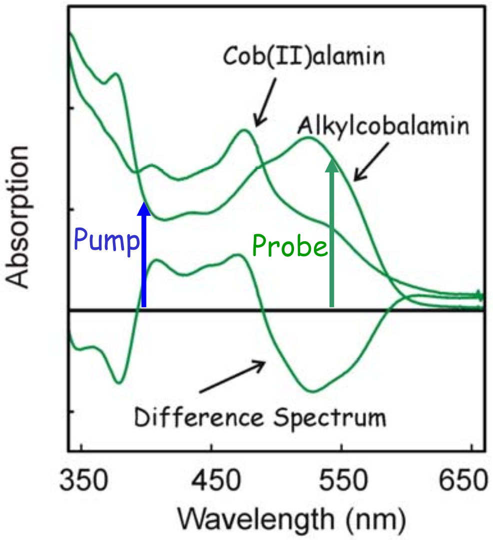

Figure 2.2. Steady state absorption spectra for alkycobalamins, cobalamin(II) radical, and their associated difference spectrum.

2.2 Probe and Pump Pulse Generation

A typical [6] (Figure 2.3) chirped pulse amplification arrangement was used to conduct these experiments. A Kapteyn-Murnane Labs Kerr lens modelocked Titanium:Sapphire oscillator was pumped with a Spectra Physics Millennia laser, producing a train of ≤ 20fs pulses at ~88MHz. Average output powers in the stable modelocking regime were ~350mW, corresponding to a pulse energy of ~350mW/88MHz ≈ 4nJ/pulse. This pulse energy is far too weak for the experiments described in this thesis. Therefore the pulse was amplified in a multipass amplifier. First the pulse was stretched, or chirped, as described in detail below (Section 2.4) to a pulse width of ~180ps. One pulse every millisecond is then picked via a pockels cell placed between crossed polarizers to seed the amplifier. Temporally dispersing the spectral components of the pulse prior to amplification serves several purposes [7]. Lengthening the pulse makes it possible to more efficiently extract energy from the amplifier, while remaining in the linear amplification regime. In this regime unwanted nonlinear effects are avoided along with possible damage to the amplification medium. Note that the ~180ps pulse width is too short by a factor of 2 [7] to achieve the highest efficiency theoretically possible, but is long enough for amplification to 1mJ/pulse energy. The imposed one kilohertz repetition rate allows plenty of time in between pulses for amplification in the multipass. More importantly, the one kilohertz repetition rate allows time for sample refreshing between pulses as described in the experimental setup.

Following amplification, the pulses are recompressed as is also described in detail in the Section 2.4. Pulses exiting the compressor have a very large peak power (~500 μJ/pulse; with an ~60fs pulse width, peak powers of ~8GW are reached). The pulses are amplified by a factor of ~10,000 (4nJ → 500μJ/ pulse), at the expense of a slower repetition rate.

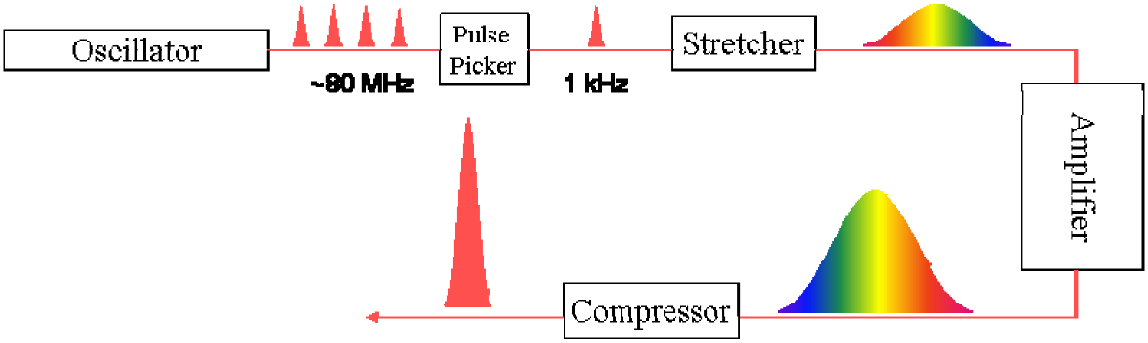

Figure 2.3. Chirped pulse amplification schematic. Figure reproduced from Reference [4].

The amplifier is an 8-pass, three mirror, triangular arrangement multipass design based on the work of Backus and coworkers [8]. It is pumped by a Quantronix Nd:YLF flashlamp laser, which produces q-switched pulses of ~150ns duration. Although considerable effort was spent in optimization of the multipass amplifier and in the maintenance (and rebuilding) of the of the Nd:YLF pump, no significant changes were made to the design already described in detail elsewhere [4]. The most significant feature of the multipass design is the ability for spatial multiplexing for pulse ejection, eliminating the need for dispersion inducing beam path optics (especially the intracavity pockels cell in a regenerative amplifier).

Now that there are pulses with enough energy on the table for experiments, they must be converted to the appropriate wavelengths for the system under study. The 800nm pulses are first sent through a variable split, consisting of a polarizing cube placed between half waveplates. The output polarization of each beam can be individually selected with the two exit waveplates. The two beams can be used to generate pump and probe pulses as described below. Figure 2.4 is a schematic of the experimental layout.

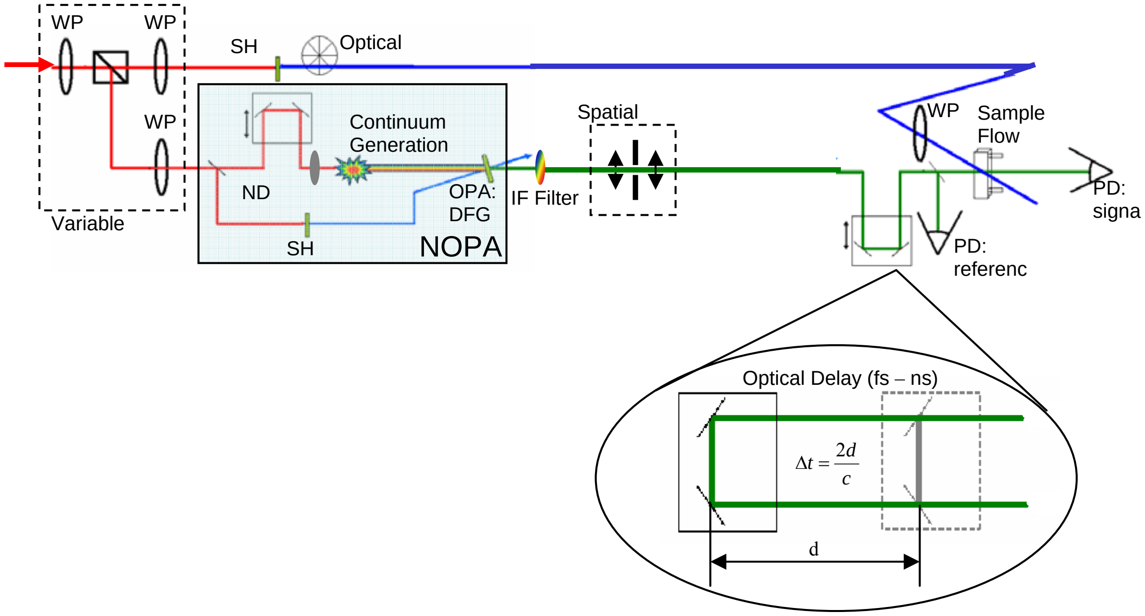

Figure 2.4. Experimental setup schematic.

2.2.1 Second Harmonic Generation

A fraction of the energy is used to make the experimental pump via second harmonic (SH) generation in a BBO crystal. Second harmonic generation arises as a result of a medium's second order nonlinear polarization and when only one frequency is incident on the nonlinear medium is described by [9]:

$$P^{(2)}(t) = 2\chi^{(2)}EE^{*} + (\chi^{(2)}E^{2}e^{-2\omega t} + c.c.). \qquad (2.6)$$

$P^{(2)}(t)$ is the time varying second order polarization of the crystal; and $\chi^{(2)}$ is the crystal's second order nonlinear susceptibility. In the expression for $P^{(2)}(t)$ there is a term with frequency 2ω resulting in a field with that frequency. Figure 2.5 illustrates the process and demonstrates that energy conservation is maintained.

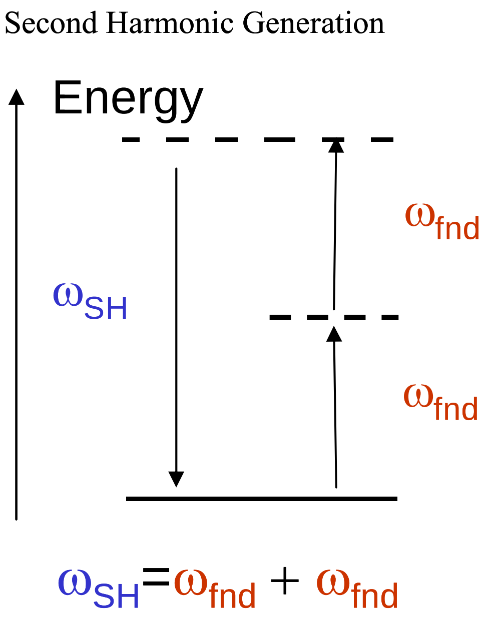

Figure 2.5. Second harmonic generation energy level diagram (virtual levels are dashed). "fnd" represents the 800nm fundamental input; and "SH" represents the second harmonic of the fundamental.

2.2.2 Noncollinear Parametric Amplification (NOPA)

The remaining fraction of the beam is injected into a noncollinear optical parametric amplifier (NOPA) based on the original design of Riedle and coworkers [10]. This design reliably produces pulses of ~100fs duration throughout the visible without further need for recompression as described momentarily. Once in the NOPA, the beam is again split. A small fraction (~4% reflection from a glass surface) is focused hard into a sapphire plate to produce a broadband supercontinuum. By carefully controlling the intensity with a variable neutral density filter [11] a stable single filament is produced with low divergence [12]. The process of spectral broadening of short pulses in transparent media such as sapphire is still the subject of debate, but is related to pulse self-steepening and resulting optical shock-wave formation as well as self phase modulation (terms due to third order nonlinear polarization) [9, 12, 13]. The useful spectrum produced by 800nm pulses in sapphire extends from ~470nm to ~720nm. Although there are spectral components above 700nm, the spectrum produced becomes very structured beyond this point and not easily compressible [14]. An example of a typical whitelight spectrum as obtained for this work is plotted in Figure 2.6. Note that in this example, the spectrometer has saturated in the region above 700nm. A hotmirror is used to cut the spectrum above 750nm.

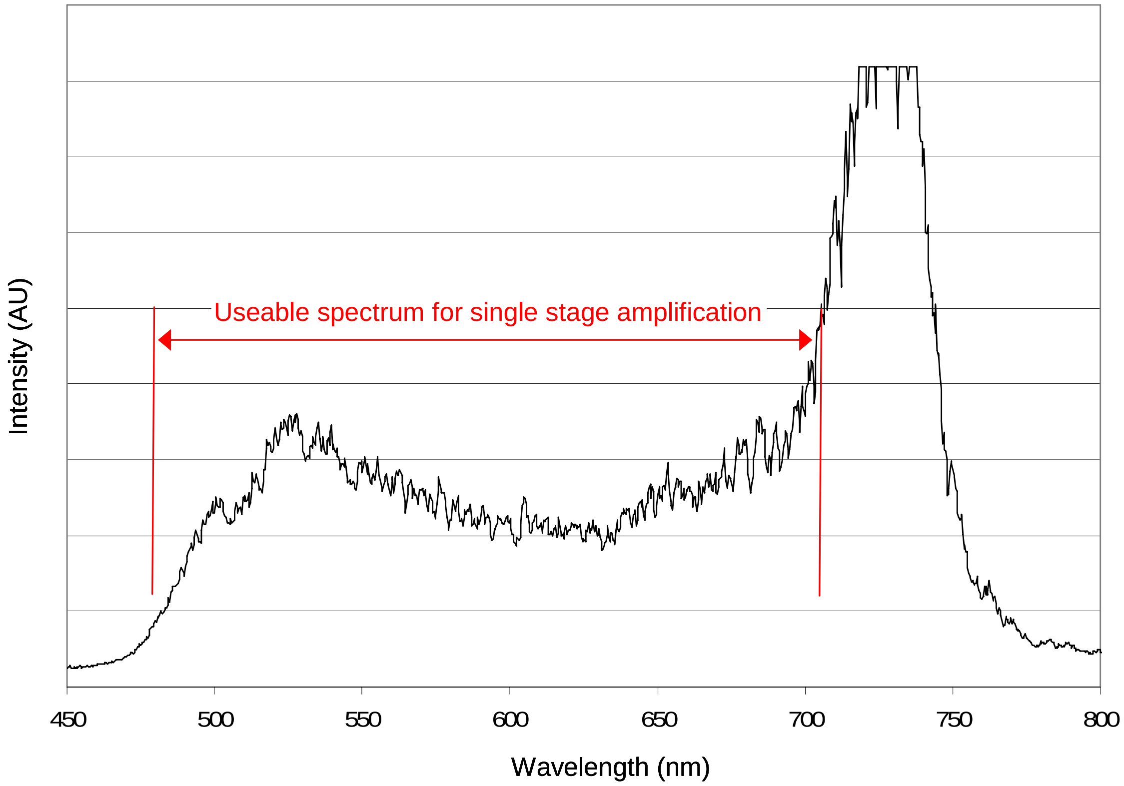

Figure 2.6. Typical spectrum from supercontinuum generation obtained for the NOPA described here in a 2mm sapphire disk. Note that the spectrometer is saturated in the region around 730nm. A hotmirror cuts the spectrum above 750nm.

The still remaining light in the NOPA is focused into another BBO crystal to produce the second harmonic. The supercontinuum is then collected and mixed with the second harmonic in another BBO crystal to produce an amplified pulse at a desired spectral component of the supercontinuum through difference frequency generation (DFG) [9]:

Difference Frequency Generation

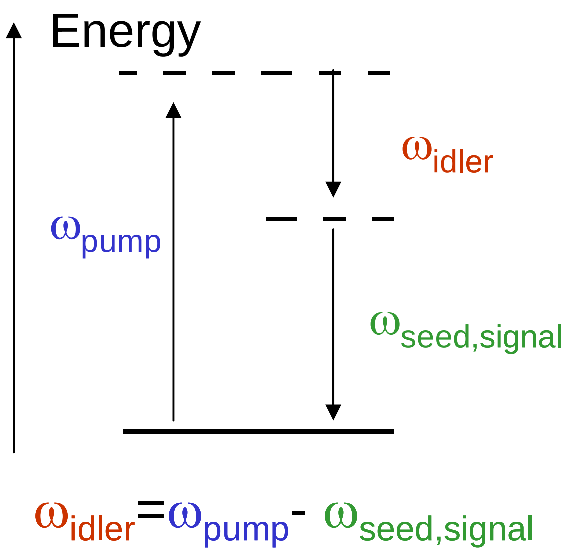

Figure 2.7. Energy level diagram for difference frequency generation.

At first glance Figure 2.7 looks very similar to Figure 2.5; however, there are some important differences. When two frequencies are incident on a medium with a nonzero second order susceptibility, five terms can result (four with nonzero frequency) from the induced second order polarization (due to phase matching – conservation of momentum – one term will typically dominate [9]). The difference frequency term is [9]

$$P_{DFG}^{(2)}(t)=2\chi^{(2)}E_1E_2^*e^{-i(\omega_1-\omega_2)t}. \qquad (2.7)$$

As the name implies, a field is produced at the difference between the two input frequencies. Figure 2.7 illustrates an important consequence of energy conservation. For each new photon created at the difference frequency, ω_{idler}, another must be produced at the signal frequency. As well, ω_{idler} can interact with the pump to produce new signal photons further "amplifying" the signal frequency. This process can occur spontaneously through superflorescence seeding [11], but is enhanced dramatically by the introduction of a seed at the signal wavelength as is implemented here.

The seed is considerably chirped by the supercontinuum process and is then longer than the second harmonic pump. As a consequence, a variable delay (stage) can temporally overlap the pump with different spectral components of the spectrally broad seed allowing selective amplification across the visible. For experiments where a large bandwidth is required, the chirp of the seed is a problem. There are many techniques for handling this issue including seed compression, chirping the pump, long crystals to allow different spectral components to amplify as the pump slips in relation to the seed, and the use of all reflective optics (mirrors in place of lenses). These techniques along with others such as pulse-front matching having been used to achieve sub-5fs pulses from NOPAs operating in the visible [15]. Following the amplification the pulses are then compressed taking advantage of the relative flat structure of the supercontinuum. For the experiments presented here, the probe pulse is filtered with an interference filter (540 ± 5nm) following parametric amplification, and such practices were not necessary. Another broadband NOPA is under development in the lab.

Since the NOPA is producing a probe for kinetic traces, broad bandwidth is not an immediate requirement. The broad bandwidth of the seed makes the NOPA in this configuration a wonderful tool for producing probe pulses throughout the visible where the electronic absorption bands of materials can be studied. Optical parametric amplification can be done through collinear mixing of the pump and signal as well as through a noncollinear geometry. The collinear geometry limits pulses widths to above 50fs [14]. Although the phase velocities of the pump and idler may be effectively phase matched by proper orientation of the birefringent medium's optic axis, group velocity matching is not ensured. The higher frequency idler will travel faster than the signal. Since the two pulses continuously amplify each other as they propagate through the crystal, the idler will introduce photons to the leading edge of the signal pulse, as the signal introduces photons to the rear of the idler. The noncollinear crossing angle makes it possible to match the group velocity of the signal and idler pulses at the expense of some spatial spread as was first demonstrated in an optical parametric oscillator [16]. Riedle extended the principle to OPAs [10] and showed that group velocity matching was equivalent to broadband phasematching [14].

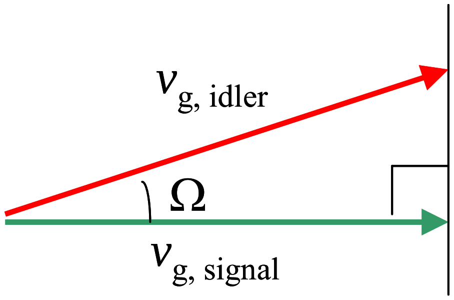

Figure 2.8. Group velocity matching through noncollinear crossing geometry in the nonlinear crystal.

Figure 2.8 illustrates graphically that the projection of the idler group velocity can be made equal to the signal group velocity (for Type I mixing, the idler will travel faster than the signal), according to [14]

$$v_{g,idler}\cos\Omega = v_{g,signal}, \tag{2.8}$$

where Ω is the angle between the signal and idler as defined in Figures 2.8 and 2.9. The experimentally relevant pump, supercontinuum crossing angle, Ψ, can be expressed in terms of the angle Ω [14].

$$\Psi \approx \frac{\Omega}{\left(1+\frac{\lambda_{idler}}{\lambda_{signal}}\right)}, \tag{2.9}$$

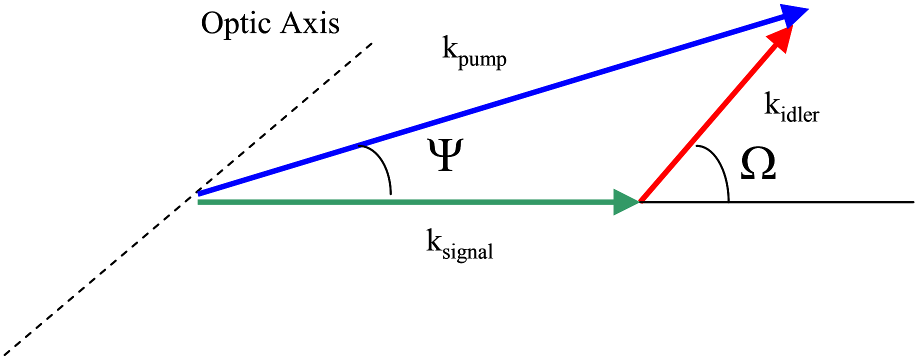

Figure 2.9. Wave vectors in noncollinear geometry [14].

Typical internal crossing angles in the employed design shown in Figure 2.4 were ~3-4°. See Appendix A for the calculation. In addition to broadband phasematching, the noncollinear geometry is easily constructed.

Possible improvements of the current NOPA setup include the improvement of efficiency and pulse stability. Bargheer [17] has demonstrated a modified design of that in reference [10] efficient enough to pump a NOPA with only 0.11mJ/pulse input energy, and deliver ~10μJ/pulse output. These results were achieved by optimized focusing conditions and wave front matching in the difference frequency generation crystal. As well, the efficiency of the second harmonic pump generation is improved to ~40% again through optimal focusing conditions. Such improvements would prove useful for two color experiments where both pump and probe are produced through parametric amplification. Improvement beyond efficiency and stability is being implemented in the broadband NOPA already mentioned. Two examples of very preliminary spectral outputs are shown in Figure 2.10. Assuming a Gaussian pulse, the spectra shown are already broad enough to support ~10fs pulse widths in the transform limit (i.e. after compression). Note that the spectra are centered at a different wavelengths than the NOPA used for the experiments described in this thesis.

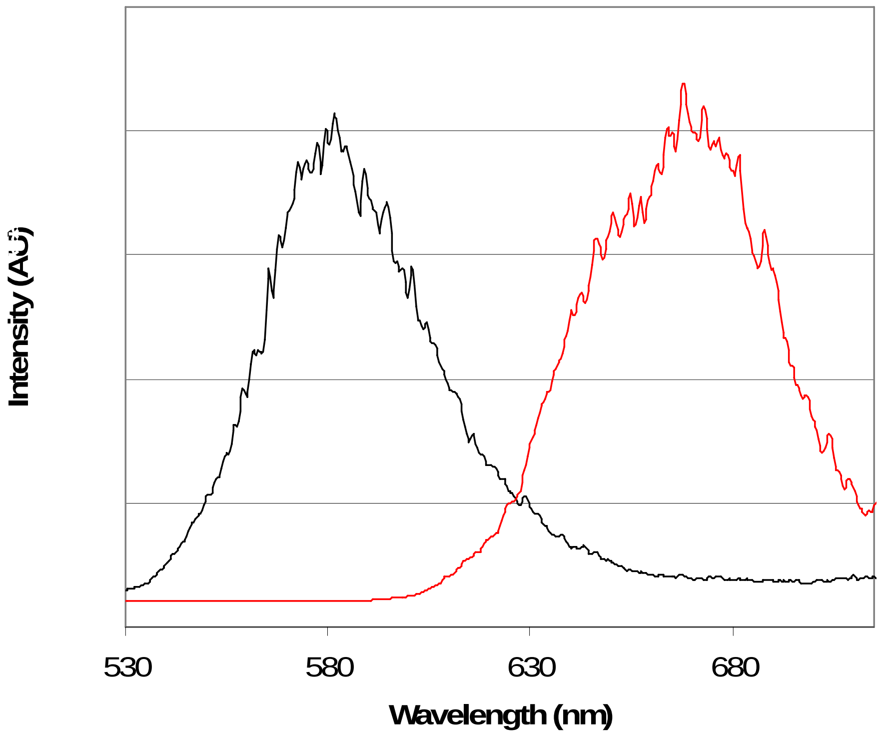

Figure 2.10. Broadband NOPA spectra (the lower wavelength, ~580nm centered spectrum was obtained with a hotmirror filter placed before the spectrometer coupling fiber; no filters were used for the ~670nm centered spectrum).

The setup described above is quite versatile and can be easily modified to change both pump and probe as has been done for previous experiments (for example [4]).

2.2.3 Beam Quality

One example of the quality of the beam produced by the laser system described above is the focusability of the beam. An example beam profile measurement is shown below in Figure 2.11.

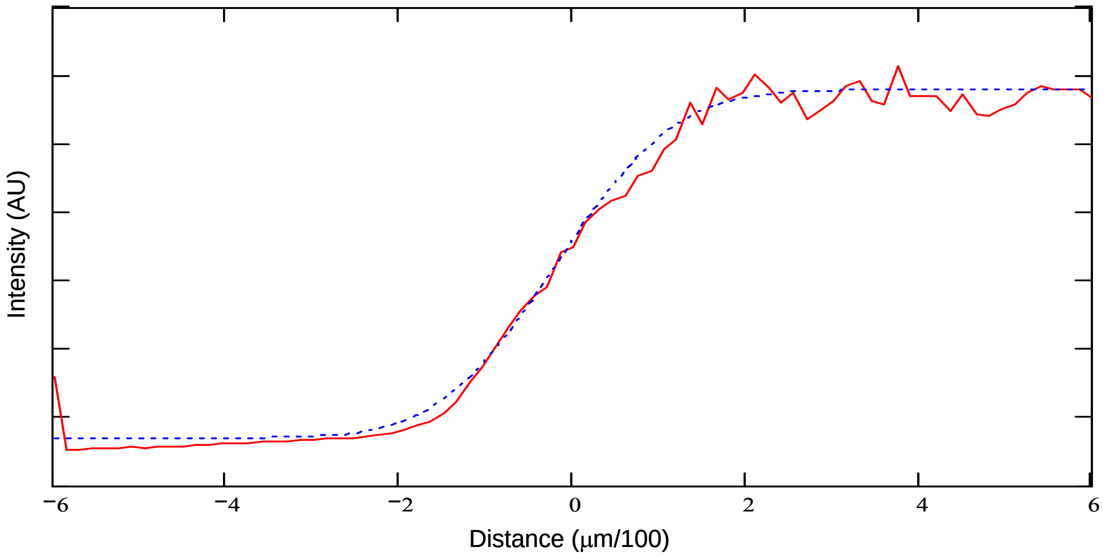

Figure 2.11. Beam focus profile measurement of the fundamental, Ti:Sapphire (red—average of two scans done with a razor blade mounted to a mechanical stage). A least squares fit to a complementary error function is shown as a dashed blue line.

The measurement done shown in Figure 2.11 was completed by using a razor blade mounted to a motorized stage to “slice” through the laser beam before imaging onto a diode which recorded the intensity. To the left side in Figure 2.11 (before ~-200μm), the beam is completely blocked. The beam is no longer obstructed by ~+200μm. The razor blade was positioned at the focus of a long focal length lens for this measurement. This measurement was completed on the 800nm beam. A least squares fit of the profile trace was done to a complementary error function (blue dashed line). Assuming a Gaussian spatial beam profile the scan shown in Figure 2.11 gives a beam diameter of (180 ± 20)μm. This result agrees well with the expected value; namely that anticipated from the expression for a focused Gaussian beam [18]:

$$D = \frac{2w_0}{\left[1+\left(\frac{z_0}{f}\right)^2\right]^{1/2}}, \tag{2.10}$$

with D the focused diameter, w_0 the beam radius at the focusing lens, f the focus length, and z_0 the Rayleigh range of the input beam,

$$z_0 = \frac{2\pi w_0}{\lambda}. \tag{2.11}$$

A very useful variant of Equation 2.10 used numerous times in setting up the optical apparatus described in this chapter is to determine the beam diameter at positions away from the focus. This expression is included in Appendix B.

2.3 Sample Setup

Now that two pulses, a pump and probe, have been produced at the proper wavelengths and with short temporal widths, transient absorption spectroscopy can be performed on the alkylcobalamin samples. The polarizations of the two pulses relative to each other are set with half wave plates so that they make the "magic angle" of ~54.7°. At this angle the observed absorption change contains only information about population kinetics and orientation dynamics are not a factor in the measured time constants [19-21]. For molecules of the size considered here, orientation times can range into several hundred picoseconds. The pump and probe beams are then crossed in a flow cell as illustrated in Figures 2.4 and 2.12.

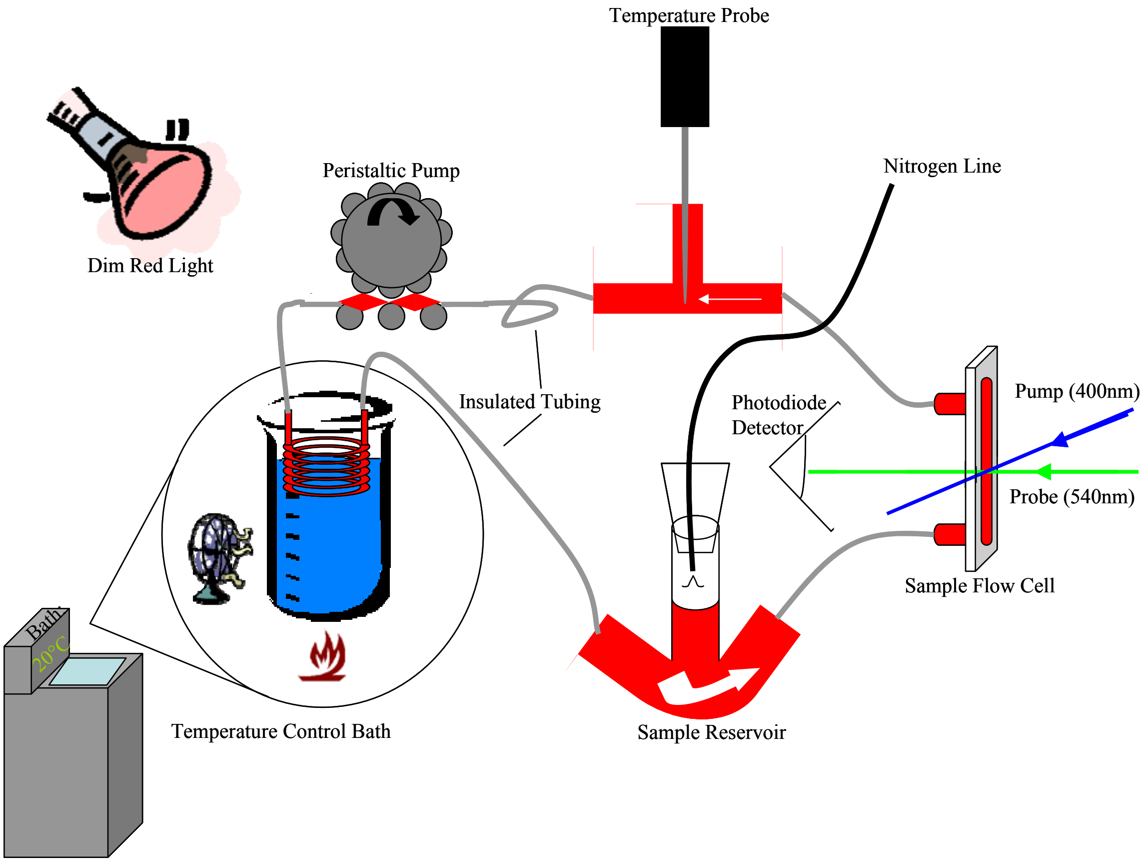

Figure 2.12. Sample setup: flow and temperature control.

The signal beam is imaged onto two matched photodiodes which monitor on a shot-to-shot basis (this is possible at 1kHz repetition). A reference diode collects ~4% reflection before the sample and the second, signal diode, is place after the sample. By taking the ratio of these two signals, pulse to pulse fluctuations can be removed from the collected data. A third diode is used to monitor the pump beam to determine whether each “shot” is pump or unpumped. An optical chopper is placed in the pump path to chop.

The sample is flown through a reservoir, coil system which can be placed in a temperature controlled bath. This setup made it possible to vary the sample temperature from less than 0°C to greater than 80°C, thereby changing the solvent viscosity as is described in detail in Chapter 4 (Section 4.1.3). The temperature is monitored immediately following the sample's exit from the flow cell with a thermocouple probe placed in the flow line. A light nitrogen over pressure was placed on the sample reservoir to maintain an anaerobic environment to maintain the homolytic bond cleave of the carbon- cobalt bond without interaction with oxygen from the ambient environment.

Due to very limited quantities of the synthesized alkylcobalamins as small a sample volume was used as possible (~13mL), in conjunction with a small volume peristaltic pump. The sample was moved fast enough to ensure a fresh sample on each shot. Due to the small volume, care had to be taken to ensure no photoproduct buildup as described in the data sections of this thesis. The sample was handled in dim, red light conditions (no light was used when possible).

The steady state absorption spectrum was obtained with a commercial two lamp UV-Vis spectrometer, capable of measuring form 190 to 1100nm.

2.4 Chirp: Compressor Improvements

Several possible improvements have been identified to increase the power output of the CPA system. The most readily tractable are in the stretching and compressing of the pulse. These components will be described in detail to establish the proposed improvements.

A grating based stretcher is employed to provide the chirp necessary for chirp pulse amplification; and a grating based compressor is used to recompress the amplified pulse. In these devices the dispersion imparted by the grating pair is exploited to produce a frequency dependent delay, thereby stretching or compressing the pulse in time. A schematic of a standard Treacy grating-pair compressor [22] is shown in Figure 2.13.

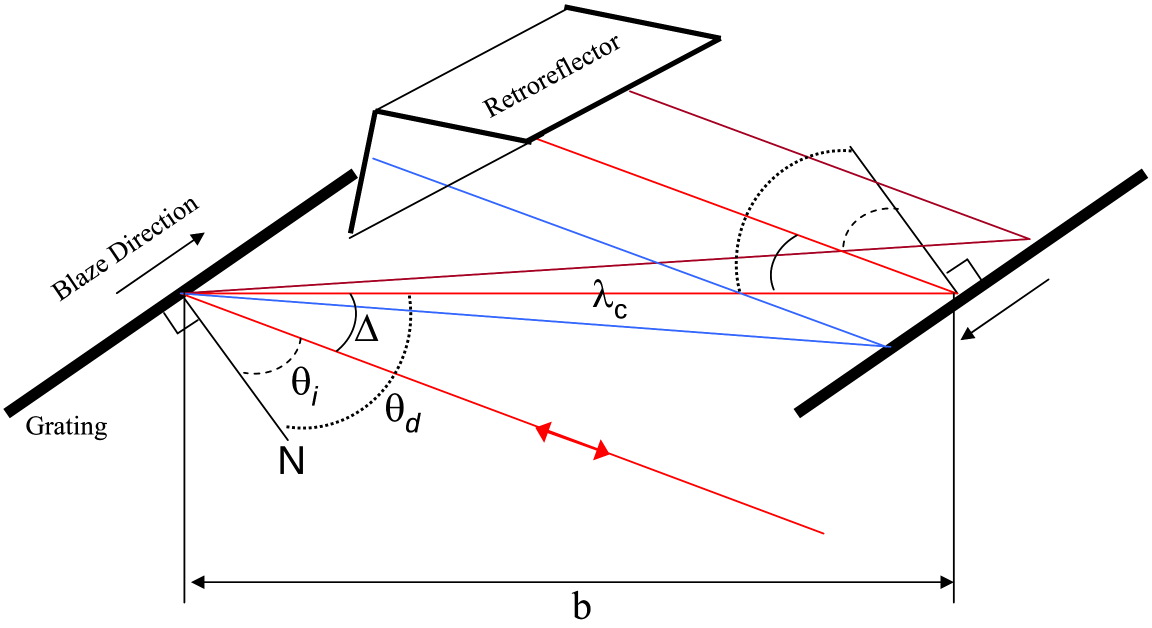

Figure 2.13. Treacy Grating Pair Compressor

The amplified pulse, represented by the red line with arrows, is injected into the compressor at an angle θ_i from the grating normal, N. The central wavelength, λ_o, is then diffracted at angle θ_d. The second grating is parallel to the first so that the diffracted frequency is incident to the second grating normal at θ_d. Wavelengths longer than λ_o are diffracted at larger angles than the central frequency and those shorter than λ_o are diffracted at smaller angles. The net result is that the pulse picks up a frequency dependent delay (temporal chirp), with the shorter (bluer) wavelengths traveling a smaller optical path length than the longer (redder) wavelengths. Since the pulse frequencies are then spatially dispersed as well, the pulse is redirected back along the same path through the grating pair to remove the spatial chirp, acquiring twice the temporal chirp in the process. The retro-reflecting mirror setup elevates or lowers the pulse so that it can be extracted after the second pass.

The accrued group delay dispersion after two passes through the grating pair is given by [7, 13, 23]:

$$\phi''(\lambda_0) = \frac{-\lambda_0^3 b}{\pi c^2 d^2 \cos^2 \theta_d}, \tag{2.12}$$

where *b* is the grating separation as defined in Figure 2.13, *d* is the grating groove density, and *c* is the speed of light. It is apparent from Equation 2.12 that the second order dispersion is necessarily negative for this design; the shorter wavelengths traverse a shorter optical path than the longer spectral components. The third order dispersion is, however, positive:

$$\phi'''(\lambda_0) = -\phi''(\lambda_0)\frac{\lambda_0}{2\pi c}\left(1 + \frac{\lambda \sin \theta_d}{d \cos^2 \theta_d}\right). \tag{2.13}$$

Providing the longer wavelengths with a shorter optical path length, imparting a positive chirp, can be done with a negative effective grating separation, *b* [7, 13, 23, 24]. Insertion of a lens pair between two gratings allows the first grating to be imaged behind the second, as depicted in Figures 2.14 through 2.16.

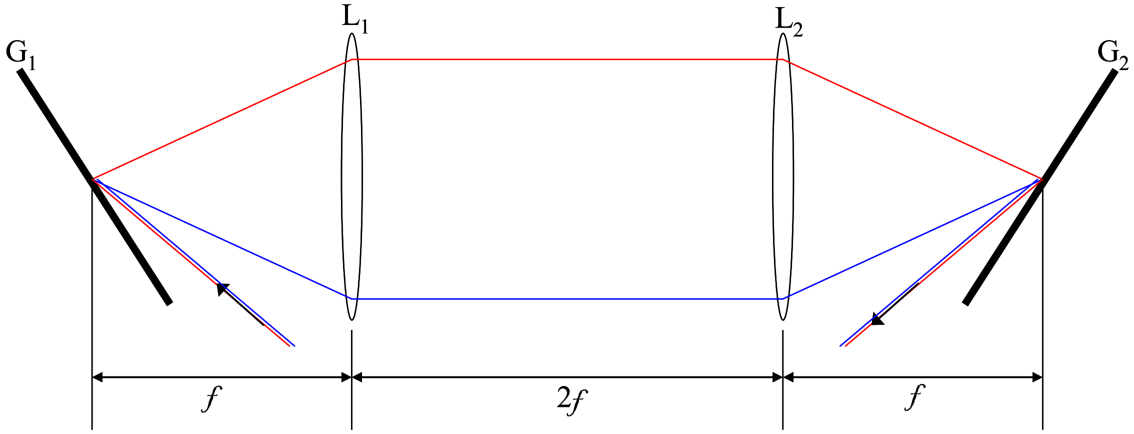

Figure 2.14. Gratings arranged in Martinez 4f telescope.

The 4*f* layout in Figure 2.14 uses a telescope to image the beam spot on the first grating, G_1, at grating 2 with magnification one; the focal lengths of lenses L_1 and L_2 are both *f*. Such a layout can be used for phase and amplitude shaping of ultrashort pulses in the frequency domain by placing an appropriate mask in the Fourier plane (midway between the two lenses of the telescope). Figure 2.15 illustrates the utility of the 4*f* design for producing positive group delay dispersion.

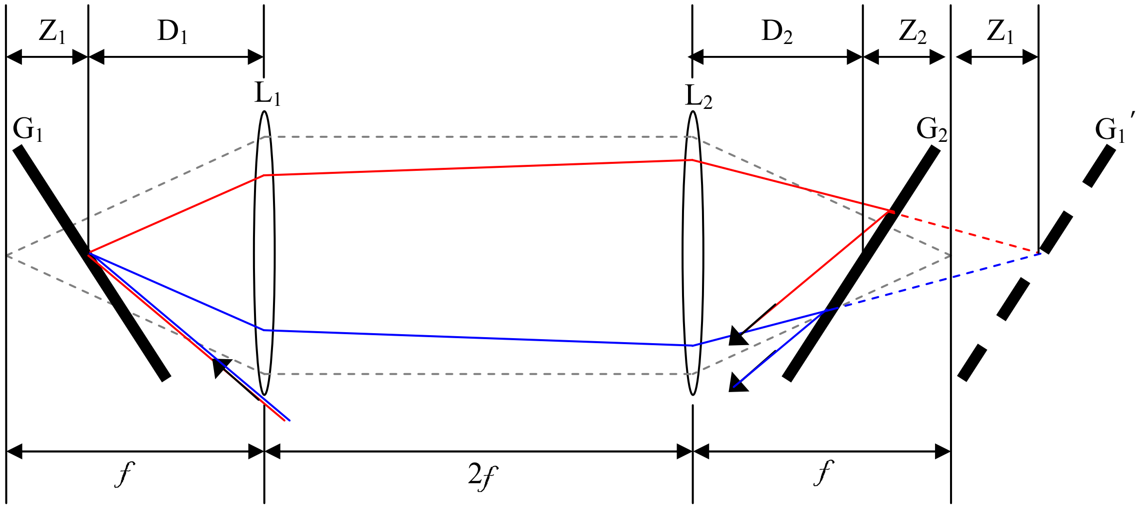

Figure 2.15. Martinez 4*f* Stretcher

Moving the second grating, G_2, nearer L_2 and away from the focus results in the image of G_1, G_1', falling behind G_2; i.e. there is an effective negative grating separation, $b = -Z_2$, between the two gratings. Similarly, moving G_1 towards L_1 places the image, G_1', further behind the second grating, such that the effective path length is given by

$$b = -(Z_1 + Z_2)\,. \tag{2.14}$$

Since the expressions describing stretcher induced dispersion will be identical to those for the compressor (Equations 2.12 and 2.13), the sign of the second and third order dispersion will be opposite to that in the compressor. The second order dispersion will be positive, and the third order dispersion negative.

Due to the large bandwidth inherent in femtosecond pulses, it is preferable to use an all reflective optical design for the stretcher. The 4*f* stretcher as experimentally realized in the chirped pulse amplification system described above [1, 2] is sketched in Figure 2.16.

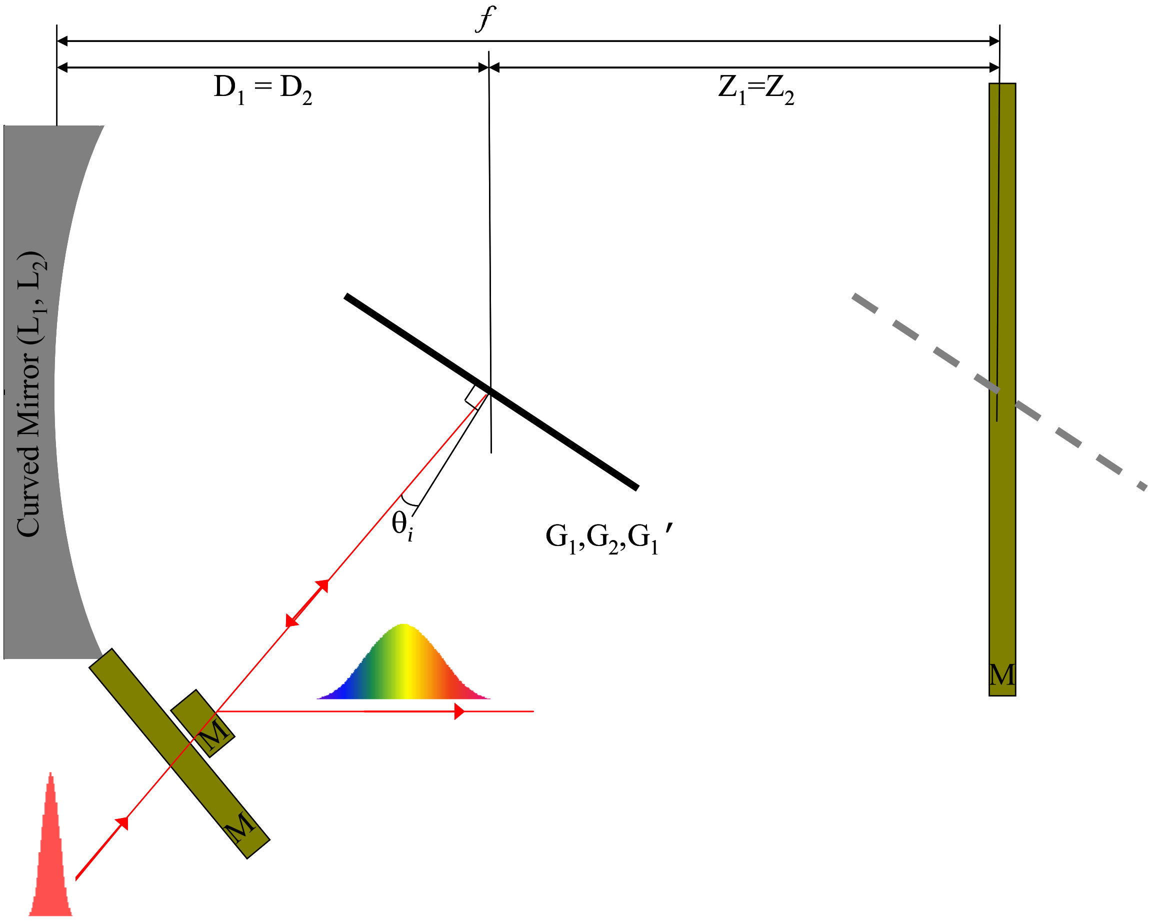

Figure 2.16. All Reflective Stretcher

Figure 2.16 illustrates the correspondence between the pertinent measurements in the Martinez stretcher and more practical all reflective design. The two lenses are replaced by multiple reflections from one large curved mirror. The diameter of the curved mirror is large so as to accommodate as large a bandwidth as possible. One grating is used as well, insuring antiparallelism between the first and second passes of the grating (or that the image of G_1 is parallel to G_2). Flat mirrors, M, are placed at the focus of the curved mirror, and such to reinject the pulse for a second pass and for pulse ejection. There is a slight tilt in the optical path length from the dispersion plane in order to allow the multiple passes and to cleanly pick off the beam. As long as the tilt is kept small, the dominant aberrations are spherical [7]. The location of the grating in the perfect $4f$ design (no stretching) is indicated by the gray dashed line crossing the curved mirror focal plane.

There are many designs for optical stretchers, some aberration free [7, 23, 25]. However, these designs are often complex, suffer from large higher order dispersion and are unnecessary for the powers and efficiencies relevant to the laser system described above and used for these experiments [7, 23]. The design in Figure 2.16 allows easy alignment (using the zeroth diffracted order) and adjustment.

If the pulse injected into the stretcher is initially unchirped, the pulse length to second order after passing through the stretcher is [13, 26]:

$$\tau_p = \tau_0 \sqrt{1 + \left(\frac{(4 \ln 2)\phi^{2"}}{\tau_0^2} \right)^2} \, . \tag{2.15}$$

Assuming an input transform limited pulse, τ_p = 20fs (the actual input pulse is probably longer as the oscillator's dispersion control prisms do not compensate for the final pass through the Titanium:Sapphire crystal or the output coupler [27]), the output pulse width can be estimated at ~180ps to second order, using Equations 2.12 and 2.15. The pulse is stretched by a factor of ~10,000. The grating separation, *b*, measured at 29.6cm., is plugged into Equation 2.12 to obtain the ~180ps pulse which is suitable for amplification in the multipass amplifier.

It would seem then that at least to third order, ignoring the aberrations which result from the stretching and compressing optics, the pulse dispersion can be perfectly corrected for by setting the incidence angles in the stretcher and compressor equal.

Unfortunately, a complication arises once the amplification process is considered as the material making up the amplifier (lenses, amplification and pulse picking crystal) will also result in further stretching of the pulse. Here the second and third order dispersion are described by [7, 13, 23]:

$$\phi''_{mat}(\lambda_0) = \frac{\lambda_0^3 l}{2\pi c^2} \left. \frac{d^2 n}{d\lambda^2} \right|_{\lambda_0}, \tag{2.16}$$

$$\phi'''_{mat}(\lambda_0) = -\left(\frac{\lambda_0^4}{4\pi c^3} \left. \frac{d^2 n}{d\lambda^2} \right|_{\lambda_0} + \frac{\lambda_0^5}{12\pi^2 c^3} \left. \frac{d^3 n}{d\lambda^3} \right|_{\lambda_0} \right) l\,. \tag{2.17}$$

l is the distance propagated through the material; and *n* is the frequency dependent refractive index, characteristic of the medium. Both of these quantities are positive, and therefore the overall second and third order dispersion cannot be simultaneously compensated with identical incidence angles to the grating normal. Kane and Squier [23] show that by introducing an angle mismatch, where the compressor incidence angle is a function of material length traversed (*l*), the second and third order dispersion can be compensated. It was determined that such an adjustment was unnecessary for the experiments described herein, based on second harmonic autocorrelation measurements. The multipass design helps to minimize dispersion as compared to the more common regenerative amplifier. A typical autocorrelation with an autocorrelation FWHM ~90fs is shown in Figure 2.15.

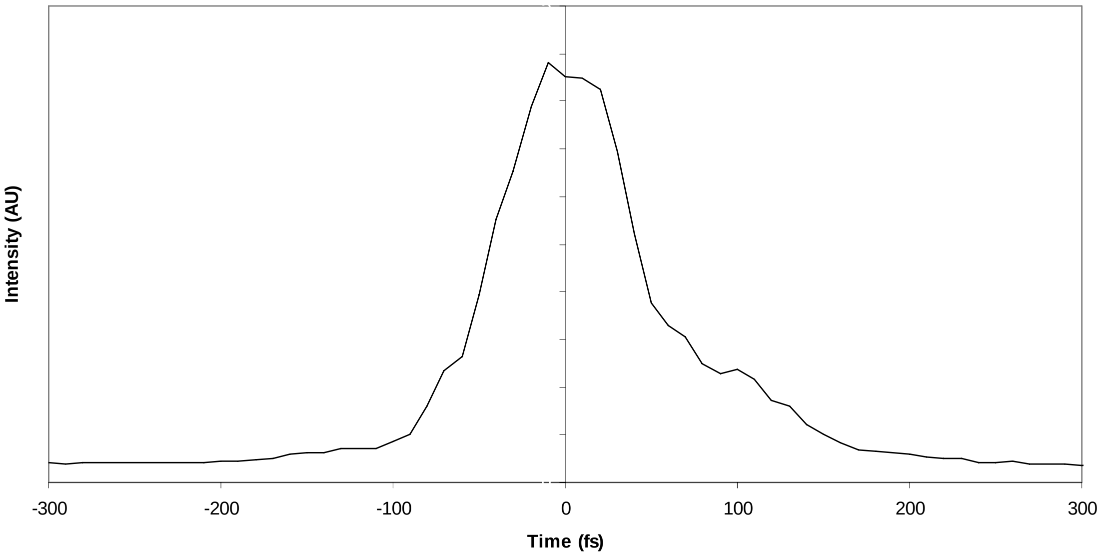

Figure 2.17. Typical SH Autocorrelation Trace

The radical recombination and escape time constants are typically on the order of 100s of picoseconds to nanoseconds. The temporal width of the pulse shown in Figure 17 is on the order of 60fs. Nonetheless, a calculation to determine the optimal compressor incidence angle is described in Appendix C, along with the arguments presented by Kane and Squier, in the hope that this result may prove fruitful for future, more temporally demanding experiments. As it turns out, slightly longer (~100fs) pulses result in better NOPA performance as described above, providing even less impetus to further improve upon stretcher and compressor design as it relates to the pulse width for these experiments.

One area in particular that has plagued the pulse compression setup currently in use and described above is the power throughput efficiency. The current setup, illustrated above in Figure 2.13 and below in Figure 2.18 has demonstrated only ~45-

49% throughput efficiency at best. Similar to the case for the pulse widths, the power and consequently the energy per pulse, exiting the compressor is more than enough to complete the experiments presented here. With typical amplifier output on the order of 1W at 1kHz repetition rate (1mJ/pulse energy), compressed pulses with energies around 500μJ were routinely available. The pulse energy requirements for the alkylcobalamin experiments described here are: 1. Second harmonic pump with pulse energy ~2μJ; 2. NOPA generated visible probe, described in detail above. With 500μJ compressed fundamental input into the experimental setup, extensive use of neutral density filters was necessary in order to keep the probe energy small (so as not to induce further excitation in the sample), and the excitation pulse at 2μJ. Although not necessary for these experiments, as for the case of pulse widths, it is likely more stringent experimental parameters will soon require larger pulse energies. Improvement of the compressor design is the best candidate to easily and dramatically improve the useable pulse energies available for experiments. The basis supporting this statement is that typical compressor efficiencies are at least greater than 60%; improvement to standard should then give >10% more useable energy per pulse compared to the current efficiency. Blazed gratings can shift the peak of the diffraction pattern away from the zeroth order (specular reflection). Careful choice of blaze angle along with the incidence angle of the input beam from the grating normal routinely results in first order efficiency on the order of ≥90% [28, 29], after one pass off a grating. After four passes from grating surfaces, as is the case in the compressor design, efficiencies on the order of $\eta^4 \sim 0.9^4 = 65\%$ are possible. As the first order diffraction efficiency is improved above 90%, the compressor efficiency continues to improve as η^4. The inclusion of the retroreflector introduces an additional source of losses, expected to be on the order of ~ 1 - $0.98^2 \approx$ 4% (two reflections from a gold mirror in this setup).

A ruled reflection grating with triangular blaze is shown in Figure 2.18. This is the type of grating employed in the compressor described above. The interference pattern resulting from a monochromatic source of light on the grating is governed by the groove density, N. The intensity of each order in the interference pattern is scaled by the diffraction pattern. In the case of no blaze, the most intense order will be the zeroth order. Since there is no dispersion for the zeroth order (when a polychromatic beam is introduced), any light directed into this order is wasted [30], as is any light directed into orders besides those employed for producing dispersion in the optical device. The peak of the diffraction pattern is that point for which there is no farfield phase delay between the different spatial components of the diffracted beam, and corresponds to the condition of specular reflection from the grating face when there is no blaze, accounting for the zeroth order's intensity domination. Introduction of a grating blaze shifts the point of zero farfield phase delay away from the zeroth order. It is possible to manufacture gratings with other types of blaze than that illustrated in Figure 2.18, such as a sinusoidal blaze [28, 31]; these will not be discussed here. The efficiency of triangular grooved gratings is not as susceptible to the angular deviation (Δ) between the incident in diffracted beams as it is for holographic gratings [32]. For a triangular blaze grating the condition of zero phase delay (peak of the diffraction intensity) is geometrical reflection from the blaze normal [30], N_B, where the angles of incidence, Θ_i, and reflection, Θ_r, from the blaze normal are equal to each other.

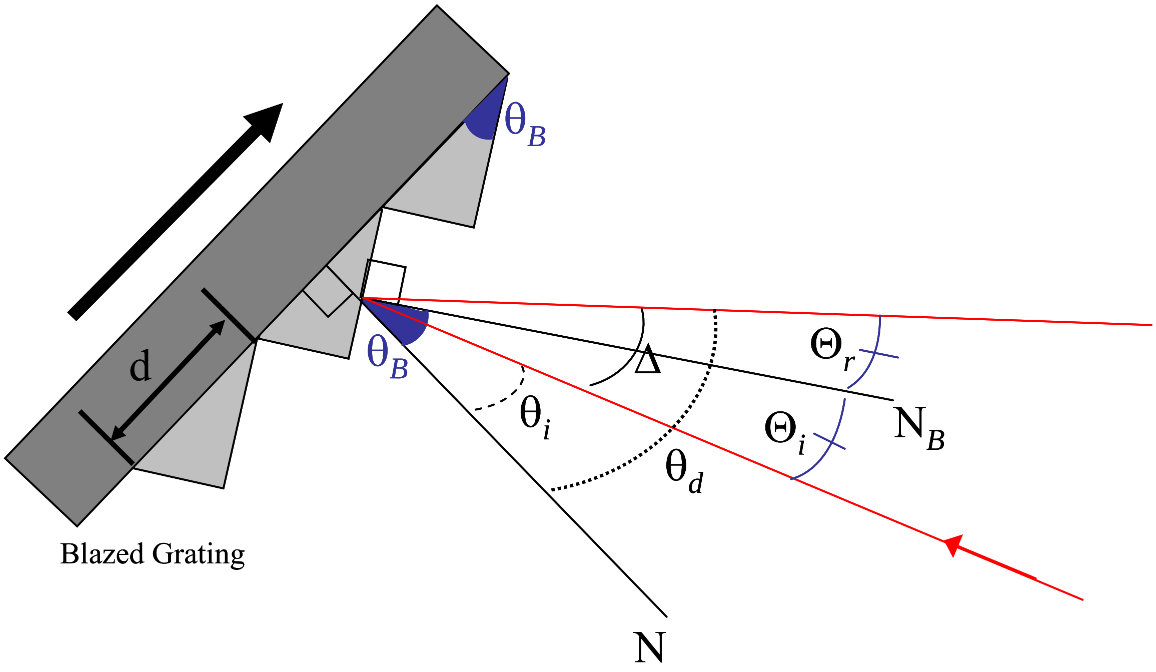

Figure 2.18. Ruled reflection grating with triangular blaze.

In terms of the most readily obtained and used experimental parameters, $\Theta_i = \Theta_r$ can be expressed as

$$\theta_d - \theta_B = \theta_B - \theta_i\,, \tag{2.18}$$

and then rearranged to give the diffracted angle in terms of the blaze angle

$$\theta_d = 2\theta_B - \theta_i\,. \tag{2.19}$$

Combining the relation for diffraction angle under optimal blaze conditions with the grating equation,

$$Nm\lambda = \sin(\theta_i) + \sin(\theta_B)\,, \tag{2.20}$$

where *m* is the order number, λ the wavelength and *N* =1/d is the groove density, gives:

$$\theta_B = \frac{1}{2}\left[\theta_i + \sin^{-1}(Nm\lambda - \sin(\theta_i))\right]. \tag{21}$$

Equation 2.21 is the optimal blaze angle, as a function of incidence angle, input wavelength, and groove density. Figure 2.19 plots the optimal blaze versus input angle, along with the associated angle of diffraction, for 800nm light and $N = 1200\text{mm}^{-1}$ groove density. The diffraction angle can be found either from the grating equation (Equation 2.20) or from Equation 2.19. The diffracted angle, θ_d, is plotted in red; and the optimal blaze angle, θ_B, is colored blue.

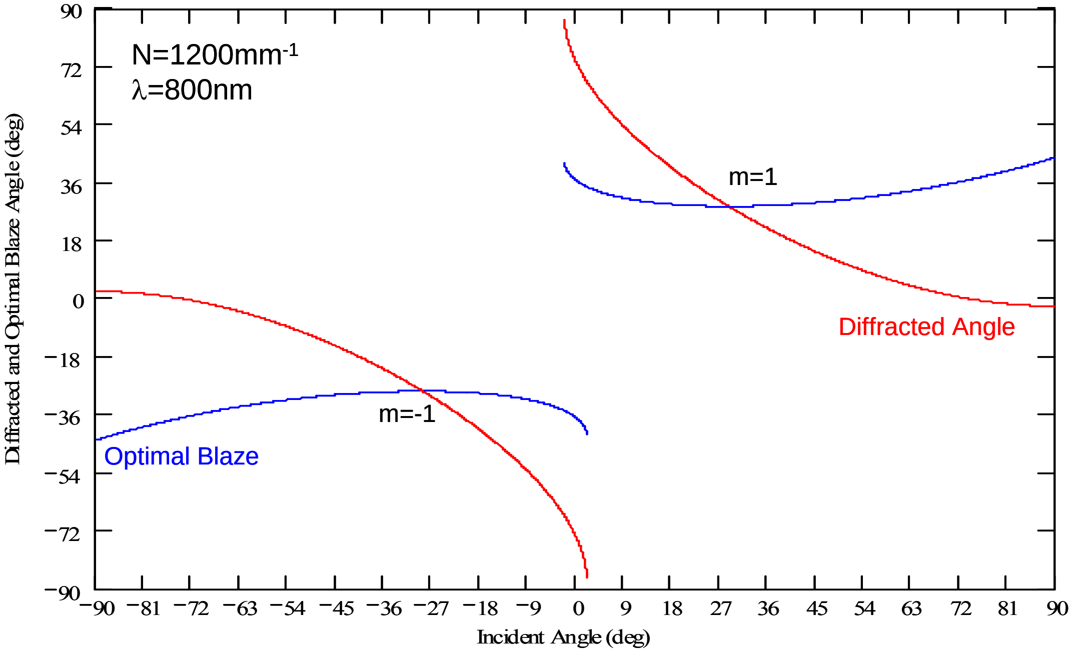

Figure 2.19. Optimal grating blaze as a function of incidence angle.

To interpret Figure 2.19 for use in grating selection the sign convention must considered. For this figure, one side of the grating normal is positive and the other is negative, so that angles produced by rotation to one side of the grating normal are positive and to the other are negative. In Figure 2.18 angles measured counterclockwise from the grating normal are positive and those measured clockwise from the grating normal are negative. Therefore, both θ_i and θ_d are positive as shown in Figure 2.18. The plots demonstrate that blaze angle is on the same side of the grating normal as the diffracted angle (under conditions of optimal blaze).

Figure 2.18 and Equation 2.21 are just guides in selecting the best blaze for a particular application as there are numerous details and complications inherent in the grating blaze and the manufacture of the grating (and its blaze) [28, 29]. Specifically there are anomalies in the efficiency curves for gratings. Individual efficiency curves should be consulted when choosing the best grating from the available selection. The efficiency and bandwidth throughput are generally best when the angle of deviation between the incident and diffracted beams (angle Δ in Figure 2.18) is kept at a minimum [29, 32]. There are several options for improving the efficiency of the compressor setup used for these experiments. These include choosing groove densities to minimize bandwidth loss. The incident angle may also be made greater in relation to the Littrow angle in order to improve bandwidth efficiency . However, the most immediate and straightforward change is to reduce the angle of deviation (Δ) between the incident beam and the diffracted order. It is desirable that the deviation not be in excess of 10° [32]. Minimizing the deviation can be done by increasing the incident injection angle. There will be complications owing to the limited space available for geometry; especially in the stretcher which must be matched (or at least correlated to depending on the angle matching program – Appendix C) to the compressor. Figure 2.20 shows a theoretical absolute efficiency plot from a product catalog [33] to illustrate the reasoning for increasing incidence angle (thereby reducing deviation angle). The calculation plotted in Figure 2.20 is for a 1200groove/mm, gold coated, holographic grating, with operation set to the first order. This is not the grating used in our lab (where plane ruled gratings are used); but the plot is useful for demonstrating the general efficiency characteristics (the efficiency for each position marked, θ_i and θ_d, will be different). Figure 2.20 shows that for the θ_i and θ_d chosen, the efficiency curves begin to drop down, especially as the wavelength varies toward the lower part of the Ti:Sapphire bandwidth (the efficiency is symmetrical about $\theta_{Littrow}$ as expected based on the reciprocity theorem [32, 34]).

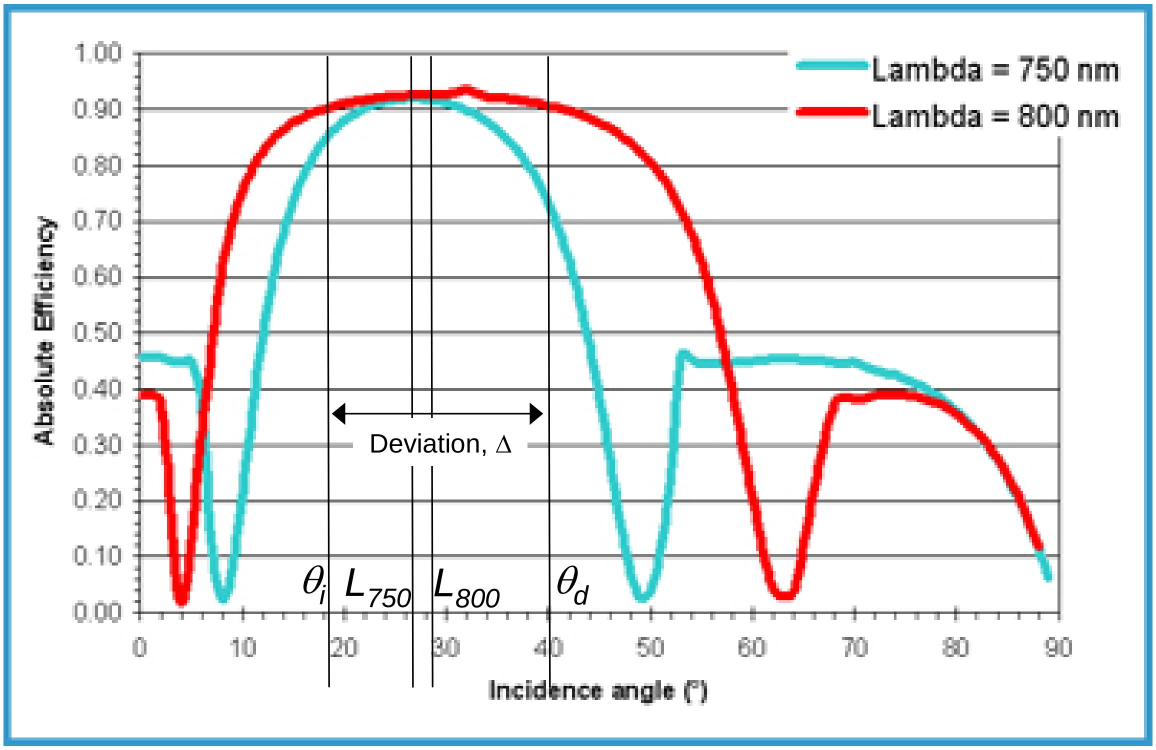

Figure 2.20. Calculated absolute efficiency curves in the first diffracted order versus incidence angle (from grating normal) for a gold coated reflection, holographically grooved grating. Plots are shown for 750 (blue) and 800nm (red). θ_i and θ_d used for the compressor described above are as indicated in the Figure. L_{750} and L_{800} are the Littrow angles at 750 and 800nm respectively. Figure modified from Reference [33].

Commercial software is available for calculating the efficiency of diffraction gratings versus incidence angle, as well as for a host of other parameters. One such example, PC-Grate [35], was used to predict the absolute efficiency versus incident angle for the gratings used in the compressor described above (blazed grooves this time versus the holographically grooved grating analyzed in Figure 2.20). The calculation was performed by I.I.G. Inc. Support. The results are plotted in Figure 2.21.

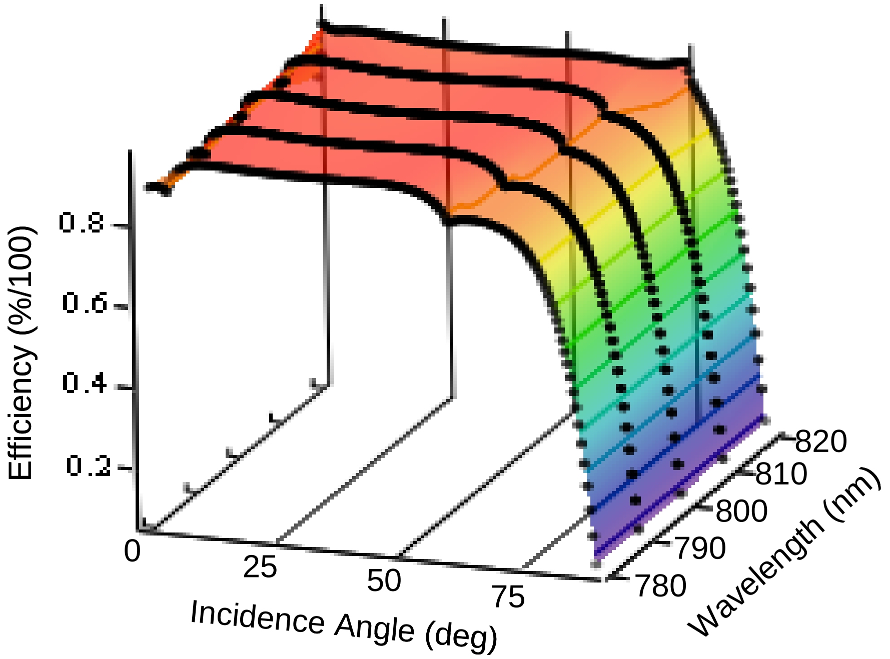

Figure 2.21. Absolute efficiency versus incidence angle calculated with PC-Grate [35]. The calculations are for the first diffracted order of a gold coated, 1200grooves/mm grating with blaze angle 21.1°. Plots are shown for several wavelengths as labeled in the Figure.

Figure 2.21 shows a relative broad plateau of high efficiency centered about the Littrow angle, which decreases in width with decreasing wavelength as anticipated from Figure 2.20. The drops in efficiency at either end of the plateau are not as pronounced as those plotted in Figure 2.20. An earlier version of this program has been shown to have difficulty in the case of TM polarization (S polarization in relation to the groove surface of the grating; this is the polarization of the incident light used to produce the maximum efficiency) for certain applications [36], and therefore should also only be considered a guide. It is still strongly anticipated that decreasing the deviation between incident and diffracted beams will greatly improve the efficiency of the compressor.

Kane suggests [37] another possibility is to maintain the larger angle in the stretcher if necessary and compensate with a higher groove density and smaller grating separation in the compressor (i.e. grating mismatch between the stretcher and compressor [38]), employing a holographic grating like that considered in Figure 2.20. This layout would allow for a smaller deviation angle, Δ, in the compressor compared to that in the stretcher. This point is important since the holographic grating is more susceptible to efficiency loss with increasing deviation angle than the plane ruled grating. As well, this design has the potential to compensate for fourth order dispersion and beam quality is expected to be improved over ruled gratings. Such a scheme has been employed in a nearly petawatt system [39].

2.6 Bibliography

1. Walker, L., *Ultrafast Transient Absorption Studies of Vitamin B12 Coenzymes: Investigation of the Cobalt-Carbon Bond in Alkylcobalamins*, in *Chemisty*. 1998, University of Michigan: Ann Arbor, Michigan.

2. Rudd, J.V., *Advanced Techniques for the Amplification of Sub-100-Femtosecond Pulses in Ti:Sapphire-Based Laser Systems*, in *Electrical Engineering*. 1994, University of Michigan: Ann Arbor, Michigan.

3. Cole, A., *Ultrafast Transient Absorption Studies of Coenzyme B12 Analogs and Derivatives: Biological Activity of Alkylcobalamins*, in *Chemistry*. 2003, University of Michigan: Ann Arbor, Michigan.

4. Harris, D.A., *Studies of Solvent Effects on Reaction Dynamics Using Ultrafast Transient Absorption Spectroscopy*, in *Applied Physics*. 2006, University of Michigan: Ann Arbor, Michigan.

5. Atkins, P., *The Elements of Physical Chemistry*. 2 ed. 1997, New York, New York: W.H. Freeman and Company.

6. Backus, S., Durfee, C.G., Murnane, M.M., and Kapteyn, H.C., *High power ultrafast lasers.* Review of Scientific Instruments, 1998. **69**(3): p. 1207-1223.

7. Kane, S. and Squier, J., *Fourth-order-dispersion limitations of aberration-free chirped-pulse amplification systems.* Journal of the Optical Society of America B-Optical Physics, 1997. **14**(5): p. 1237-1244.

8. Backus, S., Peatross, J., Huang, C.P., Murnane, M.M., and Kapteyn, H.C., *Ti-Sapphire Amplifier Producing Millijoule-Level, 21-Fs Pulses at 1 Khz.* Optics Letters, 1995. **20**(19): p. 2000-2002.

9. Boyd, R., *Nonlinear Optics*. 2003, San Diego, CA: Academic Press.

10. Wilhelm, T., Piel, J., and Riedle, E., *Sub-20-fs pulses tunable across the visible from a blue-pumped single-pass noncollinear parametric converter.* Optics Letters, 1997. **22**(19): p. 1494-1496.

11. Cerullo, G. and De Silvestri, S., *Ultrafast optical parametric amplifiers.* Review of Scientific Instruments, 2003. **74**(1): p. 1-18.

12. Brodeur, A. and Chin, S.L., *Ultrafast white-light continuum generation and self-focusing in transparent condensed media.* Journal of the Optical Society of America B-Optical Physics, 1999. **16**(4): p. 637-650.

13. Norris, T., *Course Notes, EECS 546: Ultrafast Optics*. 2005, University of Michigan: Ann Arbor, MI.

14. Riedle, E., Beutter, M., Lochbrunner, S., Piel, J., Schenkl, S., Sporlein, S., and Zinth, W., *Generation of 10 to 50 fs pulses tunable through all of the visible and the NIR.* Applied Physics B-Lasers and Optics, 2000. **71**(3): p. 457-465.

15. Kobayashi, T. and Baltuska, A., *Sub-5 fs pulse generation from a noncollinear optical parametric amplifier.* Measurement Science & Technology, 2002. **13**(11): p. 1671-1682.

16. Gale, G.M., Cavallari, M., Driscoll, T.J., and Hache, F., *Sub-20-Fs Tunable Pulses in the Visible from an 82-Mhz Optical Parametric Oscillator.* Optics Letters, 1995. **20**(14): p. 1562-1564.

17. Bargheer, M., *Ultrafast photodynamics in condensed phase, ClF, Cl2 and I2 in solid rare gases*, in *Fachbereich Physik*. 2002, Freie Universität Berlin: Berlin.

18. Saleh, B.E.A. and Teich, M.C., *Fundamentals of Photonics*. 1991, New York: Wiley-Interscience Publication.

19. Tan, H.S., Piletic, I.R., and Fayer, M.D., *Polarization selective spectroscopy experiments: methodology and pitfalls.* Journal of the Optical Society of America B-Optical Physics, 2005. **22**(9): p. 2009-2017.

20. Lessing, H.E. and Von Jena, A., *Separation of rotational diffusion and level kinetics in transient absorption spectroscopy.* Chemical Physics Letters, 1976. **42**(2): p. 213-217.

21. Anfinrud, P.A., Johnson, C.K., Sension, R., and Hochstrasser, R.M., *Ultrafast Spectroscopic Techniques*, in *Applied Laser Spectroscopy, Techniques, Instrumentation and Applications*, D.L. Andrews, Editor. 1992, VCH Publishing: New York, New York.

22. Treacy, E.B., *Optical Pulse Compression with Diffraction Gratings.* Ieee Journal of Quantum Electronics, 1969. **QE 5**(9): p. 454-&.

23. Kane, S. and Squier, J., *Grism-pair stretcher-compressor system for simultaneous second- and third-order dispersion compensation in chirped-pulse amplification.* Journal of the Optical Society of America B-Optical Physics, 1997. **14**(3): p. 661-665.

24. Martinez, O.E., Gordon, J.P., and Fork, R.L., *Negative Group-Velocity Dispersion Using Refraction.* Journal of the Optical Society of America a-Optics Image Science and Vision, 1984. **1**(10): p. 1003-1006.

25. Cheriaux, G., Rousseau, P., Salin, F., Chambaret, J.P., Walker, B., and Dimauro, L.F., *Aberration-free stretcher design for ultrashort-pulse amplification.* Optics Letters, 1996. **21**(6): p. 414-416.

26. Siegman, A.E., *Lasers*. 1986, Sausalito, California: University Science Books.

27. *Instruction Manual for Model TS Ti:Sapphire laser kit*. 2002, Kapteyn-Murnane Laboraties L.L.C.: Boulder, CO.

28. Palmer, C., *Diffraction Grating Handbook*. 5 ed. 2002, Rochester, NY: Thermo RGL.

29. Loewen, E.G., Neviere, M., and Maystre, D., *Grating Efficiency Theory as It Applies to Blazed and Holographic Gratings.* Applied Optics, 1977. **16**(10): p. 2711-2721.

30. Pedrotti, F.L. and Pedrotti, L.S., *Introduction to Optics*. Second ed. 1993, Upper Saddle River, New Jersey: Prentice Hall.

31. McPhedra.Rc and Maystre, D., *Detailed Theoretical Study of Anomalies of a Sinusoidal Diffraction Grating.* Optica Acta, 1974. **21**(5): p. 413-421.

32. Wilson, I.J., Botten, L.C., and McPhedran, R.C., *1st, 2nd and 3rd Order Blazes of Diffraction Gratings.* Journal of Optics-Nouvelle Revue D Optique, 1977. **8**(4): p. 217-229.

33. *Gratings for laser pulse compression*. 2007, Horiba Jobin Yvon Catalog Grating Catalog.

34. McPhedra.Rc and Waterwor.Md, *Theoretical Demonstration of Properties of Grating Anomalies (S-Polarization).* Optica Acta, 1972. **19**(11): p. 877-&.

35. *PCGrate-SX 6.2*. 2008, Calculation performed by I.I.G. Support: I.I.G. Inc.

36. Davidson, M., Kleemann, B., and Bischoff, J., *A comparison between rigorous light scattering methods.* Proc. SPIE, 1997. **3051**: p. 606-619.

37. Kane, S., *Personal Correspondance (Conversation)*. 2008.

38. Squier, J., Barty, C.P.J., Salin, F., Le Blanc, C., and Kane, S., *Use of mismatched grating pairs in chirped-pulse amplification systems.* Applied Optics, 1998. **37**(9): p. 1638-1641.

39. Aoyama, M., Yamakawa, K., Akahane, Y., Ma, J., Inoue, N., Ueda, H., and Kiriyama, H., *0.85-PW, 33-fs Ti : sapphire laser.* Optics Letters, 2003. **28**(17): p. 1594-1596.

Chapter 3

Environment Influence on the Excited State of Alkyl- and Nonalkylcobalamins[1]

The results of previous transient absorption studies [1-11] on the alkylcobalamins (adenosyl-, methyl-, ethyl-, and n-propylcobalamin) and the nonalkylcobalamin cyanocobalamin were reviewed in Chapter 1 (Section 1.2). These data demonstrate that the dynamics of bond cleavage and the subsequent radical escape and recombination exhibit a dependence on the solvent environment. The transient absorption techniques described in Chapter 2 were used to extend the earlier work exploring the dynamics following excitation of both the alkyl- and nonalkylcobalamins as a function of the environment. The new work reported here includes investigations of adenosylcobalamin bound to glutamate mutase and studies of methyl-, adenosyl-, and cyanocobalamin as a function of solvent polarity and solvent temperature through the introduction of a sample temperature controlled bath as detailed in Chapter 2 (Section 2.3).

The dynamics of free adenosylcobalamin in water and ethylene glycol were outlined in Chapter 1. Although ethylene glycol provides a more biologically realistic environment in terms of viscosity and dielectric constant than does water, the

---

[1] The data and analysis reported in this chapter has been published in Sension, R.J., Harris, D. A., Stickrath, A. B., Cole, A. G., Fox, C. C., Marsh, E. N. G., *Time-resolved measurements of the photolysis and recombination of adenosylcobalamin bound to glutamate mutase*. Journal of Physical Chemistry B, 2005. **109**(38): p. 18146-18152; and in Harris, D.A., Stickrath, A.B., Carroll, E.C., Sension, R. J., *Influence of environment on the electronic structure of Cob(III)alamins: Time-resolved absorption studies of the S-1 state spectrum and dynamics*. Journal of the American Chemical Society, 2007. **129**(24): p. 7578-7585.

adenosylcobalamin is still in free solution. Studying the dynamics of adenosylcobalamin while bound to the active site in a B_{12} coenzyme dependent protein and comparing to the data in free solution holds the promise of a probe into the biological interaction of the protein with the coenzyme, and ultimately towards an understanding of the biological generation and control of free radicals for the enzymatic catalysis of chemical reactions.

The Co-C bond of adenosylcobalamin in free solution has a bond dissociation energy of 32kcal/mol and associated half-life for homolysis of approximately six months [12-14]. When bound to a protein, Co-C bond homolysis is accelerated by approximately 10^{12} when there is concomitant substrate binding. Since photolysis in adenosylcobalamin is likely a better paradigm for the study of biologically relevant bond cleavage than photolysis in methylcobalamin [9, 15], it is an ideal cofactor for these studies. (Note, however, that previous work has been reported on methylcobalamin bound to protein [8].)

The protein chosen to investigate the bound dynamics of adenosylcobalamin was glutamate mutase. The enzymatic function of glutamate mutase is well characterized; and crystal structures have been determined for the protein with bound coenzyme and substrate [16, 17]. As for other adenosylcobalamin dependent enzymes, catalysis proceeds through the generation of organic free radicals via the homolytic bond cleavage of the Co-C bond. Just as for the case of free adenosylcobalamin, the spectroscopic signature of this bond breaking is that due to the creation of cob(II)alamin radical.

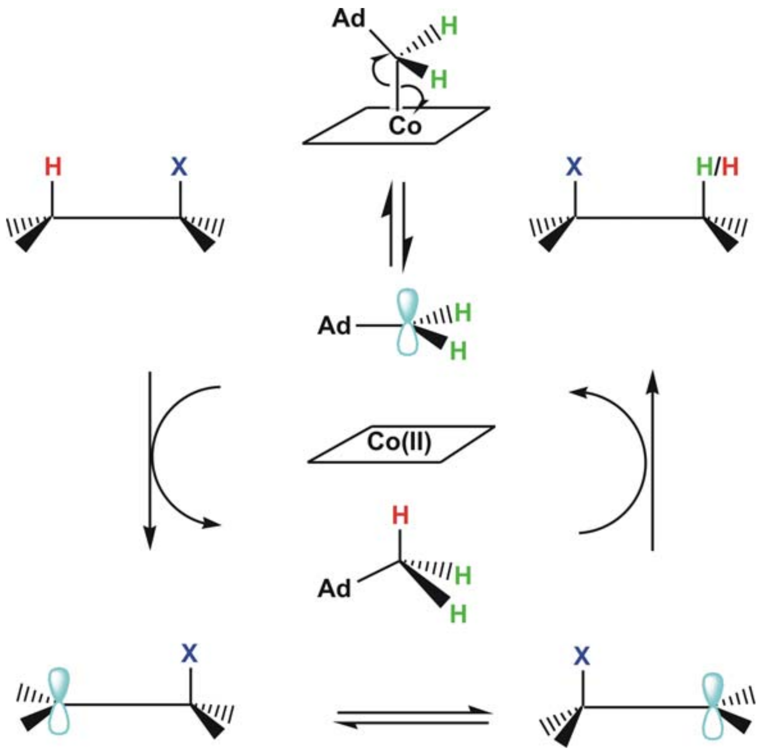

Figure 3.1. Carbon-skeletal rearrangement by the abstraction of hydrogen, and subsequent migration of group X, via the interaction of an adenosyl radical. Figure reproduced from [4].

In Figure 3.1, the generic scheme of the adenosyl radical to abstract a carbon bound hydrogen and facilitate a carbon-skeletal rearrangement is illustrated. The process begins in the top center of the figure where adenosylcobalamin undergoes thermalytic bond cleavage to produce an adenosyl radical as well as the associated cob(II)alamin radical which is observed spectroscopically. Moving counter clockwise in the figure, the adenosyl radical abstracts the hydrogen, and the group X can then migrate to where the hydrogen had been (under the influence of the protein electronic environment). The newly formed adenosine can then give up one of its hydrogens (not necessarily the one originally abstracted – indicted by the color scheme of the hydrogen in the figure), and recombine with the cob(II)alamin radical. This entire process takes place in and is controlled by the protein environment.

The specific reaction catalyzed by glutamate mutase with its conspirator coenzyme, adenosylcobalamin, is the rearrangement of L-glutamate to L-*threo*-methylaspartate. The cartoon in Figure 3.2 shows the starting and ending geometries after undergoing the process outlined in Figure 3.1.

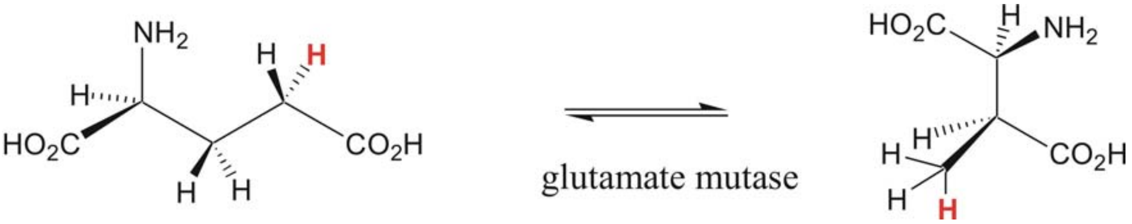

Figure 3.2. Starting (L-glutamate, left) material and ending (L-threo-methylaspartate, right) product after carbon-skeletal rearrangment through the enzymatic action of glutamate mutase. Figure reproduced from [4].

3.1 Sample Preparation

3.1.1 Alkylcobalamin (Solute) Preparation

Adenosylcobalamin, methylcobalamin, and cyanocobalamin as biologically relevant compounds are readily available commercially. These compounds were obtained from Sigma and used without any further purification.

The alkylcobalamin was introduced to the solvent immediately prior to the start of the experiment; and kept under an inert gas atmosphere for the duration of its use as described in Section 2.3 of Chapter 2. The commercially available compounds were normally mixed in at concentrations of 1mM. Using the Beer-Lambert law (Chapter 2, Equation 2.1), along with a molar extinction coefficient of ~5000$M^{-1}cm^{-1}$ at 400nm (see Figure 3.3), and optical path length (flow cell width) of 1mm, the predicted absorption of the for 400nm second harmonic excitation pump is ~68%. This absorption was typically sufficient to induce an approximately 10-20mOD change in absorption at the probe wavelengths used. With this scale of absorbance, a reasonable signal to noise ratio was readily obtained for the kinetic traces. Samples of adenosylcobalamin bound to the protein, glutamate mutase, were also reconstituted to the protein immediately prior to use. As the protein had to be expressed and purified, less sample was available for these experiments. Typical concentrations were enough to provide only 0.3OD to 0.4OD (using the Beer-Lambert law, this optical density corresponds to absorbing ~50 – 60% of the incident light) at the excitation wavelength. However, the signal to noise was still very good for the protein bound adenosylcobalamin kinetic scans. Considerable effort was placed on improving the signal to noise ratio for the small signals of the synthesized compounds through improving the quality and stability of both excitation and probe laser pulses (extending from the oscillator operation right through probe and excitation pulse generation).

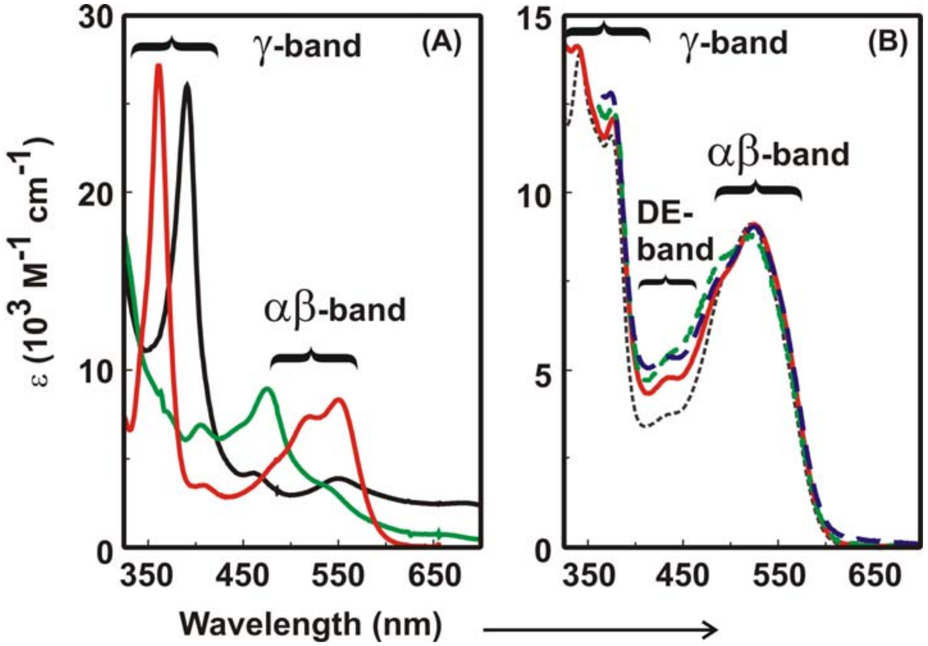

Figure 3.3. Steady-state absorption spectra for: (A) Cob(I)alamin (black), cob(II)alamin (green), and cyanocobalamin (nonalkylcob(III)alamin – red); (B) Adenosylcobalamin in water (red), bound to glutamate mutase (blue dashed), and in ethylene glycol (green dashed), and methylcobalamin in water (grey dotted). Figure reproduced from Reference [4].

Glutamate mutase samples were obtained from the Marsh Group (University of Michigan) in a potassium phosphate buffer, and introduced to the adenosylcobalamin in excess. The protein samples used were the engineered single subunit, GlmES, where the two subunits of the wildtype protein have been genetically fused. The protein was expressed and purifed as a recombinant protein from *E. coli*. The kinetics are simplified for GlmES as compared to the wildtype, but the catalytic properties have not been changed [18].

3.1.2 Solvent Preparation

Water was either distilled or purchased distilled. Ethylene glycol was purchased from Sigma in spectroscopic grade. The homolytic Co-C bond cleavage observed in the alkylcobalamins results in the formation of two radicals: cob(II)alamin and an alkyl radical. Since either of these radicals will readily react with the unpaired electrons of dissolved molecular oxygen, the solvent environment must be deoxygenated before the addition of the alkylcobalamin solute. For samples in water, the dissolved oxygen can be sufficiently displaced by purging with an inert gas [19, 20]. In fact, inert gas purging can be more effective than more involved techniques such as vacuum filtration [21]. A small volume of distilled water (≤ 250mL) was purged with nitrogen for at least one hour before the addition of any solute. Nitrogen was bubbled through any water to be introduced as a solvent including that used for mixtures with ethylene glycol and water with dissolved sucrose (the distilled water was purged before mixing with ethylene glycol or sucrose).

Due to the more viscous nature of ethylene glycol (see Chapter 4, Section 4.1.3) the method of freeze-pump-thaw [19] was chosen for deoxygenation. In this method the solvent is first frozen. The atmosphere above the frozen solvent is then evacuated and the solvent allowed to thaw. Dissolved oxygen will then boil out of the solvent into the vacuum left after pumping out the air above the frozen solvent. An inert gas is then introduced. Typically this process is repeated several times, and the solvent then left under inert gas environment until ready for use. For these experiments, <100mL of ethylene glycol was placed in Schlenk flask (round-bottomed to reduce the risk of breaking) and put on a Schlenk line. The Schlenk line was pumped first by a mechanical roughing pump capable of producing a vacuum of < 100mTorr, at which point a diffusion pump could be turned on to produce a vacuum <10mTorr. The ethylene glycol was frozen with a liquid nitrogen bath placed outside of the Schlenk flask. Once frozen, the atmosphere above of the ethylene glycol was pumped to <10mTorr. Nitrogen, vented to atmosphere through a mineral oil bubbler, was used as the inert gas. The process was carried out at least four times for each volume of ethylene glycol deoxygenated.

As described in Chapter 2 (Section 2.3), a positive pressure of inert gas (nitrogen) is maintained on the sample after the addition of alkylcobalamin and for the duration of experimental use. Each scan (or series of scans) was proceeded by a test run with free adenosylcobalamin in aqueous solution at room temperature (the kinetic traces for which are now well characterized [1, 8-11]) to ensure stage alignment over the entire 9ns window probed. The stage alignment was then periodically checked with aqueous adenosylcobalamin samples (at room temperature) to ensure maintained alignment. The test measurement also served the dual purpose of ensuring the sample flow rate was sufficient for a fresh sample volume every millisecond (1 kHz laser repetition rate).

3.2 Adenosylcobalamin Bound to Glutamate Mutase

3.2.1 Transient Absorption Data

Kinetic transient absorption scans as described in Chapter 2 were performed on adenosylcobalamin bound to glutamate mutase. Ice bath temperature traces at probe wavelengths of 470nm and 600nm are shown in Figures 3.4 through 3.7. These two scans proved particularly difficult to obtain with satisfactory signal to noise due to the experimental parameters. 600nm is at the edge of the adenosylcobalamin visible absorption (Figure 3.3) resulting in weak signals. 470nm though within the sample region of absorption is near the edge of the NOPA spectrum (Chapter 2, Figure 2.6) and presented difficulty for obtaining a quality beam to collimate for the entire 9ns of observation time.

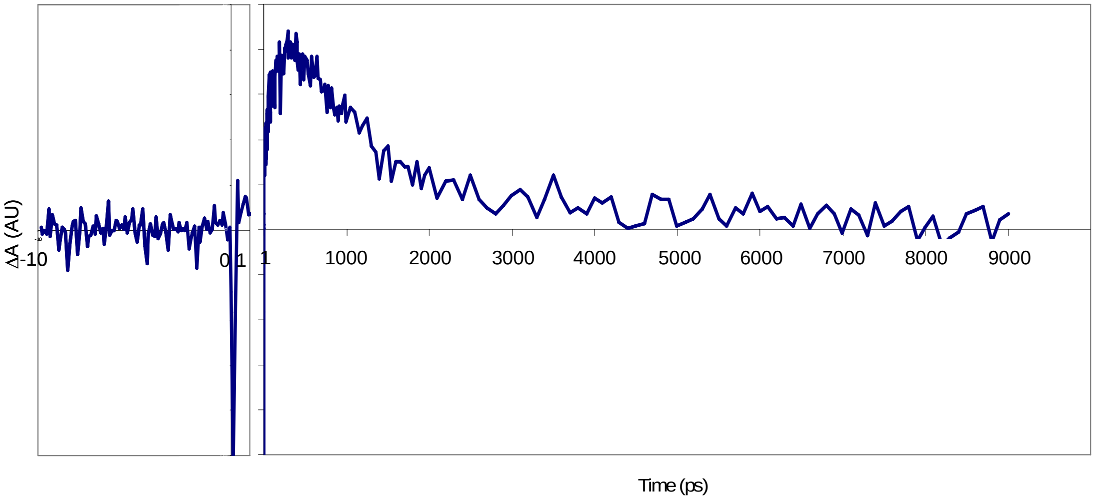

Figure 3.4. Kinetic trace for adenosylcobalamin bound to glutamate mutase. Excitation wavelength is 400nm and probe wavelength is 470nm. On the left is the first -10 to 1 picoseconds; and on the right is 1ps through 9ns. Data was collected at room temperature.

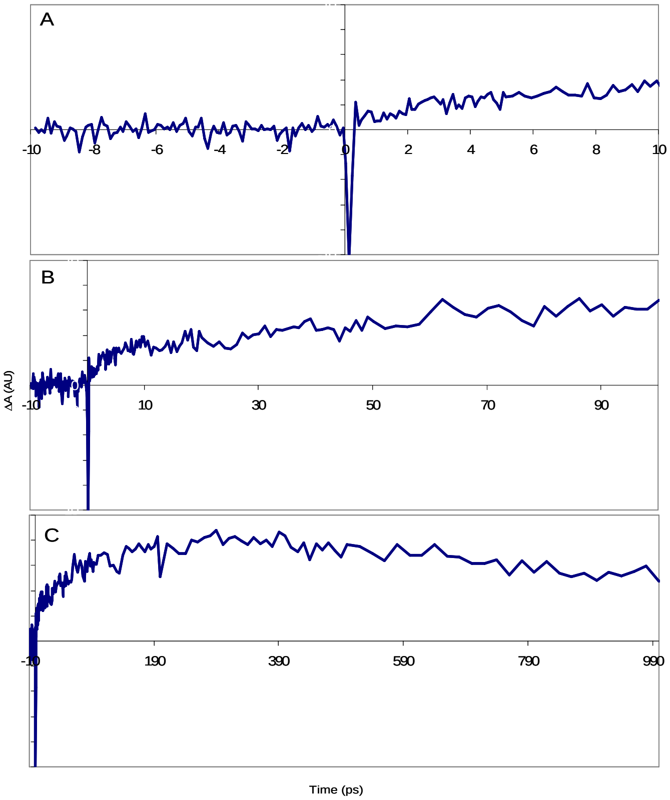

Figure 3.5. Detail of the adenosylcobalamin bound to glutamate mutase scan shown in Figure 3.4: A shows -10 through 10ps. B shows -10 through 100ps. C shows -10 through 1000ps.

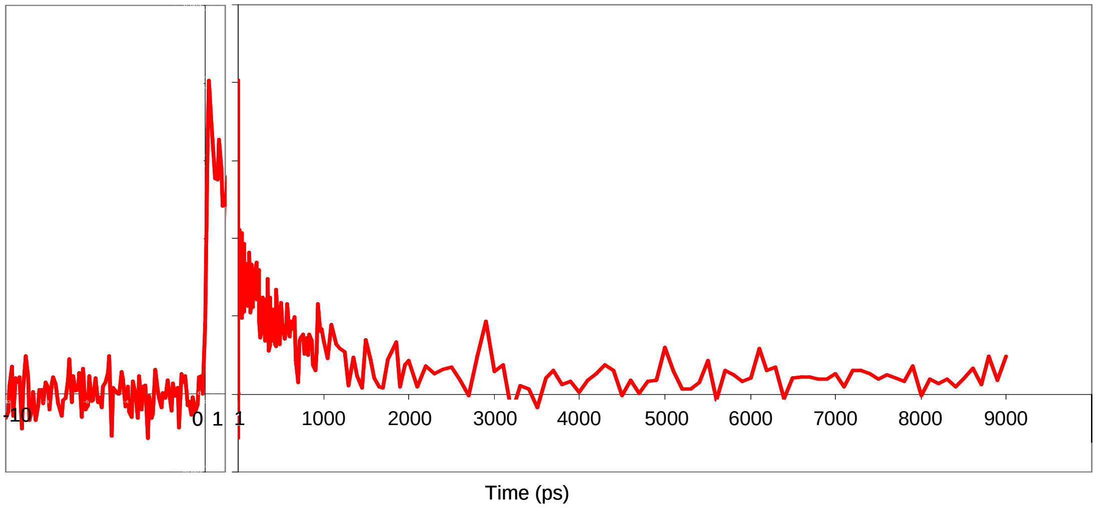

Figure 3.6. **Kinetic trace for adenosylcobalamin bound to glutamate mutase. Excitation wavelength is 400nm and probe wavelength is 600nm. On the left is the first -10 to 1 picoseconds; and on the right is 1ps through 9ns. Data was collected at room temperature.**

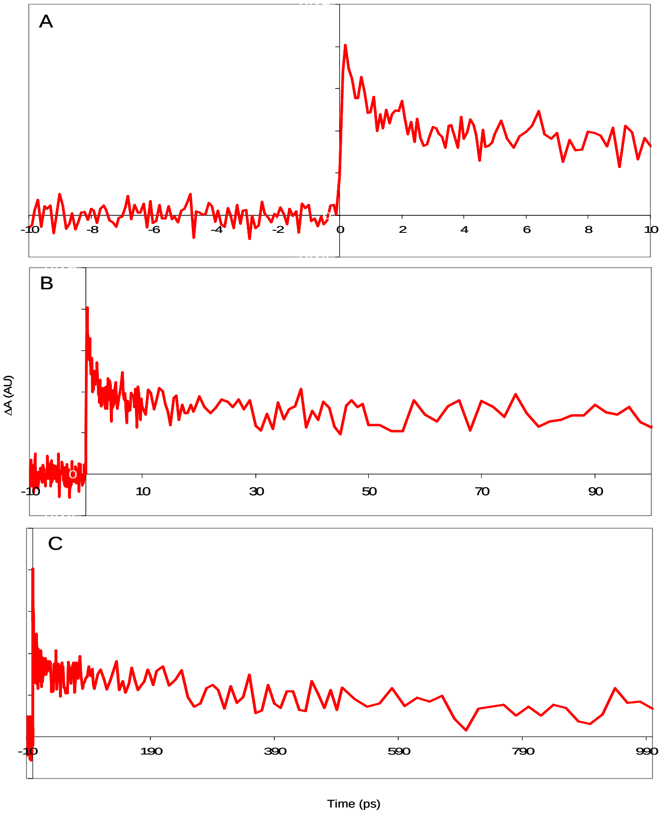

Figure 3.7. Detail of the adenosylcobalamin bound to glutamate mutase scan shown in Figure 3.6: A shows -10 through 10ps. B shows -10 through 100ps. C shows -10 through 1000ps.

The scans with 470nm probe show an initial spike followed by an increase in absorption peaking near 300ps after excitation. By 9ns the signal has returned to the baseline (established with negative times). The scans using 600nm probe show an instrument limited rise in absorption followed by decay. By 9ns the signal has nearly returned to baseline, though there remains a long lived plateau.

These data were fit globally to a sum of exponentials. For the global fit it was assumed that each kinetic trace has the same time constants, but that each time component is weighted by a wavelength specific amplitude, as described in Equation 3.1.

$$\Delta A_{\lambda} = \sum_{i=1}^{5} A_{i,\lambda} e^{-k_i t} \ . \qquad (3.1)$$

Included in the global fit were data obtained previously at probe wavelengths from 520nm to 570nm [2]. The minimum number of five time constants required to fit the data are listed in Table 3.1.

Table 3.1. Results of global fit to a sum of five exponentials for adenosylcobalamin bound to glutamate mutase.

i **(from Equation 1)**	**Rate Constant, k (ns^{-1})**	**Time Constant, τ (ps)**
1	> 2000	< 0.5
2	160 ± 50	6
3	9.5 ± 1.0	105
4	1.05 ± 0.1	950
5	0 (does not decay at by 9ns – long lived plateau)	∞

3.2.2 Results

The transient absorption data obtained for adenosylcobalamin bound to glutamate mutase is best analyzed in comparison with previously acquired data for free adenosylcobalamin in aqueous and ethylene glycol solutions [10]. Figure 3.8 shows comparison plots for adenosylcobalamin in each of these three environments at selected probe wavelengths, including the wavelengths shown above in Figures 3.4 through 3.7. Note that the temporal axis for the plots in Figure 3.8 is on a log scale in order to better elucidate changes induced by the solvent environment (water, ethylene glycol, or protein in potassium phosphate buffer) and that each scan begins at 1ps.

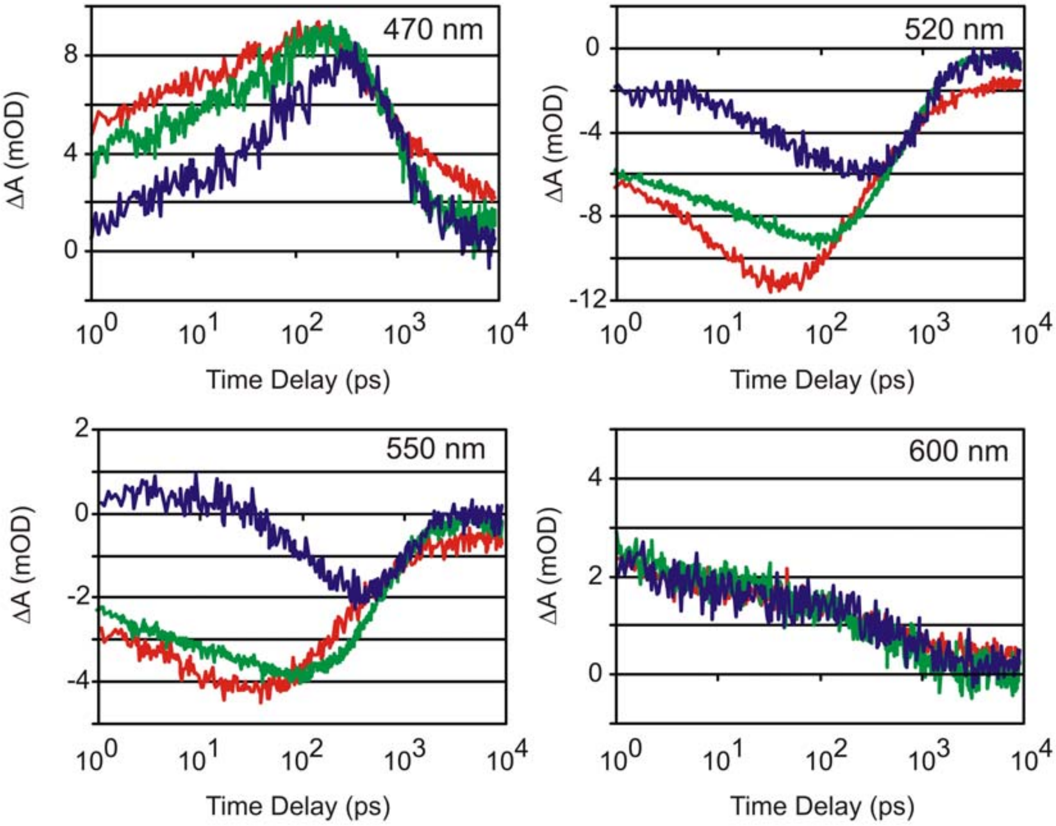

Figure 3.8. Room temperature kinetic traces for adensosylcobalamin in three different environments: free coenzyme in aqueous solution (red); free coenzyme in ethylene glycol (green); and bound to glutamate mutase (blue). The probe wavelength is indicated in the upper right corner of each plot. Note that these traces are plotted on a log scale for time and do not include subpicosend dynamics (each begins at 1 ps). Figure reproduced from Reference [4].

The adenosylcobalamin bound to glutamate mutase traces (blue) in Figure 3.8 at probe wavelengths of 470nm and 600nm are the same as those shown in Section 3.2.1 above (but with the time axis on a log scale). Free adenosylcobalamin in aqueous solution is plotted in red and in ethylene glycol is plotted in green. All traces shown were collected at room temperature.

As discussed in Chapter 1, Section 1.2.1.1, the existing literature [1, 10, 11, 22] shows that for times longer than a few hundred picoseconds the dominant feature in the transient absorption data is the formation of cob(II)alamin radical. The spectral fingerprint of cob(II)alamin can be seen by reference to Figures 3.3 and 3.8. At time delays of at least a few hundred picoseconds there is an increase in absorption for all samples at 470nm (where cob(II)alamin shows a marked increase in absorption compared to cob(III)alamin) and a decrease at each of the other probe wavelengths (where cob(II)alamin shows a marked decrease in absorption compared with cob(III)alamin). However, Figure 3.8 shows that the creation of the cob(II)alamin characteristic state is delayed as compared to free adenosylcobalamin in both water and ethylene glycol. Decay-associated difference spectra for the protein bound adenosylcobalamin obtained from the kinetic traces are shown in Figure 3.9. The clear formation of cob(II)alamin from adenosylcobalamin by 1ns is shown in Figure 9, as the 1ns decay associated difference spectrum is identical to the difference spectrum expected for the creation of cob(II)alamin from adenosylcobalamin (scaled, black dashed line). The decay associated difference spectra show the wavelength specific amplitudes obtained from the sum of exponentials fitting, $A_{i,\lambda}$, plotted versus the probe wavelength.

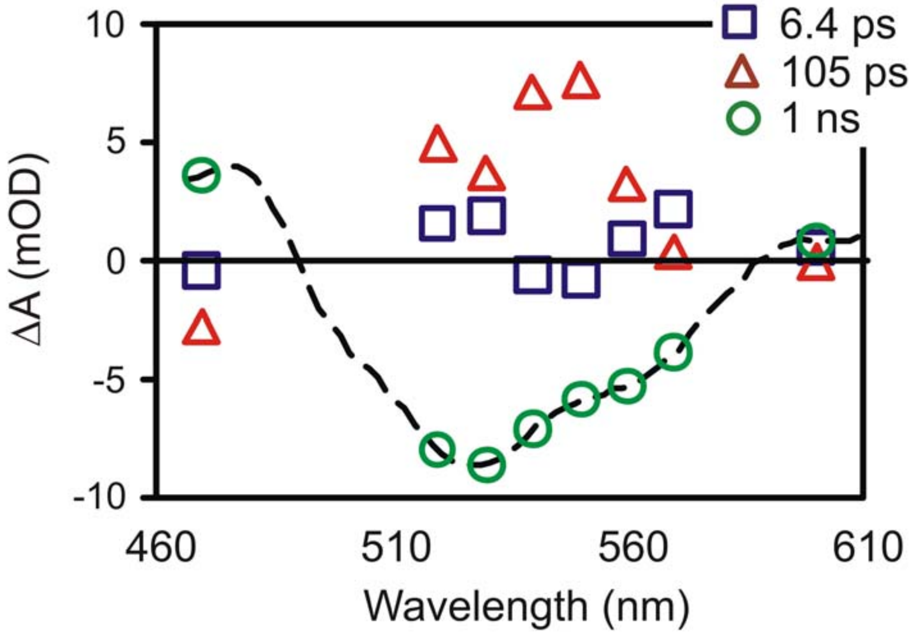

Figure 3.9. Decay associated difference spectra for adenosylcobalamin bound to glutamate mutase. Points are associated with each time component of the sum of exponential fit as indicated in the legend. The black dashed spectrum is the (scaled) difference spectrum expected for the creation of cob(II)alamin from adenosylcobalamin. Figure modified from reference [4].

Besides a delay for the formation of cob(II)alamin radical, Figures 3.8 and 3.9 show that the protein bound adenosylcobalamin sample starting at 1ps has an increase in absorption for the 550nm probe wavelength. Free adenosylcobalamin does not show any increase at this wavelength, but instead is already decreasing toward the cob(II)alamin spectrum by 1ps. Reference to Figure 1 indicates that an increased absorption near 550nm is characteristic of the creation of nonalklycob(III)alamin state (red spectrum in Figure 3.3).

If a simple step-wise model is assumed for the observed kinetics following excitation at 400nm for the protein bound adenosylcobalamin, the difference spectrum associated with the cob(III)alamin type signal can be estimated, along with any other intermediate species. These can be calculated using the model to weight the contribution of each decay associated spectra to the individual species absorption difference spectra. (For more details, see Chapter 4, Section 4.2.1.)

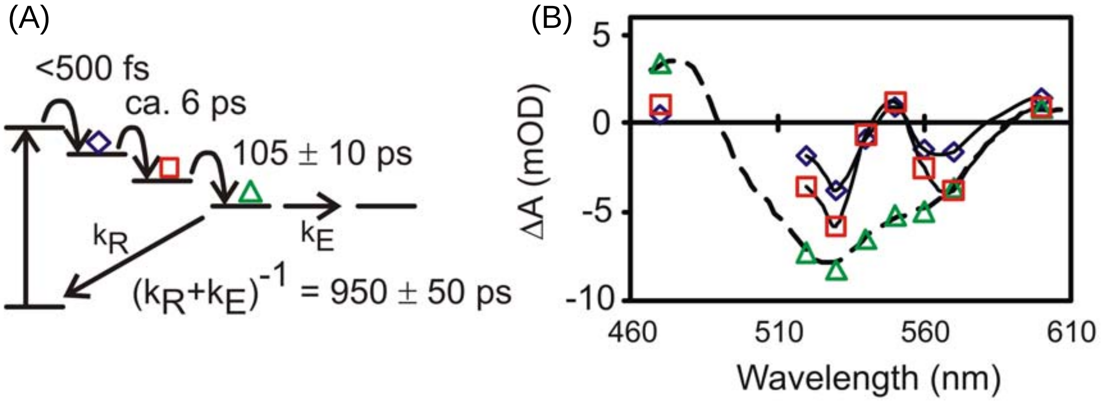

Figure 3.10. (A) Proposed step-wise model for the observed kinetics of adenosylcobalamin bound to glutamate mutase. Time constants are those listed in Table 3.1. $k_1 = k_R + k_E$ in this model. (B) Species associated difference spectra for the two intermediate states (blue diamonds and red squares as shown in (A)), as well as for the long lived cob(II)alamin (green triangles). The black dashed line represents the scaled difference spectrum anticipated for the formation of cob(II)alamin from adenosylcobalamin. Figure reproduced from Reference [4].

The weighting of the decay associated spectra in determining the species associated spectra is described in References [10] and [20]. The distinction between the decay associated difference spectra shown in Figure 3.9 and the species associated difference spectra in Figure 3.10(B) is that the decay associated spectra represent the dominant spectral component associated with a particular time constant, while the species associated spectra represent the difference spectrum of an individual species (in this case an intermediate). For a mixture of independent absorbing species, each with a characteristic time constant, the decay and species associated difference spectra are the same [23]. However, when the system being probed is an excited state reaction, the situation is complicated and the decay associated spectra no longer represent an individual absorbing species (or excited state conformer). Notice that at long times the decay and species associated difference spectra are identical to each other and identical to the difference spectrum expected for the formation of cob(II)alamin from adenosylcobalamin. The decay and species associated difference spectra are identical to each other in this instance since there is only one absorbing species left at long times and no longer a mixture of different species in the population. Of course the ground state is absorbing as well; but the transient absorption scans probe only the change in absorbance as compared to the ground state absorbance and described by the Beer-Lambert law (Equation 2.1 in Chapter 2).

As described in Chapter 1 (as reviewed from [10]), free adenosylcobalamin in ethylene glycol undergoes homolytic bond cleavage of the Co-C bond on a time scale of ≤ 28ps. In water a spectroscopic intermediate is observed, possibly characteristic of a base-off (lower nitrogenous ligand) alkylcobalamin or base-on cob(II)alamin, followed by homolysis on a time scale of 100ps. The bond dissociation pathways observed following excitation of the protein bound adenosylcobalamin are distinctly different from the free adenosylcobalamin. Not only is there a delay in the formation of the cob(II)alamin radical, but a distinct intermediate, characteristic of a nonalkylcob(III)alamin-type state, is identified by the data presented. The role of the protein in supporting an electronically distinct intermediate suggests an influence on the electronic structure of the bound coenzyme.

A cob(III)alamin type species with a marked absorption at 550nm is characteristic of nonalkylcobalamins, such as vitamin B_{12} (cyanocobalamin, shown in Figure 3.3(A), red) and hydroxocobalamin (Chapter 4, Figure 4.1)). The ligands in these cases are σ-donating anions; and more charge density will be located on the ligand. If the supported intermediate corresponds to such a state, it would then represent a metal-to-ligand charge transfer state (MLCT state). A similar suspected MLCT intermediate is observed following the excitation of methylcobalamin [8, 11].

Following bond homolysis in the protein environment, the rates for geminate recombination and cage escape, assuming the step-wise model presented in Figure 3.10(A) are:

Table 3.2. Rates for geminate recombination and cage escape of the adenosyl radical with the parent cob(II)alamin.

	Geminate Recombination	**Cage Escape**
Rate Constant (ns^{-1})	0.05 ± 0.03	1.0 ± 0.1
Time Constant (ns)	20	1

The rate constant for geminate recombination is slowed in comparison to the adenosyl radical recombining with cob(II)alamin in water and ethylene glycol (1.4ns^{-1} [10]; the protein bound sample is in an ice bath, however, the experiments in Chapter 3 Section 3.3 and in Chapter 4 demonstrate that the recombination is slowed in comparison to free samples at lower temperature as well). However, the accelerated rate of bond homolysis in response to substrate binding cannot be accounted for by this stabilization. Experiments probing the dynamics of adenosylcobalamin while in the protein environment in the presence of substrate are clearly desirable for a more thorough insight into protein's influence of bond homolysis. Such experiments may be complicated by the interaction of radical and substrate and may therefore require appropriate protein mutants. Rate constants for diffusive escape from a cage will be discussed in detail in Chapter 4.

3.3 S_1 Excited State and Dynamics

The observation of the MLCT excited state for protein bound adenosylcobalamin was unexpected and suggested that a more detailed study of the excited states of alkylcobalamins was called for. Data was taken for adenosylcobalamin, methylcobalamin, and cyanocobalamin like that described in the previous section, with the addition of temperature as a further experimental parameter. The setup is as described in Chapter 2. It is worth noting that this program of experiments cannot be readily extended to the protein environment due to the degradation of protein with temperature.

3.3.1 Cyanocobalamin

The transient absorption data for cyanocobalamin is presented in Figures 3.11 and 3.12.

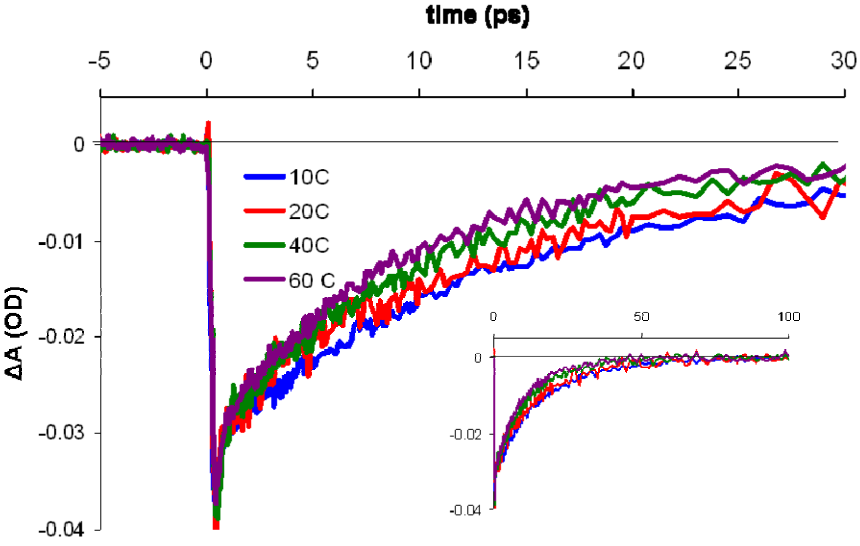

Figure 3.11. Kinetic trace for cyanocobalamin in ethylene glycol. Excitation wavelength is 400nm and probe wavelength is 520nm. The main figure shows kinetics out to 30ps, while the inset plots the data to 100ps (effectively demonstrating that the sample has returned to the ground state). Figure reproduced from Reference [24].

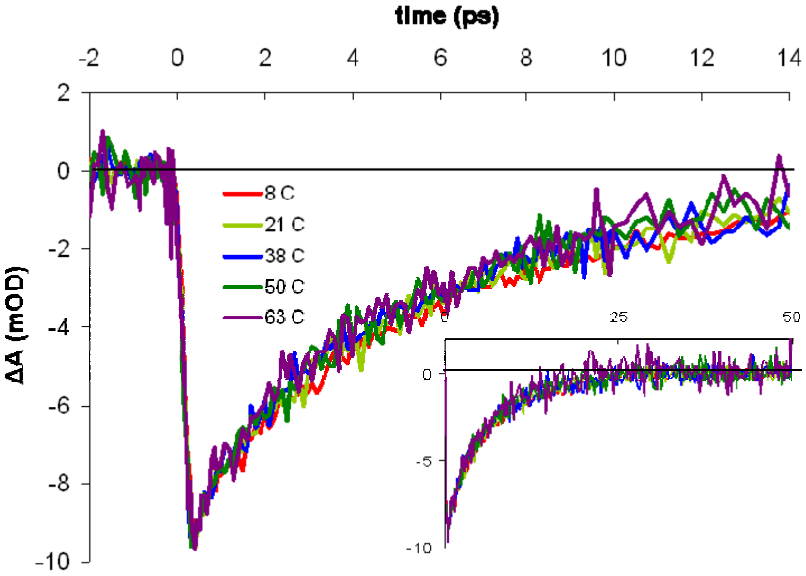

Figure 3.12. Kinetic traces for cyanocobalamin in water. Excitation wavelength is 400nm and probe wavelength is 560nm. The main figure shows kinetics out to 14ps, while the inset plots the data to 50ps (effectively demonstrating that the sample has returned to the ground state). Figure reproduced from Reference [24].

The kinetic behavior of the nonalkylcobalamins following photoexcitation is relatively simple in comparison to that for the alkylcobalamins. Excitation at both 400nm and 520nm fails to induce Co-C bond homolysis [7]. The data presented in Figures 3.11 and 3.12 demonstrate a strong bleach at the probe wavelengths (560nm in water, near the peak of the absorption; and 520nm in ethylene glycol), followed by recovery to the ground state on timescales given in Table 3.2 (obtained by fitting to a sum of two exponentials; Equation 3.1 with $i = 2$, k_2 is given in Table 3.2):

Table 3.3. Rates for cyanocobalamin ground state recovery following excitation at 400nm. Table reproduced from Reference [24].

Ethylene Glycol				Water		
T(˚C)	k_2 (ps^{-1})	τ(ps)		T(˚C)	k_2 (ps^{-1})	τ(ps)
10	0.061	16.21		8	0.137	7.25
20	0.065	15.39		21	0.152	6.56
40	0.085	11.78		38	0.148	6.74
60	0.099	10.05		50	0.166	6.01
75	0.123	8.13		63	0.176	5.67

The kinetic traces presented in Figures 3.11 and 3.12 demonstrate behavior identical to that described in the literature [7] and reviewed in Chapter 1. The introduction of a temperature variation parameter induces no change in the initial excitation and internal conversion to the S_1 excited state. The decay of the excited state to the ground state does depend on environment as detailed in Chapter 1; and this aspect is reflected in a temperature dependent intermediate lifetime as evidenced by the fitting parameters in Table 3.3.

A standard approach to analyzing the temperature dependence of reaction rates is to fit the data with an Arrenhius expression:

$$k = A_h e^{-E_a/RT} . \tag{3.2}$$

Taking the logarithm allows fitting to a straight line:

$$\ln(k) = -\frac{E_a}{RT} + \ln(A_h) . \tag{3.3}$$

A plot of the natural logarithm of the excited decay rate constant versus 1/T and the corresponding fits to Equation 3.3 are shown in Figure 3.13.

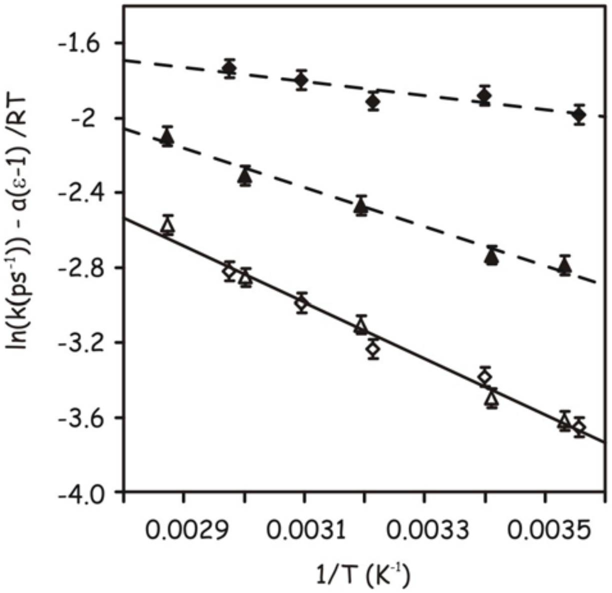

Figure 3.13. Plot of ln(k) vs. 1/T for CNCbl in water (filled diamonds, dashed line) and ethylene glycol (filled triangles, dashed line), ln(k)-a(ε-1)/RT in water (open diamonds) and ethylene glycol (open triangles). The value for a is 0.0466 kJ/mol per unit change in dielectric constant as described in the text. Figure reproduced from Reference [5].

The slopes in Figure 3.13 predict that the activation energy in ethylene glycol is approximately 3 times that in water. The fits to Equation 3.3 assume that the exponential prefactor, A_h, and the activation energy, E_a, are independent of temperature. As pointed out in Chapter 1, the excited state lifetime exhibits an inverse dependence on dielectric constant (at least at room temperature) [7]. Since the dielectric constant of the solvent varies with temperature (by 22% in water and 27% ethylene glycol over the range of temperatures studied), it is anticipated that in fact the temperature will exert some influence on the activation energy. To gauge the extent of temperature influence on the activation energy, it was first assumed that the entire dependence was through the influence of dielectric constant. If this were the case, comparing the rate constant in different solvents (to vary the dielectric constant) while holding the temperature constant would describe not only how the rate constant varies with the dielectric properties of the solvent, but also how the activation energy varies with temperature (via the associated change in dielectric constant). To this end, Figure 3.14 plots the natural logarithm of the rate constant versus dielectric constant, with the temperature held constant at room temperature.

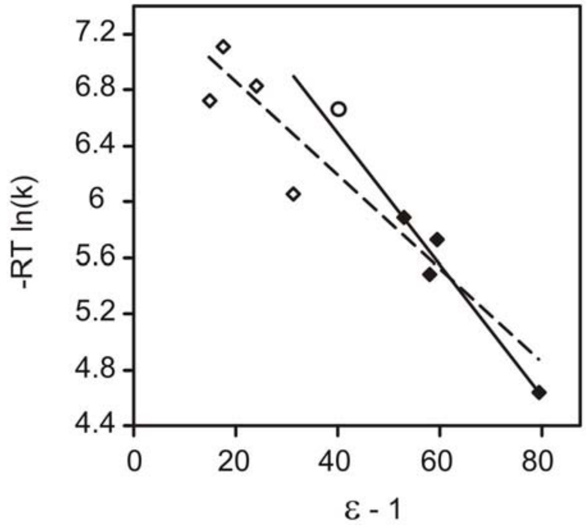

Figure 3.14. -RTln(k) (in kJ/mol) vs. dielectric constant (ε-1) for CNCbl at room temperature in a variety of solvents and solvent mixtures. There is a clear correlation with solvent polarity although the scatter is also significant. The filled diamonds represent data obtained in water or 50/50 mixtures of water and ethanol, methanol or acetonitrile [7]. The open diamonds represent data obtained in neat alcohol solvents, methanol, ethanol, 2-propanol and isobutanol [7]. The circle is the data point obtained in ethylene glycol in the present study. The dashed line is a linear fit to all of the data; the solid line is a linear fit to the filled diamonds. Figure reproduced from Reference [5].

Returning to the Arrhenius analysis, the linear dependence of the activation energy on temperature inferred in Figure 3.14 can be put to the test, by expressing the activation energy in Equation 3.3 as a linear function of the dielectric constant,

$$E_a(\varepsilon) = E_a(\varepsilon = 1) - a(\varepsilon - 1), \tag{3.4}$$

arriving at

$$\ln(k) - \frac{a(\varepsilon - 1)}{RT} = -\frac{E_a(\varepsilon = 1)}{RT} + \ln(A_h), \tag{3.5}$$

where a is a constant which should agree with the slope in Figure 3.14, while resulting in a straight line for Equation 3.5. The bottom line in Figure 3.13 is for the data in both water and ethylene glycol with $a = 0.0466$ kJ/mol. This value for a is in close agreement with the fit to high dielectric constant data in Figure 3.13, where the slope is 0.047 ± 0.005 kJ/mol. This analysis suggests that the only influence on the excited state is the electrostatic stabilization by the solvent.

This data further is consistent with the existence of a ligand-to-metal-charge-transfer (LMCT) state as proposed in the literature [7]. The charge transfer density appears modest as the activation barrier decreases with increasing dielectric constant (see Figure 3.15).

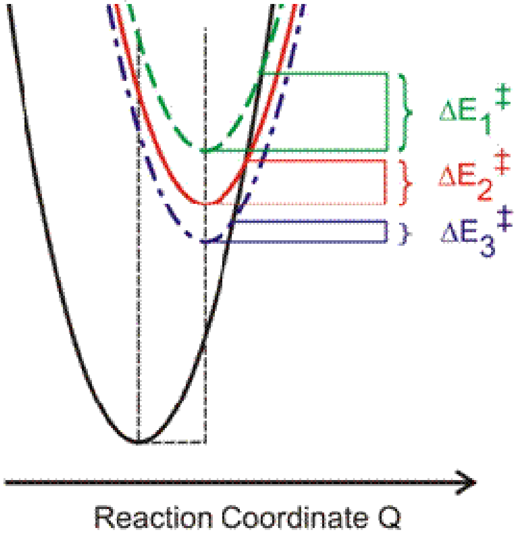

Figure 3.15. Cartoon illustrating the influence of solvent stabilization on the activation energy for internal conversion for a modest charge redistribution in a polar solvent. The solvent will stabilize the energy of the excited state leading to a lower activation energy for internal conversion. This is demonstrated as the upper potential energy surface moves down in relation to the ground state, resulting in $\Delta E_3 < \Delta E_2 < \Delta E_3$. Figure reproduced from Reference [5].

3.3.2 Methylcobalamin

Transient absorption kinetic traces for methylcobalamin following excitation at 400nm as a function of temperature and at select probe wavelengths in water and ethylene glycol are presented below in Figures 3.16 through 3.20.

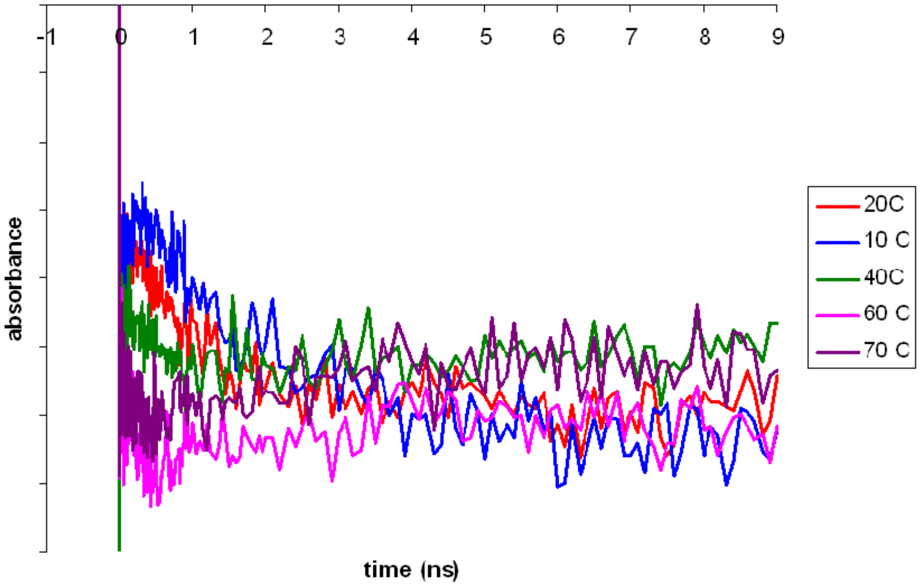

Figure 3.16. Methylcobalamin in water transient absorption kinetic scans. This data has been scaled (see Chapter 4 for a complete discussion). Probe wavelength is 520nm; pump wavelength is 400nm. This Figure is reproduced from Reference [24].

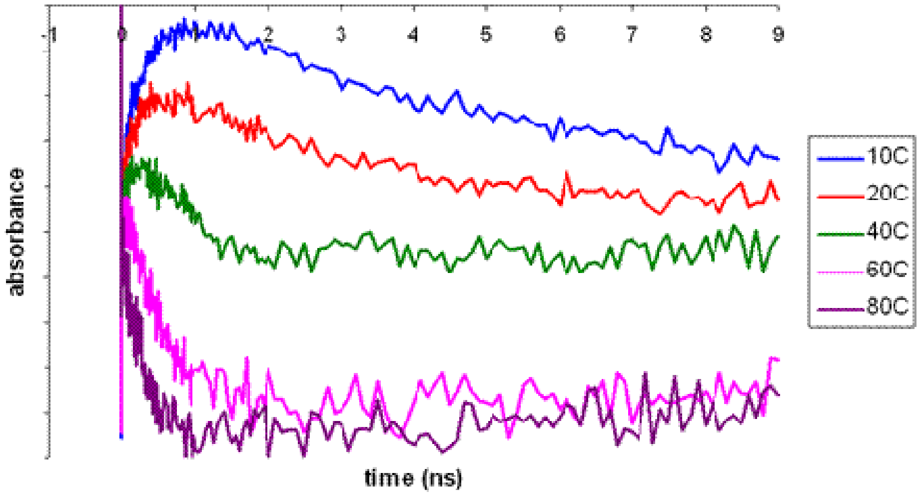

Figure 3.17. Methylcobalamin in ethylene glycol transient absorption kinetic scans. This data has been scaled (see Chapter 4 for a complete discussion). Probe wavelength is 510nm; pump wavelength is 400nm. This Figure is reproduced from Reference [24].

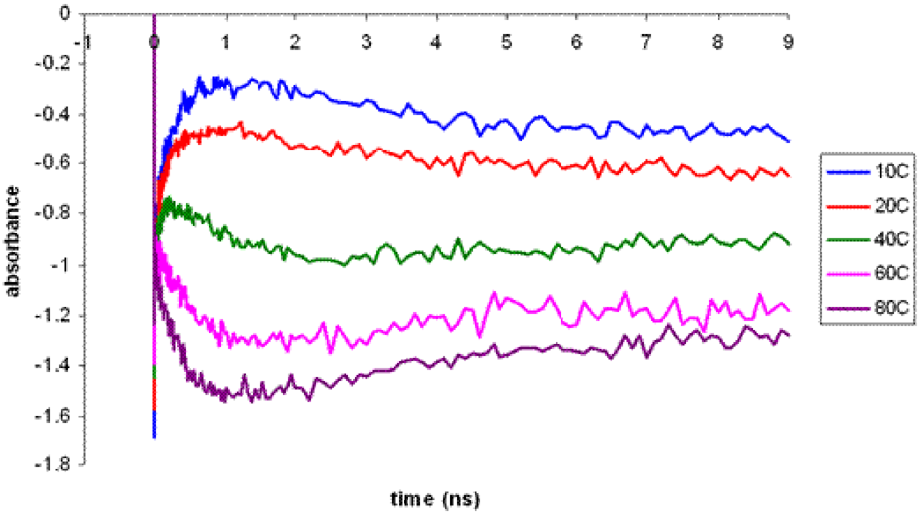

Figure 3.18. Methylcobalamin in ethylene glycol transient absorption kinetic scans. This data has been scaled (see Chapter 4 for a complete discussion). Probe wavelength is 520nm; pump wavelength is 400nm. This Figure is reproduced from Reference [24].

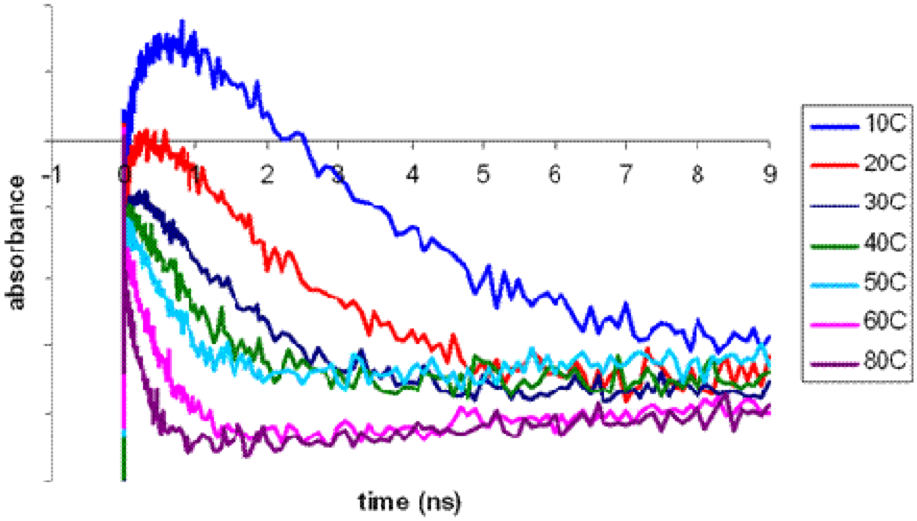

Figure 3.19. Methylcobalamin in ethylene glycol transient absorption kinetic scans. This data has been scaled (see Chapter 4 for a complete discussion). Probe wavelength is 540nm; pump wavelength is 400nm. This Figure is reproduced from Reference [24].

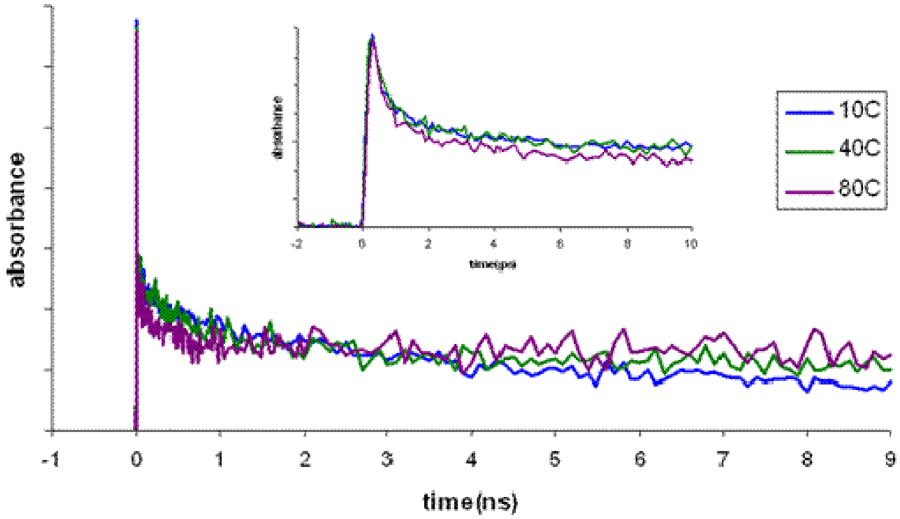

Figure 3.20. Methylcobalamin in ethylene glycol transient absorption kinetic scans. This data has been scaled (see Chapter 4 for a complete discussion). Probe wavelength is 600nm; pump wavelength is 400nm. The inset shows a blowup of the first 10ps. This Figure is reproduced from Reference [24].

Each transient absorption scan was fit to a sum of exponentials (Equation 3.1). The model in methylcobalamin due to partitioning between two photoproduct channels is different than that used for fitting the cyanocobalamin or adenosylcobalamin bound to glutamate mutase above, and is illustrated in Chapter 4, Figure 4.27. The decay of the metal-to-ligand-charge-transfer (MLCT – Chapter 1) state is considered in an Arrhenius plot as for cyanocobalamin. Figure 3.21 plots the natural logarithm of the rate constant for decay of the excited state against the inverse temperature.

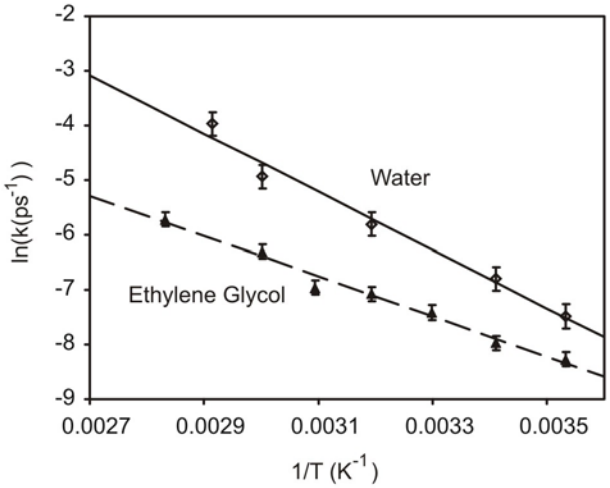

Figure 3.21. Plot of ln(k) vs. 1/T for MeCbl in water (diamonds, solid line) and ethylene glycol (triangles, dashed line). This Figure is reproduced from Reference [5].

The most interesting feature of Figure 3.21 is that the slope is steeper for methylcobalamin in water than in ethylene glycol, which is opposite of what was observed for cyanocobalamin (Figure 3.13). The larger activation energy in the solvent with a larger dielectric constant suggests that compared to the modest charge density transfer of the nonalkylcobalamin excited state (Figure 3.15), that there is a much increased charge density transfer for the cob(III)alamin like, MLCT intermediate state.

The cartoon in Figure 3.22 makes the point that increased stabilization by the solvent (upper curve moves closer to the ground state), increases the activation energy.

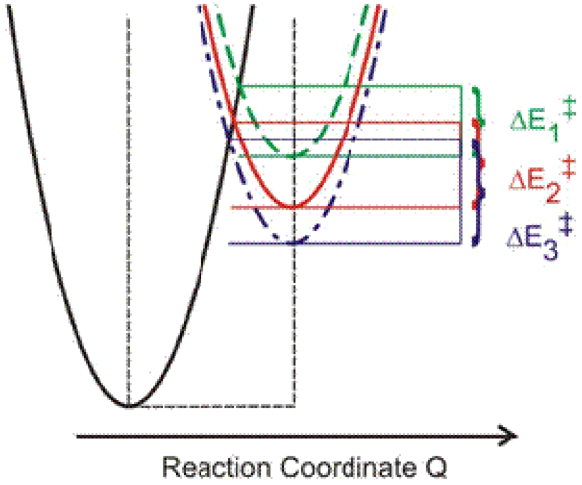

Figure 3.22. Cartoon illustrating the influence of solvent stabilization on the activation energy for internal conversion for a large charge redistribution in a polar solvent. The solvent will stabilize the energy of the excited state leading to an increased activation energy for internal conversion. This is demonstrated as the upper potential energy surface moves down in relation to the ground state, resulting in $\Delta E_3 > \Delta E_2 > \Delta E_3$. Figure reproduced from Reference [5].

Analysis according to Equation 3.5 does not result in a single straight line and dielectric constant alone cannot account for the solvent dependent decay of the excited intermediate state. The apparent insensitivity of the kinetic traces to environment at 600nm is characteristic of ligand field transitions from the cobalt 3d orbitals. (an apparent insensitivity is exhibited to functional group as well [3]).

Several transient absorption experiments were performed for methylcobalamin at fixed delay and with a wide band visible probe. These demonstrate clearly the characteristic structure of the MLCT intermediate described above.

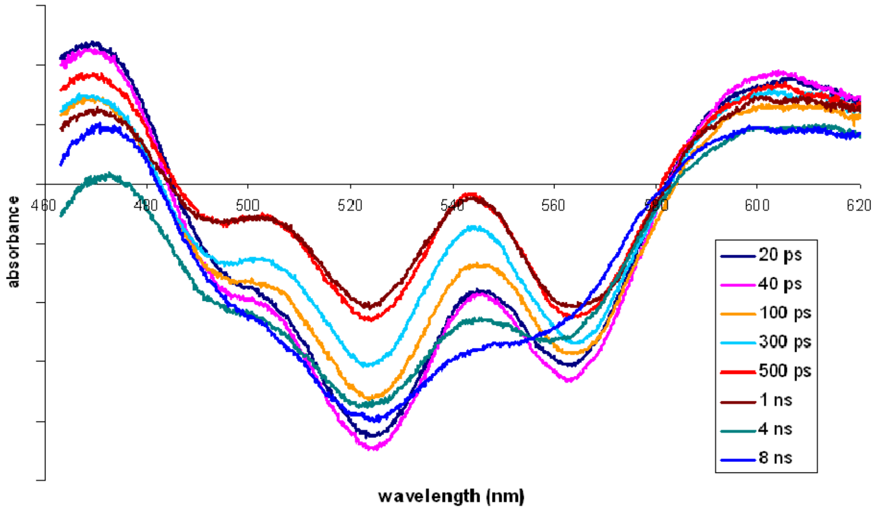

Figure 3.23. Difference spectrum for methylcobalamin at 10°C, following excitation at 400nm. The spectrum demonstrate the evolution from the MLCT intermediate to a distinctly different cob(II)alamin at longer time delay. This Figure is reproduced from Reference [24].

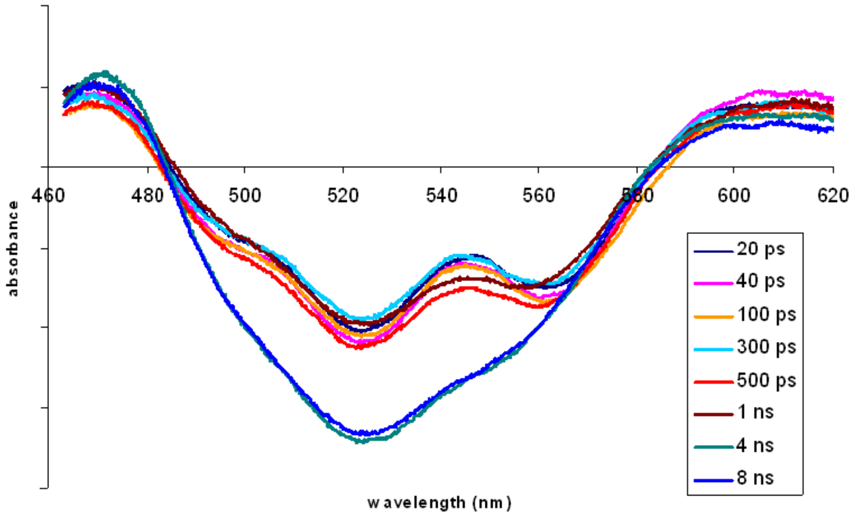

Figure 3.24. Difference spectrum for methylcobalamin at 40°C, following excitation at 400nm. The spectrum demonstrate the evolution from the MLCT intermediate to a distinctly different cob(II)alamin at longer time delay. However, the intermediate is less well defined than at 10°C (Figure 3.23), and the cob(II)alamin is more well defined by 9ns. This Figure is reproduced from Reference [24].

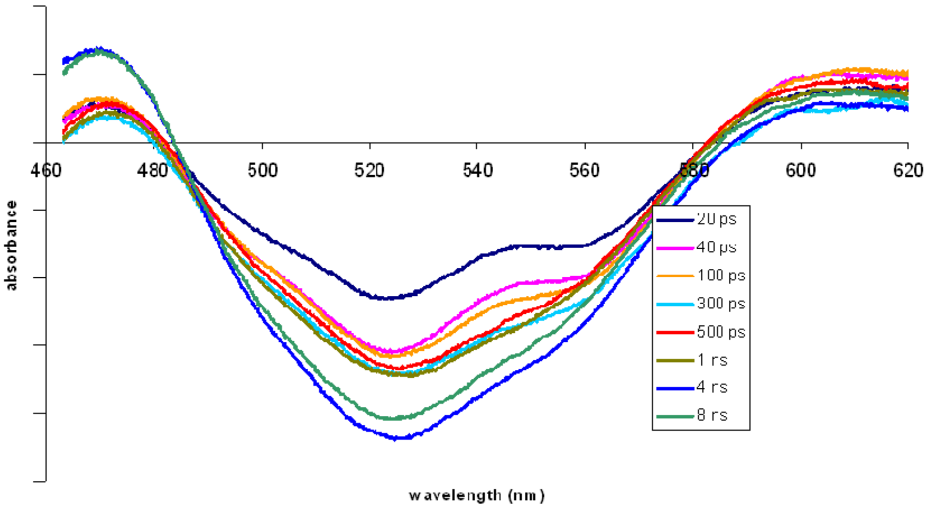

Figure 3.25. Difference spectrum for methylcobalamin at 80°C, following excitation at 400nm. At this temperature the intermediate is barely discernable at 20 ps. This Figure is reproduced from Reference [24].

The difference spectra in Figures 3.23 through 3.25 clearly illustrated the evolution through the MLCT intermediate to the cob(II)alamin spectrum expected for radical pairs. At the 80°C temperature in Figure 3.25 the intermediate lifetime is severely shortened.

3.3.3 Adenosylcobalamin

Transient absorption kinetic traces for adenosylcobalamin as a function of sample temperature in water and ethylene glycol are presented in Figures 3.26 through 3.28.

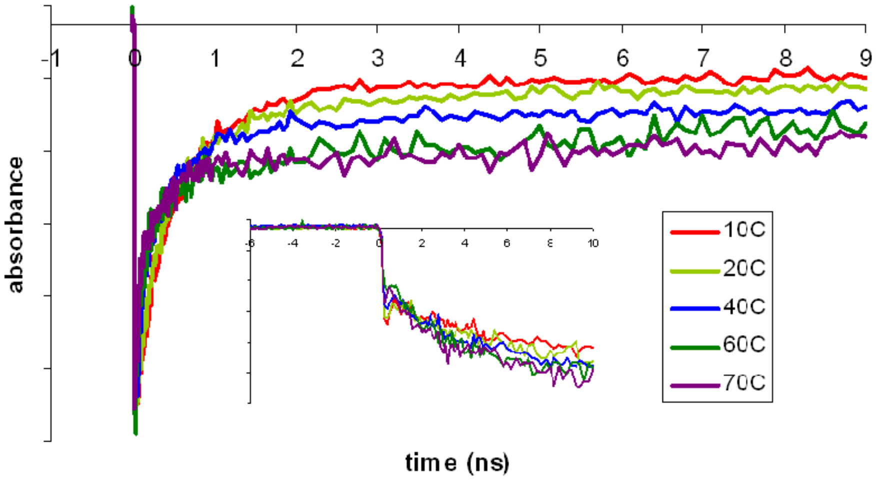

Figure 3.26. Transient absorption kinetic traces for adenosylcobalamin in water following excitation at 400nm. The probe wavelength is 520nm. The inset shows a blowup of the first 10 picoseconds following excitation. This Figure is reproduced from Reference [24].

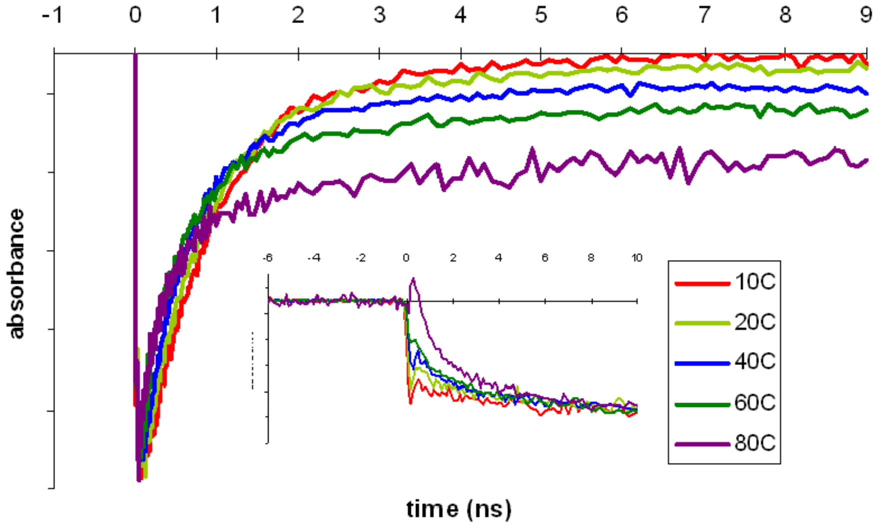

Figure 3.27. Transient absorption kinetic traces for adenosylcobalamin in ethylene glycol following excitation at 400nm. The probe wavelength is 520nm. The inset shows a blowup of the first 10 picoseconds following excitation. This Figure is reproduced from Reference [24].

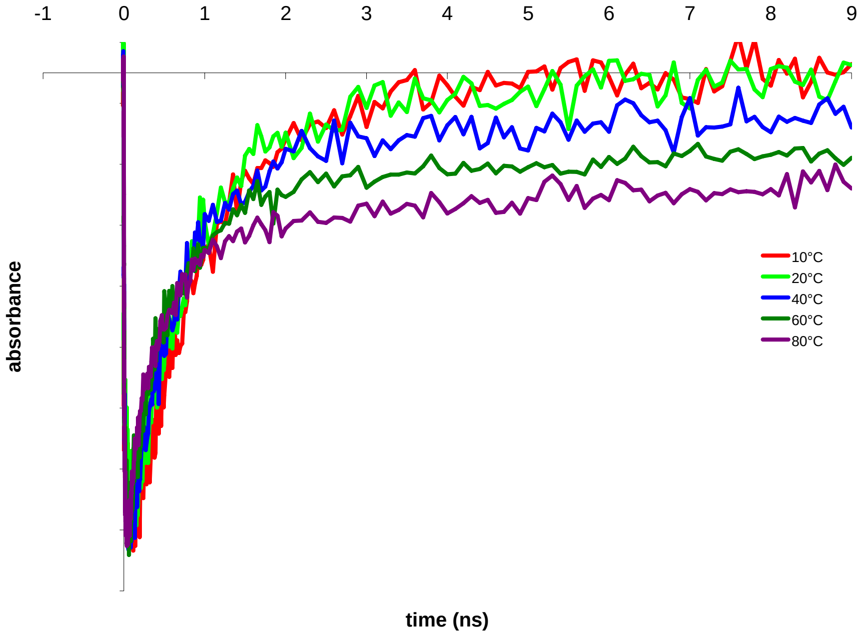

Figure 3.28. Transient absorption kinetic traces for adenosylcobalamin in ethylene glycol following excitation at 400nm. The probe wavelength is 540nm.

The adenosylcobalamin data was also fit to a sum of exponentials, resulting in the identification of several short lived intermediates on the path to homolysis (as described in Chapter 1). The rate constants from these fits are compared by environment with an Arrhenius plot in Figure 3.29.

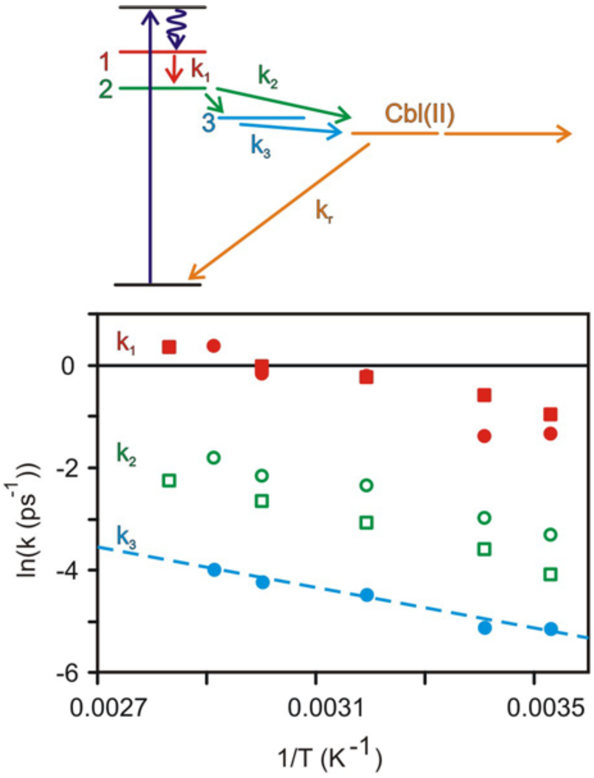

Figure 3.29. ln(k) vs 1/T for AdoCbl in water (circles) and ethylene glycol (squares). Figure reproduced from Reference [5].

Note that there are no rate constants plotted for k_3 in ethylene glycol, as the intermediate "3" is not observed in ethylene glycol. This LMCT (Chapter 1) intermediate appears stabilized in water as the higher dielectric constant stabilizes the solvation of the dimethylbenzimidazole.

3.4 Remarks

The results from the experiments on the excited states presented in the previous section (3.3) give some insight into the intermediate observed for adenosylcobalamin bound to glutamate mutase presented in Section 3.2. As this intermediate is spectroscopically identical to the MLCT state observed in methylcobalamin, the protein is likely influencing the excited state electronic structure of the adenosylcobalamin in such a way as to support the large charge density transfer to the adenosyl ligand of the MLCT state, and suppress the photophysical pathways found in Section 3.3.3. The general process should be similar to Figure 3.22.

3.5 Bibliography

1. Walker II, L.A., Shiang, J.J., Anderson, N.A., Pullen, S.H., and Sension, R.J., *Time-Resolved Spectroscopic Studies of B12 Coenzymes: The Photolysis and Geminate Recombination of Adenosylcobalamin.* Journal of the American Chemical Society, 1998. **120**: p. 7286-7292.

2. Sension, R.J., Cole, A.G., Harris, A.D., Fox, C.C., Woodbury, N.W., Lin, S., and Marsh, E.N.G., *Photolysis and Recombination of Adenosylcobalamin Bound to Glutamate Mutase.* Journal of the American Chemical Society, 2004. **126**: p. 1598-1599.

3. Stickrath, A.B., Harris, D.A., and Sension, R.J. *Ultrafast Studies of the Electronic Structure and Dynamics of B12 Cofactors*. in *Femtochemistry VII: Fundamental Ultrafast Processes in Chemistry, Physics, and Biology*. 2005. Washington D.C.: Elsevier.

4. Sension, R.J., Harris, D.A., Stickrath, A., Cole, A.G., Fox, C.C., and Marsh, E.N.G., *Time-resolved measurements of the photolysis and recombination of adenosylcobalamin bound to glutamate mutase.* Journal of Physical Chemistry B, 2005. **109**(38): p. 18146-18152.

5. Harris, D.A., Stickrath, A.B., Carroll, E.C., and Sension, R.J., *Influence of environment on the electronic structure of Cob(III)alamins: Time-resolved absorption studies of the S-1 state spectrum and dynamics.* Journal of the American Chemical Society, 2007. **129**(24): p. 7578-7585.

6. Sension, R.J., Harris, D.A., and Cole, A.G., *Time-resolved spectroscopic studies of B-12 coenzymes: Comparison of the influence of solvent on the primary photolysis mechanism and geminate recombination of methyl-, ethyl-, n-propyl-, and 5 '-deoxyadenosylcobalamin.* Journal of Physical Chemistry B, 2005. **109**(46): p. 21954-21962.

7. Shiang, J.J., Cole, A.G., Sension, R.J., Hang, K., Weng, Y., Trommel, J.S., Marzilli, L.G., and Lian, T., *Ultrafast Excited-State Dynamics in Vitamin B12 and Related Cob(III)alamins.* Journal of the American Chemical Society, 2006. **128**: p. 801-808.

8. Walker II, L.A., Jarrett, J.T., Anderson, N.A., Pullen, S.H., Matthews, R.G., and Sension, R.J., *Time-Resolved Spectroscopic Studies of B12 Coenzymes: The Identification of a Metastable Cob(III)alamin Photoproduct in the Photolysis of Methylcobalamin.* Journal of the American Chemical Society, 1998. **120**: p. 3597-3603.

9. Shiang, J.J., Walker II, L.A., Anderson, N.A., Cole, A.G., and Sension, R.J., *Time-Resolved Spectroscopic Studies of B12 Coenzymes: The Photolysis of*

Methylcobalamin Is Wavelength Dependent. Journal of Physical Chemistry B, 1999. **103**: p. 10532-10539.

10. Yoder, L.M., Cole, A.G., Walker II, L.A., and Sension, R.J., *Time-Resolved Spectroscopic Studies of B12 Coenzymes: Influence of Solvent on the Photolysis of Adenosylcobalamin.* Journal of Physical Chemistry B, 2001. **105**(48): p. 12180-12188.

11. Cole, A.G., Yoder, L.M., Shiang, J.J., Anderson, N.A., Walker II, L.A., Banaszak Holl, M.M., and Sension, R.J., *Time-Resolved Spectroscopic Studies of B12 Coenzymes: A Comparison of the Primary Photolysis Mechanism in Methyl-, Ethyl-, n-Propyl-, and 5'-Deoxyadenosylcobalamin.* Journal of the American Chemical Society, 2002. **124**: p. 434-441.

12. Finke, R.G. and Hay, B.P., *Thermolysis of adenosylcobalamin: a product, kinetic, and cobalt-carbon (C5') bond dissociation energy study.* Inorganic Chemistry, 1984. **23**(20): p. 3041-3043.

13. Garr, C.D. and Finke, R.G., *Adocobalamin (AdoCbl or coenzyme B12) cobalt-carbon bond homolysis radical-cage effects: product, kinetic, mechanistic, and cage efficiency factor (Fc) studies, plus the possibility that coenzyme B12-dependent enzymes function as "ultimate radical cages" and "ultimate radical traps".* Inorganic Chemistry, 1993. **32**(20): p. 4414-4421.

14. Hay, B.P. and Finke, R.G., *Thermolysis of the Co---C bond in adenosylcobalamin (coenzyme B12)—IV. Products, kinetics and Co---C bond dissociation energy studies in ethylene glycol.* Polyhedron, 1988. **7**(16-17): p. 1469-1481.

15. Walker, L., *Ultrafast Transient Absorption Studies of Vitamin B12 Coenzymes: Investigation of the Cobalt-Carbon Bond in Alkylcobalamins*, in *Chemisty*. 1998, University of Michigan: Ann Arbor, Michigan.

16. Reitzer, R., Gruber, K., Jogl, G., Wagner, U.G., Bothe, H., Buckel, W., and Kratky, C., *Glutamate mutase from Clostridium cochlearium: the structure of a coenzyme B12-dependent enzyme provides new mechanistic insights.* Structure, 1999. **7**: p. 891-902.

17. Gruber, K., Reitzer, R., and Kratky, C., *Radical Shuttling in a Protein: Ribose Pseudorotation Controls Alkyl-Radical Transfer in the Coenzyme B12 Dependent Enzyme Glutamate Mutase.* Angewandte Chemie-International Edition, 2001. **40**(18): p. 3377-3380.

18. Chen, H.-P. and Marsh, E.N.G., *How Enzymes Control the Reactivity of Adenosylcobalamin: Effect on Coenzyme Binding and Catalysis of Mutations in the Conserved Histidine-Aspartate Pair of Glutamate Mutase.* Biochemistry, 1997. **36**: p. 7884-7889.

19. Shriver, D.F. and Drezdzon, M.A., *The Manipulation of Air-Sensitive Compounds*. 2 ed. 1986, New York: John Wiley & Sons.

20. Cole, A., *Ultrafast Transient Absorption Studies of Coenzyme B12 Analogs and Derivatives: Biological Activity of Alkylcobalamins*, in *Chemistry*. 2003, University of Michigan: Ann Arbor, Michigan.

21. Degenhardt, O.S., Waters, B., Rebelo-Cameirao, A., Meyer, A., Brunner, H., and Toltl, N.P., *Comparison of the effectiveness of various deaeration techniques.* Dissolution Technologies, 2004. **14**: p. 6-11.

22. Sension, R.J., Harris, D.A., and Cole, A.G., *Time-Resolved Spectroscopic Studies of* B_{12} *Coenzymes: A Comparison of the Influence of Solvent on the Primary Photolysis Mechanism and Geminate Recombination of Methyl-, Ethyl-, n-Propyl-, and 5'-Deoxyadenosylcobalamin.* Journal of Physical Chemistry B, 2005. **109**: p. 21954-21962.

23. Lakowicz, J.R., *Principles of Flourescence Spectroscopy*. Third ed. 2006, New York, NY: Springer.

24. Harris, D.A., *Studies of Solvent Effects on Reaction Dynamics Using Ultrafast Transient Absorption Spectroscopy*, in *Applied Physics*. 2006, University of Michigan: Ann Arbor, Michigan.

Chapter 4

Solvent Dependence of Cage Escape for Small Nonpolar Radicals in Solution

The studies presented on alkylcobalamins in Chapter 3 address several intriguing questions of biochemical importance concerning the enzymatic generation and exploitation of free radicals. The alkylcobalamins also turn out to be scientifically interesting in their own right. The experiments described in Chapter 3, especially the temperature dependent studies presented in Section 3.3.2, also suggest that the cage escape of photodissociated alkyl radicals may be well suited, perhaps surprisingly so, as a paradigm system to study the diffusion of small particles in solution. The notion of a solvent caging influence in the photolysis of cobalamins has been suggested previously [1]. The temperature dependent determination of rate constants for cage escape of adenosylcobalamin and methylcobalamin in water and ethylene glycol present some surprising findings as will be discussed in detail below.

To further the inquiry into the solvent cage effect a systematic study was carried out, varying the solvent viscosity over as wide a range as possible and in different environments. Due to the widely disparate behavior of the methyl and adenosyl radicals in terms of cage escape, intermediate sized radicals were sought. The result was that two synthetic alkylcobalamins, ethyl and propylcobalamin, were produced. The choice of alkyl radicals was influenced by the desire to study specific interactions between the protic, hydrogen bonding solvents and the diffusing radicals. The adenosyl radical has nitrogen and oxygen atoms that may interact with the solvent, while the methyl, ethyl, and propyl radicals lack such interaction.

Despite the extensive literature on solvent cage effects [2], there is relatively little direct time-resolved investigation of caging. At least one study, more limited in scope than the one presented in this chapter, was focused on the solvent caging of radical pairs produced by the photolysis of adenosylcobalamin as a function of solvent viscosity [3]. This study undertaken by Gerards and coworkers examined the cage escape of adenosyl and cob(II)alamin radicals following photolysis in a series of eight different water and glycerol mixtures at three temperatures each. However, this experiment suffered from an inherent limitation. The photolyzed radical pairs were produced by excitation with a xenon arc lamp. Without the short time resolved capabilities of the experimental apparatus described in Chapter 2, bulk recombination of non-geminate radical pairs must be considered. Gerards and coworkers introduced the radical scavenger tempo (2,2,6,6,-tetramethylpiperidine 1-oxide) in excess to react with adenosyl radicals which have left the initial solvent cage before there is opportunity to interact with cob(II)alamin radicals in the bulk. There has been a report of reaction between cob(II)alamin and tempo[4]; however, Gerards and coworkers did not observe any interaction between the two. The study undertaken here was performed with femtosecond resolution, making possible a direct real-time measurement of cage escape and recombination, without the need for radical scavengers.

4.1 Sample Preparation

4.1.1 Alkylcobalamin (Solute) Preparation

Adenosylcobalamin and methylcobalamin as biologically relevant compounds are readily available commercially. These compounds were obtained from Sigma and used without any further purification. The synthetic alkylcobalamins, ethyl- and n-propylcobalamin, could not be obtained commercially and were synthesized according to literature methods [5-8]. The starting material for both ethyl- and n-propylcobalamin was the cob(III)alamin hydroxocobalamin, where the upper axial ligand of the cobalt atom is bonded to the oxygen of a hydroxyl functional group.

The highlights of the synthesis of ethyl- and n-propylcobalamin are sketched very briefly as follows. Cob(I)alamin is first produced through the reaction of the hydroxocobalamin with an excess of sodium borohydride. The cob(I)alamin is then reacted with an excess of the appropriate alkyl halide (either ethyl iodide or n-propyl bromide) to create the alkylcobalamin. The mixture is desalted by abstraction into a solution of dichloromethane and phenol and added to diethyl ether before being centrifuged. After being centrifuged, the precipitated alkylcobalamin is separated from the solution and the supernatant discarded. The alkylcobalamin was then redissolved in water and stored chilled until used. A more detailed description of the synthesis is described in reference [6]. Note that the final step here varies from that described previously [6], due to difficulty with sample loss. The problems with sample loss might arise in this final step as there is some evolution of the procedure between reference [6] and the earlier reference [7]. Another procedure for the purification process with increased yield percentage was evidently used in the past [9], and should be considered for future ethylcobalamin and n-propylcobalamin synthesis.

For transient absorption measurements the alkylcobalamin was introduced to the solvent immediately prior to the start of the experiment, and kept under an inert gas atmosphere for the duration as described in Section 2.3 of Chapter 2. The commercially available compounds were normally prepared at concentrations of 1mM. Using the Beer-Lambert law (Chapter 2, Equation 2.1), along with a molar extinction coefficient of ~5000$M^{-1}cm^{-1}$ at 400nm (see Chapter 3, Figure 3.3), and optical path length (flow cell width) of 1mm, the predicted absorption of the 400nm second harmonic excitation pump is ~68%. This absorption was typically sufficient to induce an approximately 10-20mOD change in absorption at the probe wavelengths used. With this scale of absorbance, a reasonable signal to noise ratio was readily obtained for the kinetic traces.

Although the molar extinction coefficient is comparable for the synthesized compounds, their scarce supply compounded with the need to constantly refresh the sample often dictated that sample concentrations were less than 1mM (and much less than the protein bound adenosylcobalamin samples described in Chapter 3, which had a signal to noise comparable to the commercially available compounds). The difficulty of the experiments increased significantly as with a comparable noise to that for the commercial compounds, the signal to noise ratio was much poorer in the traces obtained with the synthesized alkylcobalamins (which were less concentrated). Considerable effort was placed on improving the signal to noise ratio for the small signals of the synthesized compounds through improving the quality and stability of both excitation and probe laser pulses (extending from the oscillator operation right through probe and excitation pulse generation).

Typical steady-state absorption spectra for the synthesized compounds are shown in Figure 4.1. These agree with spectra reported in the literature [10]. The steady-state spectrum of the starting material, hydroxocobalamin (dashed line), is included in Figure 4.1 as well. The solid black line shows sample degradation following a prolonged exposure to a 400nm excitation laser pulse as well heating to temperatures near 80°C. Figure 4.1 demonstrates the need to carefully ensure sample quality by monitoring the sample, protecting it from light and heat when not in use, and especially by continually replacing with fresh sample. These procedures were most important for the ethyl- and n-propylcobalamin samples. As the data will show, the quantum yield for radical pairs is very large in these samples, allowing the cob(II)alamin radical to interact with the solvent producing hydroxocobalamin and aquocobalamin (upper axial ligand is to a water molecule – spectrum not shown). The degraded sample spectrum shows the evolution toward the starting material spectrum and towards aquocobalamin.

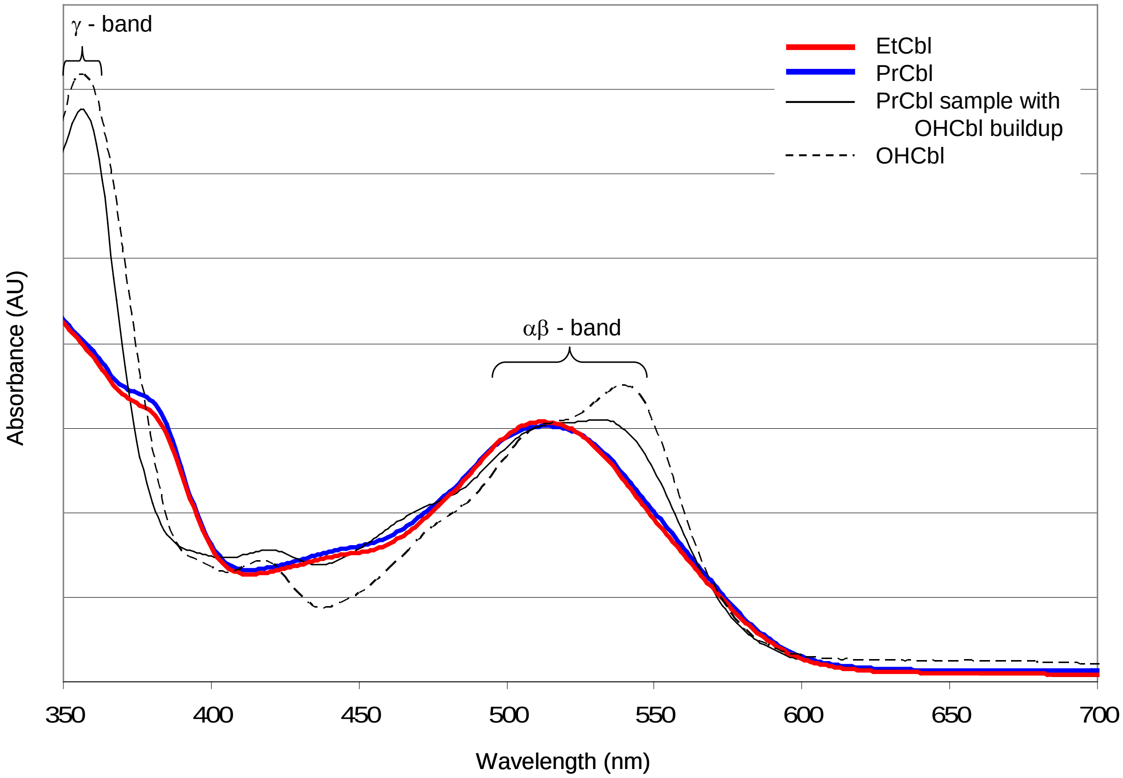

Figure 4.1. Steady-state absorption spectra of ethyl- (red) and n-propylcobalamin (blue). The steady-state spectra of the starting material for synthesis, hydroxocobalamin (black), along with a used sample (dashed) showing product buildup are included for reference.

Another example of sample reverting to the starting material is illustrated in the transient absorption kinetic traces shown in Figure 4.2. The blue trace is the first scan using the same propylcobalamin sample used to obtain the steady-state spectrum (blue) shown in Figure 4.1. The pump is at 400nm and the probe at 540nm. The red trace is the same sample after having been used for several hours and after cycling the temperature through 80°C. The steady-state spectrum (black dashed) of this sample is also shown in Figure 4.1. Clearly, the kinetics are no longer the same after extensive sample use. The black trace is a room temperature scan for hydroxocobalamin under the same conditions. Because of the problem with sample degradation all samples were changed regularly and maintained at or below room temperature except during the actual measurements.

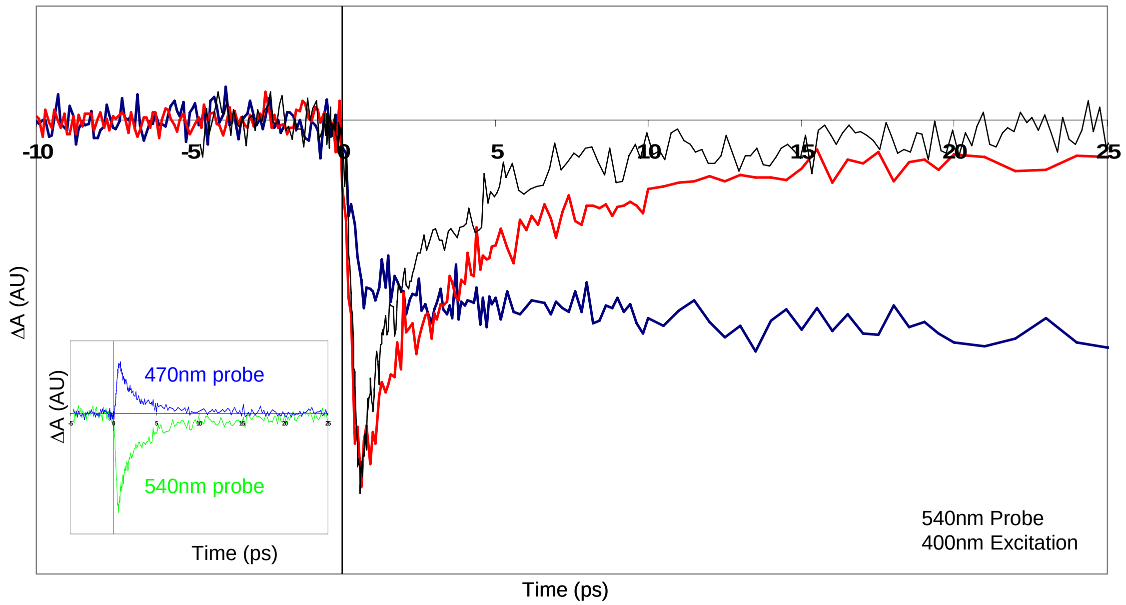

Figure 4.2. Kinetic traces demonstrating product buildup: Propylcobalamin (blue) is compared with the same sample after long time use (red), for 400nm excitation and 540nm probe wavelengths. A hydroxocobalamin trace under the same conditions is included for comparison. The inset shows hydroxocobalamin traces for 400nm excitation and 470nm (blue), 540nm (green) probe. The green trace in the inset is the same as the black trace in the main figure.

4.1.2 Solvent Preparation

As described in Chapter 3, the homolytic Co-C bond cleavage observed in the alkylcobalamins results in the formation of two radicals: cob(II)alamin and an alkyl radical. Since either of these radicals will readily react with the unpaired electrons of dissolved molecular oxygen, the solvent environment must be deoxygenated before the addition of the alkylcobalamin solute. For samples in water, the dissolved oxygen can be sufficiently displaced by purging with an inert gas [6, 11]. Due to the more viscous nature of ethylene glycol (see 4.1.3) the method of freeze-pump-thaw [11] was chosen for deoxygenation. Refer to Chapter 3, Section 3.2.1 for details on the deoxygenation techniques.

As described in Chapter 2, a positive pressure of inert gas (nitrogen) is maintained on the sample after the addition of alkylcobalamin and for the duration of experimental use. Also, as described in Chapter 3, stage alignment over the entire nine nanosecond temporal window probed was check prior to performing measurements and then periodically by taking kinetic traces of the well characterized [7, 12-15] free adenosylcobalamin in aqueous solution at room temperature.

4.1.3 Solvent Viscosity

Modeling the radical recombination and diffusive escape from the solvent cage requires knowledge of the solvent viscosity. The solvents used for these experiments are: water; ethylene glycol; mixtures of water and ethylene glycol; and mixtures of sucrose and water. The use of mixtures and solvent temperature variation as detailed in the Sample Setup description of Chapter 2 allows for a large change in solvent viscosity (from 0.40 cP in pure water at 71°C to 27.5 cP in pure ethylene glycol at 10°C). The choice of sucrose dissolved in water as a solvent makes it possible to vary the solvent viscosity without the associated large change in dielectric constant seen in switching from water to ethylene glycol [16].

4.1.3.1 Water, Ethylene Glycol, and Mixtures of Water and Ethylene Glycol

While there is considerable tabulated viscosity information available for pure water and pure ethylene glycol, there is far less data available for mixtures of water and ethylene glycol [17]. Fortunately, at least two groups [17, 18] have studied the viscosity properties of and provided fits for these mixtures over a sufficiently wide range of concentration variations and temperatures, so as to cover all compositions and temperatures used to analyze the data presented here. In choosing a method to calculate solvent viscosity, preference was given only to a good and well characterized fit to measured data points over a physical model, which might provide some motivation for the properties of the solvent but result in larger errors for the calculated viscosities. With this philosophy in mind, both the fits of Teja and coworkers [17] and Obermeier and coworkers [18] were considered and compared with each other. Calculated viscosities for each mixture concentration used are plotted in Figure 4.3, for both the fits of Teja and Obermeier. Solid lines are those from Teja and coworkers; dashed lines are from the work of Obermeier and coworkers. The pure solvents, water and ethylene glycol, are shown in red and brown, respectively. The mixtures are plotted as follows: 75% water / 25% ethylene glycol (black); 50% water / 50% ethylene glycol (green); and 25% water / 75% ethylene glycol (blue). Also included on the plot are experimentally determined points for the pure solvents [19] (red circles for water and brown diamonds for ethylene glycol). These viscosity points are used for both adenosylcobalamin and methylcobalamin in the pure solvents. The remaining viscosities for all samples (solutes) in all solvents were calculated as described in this chapter and plotted in Figure 4.3 (due to lack of available experimentally determined viscosity data).

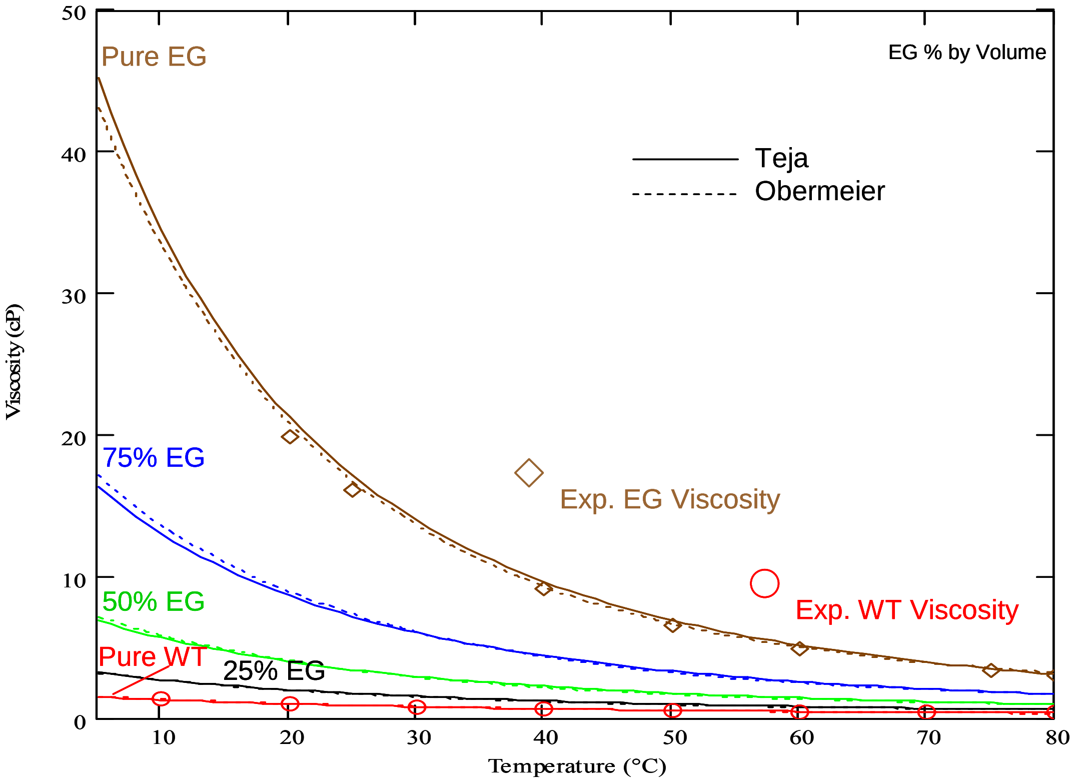

Figure 4.3. Calculated and measured solvent viscosity: water, ethylene glycol, and mixtures of water and ethylene glycol.

The plots of viscosity, η, in Figure 4.3 were arrived at according to [17, 18]:

$$\ln \eta_{Teja} = w_1 y_1 + w_2 y_2 + (y_1 - y_2) w_1 w_2 (A_4 + A_5 w_1 + A_6 t)\,, \tag{4.1}$$

and

$$\ln \eta_{Obermeier} = \sum_{i=1}^{2} \sum_{j=1}^{3} B_{i,j} x^{(j-1)} t^{(i-1)} + \left(\sum_{j=1}^{3} B_{3,j} x^{(j-1)} \right)^{\frac{1}{4}}\,. \tag{4.2}$$

w_1 and w_2 in Equation 4.1 are the mass fractions of ethylene glycol and water respectively, in a solvent mixture. In Equation 4.2, x is the mass fraction of ethylene glycol in the mixture (the notation has been kept consistent with each group's convention). y_1 and y_2 are fits to the pure solvent viscosities [17] for ethylene glycol (1) and water (2) and are given by:

$$y_1 = \ln \eta_{EG} = A_1 + \frac{A_2}{t + A_3}; \tag{4.3}$$

$$y_2 = \ln \eta_{WT} = A_7 + \frac{A_8}{t + A_9}. \tag{4.4}$$

t is the temperature, in degrees centigrade, in Equations 4.1 through 4.4. The coefficients, A_i and $B_{i,j}$, are constants determined from fits and are listed in Tables 4.1 (Teja) and 4.2 (Obermeier).

Table 4.1. Coefficients for the viscosity calculations according to the fits of Teja and coworkers [17].

***i*: *A*$_i$**	**Value η in mPa*s = cP**
1	-3.61359
2	986.519
3	127.861
4	-0.165301
5	-0.287325
6	$1.10978*10^{-3}$
7	-3.758023
8	590.9808
9	137.2645

Table 4.2. Coefficients for the viscosity calculations according the fits of Obermeier and coworkers [18].

$B_{i,j}$ η in mPa*s = cP	*j* = 1	*j* = 2	*j* = 3
***i* = 1**	$5.5164*10^{-1}$	2.6492	$8.2935*10^{-1}$
***i* = 2**	$-2.7633*10^{-2}$	$-3.1496*10^{-2}$	$4.8136*10^{-3}$
***i* = 3**	$6.0629*10^{-17}$	$2.2389*10^{-15}$	$5.8790*10^{-16}$

References [17] and [18] state Equations 4.1 and 4.2 without motivation. This approach is reasonable given the goal of merely reproducing the actual data with the best accuracy. Obermeier and coworkers characterize the fit given by Equation 4.2 as having an accuracy of ±5% when compared to experimental data over the range fitted (-10°C to 100°C); while the method of Teja is characterized to have an average absolute deviation of 0.80% and maximum absolute deviation of 2.35% over the range 16.85°C to 176.85°C. The fit provided by Teja is preferable since it is in general a better fit. However, it has not been characterized to the lowest temperatures reached for the alkylcobalamin experiments. The lowest temperature was 6.3°C for the water and ethylene glycol mixtures. Therefore comparisons of the deviation between the two fits are shown in Figures 4.4 and 4.5.

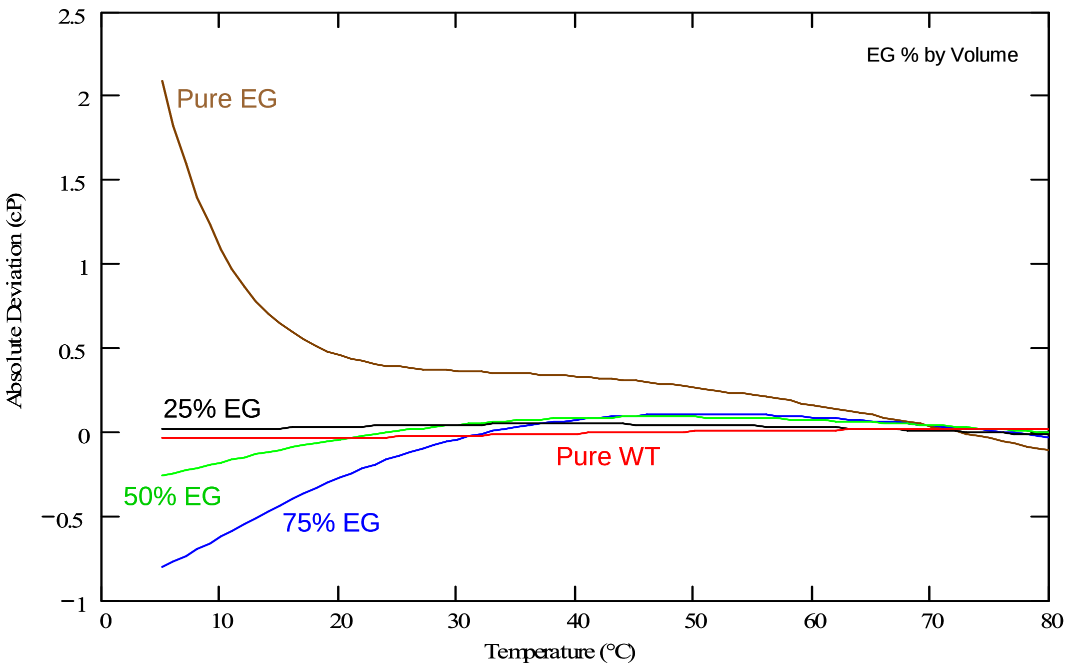

Figure 4.4. Absolute deviation between the fits of Teja and Obermeier.

Figure 4.4 shows the absolute deviation of the fits due to Teja from those to Obermeier, while Figure 4.5 shows the relative deviations (plots in Figure 4.4 are divided by the Obermeier viscosities to produce the plots in Figure 4.5). These two Figures show that the two methods never deviate by more than 6% from each other over the range of interest (6°C to 80°C). Figure 4.5 also shows that the viscosities obtained from Equation 4.1 do not deviate any more from those obtained from Equation 4.2 below 16.85°C than above 16.85°C, which is the lower limit of the characterization by Teja. The method of Teja was then chosen to calculate the viscosities used to analyze and model the escape data described in this thesis. It is worth noting that for several sets of data, the viscosities due to Obermeier were also used and no discernable difference was identified in the escape and recombination analysis.

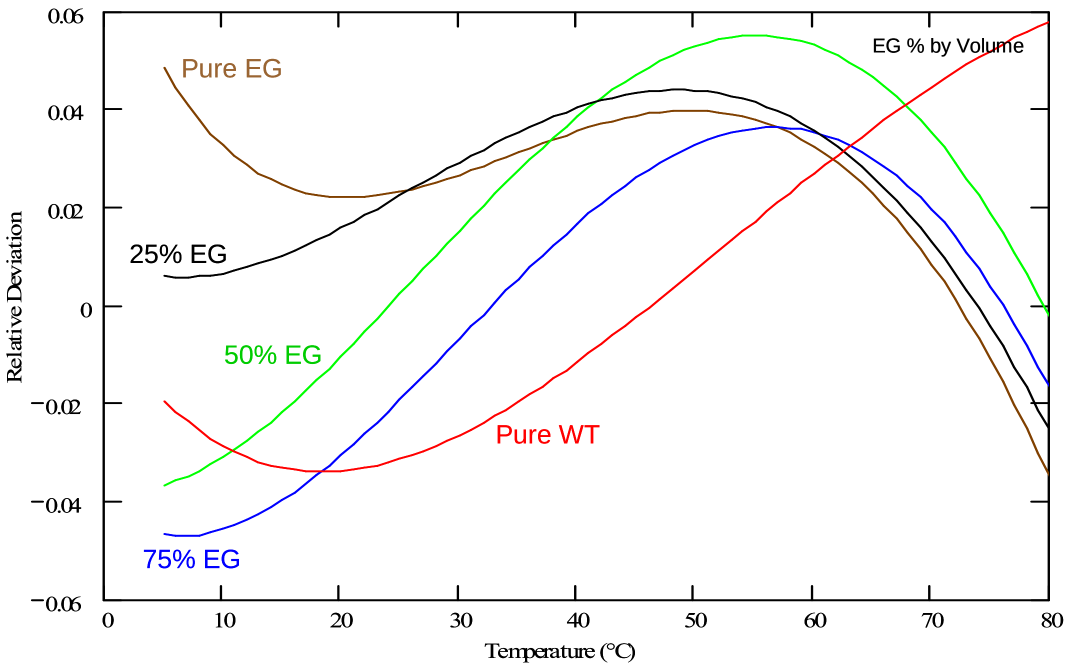

Figure 4.5. Relative deviation of fits due to Teja from those due to Obermeier.

Both Equations 4.1 and 4.2 are expressed in terms of the mass fraction of water and ethylene glycol in the solvent mixture. The knowledge of this experimental parameter imposes a problem since each solvent mixture was prepared as a volume fraction. The volume of a water and ethylene glycol mixture will be contracted when compared to the sum of the individual volumes of water and ethylene glycol mixed (though, of course, mass and mole fractions will remain constant). Ideally, one would prepare the samples measuring the mass of each volume of the individual components of the mixture before mixing them together. However, this complication was not appreciated until viscosity calculations were begun already following data collection. The problem of determining mass fractions from the known volume fractions remains.

To ascertain the extent to which volume contraction might impact the final sample volume (typically of 15mL), the densities of the mixtures were calculated as a function of temperature and concentration. The mixture density was also calculated to the according to the method of Teja and coworkers [17], again using the form of Equation 4.1, with a new set of fit coefficients (Table 4.3):

$$\rho = w_1 y_1 + w_2 y_2 + (y_1 - y_2) w_1 w_2 (C_4 + C_5 w_1 + C_6 t) . \tag{4.5}$$

This time, however, $y_1 = \rho_{EG}$ and $y_2 = \rho_{WT}$ are given by:

$$y_1 = \rho_{EG} = C_1 + C_2 + C_3 t ; \tag{4.6}$$

$$y_2 = \rho_{WT} = C_7 + C_8 t + C_9 t^2 + C_D t^3 . \tag{4.7}$$

Table 4.3. Coefficients for solvent mixture density calculations [17].

***i*: *C*$_i$**	**Value** **ρ in kg*m^{-3}**
1	1127.68
2	-0.65816
3	-6.1765*10^{-4}
4	0.30590
5	0.13781
6	-1.8961*10^{-3}
7	1002.17
8	-0.116189
9	-0.358024*10^{-2}
10	0.37667*10^{-5}

The stated accuracy when compared to experimental data for the density fits is: average absolute deviation 0.038% and maximum absolute deviation 0.133%. The expected mixture volume contraction can be calculated by comparing volumes determined through densities calculated via Equation 4.5 to those expected if the volumes were simply additive. The change in volume is known as an excess volume; the excess volume will be negative since a contraction is expected. To make the comparison, first an initial volume of water and ethylene glycol are chosen and the associated mass calculated, using the liquid density at the laboratory room temperature, m = ρ*v. Once an initial mass is known for the two solvents, these values are divided by the temperature dependent densities (Equations 4.6 and 4.7 with appropriate scaling factors for units). The result is the temperature dependent volume of the initially prepared water or ethylene glycol. These two values are then summed and subtracted from the volume calculated for the mixture from Equation 4.5. This procedure is summarized in Equation 4.8 (modified version of Equation 4a in reference [17]):

$$V_E = \frac{\rho_{EG}^{RmT} * v_{EG}^{Init} + \rho_{WT}^{RmT} * v_{WT}^{Init}}{\rho_{mix}^{Eq5}} - \left(\frac{\rho_{EG}^{RmT} * v_{EG}^{Init}}{y_1^{Eq6}} + \frac{\rho_{WT}^{RmT} * v_{WT}^{Init}}{y_2^{Eq7}} \right). \tag{4.8}$$

The superscript, *RmT*, represents room temperature and ρ^{RmT} refers to a specific density at room temperature (i.e. it is a constant, not a function like ρ_{mix} or y_1 and y_2). The superscripts *Eq5, Eq6,* and *Eq7* represent that these densities are expressed in Equations 4.5, 4.6, and 4.7 respectively. The results for the mixture concentrations and volumes used are plotted in Figure 4.6.

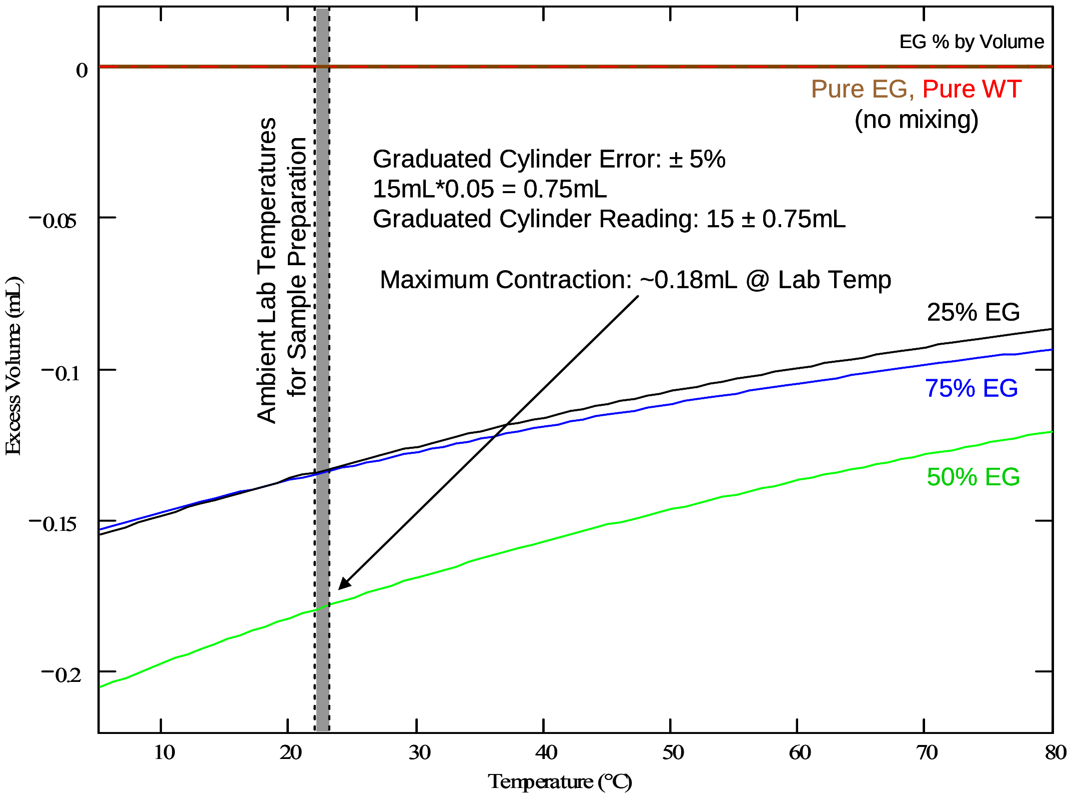

Figure 4.6. Calculated excess volumes of water / ethylene glycol mixtures.

Since the volume concentrations only need to be considered at the ambient laboratory temperature at the time of sample preparation to determine the mass fraction of water or ethylene glycol in a mixture, Figure 4.6 shows a maximum contraction of approximately 0.18mL (for a mixture made of 7.5mL of water and 7.5mL of ethylene glycol). The graduated cylinder used to prepare the solvent samples however had a stated error of ±5%. For 15mL solutions, this accuracy translates to ±0.75mL which is four times larger than the largest deviation from additive volumes. Figure 4.6 predicts then that any excess volume will be lost within the accuracy of the measurement. With this justification then, the mass fractions necessary to calculate mixture viscosities were determined from the volume fractions (i.e. Figure 4.3) assuming no excess volume.

4.1.3.2 Sucrose Dissolved in Water

Whereas there is comparatively little data for the viscosity of water and ethylene glycol mixtures (surprisingly so, given the industrial importance of such mixtures), there is a considerable literature on and varied approaches to the viscosity of solutions made from sucrose dissolved in water (for example[20, 21]). Sucrose solutions are important as a gradient medium for the separation of biological material in centrifuges [22], requiring viscosity information as a function of temperature and sucrose concentration. As an interesting aside, the diffusive movement of sugar in water was considered by Albert Einstein in his dissertation [23]. Along with the viscosity of the solvent, he used the diffusive movement of the sugar molecule to estimate both the size of the sugar molecule as well as Avogadro's number. The results of this theory led directly to his work on Brownian motion [24]. This hydrodynamic approach will be important in the data analysis of the diffusive cage escape of radicals following photolysis. Again a turn key equation was desired to produce viscosity values with well characterized accuracy. The fits of Barber [22] were chosen; and the relevant plots are shown in Figure 4.7.

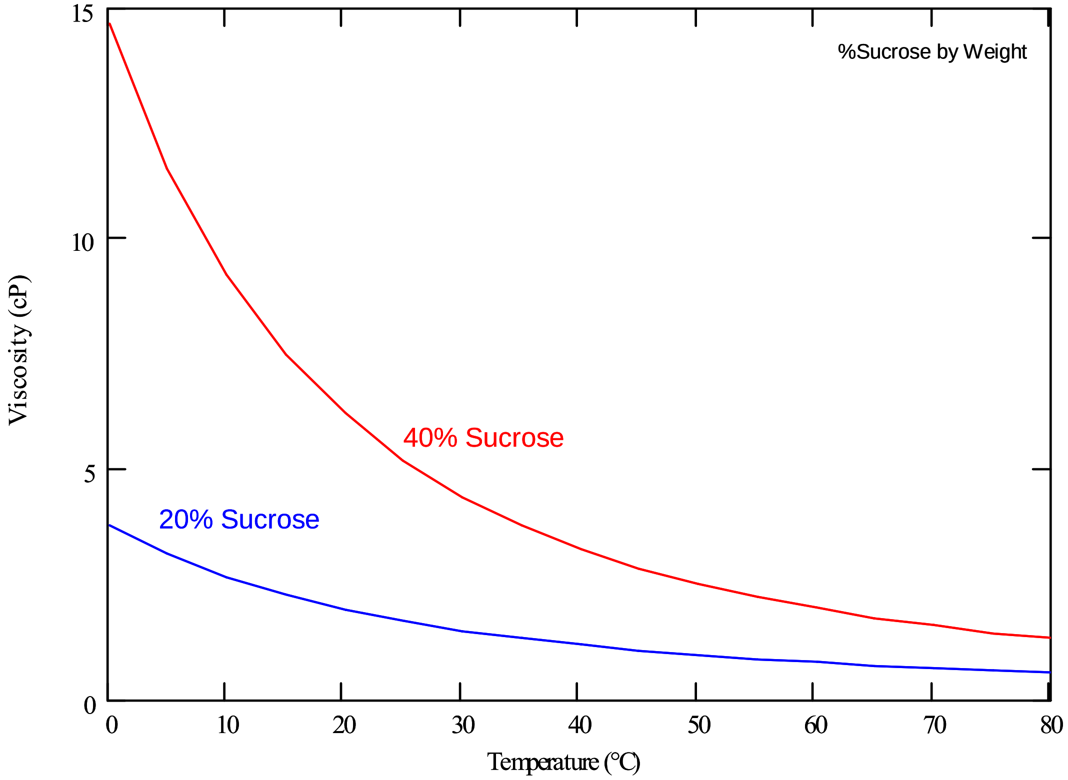

Figure 4.7. Viscosities for 20% and 40% by weight sucrose solutions.

Barber compared his fit with tabulated data [25] and found that for the concentrations of interest here, no point deviated from the actual value by more than three parts per thousand from 5°C to 40°C. Outside of this range, some values may deviate by as much as eight parts per thousand from the experimental values. Even for the smallest calculated viscosity used (0.684 cP for 20% sucrose by mass at 70°C), a deviation of 8 parts per thousand corresponds to a relative error of only ~ 1.2%. The viscosities plotted in Figure 4.7 are obtained from:

$$\log \eta = A + \frac{B}{t + C}. \qquad (4.9)$$

t is still the temperature in degrees centigrade. *A* and *B* are polynomials described by:

$$A, B = D_0 + D_1 y + D_2 y^2 + \ldots + D_7 y^7 , \tag{4.10}$$

with the coefficients D given in Table 4.4.

Table 4.4. Coefficients for polynomials *A* and *B* (Equation 4.9) [22].

***i*: *D*$_i$**	**Coefficients for *A*** **η in mPa*s = cP** ***(for 5 to 48% mass sucrose)***	**Coefficients for *B*** **η in mPa*s = cP** ***(for 5 to 48% mass sucrose)***
0	-1.5018327	$2.1169907*10^{2}$
1	9.4112153	$1.6077073*10^{3}$
2	$-1.1435741*10^{3}$	$1.6911611*10^{5}$
3	$1.0504137*10^{5}$	$-1.4184371*10^{7}$
4	$-4.6927102*10^{6}$	$6.0654775*10^{8}$
5	$1.0323349*10^{8}$	$-1.2985834*10^{10}$
6	$-1.1028981*10^{9}$	$1.3532907*10^{11}$
7	$4.5921911*10^{9}$	$-5.4970416*10^{11}$

C is give by

$$C = G_1 - G_2 \left[1 + \left(\frac{z}{G_3} \right)^2 \right]^{\frac{1}{2}} , \tag{4.11}$$

with *z* the mole fraction of sucrose in the solution and G_i constants listed in Table 4.5.

Table 4.5. Coefficients for constant *C* (Equation 4.11) [22].

Coefficients in *C*	**Value** **η in mPa*s = cP**
G_1	146.06635
G_2	25.251728
G_3	0.070674842

Unlike the case of water and ethylene glycol, determining mole fractions, *z*, does not pose a significant problem. For the sucrose mixtures, a mass of sucrose was weighed and dissolved in a known volume of water. 15mL was then measured out of a mixture prepared in this way to use as the experimental solvent.

The fits to sucrose solution viscosity described by Equations 4.9 through 4.11 were physically motivated by the Antoine (modified Arrhenius) equation which is described in reference [22].

4.2 Transient Absorption Data and Fits

4.2.1 Adenosylcobalamin

Kinetic transient absorption scans were collected for adenosylcobalamin, methylcobalamin, ethylcobalamin, and n-propylcobalamin in a series of environments and temperatures to systematically address the diffusive cage escape of the geminate radical pair. Transient scans were presented in Chapter 3 for adenosylcobalamin (Figures 3.26 through 3.28) and methylcobalamin (Figures 3.16 through 3.20) in the pure solvents (water and ethylene glycol). The data below is presented over the full 9ns time window collected without insets on the early time behavior. This presentation style is adopted since this chapter addresses the cage escape which occurs on time scales of picoseconds to 100s of picoseconds (as to which the following plots attest).

Adenosylcobalamin data is presented in Figures 4.8 through 4.16. Each of the following traces was collected following excitation at 400nm and with a probe of 540nm. Solvent environments consisting of mixtures of ethylene glycol and water are presented first, in Figures 4.8 through 4.13. The data for samples in sucrose solutions follows in Figures 4.14 and 4.15. Figure 4.16 is a comparison plot to develop the influence of solvent on the excited state dynamics of adenosylcobalamin.

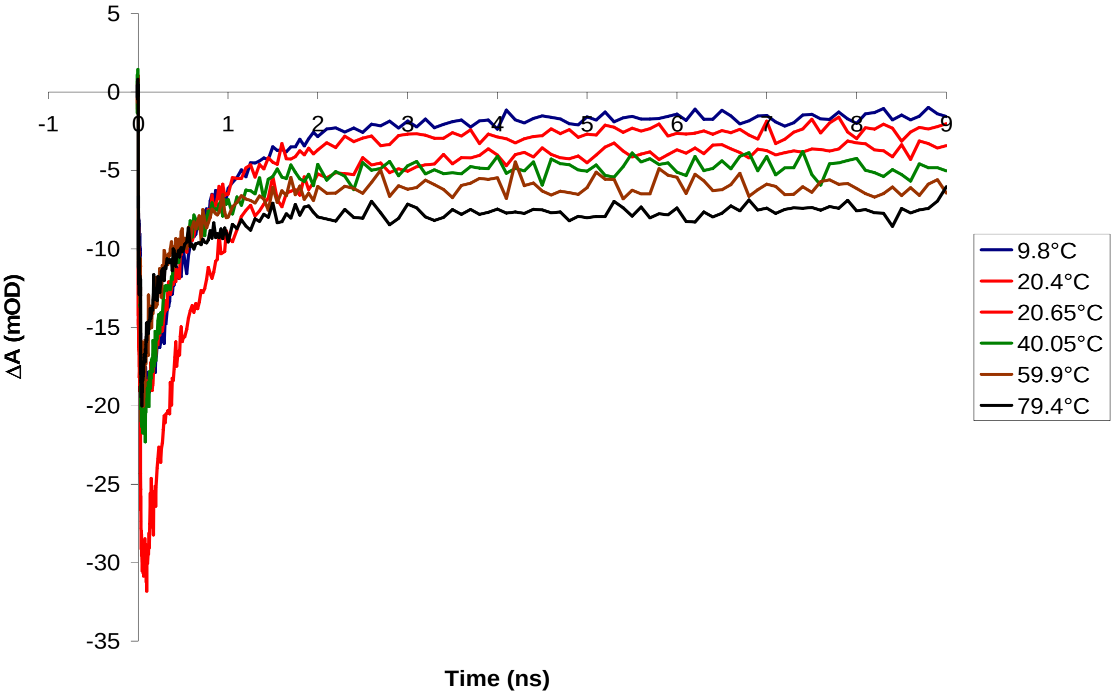

Figure 4.8. Adenosylcobalamin in a 50% ethylene glycol / 50% water solvent. The kinetic traces have not been scaled in this Figure, and the ordinate axis is therefore plotted in mOD.

The data in Figure 4.8 for adenosylcobalamin in a mixture of 50% ethylene glycol and 50% water have not been scaled. The ordinate axis is plotted in mOD; and each trace is reflective of the magnitude of actual measured signal. These experiments were carried out over the course of many months and many samples. The absolute magnitude of the signal reflects these variations. For example there are two traces in Figure 4.8 with the sample held near 20°C (20.4°C and 20.65°C, both red), with one of the traces exhibiting a magnitude nearly 50% larger than the other. However, if either of these two traces is scaled both will sit on top of each other very well within the noise of the measurement. The result is shown in Figure 4.9 where all the traces from Figure 4.8 have been scaled to normalize the data to the peak of the absorption bleach. Notice that the two 20°C scans (both red) follow along with each other. Scaling the data in this manner helps to graphically demonstrate the influence of temperature on the recombination and escape of the geminate radical pairs.

As the temperature is increased, the plateau at long times settles at a more negative value. This trend is a result of the increased cage escape of the radical pairs to produce a solvent separated radical pair, and thus an absorbing cob(II)alamin species which does not recombine geminately or with any radicals in free solution on the timescales of this experiment. The slope of the recovery of the ground state bleach towards the long lived plateau reflects the geminate recombination. The ordinate coordinate in Figure 4.9 has been adjusted to arbitrary units due to the scaling of the data.

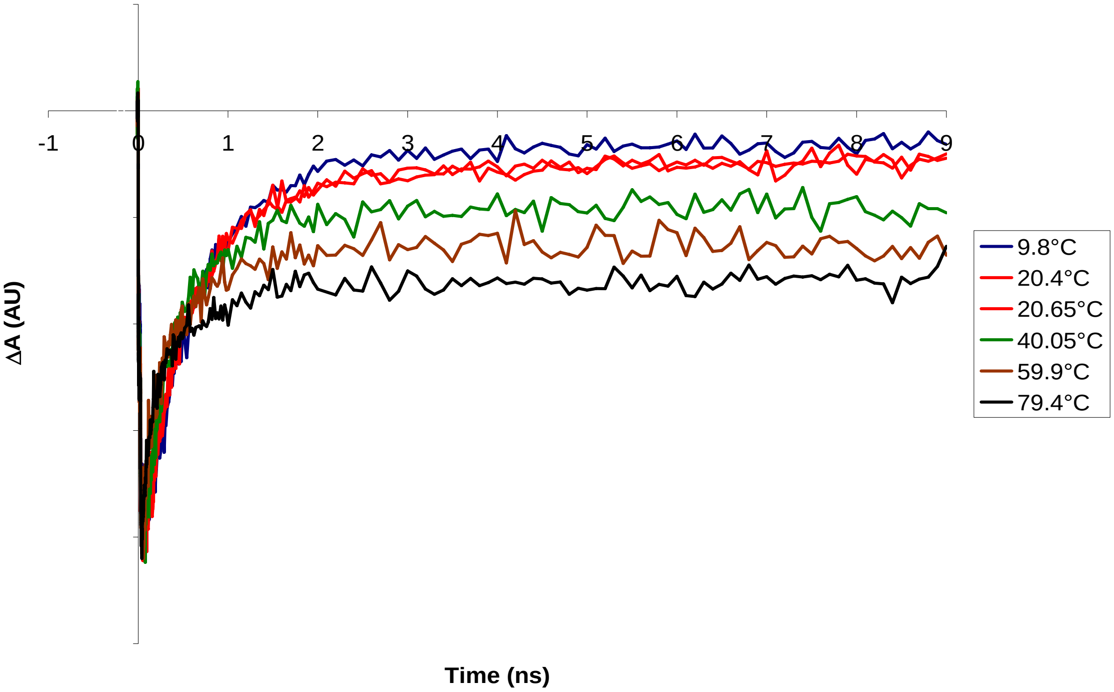

Figure 4.9. Adenosylcobalamin in 50% ethylene glycol / 50% water. This data is the same as for Figure 4.8, except the data has been scaled to normalize the magnitude at the peak of the ground state bleach. The ordinate axis is then simply in arbitrary units (AU), due to the scaling.

The rest of the adenosylcobalamin kinetic data will presented scaled as in Figure 4.9 (and in Figure 4.10), since this presentation provides a more meaningful interpretation of the data. A quantitative analysis follows. Another useful presentation of the data from Figures 4.8 and 4.9 is shown in Figure 4.10.

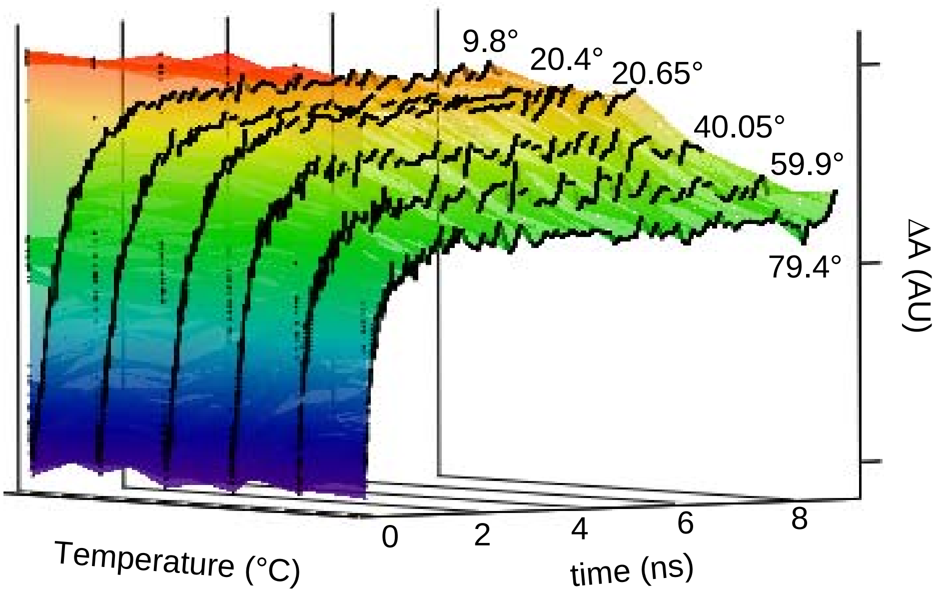

Figure 4.10. Data from Figure 4.9 (scaled adenosylcobalamin in 50% ethylene glycol / 50% water), presented in a surface plot format. The sample temperature has been added as a third plotting parameter. The surface representing the initial subpicosecond bleaching of the ground state has been made partially transparent to provide a better perspective view of the ensuing dynamics.

Figure 4.10 consists of the same data as shown in Figure 4.9, with the sample temperature included as a plotting parameter (x-axis). The surface representing the decrease in absorption representative of the initial subpicosecond ground state bleach has been made partially transparent to allow a better perspective view of the ensuing dynamics. Data for adenosylcobalamin in the other solvent mixtures used in these investigations are shown in Figures 4.11-4.16 below.

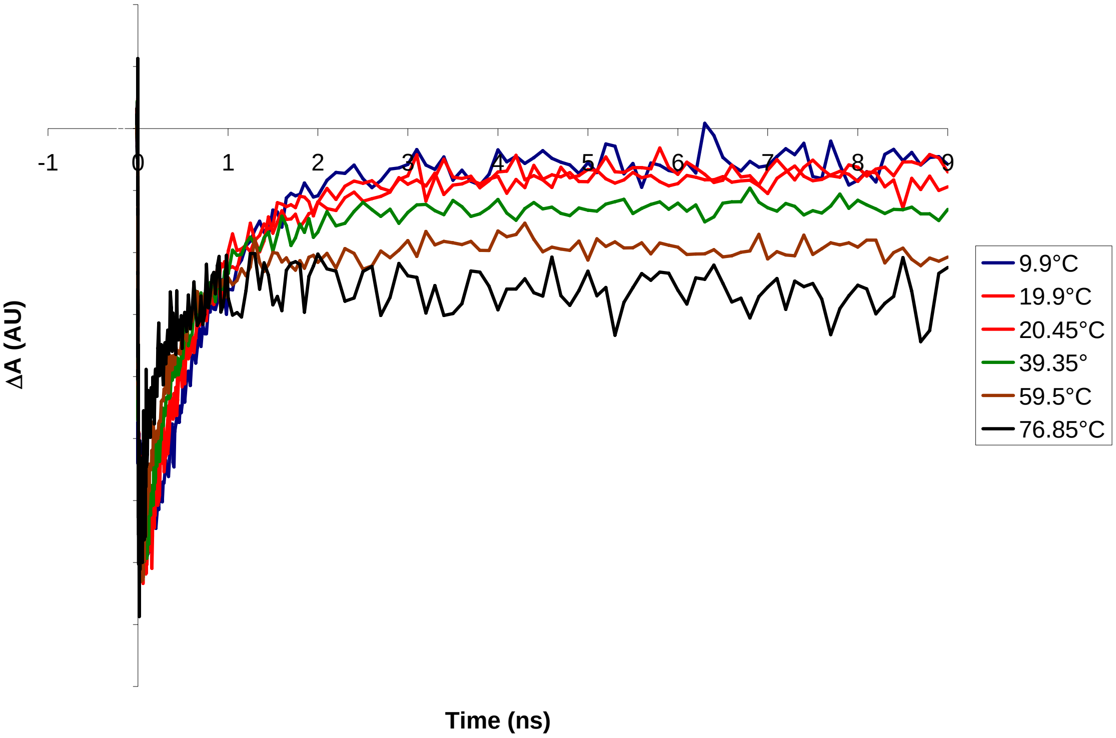

Figure 4.11. Adenosylcobalamin in 75% ethylene glycol / 25% water. This data has been scaled so that the ground state bleach in each trace has the same magnitude.

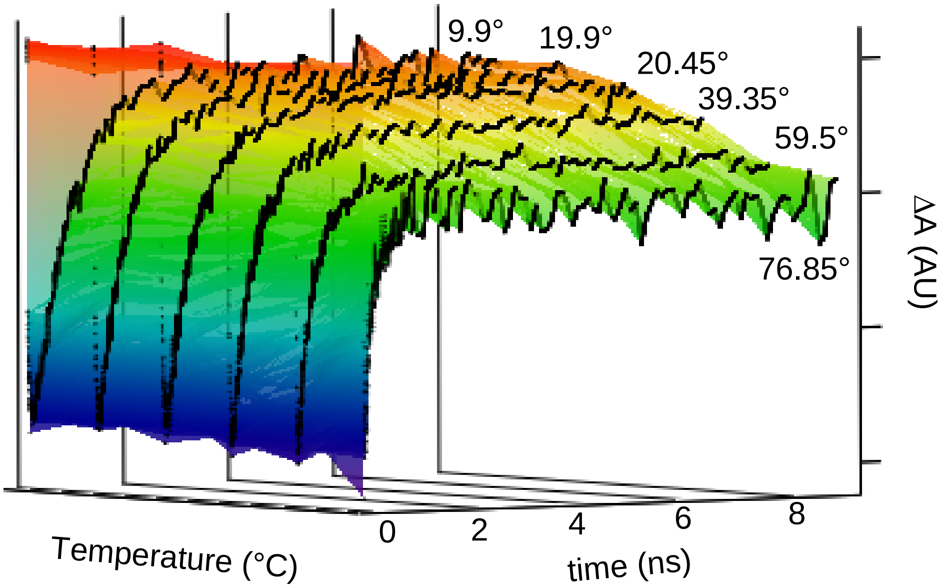

Figure 4.12. Data from Figure 4.11 (scaled adenosylcobalamin in 75% ethylene glycol / 25% water), presented in a surface plot format. The sample temperature has been added as a third plotting parameter. The surface representing the initial subpicosecond bleaching of the ground state has been made partially transparent to provide a better perspective view of the ensuing dynamics.

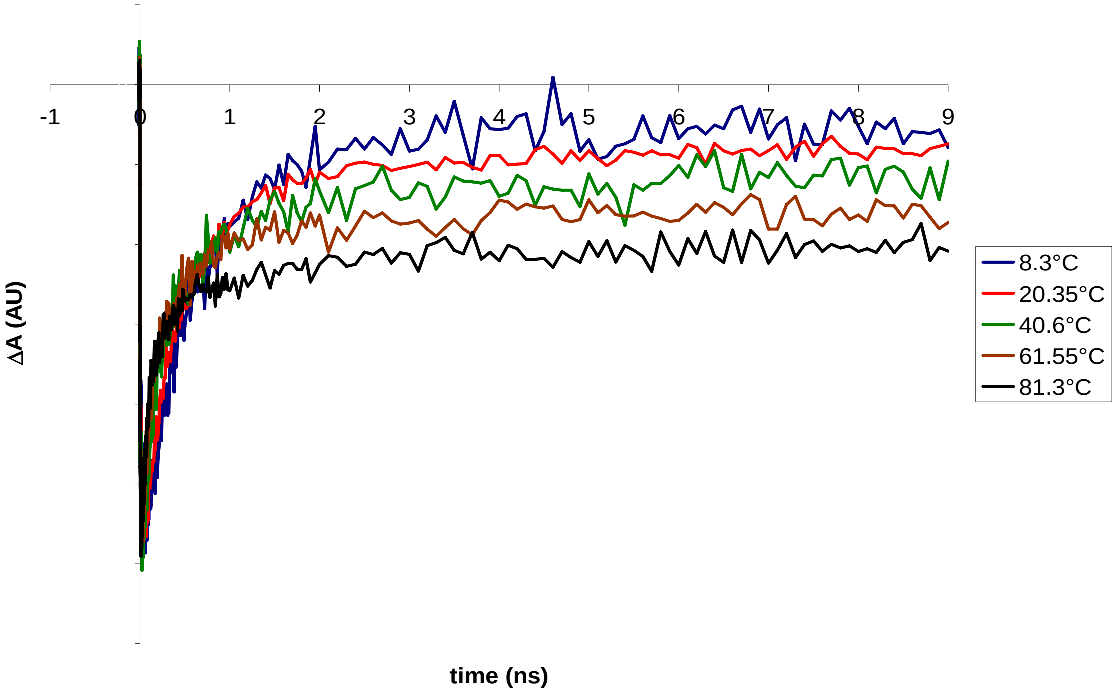

Figure 4.13. Adenosylcobalamin in 25% ethylene glycol / 75% water. This data has been scaled so that the ground state bleach in each trace has the same magnitude.

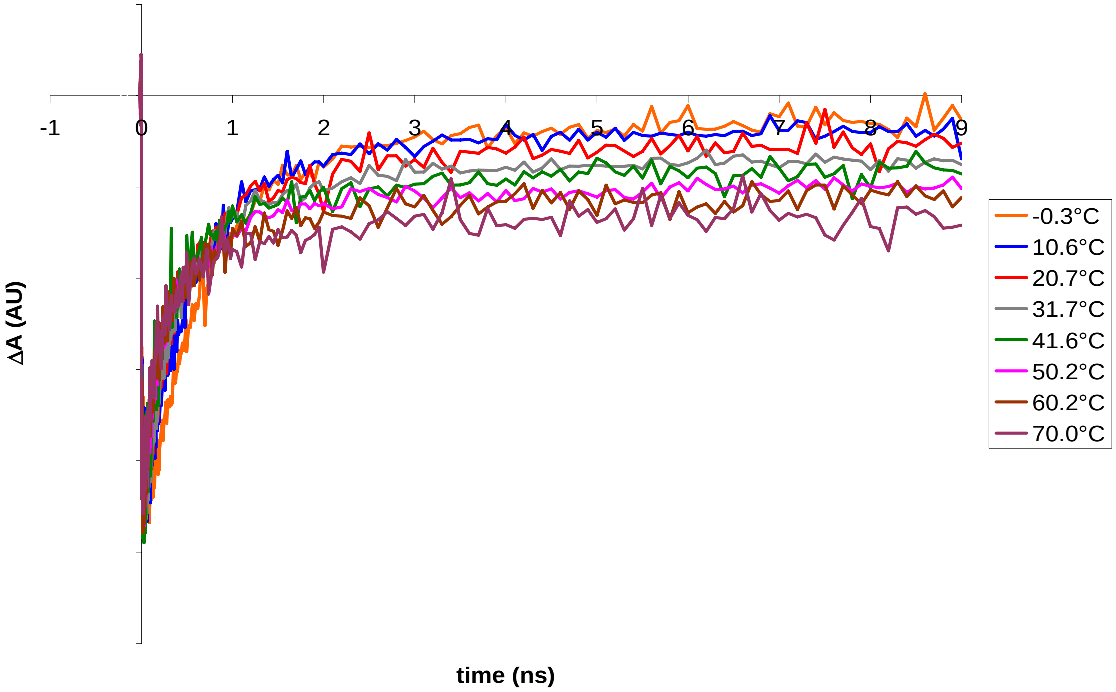

Figure 4.14. Adenosylcobalamin in sucrose solution (20% sucrose by mass). This data has been scaled so that the ground state bleach in each trace has the same magnitude, as for the data in mixtures of ethylene glycol and water. The colligative properties of sucrose dissolved in water makes the negative temperatures possible.

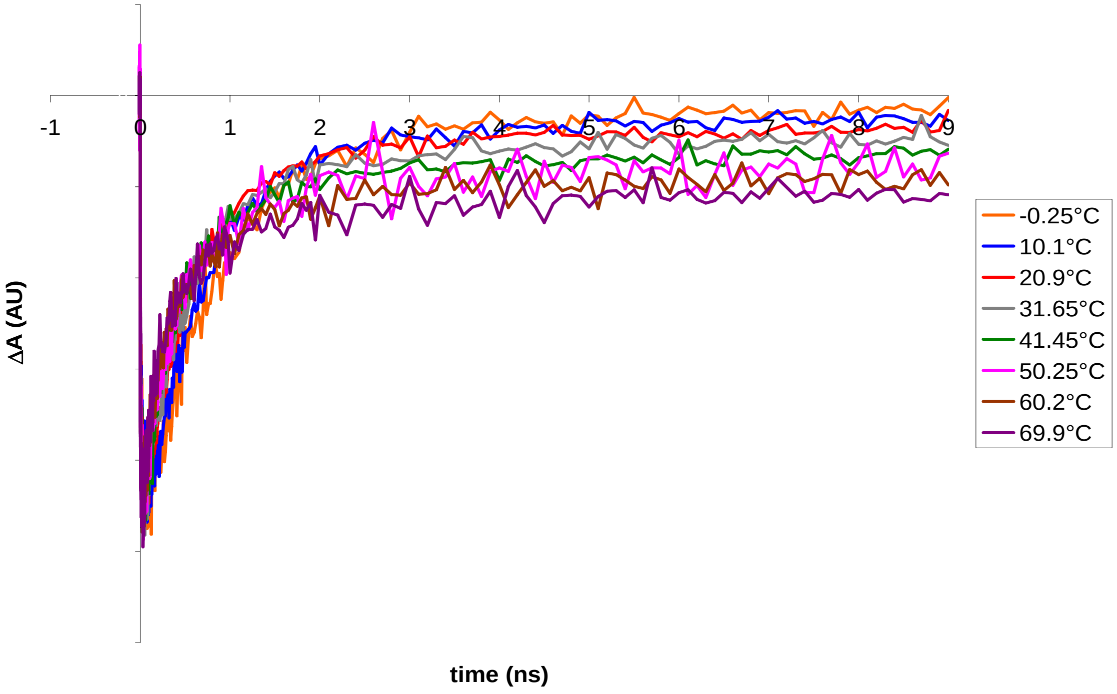

Figure 4.15. Adenosylcobalamin in sucrose solution (40% sucrose by mass). This data has been scaled so that the ground state bleach in each trace has the same magnitude, as for the data in mixtures of ethylene glycol and water. The colligative properties of sucrose dissolved in water makes the negative temperatures possible.

Figure 4.16 shows selected traces near 10°C for several scans (75% ethylene glycol / 25% water, 9.9°C; 25% ethylene glycol / 75% water, 8.3°C; 20% sucrose solution, 10.6°C). The upper plot compares the scans with 75% ethylene glycol versus that with 25% ethylene glycol, while the bottom plot compares the same scan with 75% ethylene glycol versus the 20% sucrose solution scan. These plots have also been scaled to match the magnitude of the ground state bleach.

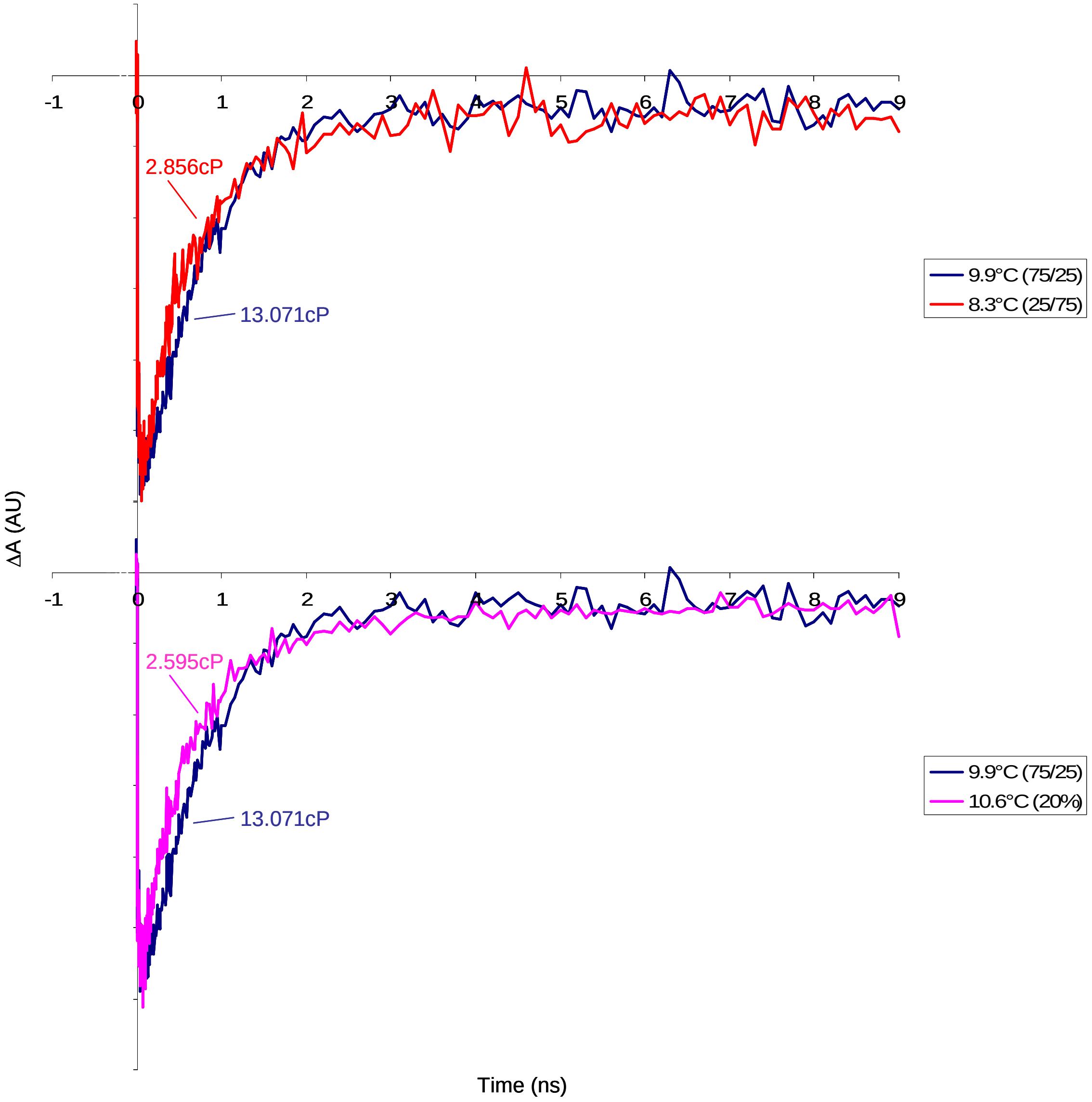

Figure 4.16. Selected adenosylcobalamin kinetic traces (from Figures above) compared to demonstrate solvent influence. The sample temperature for each scan was near 10°C (temperatures as indicated in the legends). "75/25" in the legends indicates 75% ethylene glycol / 25% water for the solvent, and likewise for "25/75." "20%" indicates the solvent was 20% sucrose solution by mass. Viscosities are listed in centipoises.

This comparison (Figure 4.16) of scans near the same temperature but in different environments demonstrates that there is some environmental influence on the dynamics of adenosylcobalamin following excitation. The viscosities of each solution are also indicated in the Figure. In both the top and bottom panels of Figure 4.16 there is a clear discrepancy in the slope towards ground state recovery and a slight difference in the level of the plateau. Notice that the traces in both plots cross each other near 1.5ns.

Each of the transient absorption kinetic traces in Figures 4.8 through 4.16, as well as those for adenosylcobalamin in pure water and pure ethylene glycol (Chapter 3) was fit to a sum of exponentials like that in Chapter 3:

$$\Delta A(\lambda) = \sum_{i=1}^{5} A_i(\lambda) e^{-k_i t} \; . \tag{4.11}$$

For some of the alkylcobalamins fits as few as three exponentials were necessary, while for others four were required for an adequate fit. The same model (number of exponentials in the sum) was used for a particular alkylcobalamin in a specific solvent for consistency. A nondecaying component was introduced to account for the long lived escape of adenosyl radicals from cob(II)alamin radical (plateau in Figures 4.8 through 4.16). Analysis of the data in this manner can be justified on the basis of the previous studies (as reviewed in Chapter 1) An example fit with the residual difference between the data trace and fit is plotted in Figure 4.17.

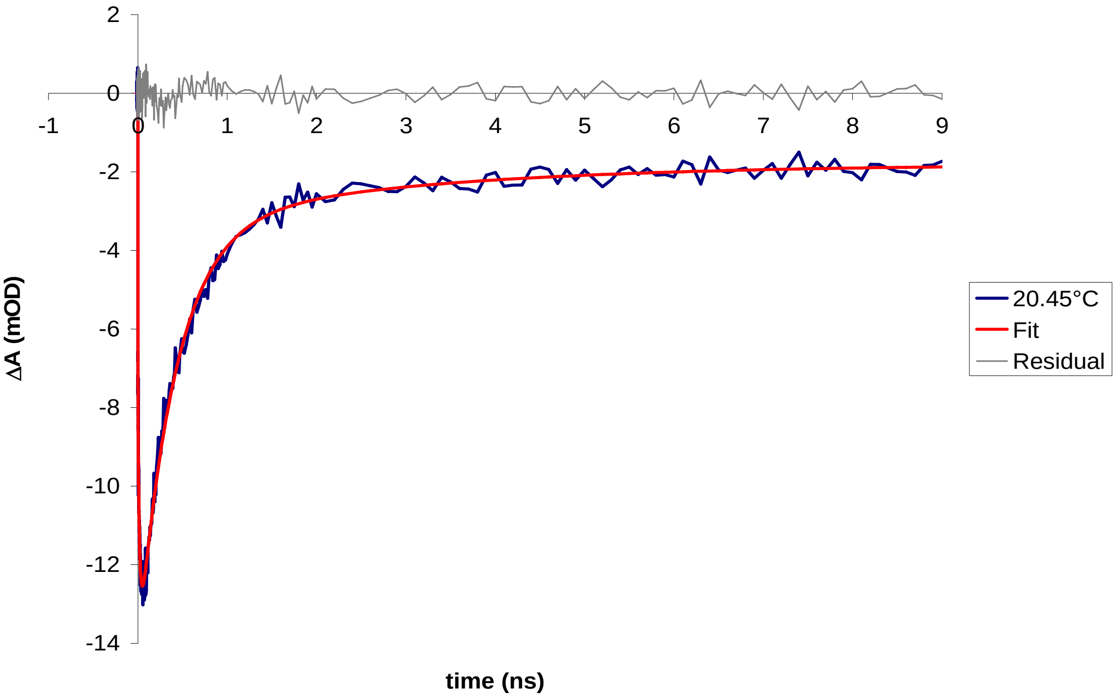

Figure 4.17. Example of a sum of exponential fit to the data presented above. The data trace (blue) is for adenosylcobalamin in 25% ethylene glycol / 75% water at 20.45°C (taken from Figure 4.13). The fit is plotted in red and the residuals are included in grey.

The step-wise model presented in Chapter 3 was again assumed as a plausible explanation for the adenosylcobalamin dynamics, based on the background literature. As will be developed below, this model is not a complete description of the experimental data; but it was the first approach taken to analyze the data. A different fitting program to calculate cage escapes, than that based on the sum of exponentials and a stepwise model may be required. With this model in mind (Figure 4.18) the rate constant for escape from the solvent cage was calculated according to the following program.

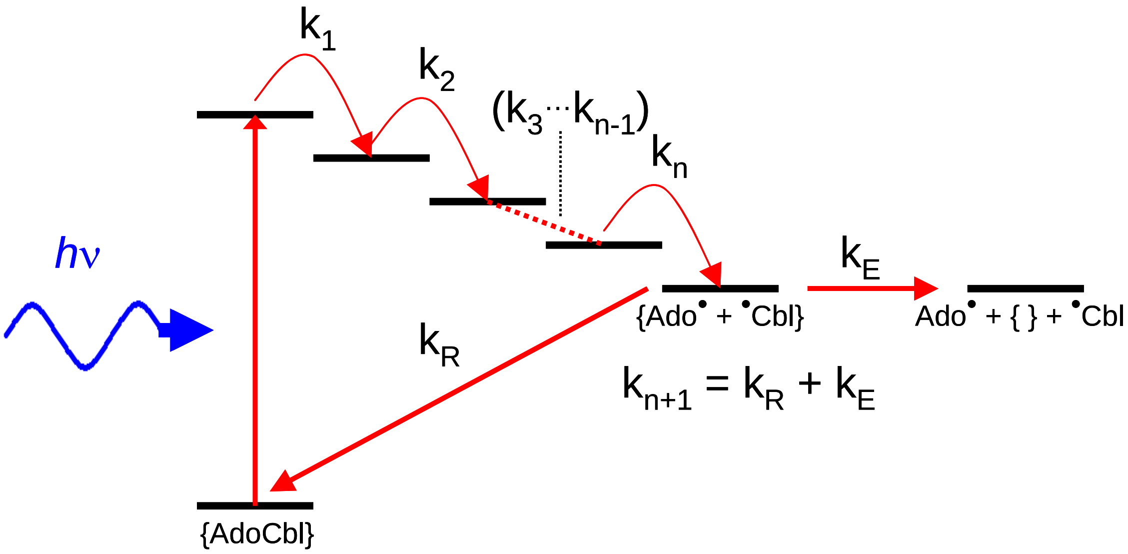

Figure 4.18. Stepwise model assumed for initial modeling of the transient absorption data for adenosylcobalamin, as well as the other alkylcobalamins. The brackets, { }, represent the solvent cage, and the "•" represent the unpaired electron of the adenosyl and cobalamin radicals. Thus "{ Ado• + •Cbl }" represents a solvent caged (and relaxed) radical pair, while "Ado• + { } +•Cbl" represents a solvent separated radical pair.

According to the model in Figure 4.18, with n = 3 (4 exponential decays in the sum of exponentials fit, with $k_4 = k_E + k_R$), the wavelength specific amplitudes of the species associated spectra for the solvent caged and solvent separated radical pairs are given in terms of the amplitudes of the decay associated spectra ($A_i(\lambda)$ in Equation 4.11 – determined by the sum of exponentials fits), by [14]:

$$S_{\{RP\}}(\lambda) = \frac{(k_3 - k_4)(k_2 - k_4)(k_1 - k_4)}{k_1 k_2 k_3} A_4(\lambda) + A_{ND}(\lambda), \tag{4.12}$$

and

$$S_{RP}(\lambda) = \frac{k_4}{k_E} A_{ND}(\lambda). \tag{4.13}$$

The subscript "ND" refers to the nondecaying amplitude (i.e. $k_5 = 0$). The key relation between Equations 4.12 and 4.13 is that they should be equal to each other since the solvent caged and solvent separated radical pairs are spectroscopically indistinguishable. Equating Equations 4.12 and 4.13 and solving for k_E (rate constant for escape) gives [14]:

$$k_E = k_4 \frac{QR}{1+QR}, \tag{4.14}$$

where

$$R = \frac{A_{ND}(\lambda)}{A_4(\lambda)}, \tag{4.15}$$

and

$$Q = \frac{k_1 k_2 k_3}{(k_1 - k_4)(k_2 - k_4)(k_3 - k_4)}. \tag{4.16}$$

Since the amplitudes obtained through fitting show up only as the ratio, *R*, in the expression for the cage escape rate constant, the varying experimental parameters described in the presentation of the scaled data can be bypassed. The quantum yield for cage escape to produce solvent separated radical pairs can be determined from

$$\varphi = \frac{k_E}{k_E + k_R} = \frac{k_E}{k_4} = \frac{QR}{1+QR}. \tag{4.17}$$

The results of these fits are summarized in Table 4.6 for mixtures of water and ethylene glycol and Table 4.7 for sucrose solutions.

Table 4.6. Summary of escape rate constants for adenosylcobalamin in mixtures of water (WT) and ethylene glycol (EG). The quantum yield for escape, φ, is also tabulated.

Water / Ethylene Glycol Mixtures:				
Solvent	**Temperature (°C)**	**k_E (ns^{-1})**	**τ (ns)**	**φ**
100% EG	10	0.02	62.71	0.01
	20	0.05	20.43	0.04
	40	0.14	7.27	0.09
	60	0.47	2.11	0.22
	80	1.08	0.93	0.38
75% EG / 25% WT	9.9	0.10	10.41	0.071
	19.9	0.16	6.35	0.098
	20.45	0.18	5.47	0.11
	39.35	0.44	2.29	0.20
	59.5	0.89	1.12	0.295
	76.85	2.08	0.48	0.39
50% EG / 50% WT	9.8	0.24	4.10	0.23
	20.4	0.29	3.42	0.27
	20.65	0.31	3.22	0.27
	40.05	0.70	1.43	0.43
	59.9	0.88	1.13	0.52
	79.4	0.99	1.01	0.63
25% EG / 75% WT	8.3	0.23	4.43	0.18
	20.35	0.40	2.49	0.26
	40.6	0.61	1.64	0.35
	61.55	0.79	1.27	0.51
	81.3	1.23	0.82	0.71
100% WT	10	0.43	2.33	0.28
	20	0.62	1.61	0.37
	40	0.93	1.07	0.44
	60	1.21	0.83	0.52
	70	1.69	0.59	0.60

Table 4.7. Summary of escape rate constants for adenosylcobalamin in sucrose solutions. The sucrose solution is labled by mass percent sucrose. The quantum yield for escape, φ, is also tabulated.

Sucrose Solutions Solvent	Temperature (°C)	k_E (ns^{-1})	τ (ns)	φ
20% Sucrose	-0.3	0.15	6.64	0.10
	10.6	0.21	4.67	0.13
	20.7	0.46	2.17	0.20
	31.7	0.58	1.74	0.22
	41.6	0.97	1.03	0.28
	50.2	1.11	0.90	0.31
	60.2	1.48	0.67	0.35
	70	1.87	0.54	0.38
40% Sucrose	-0.25	0.06	15.97	0.057
	10.1	0.12	8.59	0.083
	20.9	0.20	5.01	0.12
	31.65	0.33	3.01	0.17
	41.45	0.50	2.01	0.21
	50.25	0.66	1.51	0.25
	60.2	0.84	1.19	0.29
	69.9	1.21	0.83	0.33

4.2.2 Propylcobalamin

Kinetic transient absorption data for propylcobalamin was collected in the same manner as described above in mixtures of water and ethylene glycol. Each scan is for 400nm excitation and 540nm probe wavelengths. Propylcobalamin studies were not pursued in sucrose solution to due limited sample supply. The propylcobalamin kinetic traces follow in Figures 4.19 through 4.21. Traces in Figures 4.20 (50% ethylene glycol / 50% water) and Figure 4.21 (75% ethylene glycol / 25% water) have been scaled by normalizing the peak of the ground state bleach as prescribed for adenosylcobalamin traces. The traces in Figure 4.19 were left unscaled for aesthetic reasons, as with the large number of traces and less than optimal signal to noise ratio it is difficult to discern a particular trace from its neighbors when scaled.

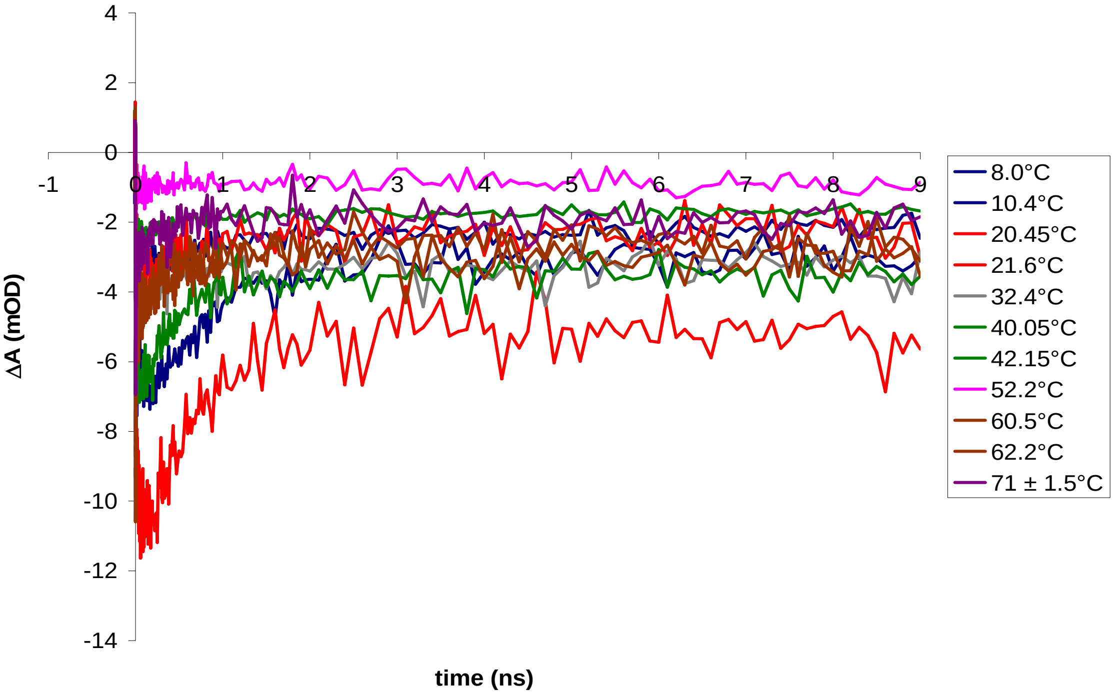

Figure 4.19. Propylcobalamin in 100% water. This data has not been scaled; the small magnitude of the absorbance is indicative of the difficulty of the transient absorption measurements on the synthesized alkylcobalamins. Indeed, many of the absorbance magnitudes for scaled data in the remaining plots were only a couple of mOD in magnitude.

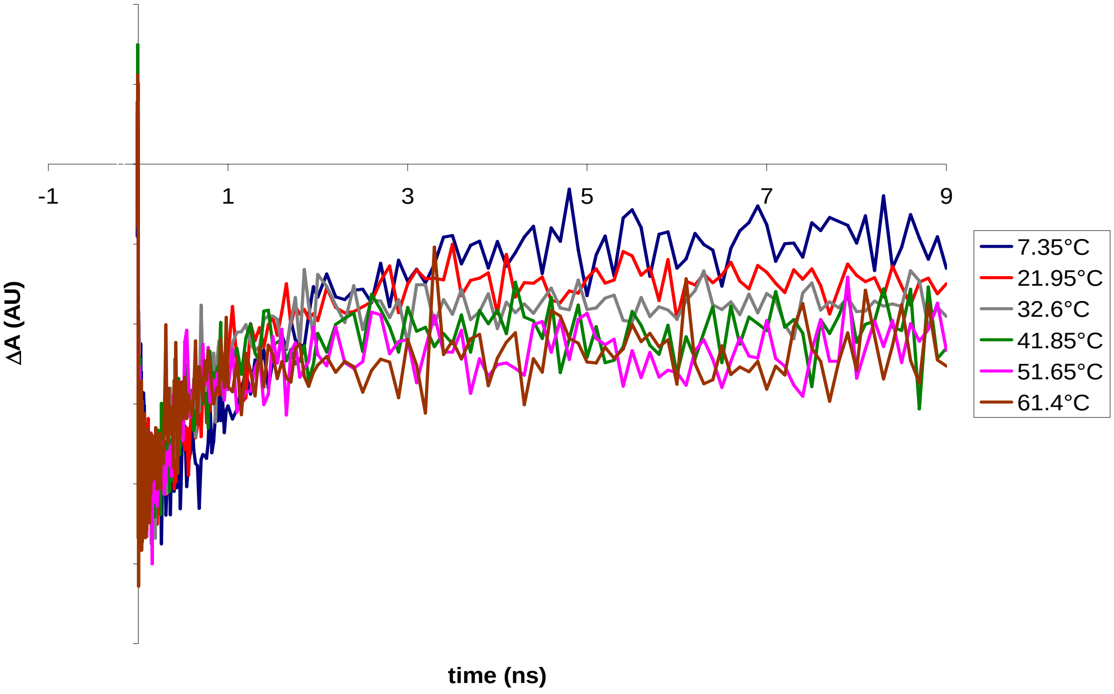

Figure 4.20. Propylcobalamin in 50% ethylene glycol / 50% water. This data has been scaled to normalize the magnitude of the ground state bleach.

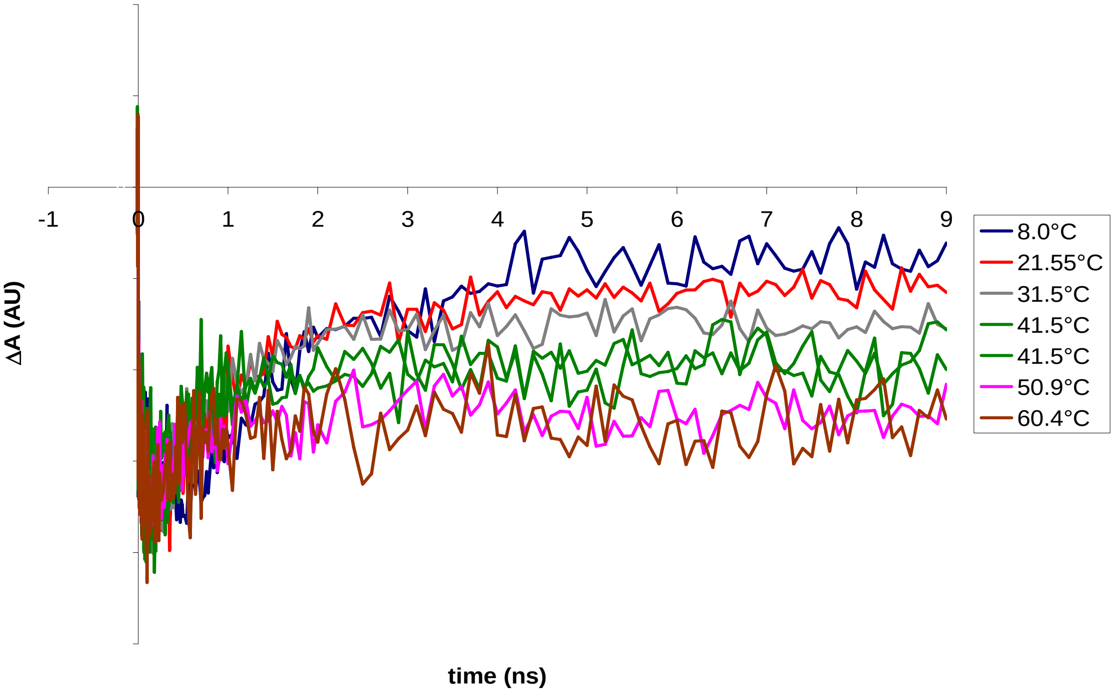

Figure 4.21. Propylcobalamin in 75% ethylene glycol / 25% water. This data has been scaled to normalize the peak of the ground state bleach.

Synthesis complications dictated that no studies were performed in pure ethylene glycol. Difficulty in the purification step of the synthesis meant that in order to have viable sample, it was left in an aqueous solution. It was then possible to make mixtures with ethylene glycol, but pure solutions could not be produced. The higher the percentage of volume occupied by ethylene glycol, the lower the concentration of propylcobalamin since it was present already in aqueous solution at fixed concentration. The propylcobalamin dynamics show very qualitatively similar behavior to the adenosylcobalamin evolution. This data was also fit to a sum of exponentials and the escape rate constant determined according to Equations 4.10 through 4.17. The results are summarized in Table 4.8.

Table 4.8. Summary of escape rate constants for propylcobalamin in mixtures of water (WT) and ethylene glycol (EG). The quantum yield for escape, φ, is also tabulated.

Solvent	Temperature (°C)	k_E (ns^{-1})	τ (ns)	φ
75% EG / 25% WT	8	0.13	7.71	0.18
	21.55	0.29	3.43	0.30
	31.5	0.49	2.06	0.36
	41.5	0.81	1.23	0.46
	50.9	1.45	0.69	0.68
	60.4	1.78	0.56	0.68
50% EG / 50% WT	7.35	0.14	7.25	0.19
	21.95	0.37	2.73	0.31
	32.6	0.63	1.59	0.40
	41.85	1.00	1.00	0.47
	51.65	1.28	0.78	0.49
	61.4	2.03	0.49	0.55
100% WT	10.4	0.52	1.91	0.40
	20.45	0.66	1.51	0.44
	40.05	1.18	0.85	0.50
	60.5	1.41	0.71	0.56
	62.2	1.59	0.63	0.70

4.2.3 Ethylcobalamin

The transient absorption kinetic traces for ethylcobalamin are presented in Figures 4.22 and 4.23. Similar to the case for propylcobalamin, Figure 4.22 (100% water) has not been scaled for aesthetic reasons (to make the individual scans more discernable). There are few data sets for ethylcobalamin since it was in even shorter supply than the propylcobalamin sample (and there are again no transient scans for sucrose solutions). Since ethylcobalamin suffered from the same purification difficulty in the synthesis procedure as propylcobalamin, there is no study in pure ethylene glycol. This data was also collected with 400nm pump and 540nm probe wavelengths.

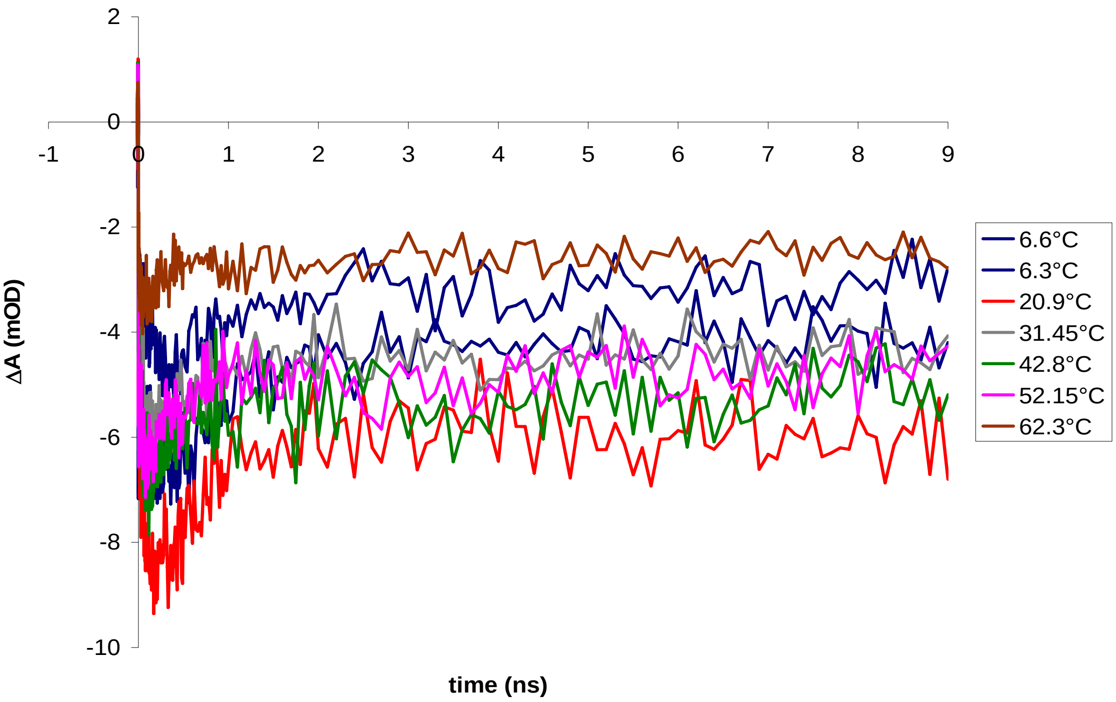

Figure 4.22. Ethylcobalamin in pure water. This data has not been scaled.

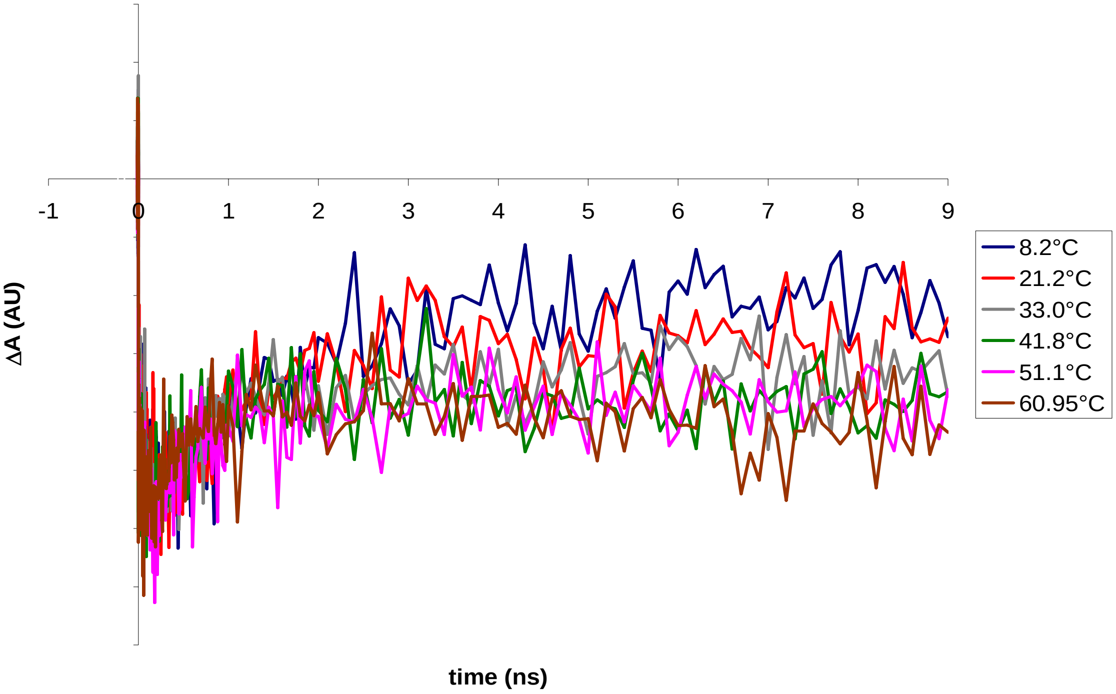

Figure 4.23. Ethylcobalamin in 75% ethylene glycol / 25% water. This data has been scaled to make the magnitude of the ground state bleach the same for each scan.

A summary of the rate constants for cage escape determined from a fit to a sum of exponentials and the model presented in Figure 4.18 is documented in Table 4.9.

Table 4.9. Summary of escape rate constants for ethylcobalamin in mixtures of water (WT) and ethylene glycol (EG). The quantum yield for escape, φ, is also tabulated.

Solvent	Temperature (°C)	k_E (ns^{-1})	τ (ns)	φ
75% EG / 25% WT	8.2	0.28	3.56	0.34
	21.2	0.56	1.77	0.44
	33	0.95	1.05	0.56
	41.8	1.51	0.66	0.59
	51.1	1.15	0.87	0.61
	60.95	2.88	0.35	0.64
100% WT	6.6	0.78	1.28	0.52
	6.3	0.83	1.20	0.58
	20.9	1.05	0.95	0.62
	31.45	1.33	0.75	0.71
	42.8	1.94	0.52	0.72
	52.15	2.28	0.44	0.70
	62.3	3.67	0.27	0.69

4.4.4 Methylcobalamin

The same process as outlined in Sections 4.2.1 through 4.2.3 was carried out with methylcobalamin in varying solvent environments. Like it's biologically (and commercially) relevant counterpart, adenosylcobalamin, there was plenty of sample to extend the studies through a wider range of environments and experimental parameters. The methylcobalamin kinetic data presents a complication as a result of the rise of a cob(III)alamin-type intermediate as described in Chapter 1 (Section 1.2.1.2, and similar to the intermediate observed following excitation of adenosylcobalamin in the protein environment, Chapter 3, Section 3.3.2). The metastable metal-to-ligand-charge-transfer (MLCT) state arises on a time similar to the recombination time and a only a small percentage of the solvent caged radical pairs recombine; although a large percentage of the molecules initially in the MLCT state return to the ground state. It is not clear how to best scale the data for presentation; instead the data is left unscaled. Figures 4.24 through 4.28 show the kinetic traces in mixtures of water and ethylene glycol, while Figures 4.29 and 4.30 present the traces collected in sucrose solutions. The plots for methylcobalamin in pure water and in pure ethylene glycol have already been presented in Chapter 3. Also data presented in Figures 4.24 through 4.30 is for 400nm pump and 540nm probe. Data collected in the pure solvents were excited with 400nm pump; the probe wavelengths are as indicated in Chapter 3.

There are several sets of data presented for methylcobalamin in mixtures of 50% ethylene glycol and 50% water. Each of these performed at widely separated time (~months). They are kept separate in the following presentation only to keep from cluttering the plots.

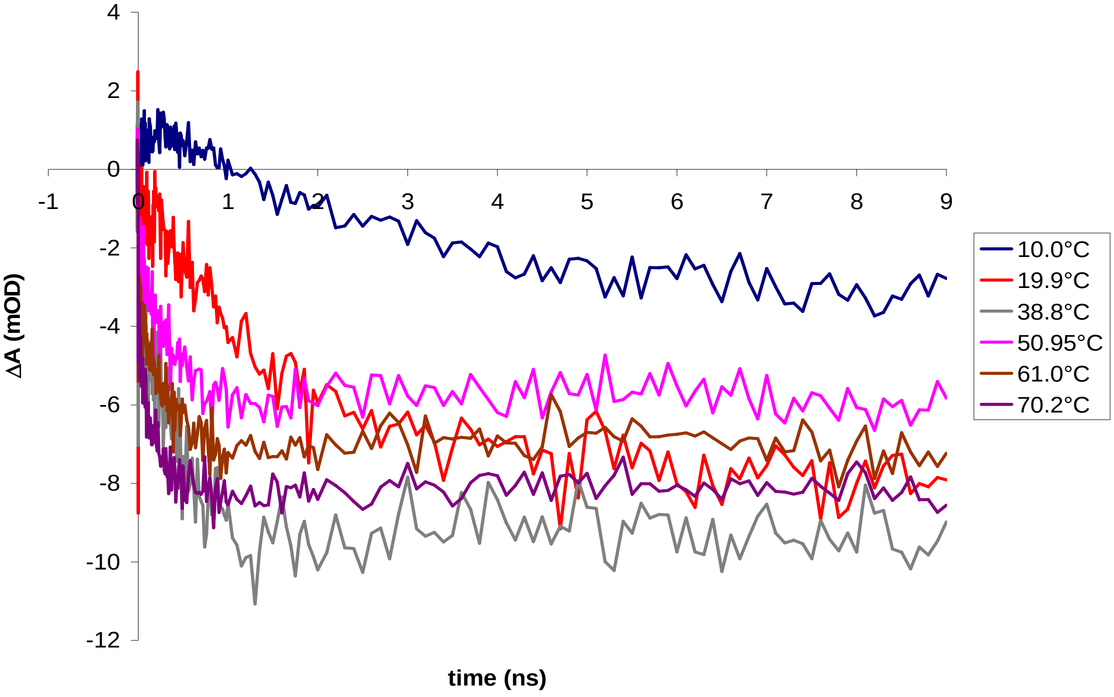

Figure 4.24. Methylcobalamin in 50% ethylene glycol / 50% water, Set A. This data has not been scaled; the ordinate axis is labeled in mOD.

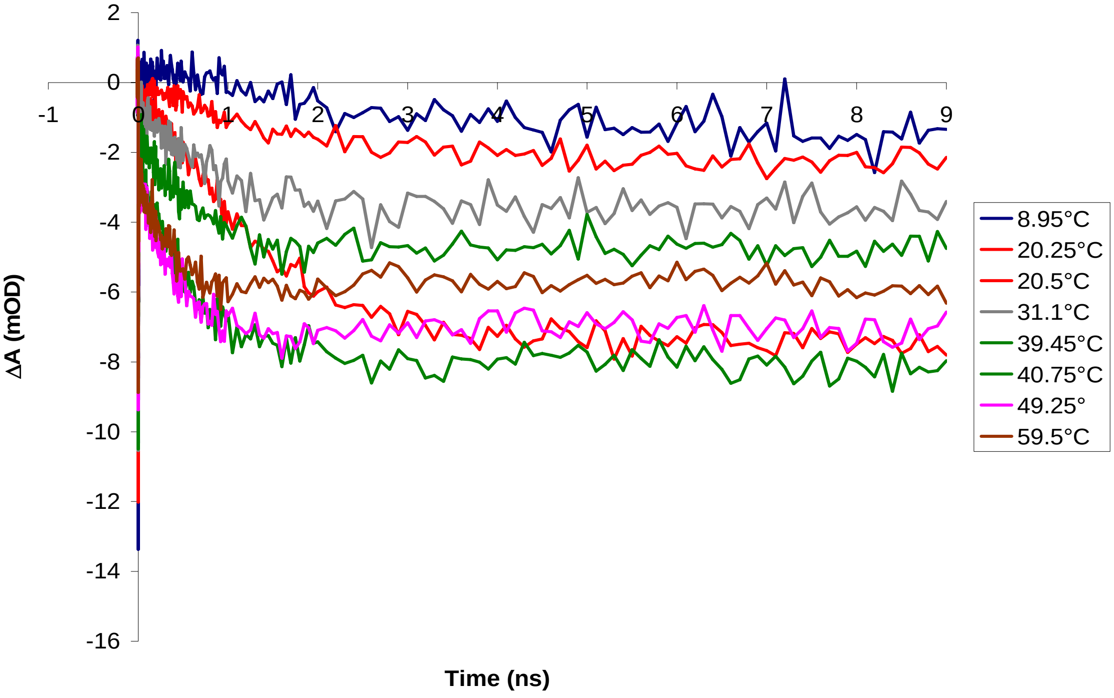

Figure 4.25. Methylcobalamin in 50% ethylene glycol / 50% water, Set B. This data has not been scaled.

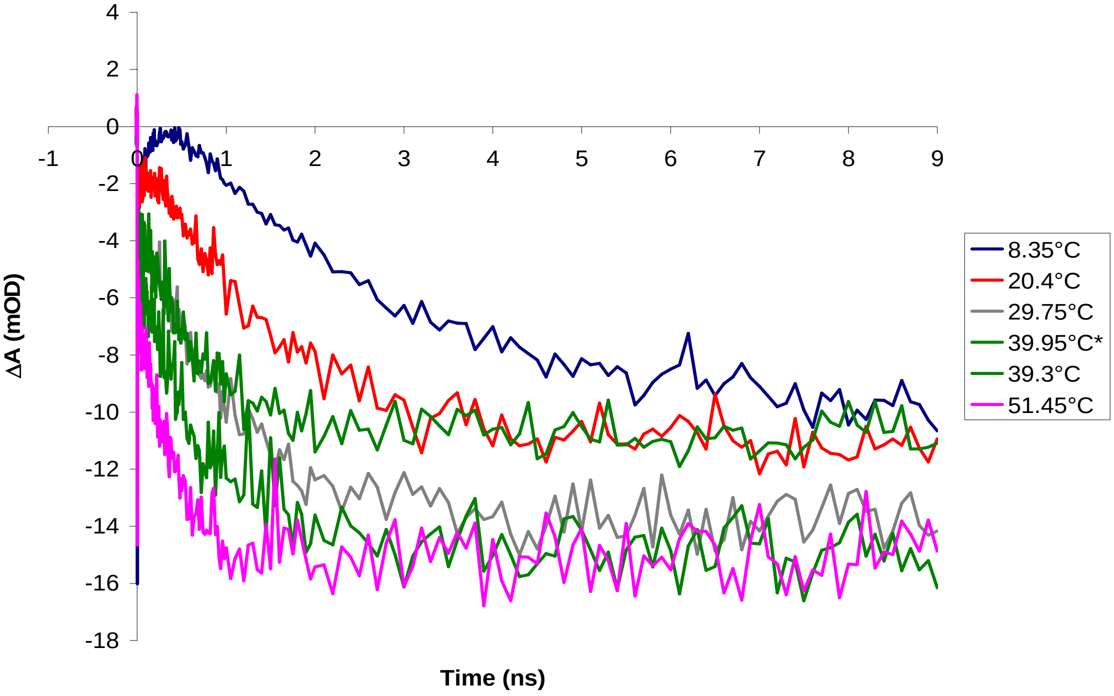

Figure 4.26. Methylcobalamin in 50% ethylene glycol / 50% water, Set C. This data has not been scaled.

The collection of multiple data sets in the same solvent environment (50% ethylene glycol / 50% water) as presented in Figures 4.24 through 4.26 invites a comparison of traces collected near the same temperatures. Figure 4.27 shows a comparison of several selected temperatures taken from the plots above to demonstrate the reproducibility of the data collected. The scans in Figure 4.27 have been scaled, since they are only being compared with other scans near the same temperature. These comparisons should then be expected to lie on top of each other within the noise of the experiment (as Figure 4.27 verifies) making the scaling worthwhile here.

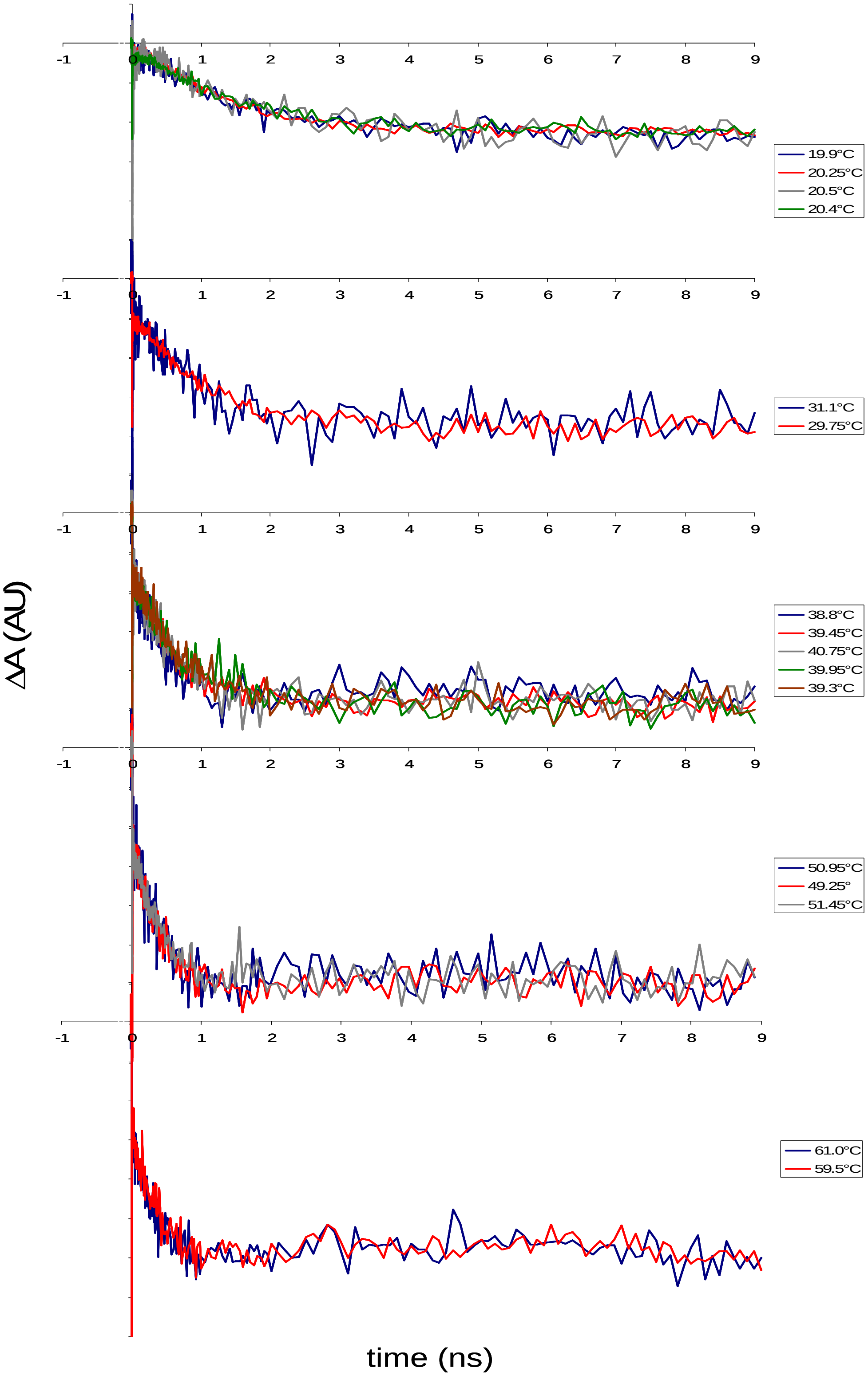

Figure 4.27. Comparison of selected temperatures for methylcobalamin in mixtures of 50% ethylene glycol / 50% water. Data has been scaled to demonstrate the reproducibility inherent in the experimental setup.

The remaining methylcobalamin in ethylene glycol and water mixture (75% ethylene glycol / 25% water) is shown in Figure 4.28, while methylcobalamin in 20% sucrose and 40% sucrose solutions is shown in Figures 4.29 and 4.30.

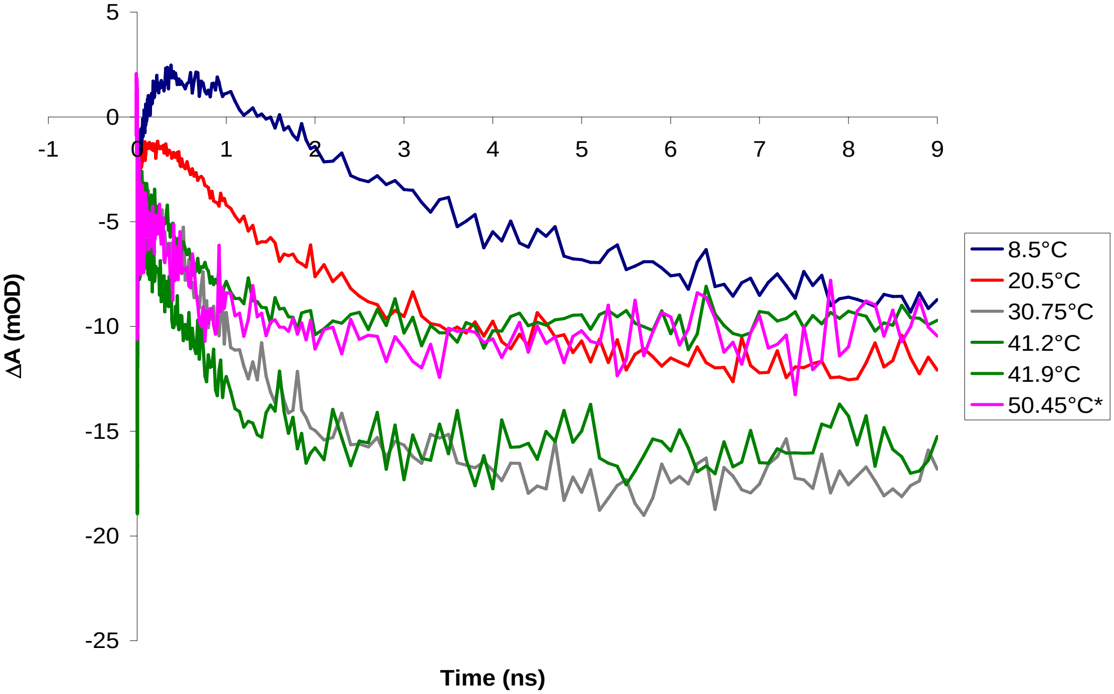

Figure 4.28. Methylcobalamin in 75% ethylene glycol / 25% water. This data has not been scaled.

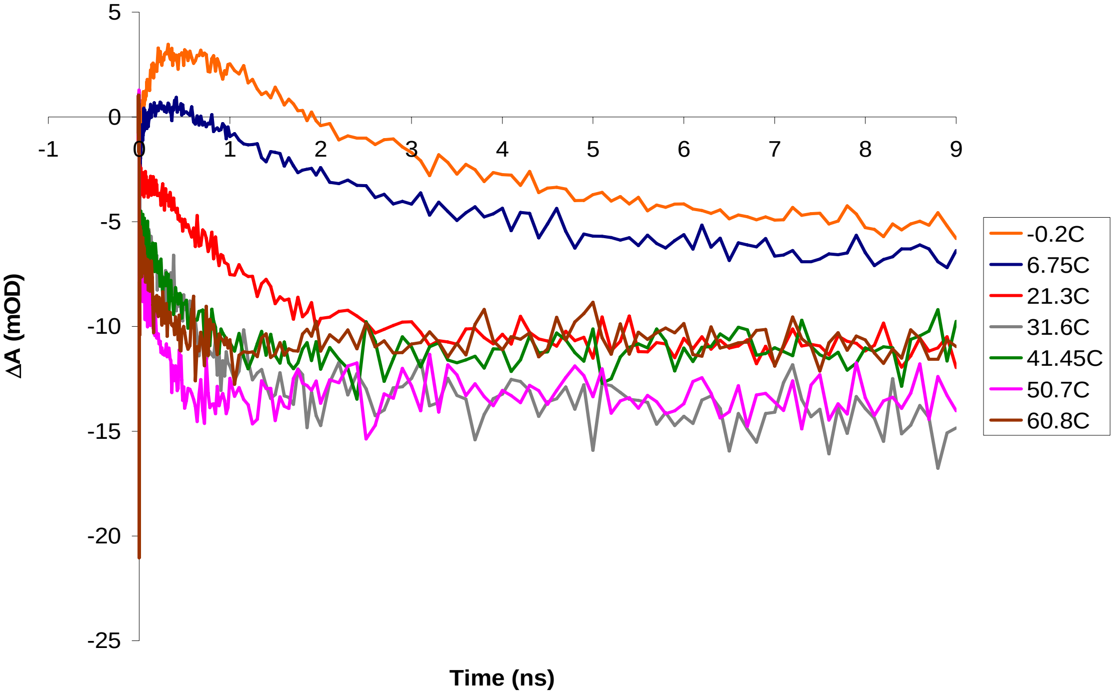

Figure 4.29. Methylcobalamin in 20% (by mass) sucrose solution. This data has not been scaled.

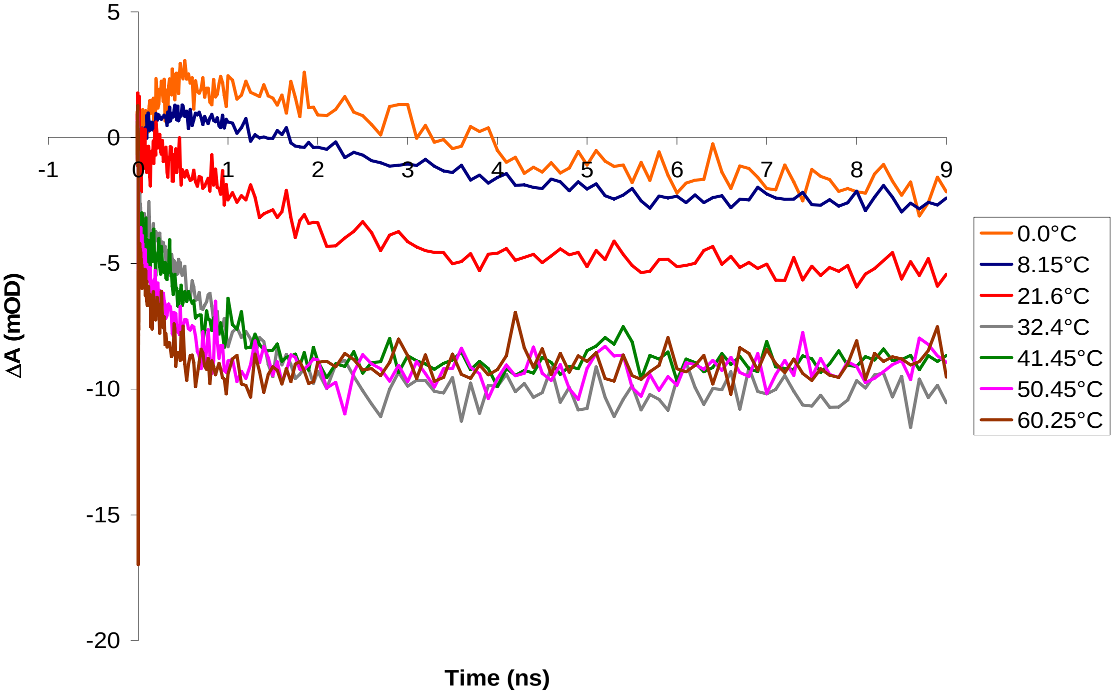

Figure 4.30. Methylcobalamin in 40% (by mass) sucrose solution. This data has not been scaled.

The methylcobalamin dynamics are distinct from the dynamics of adenosylcobalamin, ethylcobalamin and propylcobalamin (though there remains some similarity in the intermediate formation as described in the review). In fact, at higher temperatures, there is no geminate recombination of the methyl and cob(II)alamin radicals. There is a subpicosecond bleach, which is difficult to see in the 9ns timescale plotted above. Figure 4.31 is a blowup of the methylcobalamin dynamics in pure ethylene glycol over the first 100ps following excitation. The initial bleach can be seen in this Figure. It is immediately pursued by a subpicosecond recovery toward the ground state. The model adopted for analysis [15, 26] (Figure 4.32) assigns the subpicosecond dynamics to competition between prompt bond homolysis and the formation of the intermediate nonalkylcob(III)alamin like state.

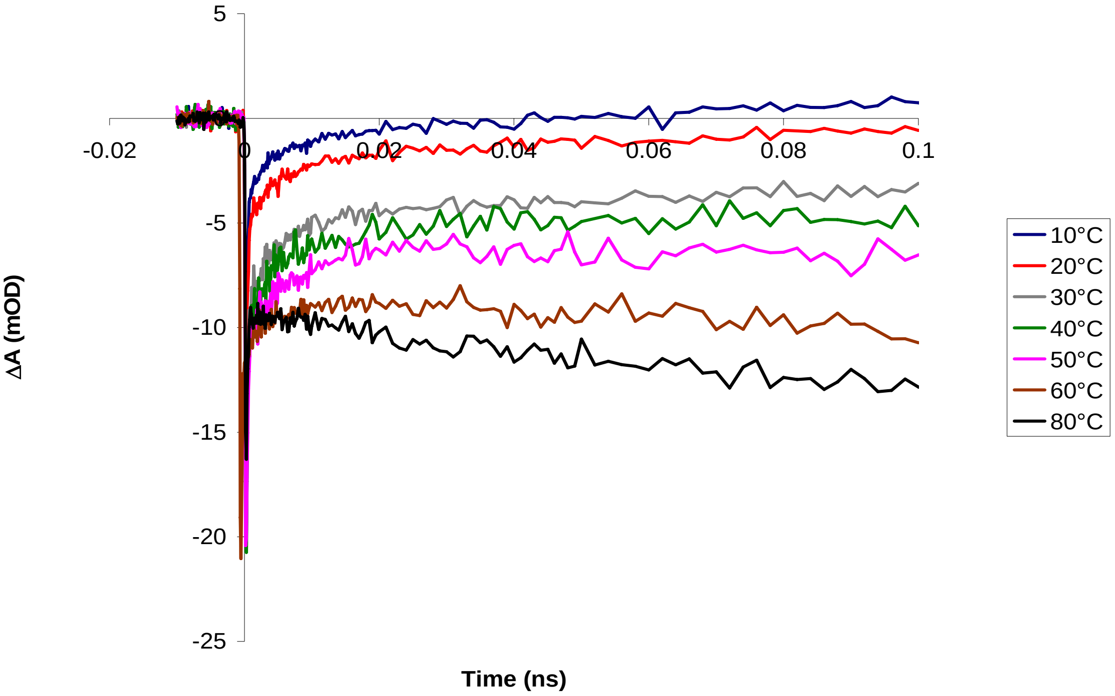

Figure 4.31. Blowup showcasing the dynamics of methylcobalamin in ethylene glycol over the first 100ps following excitation. The pump is 400nm and the probe is 540nm.

.

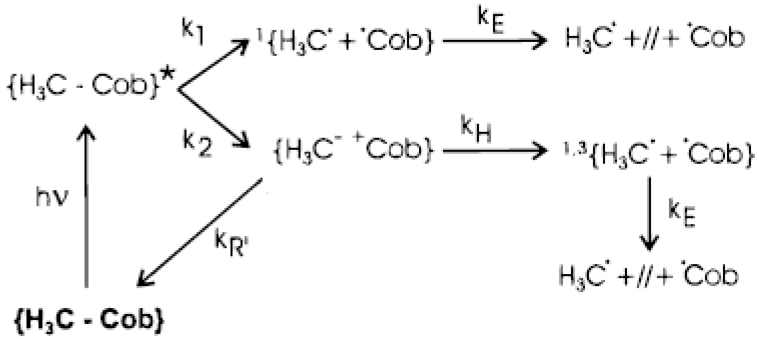

Figure 4.32. Model for methylcobalamin dynamics following excitation at 400nm pump. Brackets represent the solvent cage as for the model presented in Figure 4.18. The superscripts, "+" and "-" represent the transfer of charge density to support the MLCT intermediate. $k_3 = k_R + k_E$. The ampersand represents an excited state. This Figure is reproduced from Reference [15].

The nonalkylcob(III)alamin like, MLCT state manifests itself at 540nm probe wavelength by an increase in absorption. The metastable MLCT state can then relax to the ground state, or a small percentage results in solvent separated radical pairs. The 10-100 ps absorption increase in Figure 4.31 arises from the geminate recombination of methylcobalamin.

The methylcobalamin data was fit to a sum of four exponentials and one nondecaying component (n =5, with $k_5 = 0$ in Equation 4.11). For the model in Figure 4.32, $k_3 = k_R + k_E$, instead of k_4 (as was the case for the other alkylcobalamins). The results of fitting to this model are summarized in Tables 4.10 (for mixtures of water and ethylene glycol) and 4.11 (for sucrose solutions). Only those traces for which there was a clearly discernable recombination component present were subject to the escape analysis. Higher temperature data was collected despite a clear lack of recombination to further studies on the dielectric influence on dynamics, as introduced in Chapter 3.

Table 4.10. Summary of escape rate constants for methylcobalamin in mixtures of water (WT) and ethylene glycol (EG). The quantum yield for escape, φ, is also tabulated. Only those traces with clearly evident recombination components are included.

Water / Ethylene Glycol Mixtures Solvent	Temperature (°C)	k_E (ns^{-1})	τ (ns)	φ
100% EG	10	1.30	0.77	0.41
	20	2.79	0.36	0.55
	30	4.37	0.23	0.73
	40	6.49	0.15	0.80
	50	15.93	0.06	0.92
	60	23.44	0.04	0.95
75% EG / 25% WT	8.5	2.90	0.35	0.57
	20.5	6.16	0.16	0.75
50% EG / 50% WT	8.35	3.86	0.26	0.67
	10	4.09	0.24	0.62
	20.4	5.60	0.18	0.79
	20.25	4.81	0.21	0.75
	29.75	5.94	0.17	0.84
	31.1	8.91	0.11	0.86
100% WT	10	5.50	0.18	0.96
	20	7.50	0.13	>0.98

Table 4.11. Summary of escape rate constants for methylcobalamin in sucrose solutions. The sucrose solution is labeled by mass percent sucrose. The quantum yield for escape, φ, is also tabulated. Only those traces with clearly evident recombination components are included.

Water / Ethylene Glycol Mixtures Solvent	Temperature (°C)	k_E (ns^{-1})	τ (ns)	φ
20% Sucrose	-0.2	2.54	0.39	0.46
	6.75	4.82	0.21	0.64
40% Sucrose	0	1.38	0.72	0.365
	8.15	2.50	0.40	0.50
	21.6	4.91	0.20	0.78

4.3 Cage Escape and Recombination Analysis

The time constants and quantum yields presented in Tables 4.6 through 4.11 testify to the fact that the solvent environment exerts a significant influence on the ability of the photolytically produced radical pair to escape each other and formed long lived, solvent separated radicals. It is also clear that the alkyl group significantly influences the rates and yields for escape. There are many possible factors at play in determining the outcome of cage escape, such as entropic influences (do the radicals need to be oriented in a particular geometry to recombine?), and excess kinetic energy following homolysis. A previous study found a qualitative correlation between recombination and the orientation requirements for recombination for methylcobalamin compared with ethylcobalamin and propylcobalamin. However, it was found that the larger adenosyl radical recombined with the cob(II)alamin with a rate constant similar to the methyl radical [26]. It was speculated that following homolysis the adenosyl radical has little time to rotate and thus is already in a favorable geometry for recombination, while the methyl radical need not have a specific orientation relative to the cob(II)alamin. The two intermediate sized alkyls, methyl and propyl, will have had some opportunity to rotate on the times relevant for recombination, and require a specific orientation to recombine.

These complications will be ignored in the initial analysis. Instead, it will be first assumed that the cage escape is a purely diffusive controlled process, dependent only on solvent viscosity (this approach will then be contrasted with a kinetic theory). The results of such a model will then be compared with the experimental data from Section 4.2. A significant assumption made is that there is no external barrier to cage escape. With this model, cage escape can be treated as a solely diffusive process, dependent on the behavior of the alkyl and cob(II)alamin radicals in a solvent environment characterized by the temperature and solvent's temperature dependent viscosity. Also, though not an assumption, it is important to note that following homolysis neither the cob(II)alamin or alkyl radicals are charged. When an ion radical pair is generated, the escape and recombination process is dominated by the Coulombic interaction between the ions [2]; and a test of the diffusive behavior of the small molecule would not be possible.

With this model in mind, the expected behavior of the alkyl radical in a viscous environment and the associated rate constant for escape must be determined for comparison to the experimental data. The diffusive behavior of a particle in a viscous environment can be described by the diffusion coefficient, *D* [2, 27, 28]:

$$D = \frac{k_B T}{\xi}. \tag{4.18}$$

k_B is the Boltzmann constant, T the temperature, and ξ a parameter describing friction. An expression for the friction coefficient is complicated by the molecule's structure and relative size in comparison to the surrounding solvent molecules. It is commonly chosen for the case of a spherical particle much larger than the solvent molecules (i.e. the sphere is moving in a continuum) to be [27-29]

$$\xi = 6\pi\eta r\ , \tag{4.19}$$

for the case of no slip between the sphere and "fluid continuum." η is the solvent viscosity and r the spherical diffusive radius of the sphere. For the case of slip between the sphere and surrounding continuum the friction coefficient is

$$\xi = 4\pi\eta r\ . \tag{4.20}$$

The radicals relevant to this study have sizes comparable to the solvent molecules calling the solvent continuum model into question. It is also not clear that a spherical approximation is reasonable, and if so how to best define the diffusive radius. Due to these concerns, the friction coefficient is also sometimes expressed empirically as

$$\xi = n\pi\eta r\,, \tag{4.21}$$

where n is an empirically determined constant, which is found to not be particularly sensitive to shape [30].

Equations 4.19 and 4.20 have been shown to be increasingly poor as the diffusional radius decreases. Attempts at introducing the discrete nature of the solvent also suffer from poor agreement with the experimental data [2]. Estimated diffusive radii [26] for each alkyl radical assuming a spherical shape are given in Table 4.12. These values were calculated based on equilibrium geometry and volume.

Table 4.12. Calculated diffusive radii for alkyl radicals [26]. The adenosyl radius is in agreement with the value found for an adenosine molecule assuming a van der Wals volume [31].

	Methyl	**Ethyl**	**Propyl**	**Adenosyl**
***r* (Å)**	2.0	2.3	2.5	3.8

It has been determined empirically that for quasi-spherical particles with radii similar to the adenosyl radical that Equation 4.20 is a reasonable approximation in protic solvents. Considerable deviation is expected for the smaller radii [30] of the other alkyl radicals.

Experimentally determined adenosine diffusion coefficients in water give a larger radius, r = 4.42Å, (assuming the relation in Equation 4.19 to calculate the radius from the experimentally measured diffusion constant) [31], than that determined using molecular volume. An estimate of the radius using Equation 4.20 will return an even larger value. This result is a double edged sword for the hydrodynamic models presented. Since the adenosyl radical diffuses as though the radius is larger, the continuum model may seem more accurate. However, this means that the calculated diffusive coefficient based on molecular volume is likely to be inaccurate. Even with these reservations, the hydrodynamic model is often applied for similar diffusive parameters with surprising success [2, 30]. For the case of this analysis, Equation 4.19 will be assumed for the adenosyl radical with the radius given by r = 4.42Å as in reference [31]. Nishida and coworkers [31] measured the diffusion coefficient in aqueous solution for the adenosine radical, so it is expected that this choice will return the experimentally determined diffusive coefficient.

There are several approaches in the literature for modeling the specific situation of geminate recombination and escape of photoinduced radical pairs, along with many attempts at modifying the general approaches [2, 32, 33]. All suffer from difficulty when it comes to quantitatively comparing with experimental data [2]. Two main avenues will be considered in this analysis. The first is a diffusive approach, with the simplifications introduced in the preceding discussion. The second is a kinetic approach which takes into account the discrete nature of the solvent, though it will also rely on the diffusive coefficient in Equations 4.19 and 4.20 for application. These approaches have been shown to agree in the long time limit [2, 34], lending credence to the diffusive models.

As a preliminary matter, both the kinetic and diffusive approaches require some knowledge of the initial particle distribution. For the geminate recombination and escape of photoinduced radical pairs, the distribution information reduces to the initial separation between the two radicals following homolysis. If the pairs are generated with no excess translational energy, but separate from each other only with thermal energy $3k_BT/2$, the radical separation can be estimated at [2, 35]:

$$\sigma \sim \frac{\sqrt{6mk_BT}}{6\pi\eta r}. \tag{4.22}$$

m is the radical mass; all other parameters are as defined in Equations 4.19 and 4.20. Initial separations estimated with Equation 4.22 are plotted in Figure 4.33, for adenosylcobalamin (red) and methylcobalamin (blue) in water (dashed) and ethylene glycol (solid).

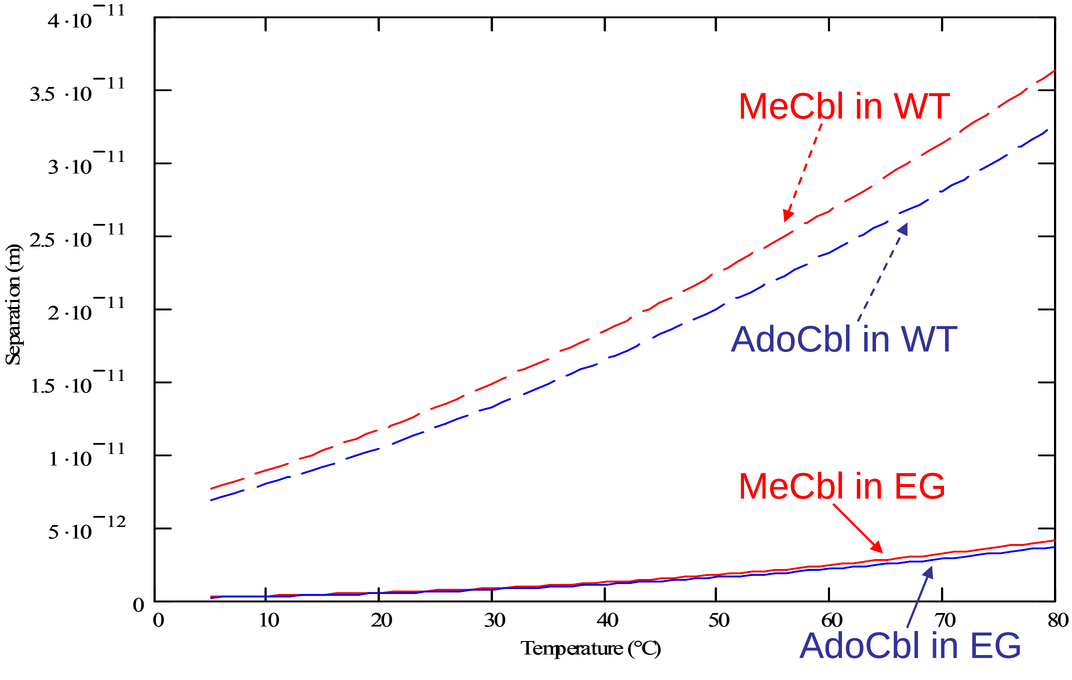

Figure 4.33. Initial radical separation for homolysis estimated from Equation 4.22. Adenosylcobalamin is colored red and methylcobalamin blue. Dashed lines are for water (WT) and solid for ethylene glycol (EG) solvent environments.

The small (less than 1Å versus the ~2-4Å diffusive radii for the alkyl radicals and larger for the cob(II)alamin radical) initial separations plotted Figure 4.33 suggest that the assumption of "contact" radical pairs may be valid (although the large quantum yields for solvent separated radical pairs following homolysis in methylcobalamin suggests that Equation 4.22 which is based on no excess translational energy may not be appropriate). In future analysis it may be advantageous to assume a distribution of initial separations surrounding a mean distance [36].

Under the simplification of contact radical pairs, the diffusive approach predicts that the unimolecular cage escape rate constant is [37]

$$k_E = \frac{D}{R^2} = \frac{k_B}{n\pi R^2}\left(\frac{1}{r_{Cbl}} + \frac{1}{r_{Alkyl}}\right)\left(\frac{T}{\eta}\right) \propto Const.\left(\frac{T}{\eta}\right); \tag{4.23}$$

and the recombination probability for a photoinduced pair (which appears to be a commonly characterized parameter) can be described by [37]:

$$F_C = \frac{k_R}{k_R + k_E} = \frac{1}{1 + \frac{D}{R^2 k_R}}. \tag{4.24}$$

R is the reaction radius. The result in Equation 4.24 agrees with that presented in Reference [2] when the unimolecular rate constant for recombination, k_R, is related to the bimolecular rate constant by $k_{Bi} = 4\pi R^3 k_R$ [37]. Equations 4.23 and 4.24 were derived under the assumption of stationary recombination kinetics [2, 37]. The quantum yield, ϕ, for solvent separated radical pairs logged in the Tables of Section 4.2 are simply related to F_C, by $\phi = 1 - F_c$.

Using Equations 4.18 through 4.21 to substitute for the diffusive coefficient in Equation 4.23 suggests that the experimentally determined (Section 4.2) cage escape rate constants be plotted versus the solvent fluidity (T/η). These are shown in Figures 3.34 (adenosyl, ethyl, and propyl radicals) and 3.35 (methyl radical).

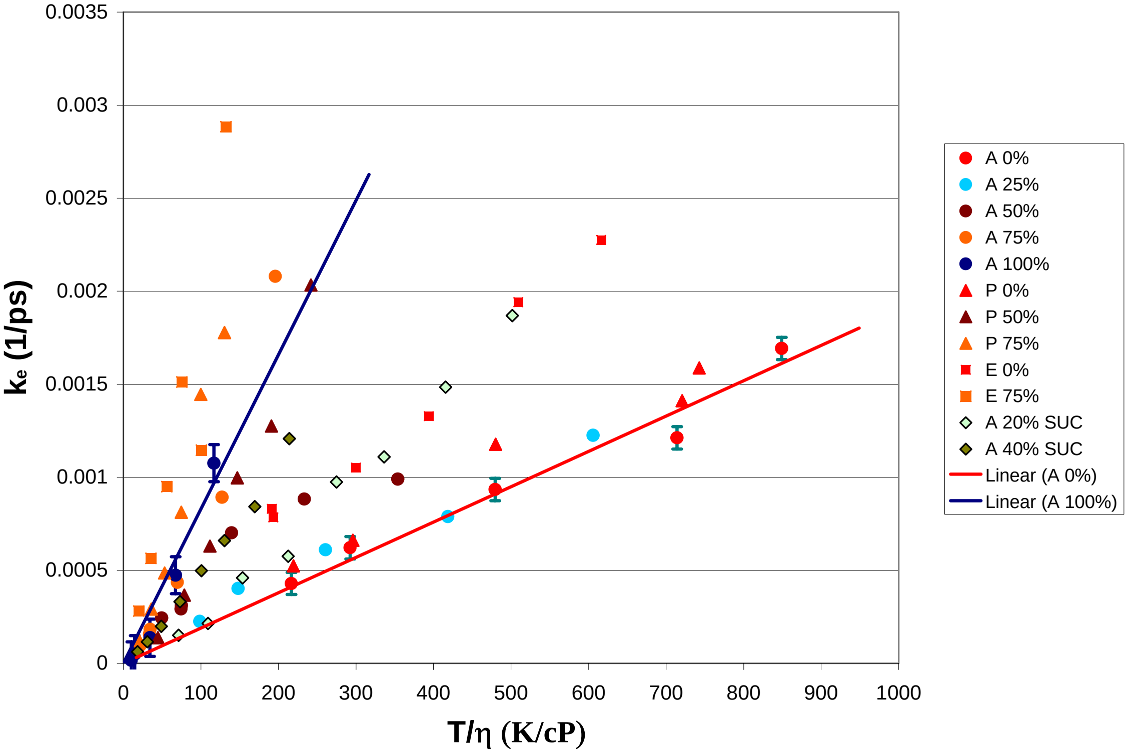

Figure 4.34. Rate constants for cage escape for adenosyl (circles), ethyl (squares), and propyl (triangles) radicals, versus fluidity (T/η). 0 (red), 25 (light blue), 50 (brown), 75 (orange), and 100 (blue) percentages reflect percent ethylene glycol by volume. 20 (light blue) and 40 (gold) percent reflect percent sucrose (diamonds) by mass. Linear fits are included for the data in pure water (red) and pure ethylene glycol (blue).

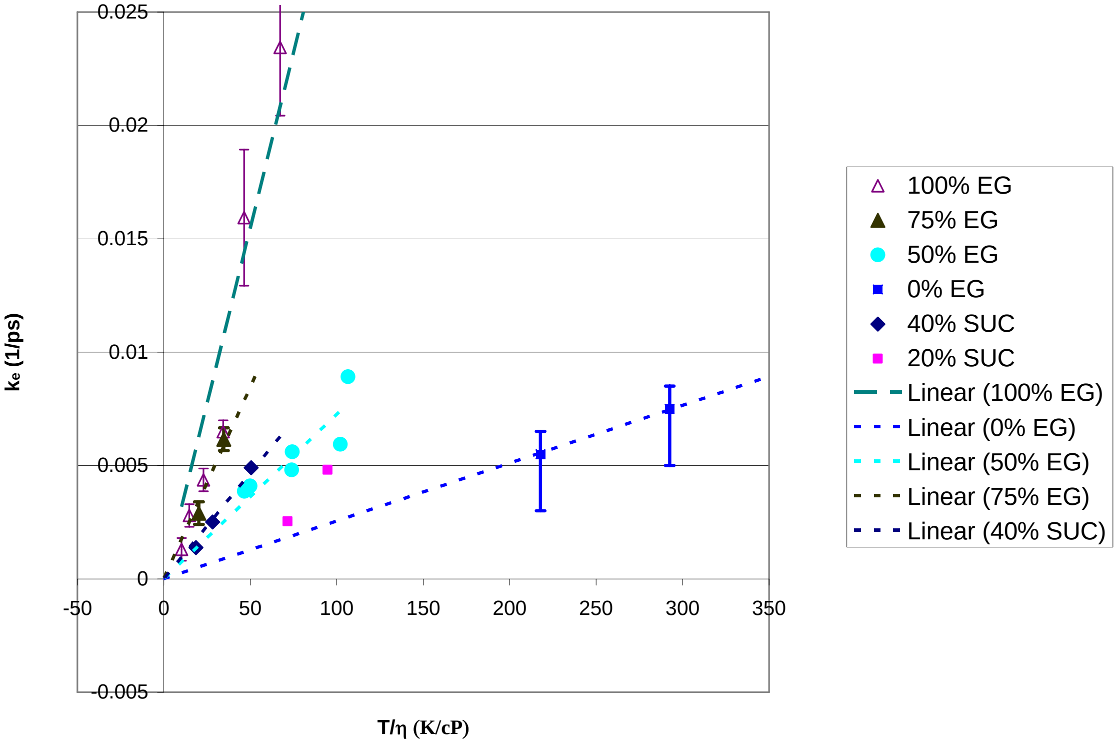

Figure 4.35. Rate constants for cage escape for methyl radicals, versus fluidity (T/η). 0, 50, 75, and 100 percentages reflect percent ethylene glycol by volume. 20 and 40 percent reflect percent sucrose by mass. Linear fits are included for the data in several solvents.

If Equation 4.23 were to hold strictly true, it should be expected that each radical would present the same slope when escape rate constant is plotted versus fluidity, regardless of solvent. Certainly, such is not the case for any of the radical escape constants calculated and shown above in Figures 4.34 and 4.35! Also highlighted in these figures is that the relative magnitudes for escape rate constant are all similar for adenosyl, ethyl, and propyl radicals, while the methyl radical's rate constants are an order of magnitude larger (which is why they are plotted separately from the rest).

The initial quantitative comparison of the diffusive hydrodynamic theory with the experimental data will be done with the adenosylcobalamin data set since this is the most well characterized data set (largest variety of solvent environments) with the best signal to noise. Figure 4.36 shows the experimental diffusive escape rate constants for adenosylcobalamin in water and ethylene glycol (the same as for Figure 4.34, scaled by units) compared with the expected slope based on the diffusive hydrodynamic model (Equation 4.23).

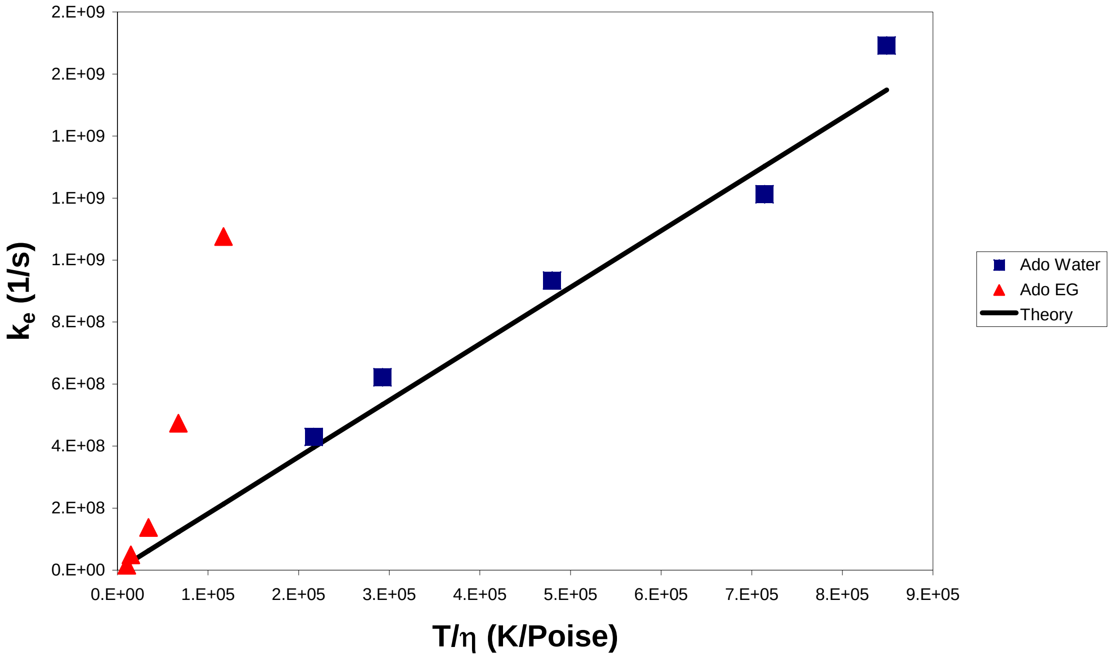

Figure 4.36. Rate constants for adenosylcobalamin cage escape in water (blue squares) and ethylene glycol (red triangles). The trend anticipated from the hydrodynamic model (black line) is compared.

The predicted trend based on the hydrodynamic model (black line) shows general agreement with the data in water (blue squares), and the lower fluidity data in ethylene glycol (red triangles). This result may be due the relative sizes of the water and ethylene glycol molecules compared with the adenosyl radical, but is more likely related to the recombination rate (see below). This analysis is ongoing and will be applied to the other alkyl radicals.

It is not clear that the hydrodynamic approach of diffusive motion in a continuum solvent is a valid model on the relevant time scales of these experiments [2, 34, 38], as

Equations 4.23 and 4.24 were derived under the assumption of steady state (although the hydrodynamic model has been successfully applied to the escape and recombination of iodine atoms photodissociated from molecular iodine [2, 39]) . The kinetic approach can be more readily applied to the femtosecond to nanosecond timescales of the cage escape and recombination.

Before moving on to the kinetic model a brief look at the caging fraction and the quantum yield for solvent separated pairs may be worthwhile. Since these yields (the caging fraction is the quantum yield for recombination) are the expected long time values (before the onset of bulk recombination, which is not probed here, and moreover, to which the kinetic model has not been successfully applied [38]), the assumptions of the diffusive hydrodynamic model may be more realistic. To make a comparison of the caging fraction as defined in Equation 4.24 to the experimental data it is helpful to plot the inverse fraction [2], to obtain a linear function versus fluidity (in T/η):

$$F_C^{-1} = 1 + \frac{D}{R^2 k_R} \propto Const.\left(\frac{T}{\eta}\right)\frac{1}{k_R}. \tag{4.25}$$

There is still the complication of the reaction rate for recombination in Equation 4.25. This rate is relatively insensitive to solvent environment [26]; so we begin by plotting the inverse cage fraction against fluidity (T/η).

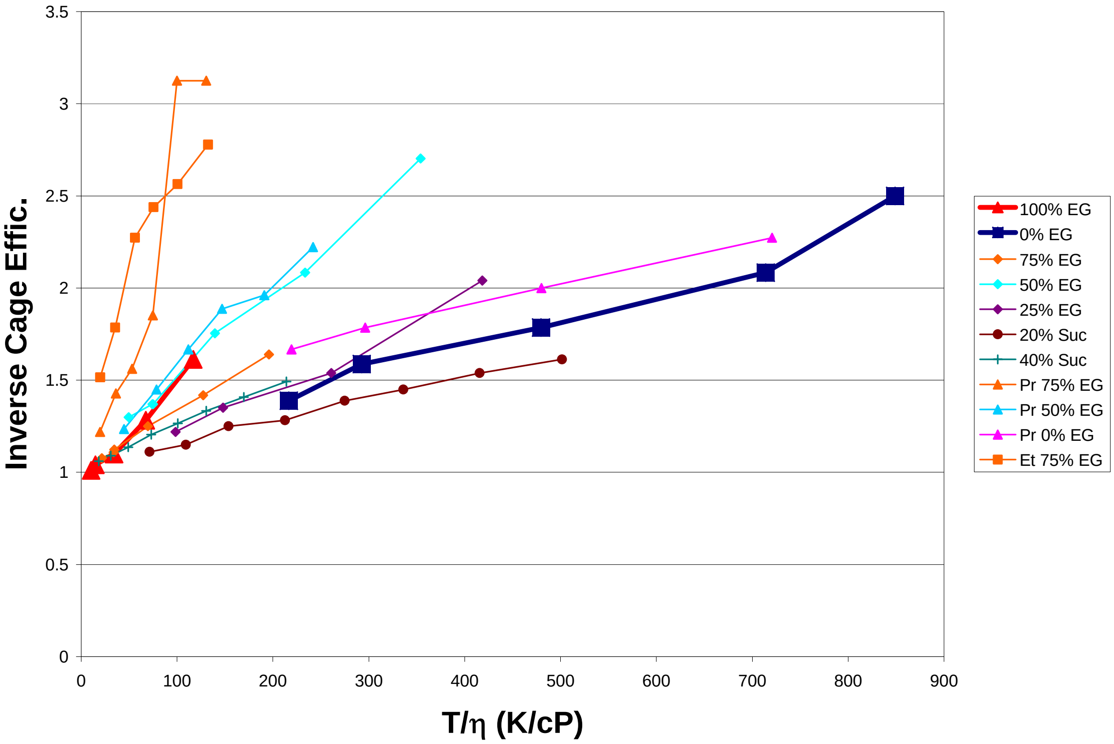

Figure 4.37. Inverse caging fraction versus fluidity for adenosyl-, ethyl-, and propylcobalamin in mixtures of water and ethylene glycol and in sucrose mixtures. Pure ethylene glycol (red triangles) and pure water (blue squares) are labeled as in Figure 4.36. Otherwise, mixtures are color coded (i.e. 75% ethylene glycol is orange for adenosyl, ethyl, and propyl). Diamonds indicate adenosyl, triangles indicate propyl, and squares for ethyl.

The inverse cage efficiency data also demonstrates the generally linear behavior as expected. However, this analysis still demonstrates a clear discrepancy in the recombination efficiency between different solvents, despite the prediction of identical behavior (Equation 4.25).

To help identify a reason for the observed discrepancy, a couple presentations of the experimental data are helpful. In Figure 4.38, the caging efficiency is plotted versus viscosity; it demonstrates that at high viscosities (greater than ~ 5cP) the caging fraction begins to “plateau” as 100% recombination is approached. Data in pure ethylene glycol is again plotted as red triangles and in pure water as blue squares.

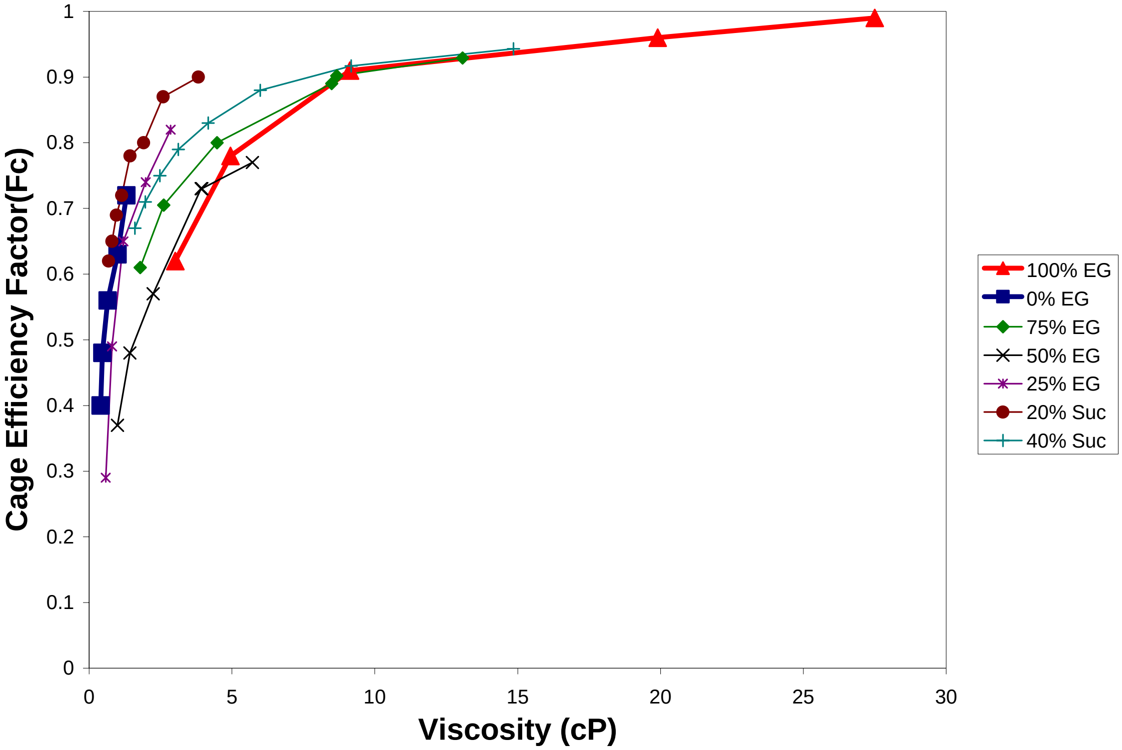

Figure 4.38. Caging fraction (yield for recombination) of radical pairs versus solvent viscosity for adenosylcobalamin in a range of environments. Note the plateau at viscosities greater than ~ 5cP.

The plateau feature of the caging efficiency with increased solvent viscosity points toward the influence of recombination rate which was not considered in the analysis above. The relation for cage escape rate constant in terms of the solvent viscosity (Equation 4.23) is derived under the assumption of steady state diffusive dissociation of radical pairs only. Figure 4.39 plots the recombination rate constants obtained via the sum of exponentials fitting and model application for adenosylcobalamin in water (blue squares) and ethylene glycol (red triangles).

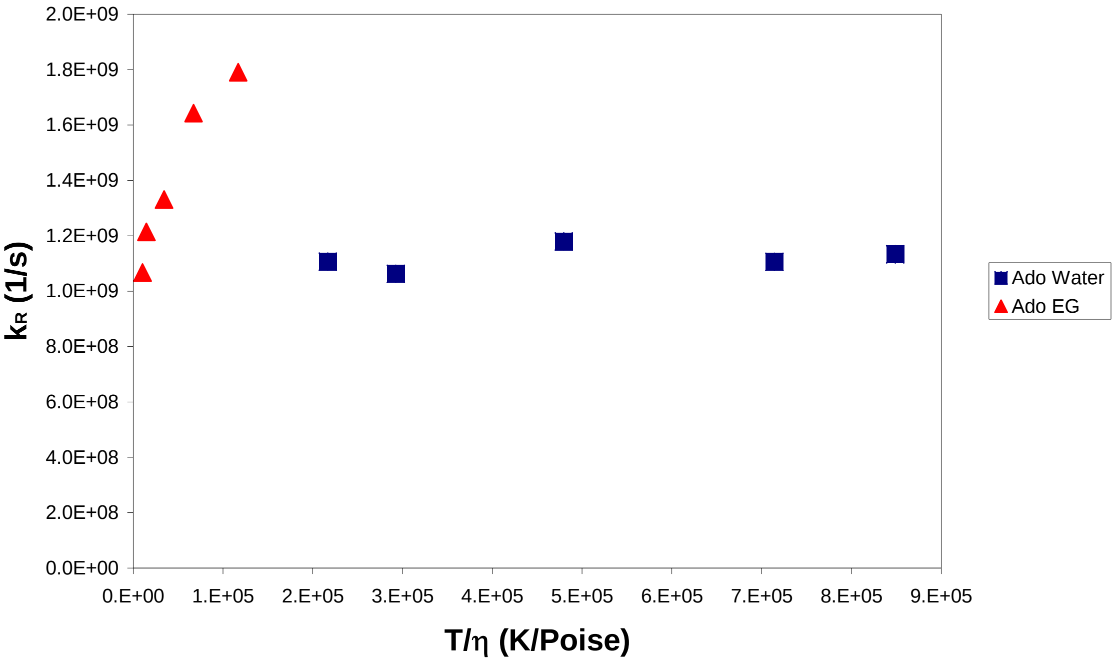

Figure 4.39. Recombination rate constants versus fluidity for adenosylcobalamin in water (blue squares) and ethylene glycol (red triangles).

The assumption of constant recombination rate seems reasonable for the water data, but not for the data in ethylene glycol. The recombination rates in water are also comparable to the escape rates; however, the recombination rates in ethylene glycol are as much as ~60 times greater than the escape rates in water for the higher fluidity data points. Dropping the assumption of constant recombination rate, the adenosylcobalamin inverse caging fraction in water and ethylene glycol (originally plotted above in Figure 4.37 without consideration of recombination) is shown in Figure 4.40.

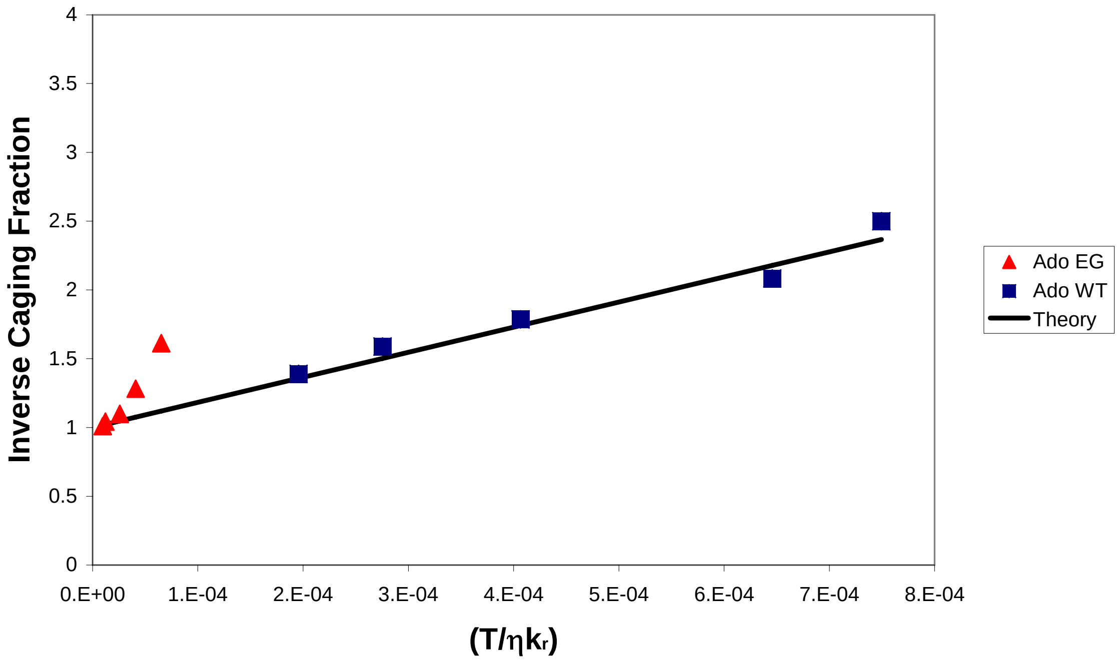

Figure 4.40. Adenosylcobalamin inverse caging fraction in water (blue squares) and ethylene glycol (red triangles), with the assumption of constant recombination rate relaxed.

With the assumption of constant recombination rate relaxed, a quantitative comparison to the diffusive hydrodynamic theory (Equation 4.25) can now be made. The result is shown as the black line in Figure 4.40. Again, there is agreement between the hydrodynamic theory and the data in water. As for the case of escape rate constants, the agreement between theory and data in ethylene glycol is reasonable only at low fluidity. This comparison, despite explicitly including recombination rate, still relies on Equation 4.24 (steady state diffusive escape) to express the escape rate. A more sophisticated model than the steady state diffusive dissociation of radical pairs is necessary to successfully explain the observed data. This model should explicitly include the recombination behavior at various viscosities.

Besides the recombination rate assumption, another was the initial formation of "contact" radical pairs. The influence of initial radical separation following homolysis may be considered with reference to Figure 4.33. As expected, the initial separation is predicted to be larger in water, the less viscous solvent, and to increase in both solvents with temperature. At the largest shown separations, a change in the expected caging fraction of near ten percent can be expected . A quantitative treatment of the initial separation results in the inverse caging fraction no longer behaving in a linear (or easily plotted) manner [2]. This analysis is also ongoing.

The methyl radical has not been included in the diffusive analysis so far due to its clearly larger rates. The plot of initial separation in Figure 4.33 may not even be a valid approach, as with excess kinetic energy the methyl radical may not stop. A further study as a function of excitation wavelength would be a worthwhile pursuit. The caging fraction can be considered however with reference to Equations 4.24 and 4.25. For methyl, the recombination rate constant is very small, and therefore the caging fraction becomes very small.

Aside from the consideration of recombination rate and initial pair distribution, the model based on steady state diffusive dissociation of radical pairs is approached only on timescales of R^2/D [37]. With the kinetic approach it should be possible to work directly with the raw data presented in Section 4.2 by fitting to the anticipated probability for time dependent radical pair survival (a time dependent quantum yield). According to method of Shin and Kapral [34, 40-42], in the long time limit the time dependent pair survival probability can be expressed as [34]:

$$P(\tau) = 1 - \frac{\lambda}{\kappa(\lambda+1)}\left\{ erfc\left(\frac{\kappa-1}{2\tau^{1/2}}\right) - e^{[(1+\lambda)(\kappa-1)]} e^{(1+\lambda)^2\tau} erfc\left[\left(1+\lambda\right)^2\tau + \frac{\kappa-1}{2\tau^{1/2}}\right]\Bigg]\right\}. \qquad (4.26)$$

κ is the ratio of the initial separation to the reaction radius. λ is the ratio of the recombination and escape rate constants. τ is the ratio of time to the to R^2/D. There are alternative kinetic expressions in the literature [36, 37, 43]; however, the method of Shin and Kapral has been applied to both experimental and simulated studies [38, 40, 41]. The diffusive rate coefficient still comes into play as for the hydrodynamic model, and consideration must still be made of the initial radical pair separation. It is hoped that fitting to a kinetic model will make possible an estimate of rate constants and initial pair separation [40, 42], which more realistically models the experimental parameters..

Figure 4.41 shows the behavior of Equation 4.26 for selected values of the parameters λ and κ.

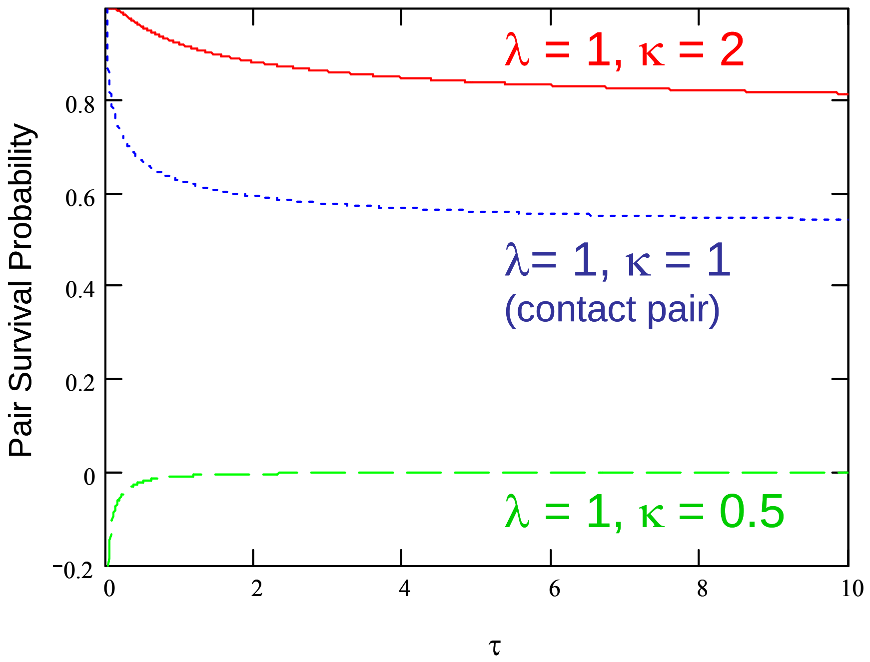

Figure 4.41. Kinetic model [34] pair survival probability for several different choices of initial pair separation. The green line is for an initial (artificial) separation less than the contact distance. The red line is for an initial separation twice the contact distance, and the blue for a contact pair. The ratio λ has been set to 1 for all three plots.

Following the approach of Scott and Liu [40-42], the probability can be integrated with a Gaussian representing the instrument response function of the transient absorption apparatus to fit to the data, an example of which is shown in Figure 4.42.

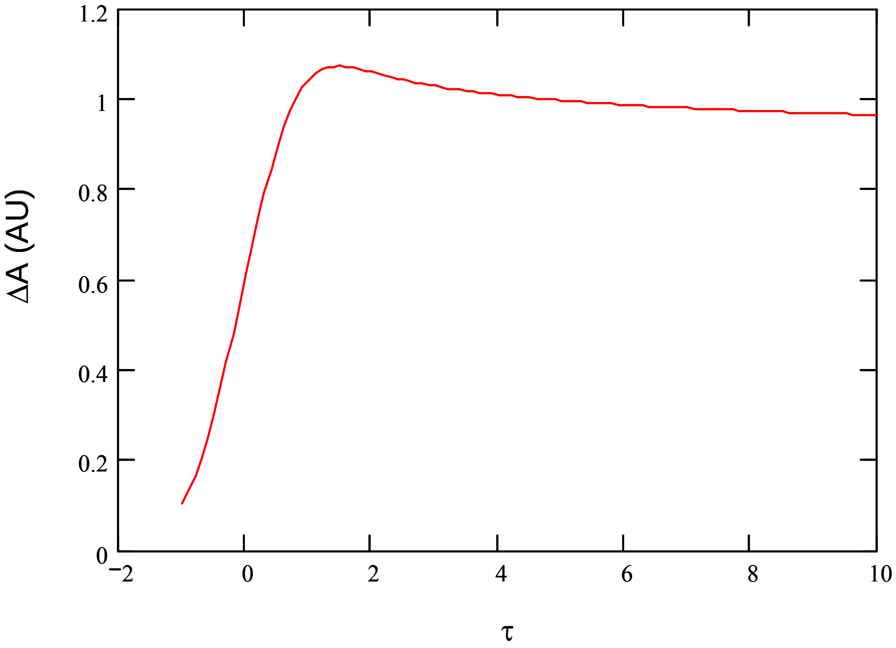

Figure 4.42. The blue trace from Figure 4.41 (contact pair, κ = 1) convoluted with a Gaussian.

Or since the signal monitored in Section 4.2 is a bleach, the trace can be made negative:

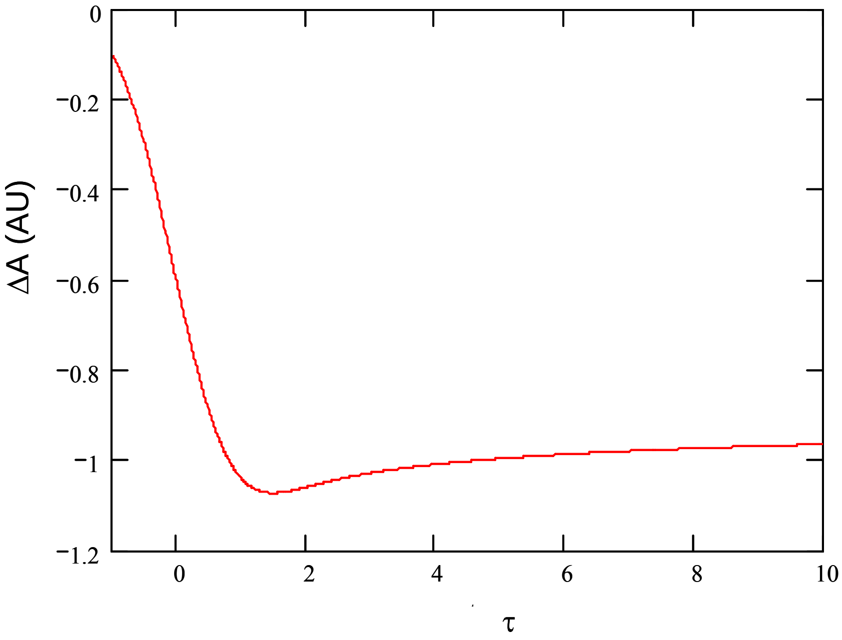

Figure 4.43. Same as Figure 4.42, but negative to represent the ground state bleach.

Another feature of a kinetic approach is worth describing to emphasize that the analysis should be pursued. Bagdasar'yan has shown that the time dependent caging fraction for contact radical pairs under a simple kinetic (pair population described by the sum of diffusive and recombination processes) model can be described in the long time limit (t → ∞) by [37]

$$F_C = \frac{1 - \sqrt{\pi} A e^{A^2} erfc(A)}{1 + \dfrac{D}{R^2 k_R}}, \tag{4.27}$$

with

$$A = \sqrt{\frac{\dfrac{D}{R^2 k_R}}{\pi \left(1 + \dfrac{D}{R^2 k_R}\right)}}. \tag{4.28}$$

Since the numerator in Equation 4.27 will be less than 1, the caging fraction will be smaller than that expected for steady state diffusive behavior (Equation 4.24). Such a result is encouraging for the ethylene glycol data since the inverse caging fractions plotted in Figure 4.40 are larger than expected when the recombination rate constant becomes large in comparison to the escape rate constant. Figure 4.44 shows the behavior of Equation 4.27 compared with the steady state caging fraction (Equation 4.24), as a function of recombination rate for adenosylcobalamin. The diffusive coefficients have been selected for each temperature listed.

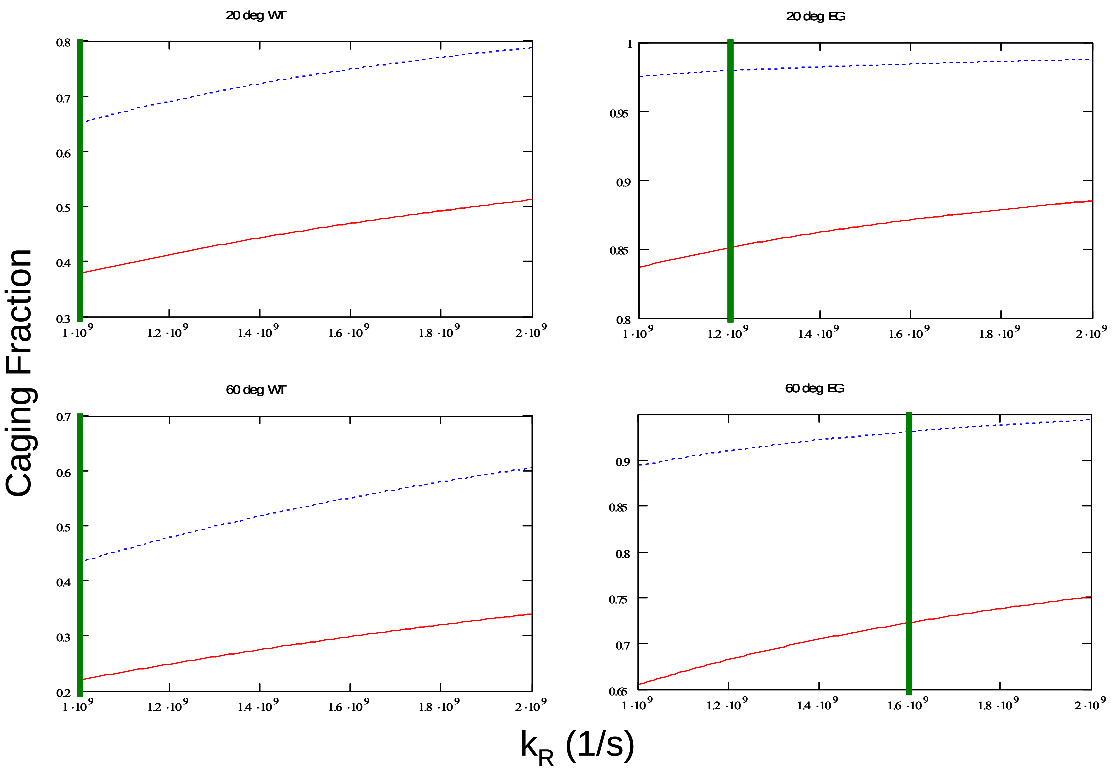

Figure 4.44. Caging fraction as calculated from Equation 4.27 (red) and 4.24(blue). The green line indicates the measured recombination rate.

Figure 4.44 shows that the efficiency calculated from Equation 4.27 underestimates the caging fraction for adenosylcobalamin in water and in ethylene glycol at 20°C. (The green line indicates measured recombination rates.) Although Equation 4.27 overestimates the caging fraction for ethylene glycol at 60°C (expected value ~0.5), it is much closer than the steady state model. A continued analysis is necessary.

4.4 Remarks

There is a wealth of data presented in this chapter with which to further the beginnings of the analysis presented in Section 4.3. Already, these data have shown that a simple steady state diffusive hydrodynamic model of the alkyl radical cage escape does not sufficiently describe the experiments, at least given the level of approximation introduced. Continued application of the hydrodynamic approach is still a worthwhile pursuit. Relaxing the various assumptions and observing any change in agreement with the experimental data may provide insight into the specific failures plaguing the initial analysis. Also, the work should be continued for each of the radicals in all environments, as the full analysis has been limited to select situations (adenosylcobalamin in water and ethylene glycol) thus far.

The kinetic models present some hope for better fit to the experimental data and for estimation of some of the parameters, such as the distribution of initial radical separation. This work is only in the preliminary stages and has not yet been actively fit to the data presented in this Chapter. With such an approach it may also be possible to characterize the degree to which the system may be considered steady state diffusive in nature. With the comparison of the kinetic model to the experimental data, it is hoped that some insight may be gained into what features of the experimental environment influence the cage escape and direct it away from the steady state diffusive behavior.

Already though, this data has demonstrated an important result. The temperature dependent data presented in Chapter 3 exhibits the striking order of magnitude difference between rate constants for escape of the adenosyl and methyl radicals. Based on that data, one plausible explanation for the discrepancy in escape rates is specific interaction of the adenosyl radical with the solvent molecules via hydrogen bonding. The extension of these studies to ethyl and propyl radicals has rendered that explanation less plausible since the constants for escape of ethyl and propyl radicals are comparable with the adenosyl rates, and are much smaller than the methyl escape rate constants.

Another avenue of investigation which should be pursued simultaneously is a molecular dynamics simulation of the cage escape process as suggested by Geva [44]. Kinetic approaches can help to account for the buildup to steady state diffusive behavior (on timescales of order R^2/D). Simulations should prove a useful complementary approach.

4.5 Bibliography

1. Garr, C.D. and Finke, R.G., *Adocobalamin (AdoCbl or coenzyme B12) cobalt-carbon bond homolysis radical-cage effects: product, kinetic, mechanistic, and cage efficiency factor (Fc) studies, plus the possibility that coenzyme B12-dependent enzymes function as "ultimate radical cages" and "ultimate radical traps".* Inorganic Chemistry, 1993. **32**(20): p. 4414-4421.

2. Rice, S.A., *Diffusion-Limited Reactions*. Comprehensive Chemical Kinetics, ed. C.H. Bamford, C.F.H. Tipper, and R.G. Compton. Vol. 25. 1985, Amsterdam, The Netherlands: Elsevier.

3. Gerards, L.E.H., Bulthuis, H., Debolster, M.W.G., and Balt, S., *A Study of the Cage Mechanism for the Homolytic Cleavage of the Cobalt Carbon Bond in Coenzyme-B12 by Varying the Solvent Viscosity.* Inorganica Chimica Acta, 1991. **190**(1): p. 47-53.

4. Hay, B.P. and Finke, R.G., *Thermolysis of the cobalt-carbon bond of adenosylcobalamin. 2. Products, kinetics, and cobalt-carbon bond dissociation energy in aqueous solution.* Journal of the American Chemical Society, 1986. **108**(16): p. 4820-4829.

5. Chemaly, S.M. and Pratt, J.M., *The Chemistry of Vitamin-B12 .17. The Effect of Steric Distortion of the Cobalt-Carbon Bond on the Pk Values and Spectra of Organocobalamins.* Journal of the Chemical Society-Dalton Transactions, 1980(11): p. 2259-2266.

6. Cole, A., *Ultrafast Transient Absorption Studies of Coenzyme B12 Analogs and Derivatives: Biological Activity of Alkylcobalamins*, in *Chemistry*. 2003, University of Michigan: Ann Arbor, Michigan.

7. Cole, A.G., Yoder, L.M., Shiang, J.J., Anderson, N.A., Walker II, L.A., Banaszak Holl, M.M., and Sension, R.J., *Time-Resolved Spectroscopic Studies of B12 Coenzymes: A Comparison of the Primary Photolysis Mechanism in Methyl-, Ethyl-, n-Propyl-, and 5'-Deoxyadenosylcobalamin.* Journal of the American Chemical Society, 2002. **124**: p. 434-441.

8. Kim, S.H., Chen, H.L., Feilchenfeld, N., and Halpern, J., *Thermal-Decomposition and Cobalt Carbon Bond-Dissociation Energies of Organocobalamins - Neopentyl, (Cyclopentylmethyl), (Cyclohexylmethyl), (Tetrahydrofurfuryl) and ((Tetrahydro-2h-Pyryl)Methyl)Cobalamin.* Journal of the American Chemical Society, 1988. **110**(10): p. 3120-3126.

9. Walker, L., *Ultrafast Transient Absorption Studies of Vitamin B12 Coenzymes: Investigation of the Cobalt-Carbon Bond in Alkylcobalamins*, in *Chemisty*. 1998, University of Michigan: Ann Arbor, Michigan.

10. Taylor, R.T., Smucker, L., Hanna, M.L., and Gill, J., *Aerobic photoiysis of alkylcobalamins: Quantum yields and light-action spectra.* Archives of Biochemistry and Biophysics, 1973. **156**(2): p. 521-533.

11. Shriver, D.F. and Drezdzon, M.A., *The Manipulation of Air-Sensitive Compounds*. 2 ed. 1986, New York: John Wiley & Sons.

12. Walker II, L.A., Jarrett, J.T., Anderson, N.A., Pullen, S.H., Matthews, R.G., and Sension, R.J., *Time-Resolved Spectroscopic Studies of B12 Coenzymes: The Identification of a Metastable Cob(III)alamin Photoproduct in the Photolysis of Methylcobalamin.* Journal of the American Chemical Society, 1998. **120**: p. 3597-3603.

13. Walker II, L.A., Shiang, J.J., Anderson, N.A., Pullen, S.H., and Sension, R.J., *Time-Resolved Spectroscopic Studies of B12 Coenzymes: The Photolysis and Geminate Recombination of Adenosylcobalamin.* Journal of the American Chemical Society, 1998. **120**: p. 7286-7292.

14. Yoder, L.M., Cole, A.G., Walker II, L.A., and Sension, R.J., *Time-Resolved Spectroscopic Studies of B12 Coenzymes: Influence of Solvent on the Photolysis of Adenosylcobalamin.* Journal of Physical Chemistry B, 2001. **105**(48): p. 12180-12188.

15. Shiang, J.J., Walker II, L.A., Anderson, N.A., Cole, A.G., and Sension, R.J., *Time-Resolved Spectroscopic Studies of B12 Coenzymes: The Photolysis of Methylcobalamin Is Wavelength Dependent.* Journal of Physical Chemistry B, 1999. **103**: p. 10532-10539.

16. Malmberg, C.G. and Maryott, A.A., *Dielectric Constants of Aqueous Solutions of Dextrose and Sucrose.* Journal of Research of the National Bureau of Standards, 1950. **45**(4): p. 299-303.

17. Sun, T. and Teja, A.S., *Density, Viscosity, and Thermal Conductivity of Aqueous Ethylene, Diethylene, and Triethylene Glycol Mixtures between 290 K and 450 K.* J. Chem. Eng. Data, 2003. **48**(1): p. 198-202.

18. Bohne, D., Fischer, S., and Obermeier, E., *Thermal-Conductivity, Density, Viscosity, and Prandtl-Numbers of Ethylene Glycol-Water Mixtures.* Berichte Der Bunsen-Gesellschaft-Physical Chemistry Chemical Physics, 1984. **88**(8): p. 739-742.

19. Weast, R.C., ed. *Handbook of Chemistry and Physics*. 62 ed. 1982, CRC Press: Boca Raton, FL.

20. Bouchard, C. and Grandjean, B.P.A., *A Neural-Network Correlation for the Variation of Viscosity of Sucrose Aqueous-Solutions with Temperature and Concentration.* Food Science and Technology-Lebensmittel-Wissenschaft & Technologie, 1995. **28**(1): p. 157-159.

21. Meade, G. and Chen, J., *Cane Sugar Handbook*. Tenth ed. 1977, New York: John Wiley & Sons, Inc.

22. Barber, E.J., *Calculation of Density and Viscosity of Sucrose Solutions as a Function of Concentration and Temperature.* National Cancer Institute Monograph, 1966. **21**: p. 219-239.

23. Einstein, A., *A New Determination of Molecular Dimensions, Translation in Einstein's Miraculous Year*, ed. J. Statchel. 1998, Princeton, New Jersey: Princeton University Press.

24. Pais, A., *Subtle is the Lord... The Science and the Life of Albert Einstein*. 1982, Oxford, New York: Oxford University Press.

25. Swindells, J.F., Snyder, C.F., Hardy, R.C., and Golden, P.E., *Supplement to National Bureau of Standards Circular 440, Table 132*. 1958.

26. Sension, R.J., Harris, D.A., and Cole, A.G., *Time-Resolved Spectroscopic Studies of B_{12} Coenzymes: A Comparison of the Influence of Solvent on the Primary Photolysis Mechanism and Geminate Recombination of Methyl-, Ethyl-, n-Propyl-, and 5'-Deoxyadenosylcobalamin.* Journal of Physical Chemistry B, 2005. **109**: p. 21954-21962.

27. Tyrrell, H.J.V. and Harris, K.R., *Diffusion in Liquids A theoretical and experimental study*. Butterworth's monographs in chemistry. 1984, London: Butterworth & Co Ltd.

28. Houston, P.L., *Chemical Kinetics and Reaction Dynamics*. 2001, New York, NY: McGraw-Hill Higher Education.

29. Rice, S.A. and Kenney-Wallace, G.A., *Time-Resolved Fluorescence Depolarization Studies of Rotational Relaxation in Viscous Media.* Chemical Physics, 1980. **47**(2): p. 161-170.

30. Caldin, E.F., *The Mechanisms of Fast Reactions in Solution*. 2001, Amsterdam, The Netherlands: IOS Press.

31. Nishida, K., Ando, Y., and Kawamura, H., *Diffusion-Coefficients of Anti-Cancer Drugs and Compounds Having a Similar Structure at 30-Degrees-C.* Colloid and Polymer Science, 1983. **261**(1): p. 70-73.

32. Northrup, S.H. and Hynes, J.T., *Short-Range Caging Effects for Reactions in Solution .1. Reaction-Rate Constants and Short-Range Caging Picture.* Journal of Chemical Physics, 1979. **71**(2): p. 871-883.

33. Northrup, S.H. and Hynes, J.T., *Short-Range Caging Effects for Reactions in Solution .2. Escape Probability and Time-Dependent Reactivity.* Journal of Chemical Physics, 1979. **71**(2): p. 884-893.

34. Shin, K.J. and Kapral, R., *Kinetic-Theory of Reactive Pair Dynamics in Liquids.* Journal of Chemical Physics, 1978. **69**(8): p. 3685-3696.

35. Noyes, R.M., *Tests of Solution Models by Quantum Yields for Dissociation.* Zeitschrift fur Elektrochemie, 1960. **64**: p. 153-156.

36. Thomsen, C.L., Madsen, D., Poulsen, J.A., Thogersen, J., Jensen, S.J.K., and Keiding, S.R., *Femtosecond photolysis of aqueous HOCl.* Journal of Chemical Physics, 2001. **115**(20): p. 9361-9369.

37. Bagdasar'yan, K.S., *Kinetics of the Recombination of Radicals and Radical-ions in the Liquid Phase.* Russian Chemical Reviews, 1984. **53**: p. 623-639.

38. Kim, H., Shin, S., Lee, S., and Shin, K.J., *Monte Carlo simulation study of recombination dynamics in solution.* Journal of Chemical Physics, 1996. **105**(17): p. 7705-7711.

39. Otto, B., Schroeder, J., and Troe, J., *Photolytic Cage Effect and Atom Recombination of Iodine in Compressed Gases and Liquids - Experiments and Simple-Models.* Journal of Chemical Physics, 1984. **81**(1): p. 202-213.

40. Bultmann, T. and Ernsting, N.P., *Competition between geminate recombination and solvation of polar radicals following ultrafast photodissociation of bis(p-aminophenyl) disulfide.* Journal of Physical Chemistry, 1996. **100**(50): p. 19417-19424.

41. Scott, T.W. and Doubleday, C., *Picosecond Photolysis of Azo-Compounds in Liquid Alkanes - Geminate Recombination Kinetics for Polyatomic Free-Radical Pairs.* Chemical Physics Letters, 1991. **178**(1): p. 9-18.

42. Scott, T.W. and Liu, S.N., *Picosecond Geminate Recombination of Phenylthiyl Free-Radical Pairs.* Journal of Physical Chemistry, 1989. **93**(4): p. 1393-1396.

43. Green, N.J.B., Pilling, M.J., Pimblott, S.M., and Clifford, P., *Stochastic Modeling of Fast Kinetics in a Radiation Track.* Journal of Physical Chemistry, 1990. **94**(1): p. 251-258.

44. Geva, E., *Comments on Thesis Defense*, A. Stickrath, Editor. 2008: Ann Arbor, MI.

Chapter 5

Back to The Future

5.1 Summary, Conclusions, and Questions

The systematic transient absorption studies presented in this thesis have addressed several problems related to the physiological basis of cobalamin coenzyme function in enzymatically catalyzed reactions (Chapter 3), influence of environment on the electronic structure of alkylcobalamins (Chapter 3), and escape from solvent cage or more generally on the diffusion of small particles in solution (Chapter 4). There remain many more outstanding questions.

Transient absorption studies on adenosylcobalamin bound to an engineered single subunit variation of glutamate mutase [1] (without substrate present) demonstrate the support of an intermediate cob(III)alamin type, metal-to-ligand-charge-transfer (MLCT) state. This state is spectrally similar to that observed following excitation of methylcobalamin, ethylcobalamin, and propylcobalamin but does not exist for free adenosylcobalamin. The electronic environment of the protein influences the excited state in such a way as to support the charge density transfer associated with the MLCT state (which is not observed for free adenosylcobalamin).

Systematic sample temperature dependent transient absorption studies on environment influence for adenosylcobalamin, cyanocobalamin, and methylcobalamin [2] lead to the designation of two distinct excited state spectra. The spectra observed following excitation of cyanocobalamin and adenosylcobalamin are both characteristic of a weakened interaction between the cobalt atom and the lower axial nitrogen ligand. The methylcobalamin state is characteristic of the nonalkylcob(III)alamin MLCT state discussed above and in the review of literature. The protein environment influences the excited state structure of adenosylcobalamin to support an intermediate with the excited state spectrum observed for methylcobalamin.

Systematic sample temperature dependent transient absorption studies performed on a variety of alkylcobalamins (adeno-, ethyl-, methyl-, and propylcobalamin) as a function of temperature (viscosity) and environment demonstrate a cage escape mechanism which is not consistent with standard steady state diffusive models. Further analysis is pending for both the diffusive hydrodynamic model and a kinetic model. This data has demonstrated that specific interaction between the adenosyl radical and solvent molecules via hydrogen bonding is not likely to play a significant role in the cage escape process.

5.2 Future Directions: Immediate and Long Term

5.2.1 Cage Escape and Diffusion (Chapter 4)

The most immediate work to be continued, in terms of this thesis, is to further the analysis of radical cage escape, as begun in Chapter 4. There remains a wealth of information to be unlocked via continued modeling of the of the already collected data as outlined in the on going analysis of Chapter 4. Effort should also be directed towards a molecular dynamics simulation of the diffusive process as suggested by Geva [3].

On a slighter longer term timescale, an intriguing study might be to perform transient absorption scans on methylcobalamin as a function of excitation wavelength. The large changes reported in the literature [4] in excited state response between excitation at 400nm and 520nm suggest that it may be possible to study the initial radical separation [5, 6]. The NOPA under development and described in Chapter 2 is an ideal source for the excitation pulses covering the wavelength region from ~470nm to 520nm. Surprising results for some caged systems exhibiting increased caged efficiency with increased excitation energy have been reported [7].

5.2.2 Protein Environment (Chapter 3)

A multitude of avenues exist for complementary transient absorption studies, such as that just described. A few of these include continued study of coenzyme bound to protein, and the systematic study of newly synthesized alkylcobalamins. For future protein studies, the University of Michigan is fortunate to have the Marsh group's expertise in the expression and purification of mutant proteins. By substituting strategically chosen amino acid residues with others, it may be possible to determine specific interactions between the protein and coenzyme X-ray crystal structures identify at least two amino acids, Glu 330 and Lys 326, within range to interact via hydrogen bonding with the adenosyl radical (Figure 5.1, [2]).

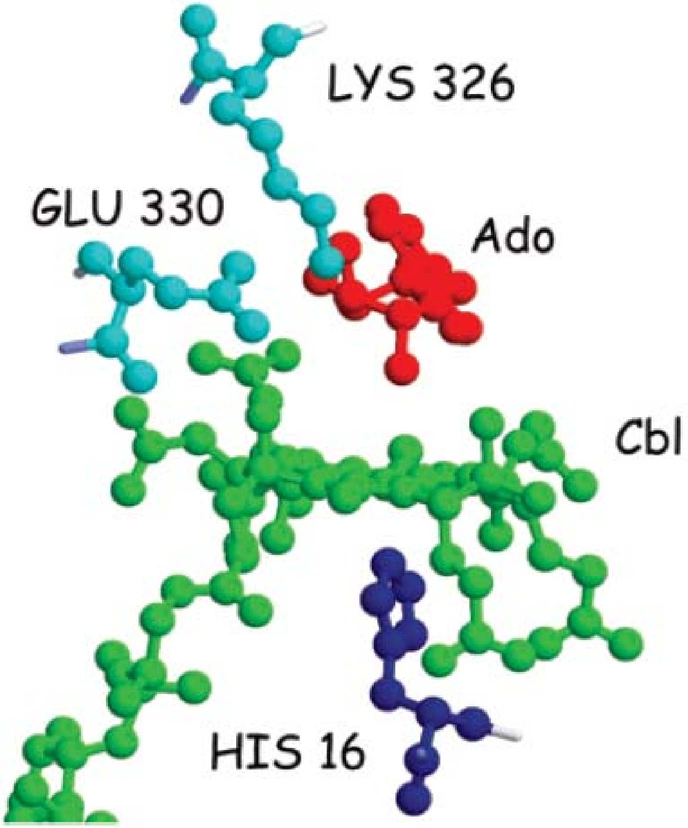

Figure 5.1. Structure of adenosylcobalamin bound to glutamate mutase. Figure reproduced from Reference [2].

5.2.3 Light Modulated X-Ray Absorption Spectroscopy

Another experimental direction is already under way. The transient absorption experiments performed for this thesis exploited the distinct variations in visible steady-state absorption spectra unique to each oxidation state (and also indicative of axial ligation) of the cobalt atom in a cobalamin. The visible spectrum makes it possible to probe electronic transitions. However, with x-rays it is possible to probe the actual molecular structure. Although the molecular structure has been determined for several of the cobalamins including methylcobalamin [8], and most famously for adenosylcobalamin [9], time resolved x-ray studies would make possible a direct measure of the Co-C bond separation during the cleavage process. The capabilities do not yet exist or are under development to make a truly time resolved x-ray study of the active bond separation with satisfactory signal to noise; several groups are doing exciting work towards this goal [10] (in particular a charge transfer state of an organometallic has been studied [11], but the pulses were 100ps).

The intermediate nonalkylcob(III)alamin type state supported by methylcobalamin following photoexcitation makes an enticing case for a complementary x-ray approach with the potential of improved signal to noise. Ohta and coworkers have shown that it is possible to introduce a light modulation detection technique [12, 13] to photoexcited x-ray absorption studies to characterize an excited state [14]. This technique does not give time resolved data of excited state dynamics. It does provide information about a single, relatively long lived excited state (or if there are many intermediates the data is representative of the integration of each contributing species). The central cobalt atom makes methylcobalamin an interesting candidate for similar studies. There are several reasons to pursue these studies with methylcobalamin over other possible organometallic candidates. Ohta and colleagues studied thin layers of powdered samples; with methylcobalamin it will be possible to conduct experiments in solution. Second, if successful, the methylcobalamin experiments may provide biologically rich information.

Early attempts at conducting light modulated x-ray absorption studies have met with experimental difficulty. Methylcobalamin has not yet been studied. In order to maximize the chance for success it is desirable that the intermediate excited state be as long lived as possible. It was for this purpose that sucrose solutions were chosen as a solvent [15]. The sucrose solution has increased viscosity compared to water, but does not impose as large a decrease in dielectric constant as does switching to ethylene glycol [16]. The combination of increased viscosity and maximized dielectric constant (so that the activation barrier remains high) serves to increase the lifetime of the intermediate as demonstrated in Figures 5.2 and 5.3.

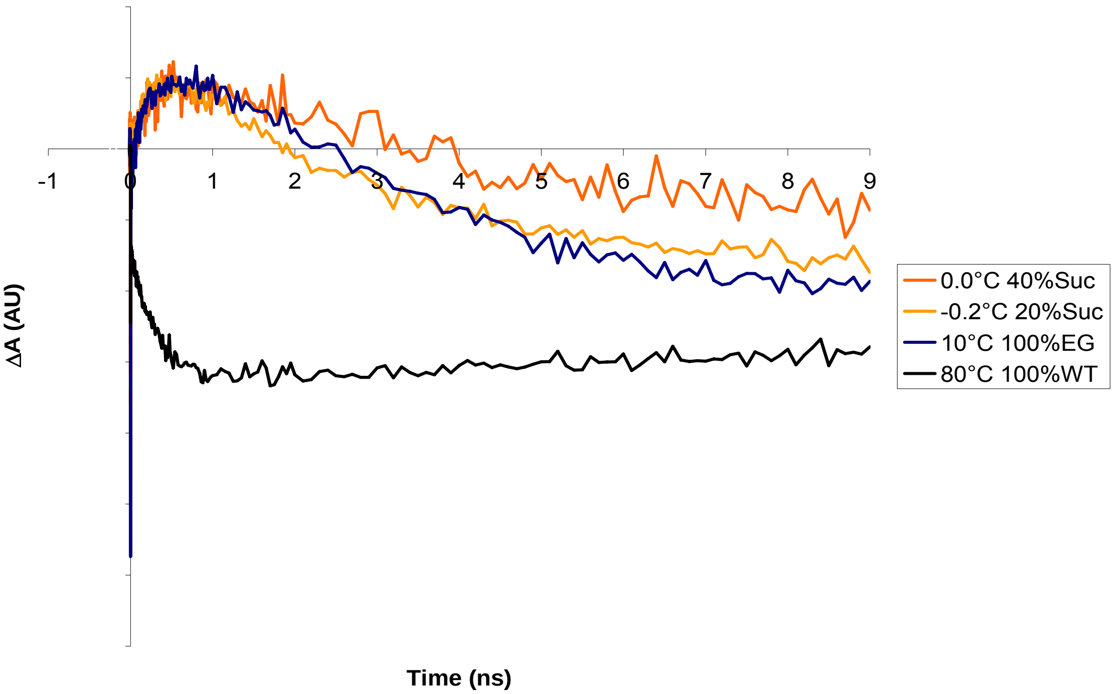

Figure 5.2. Demonstration of intermediate lifetime variation of the MLCT state observed following excitation of methylcobalamin in varying environments. It is longest for the 40% sucrose (by mass) solution at 0.0°C (orange in the Figure). The lifetime of the intermediate is longer than the 9ns window of this plot. Traces at the lowest recorded temperatures in 20% sucrose and ethylene glycol solutions are included to show the progression in lifetime. A plot at 80°C in water is included for a comparison reference.

In Figure 5.2, neither the trace for 0.0°C in 40% sucrose (by mass) solution nor the trace for -0.2°C in 20% sucrose solution have reached plateaus within the 9ns window. Another study in a 60% sucrose showed continued progression towards increased lifetime, though with slightly worse signal to noise, possibly due to scatter from the highly concentrated sucrose. The influence of solvent environment, studied heavily in this thesis, is thus *applied* to increase the intermediate lifetime by greater than ten times. Figure 5.3 presents a 3D presentation of the progression of excited state lifetime with selected solvent environments.

It may also be possible to perform direct time-resolved EXAFS studies on the methylcobalamin excited state at the Advanced Photon Source at Argonne, similar to the work reported in Reference [11]. The 100 ps x-ray pulses available at this source should permit direct measurement of the methylcobalamin excited state in water where the lifetime is 1 ns. A collaborative effort is being discussed to pursue this line of research.

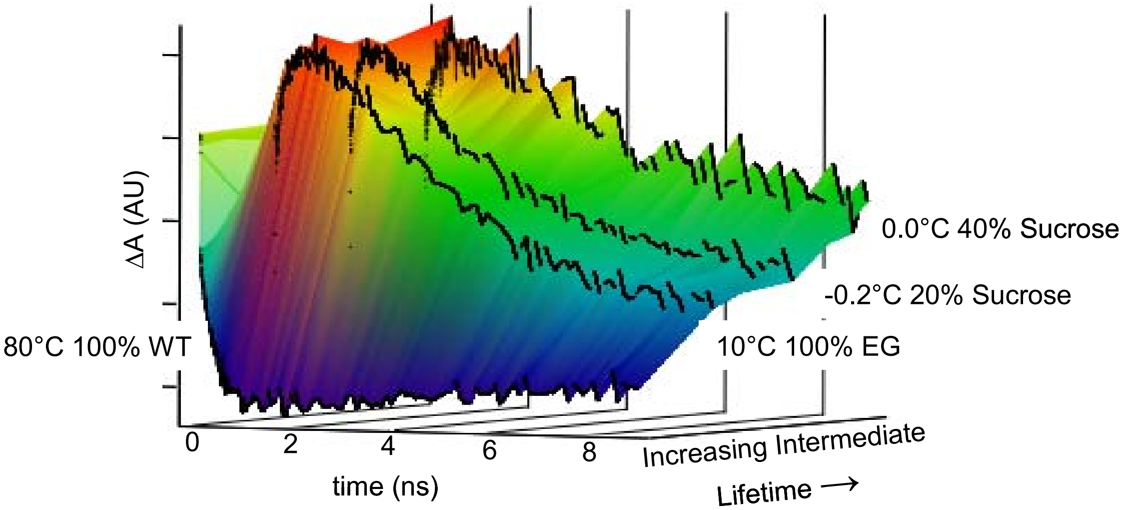

Figure 5.3. Progression of intermediate methylcobalamin excited state lifetime with choice of solvent environment. This data is that same as that presented in Figure 5.2.

5.3 Bibliography

1. Sension, R.J., Harris, D.A., Stickrath, A., Cole, A.G., Fox, C.C., and Marsh, E.N.G., *Time-Resolved Measurements of the Photolysis and Recombination of Adenosylcobalamin Bound to Glutamate Mutase.* Journal of Physical Chemistry B, 2005. **109**(38): p. 18146-18152.

2. Harris, D.A., Stickrath, A.B., Carroll, E.C., and Sension, R.J., *Influence of environment on the electronic structure of Cob(III)alamins: Time-resolved absorption studies of the S-1 state spectrum and dynamics.* Journal of the American Chemical Society, 2007. **129**(24): p. 7578-7585.

3. Geva, E., *Comments on Thesis Defense,* A. Stickrath, Editor. 2008: Ann Arbor, MI.

4. Shiang, J.J., Walker II, L.A., Anderson, N.A., Cole, A.G., and Sension, R.J., *Time-Resolved Spectroscopic Studies of B12 Coenzymes: The Photolysis of Methylcobalamin Is Wavelength Dependent.* Journal of Physical Chemistry B, 1999. **103**: p. 10532-10539.

5. Thomsen, C.L., Madsen, D., Poulsen, J.A., Thogersen, J., Jensen, S.J.K., and Keiding, S.R., *Femtosecond photolysis of aqueous HOCl.* Journal of Chemical Physics, 2001. **115**(20): p. 9361-9369.

6. Madsen, A., Thomsen, C.L., Poulsen, J.A., Jensen, S.J.K., Thogersen, J., Keiding, S.R., and Krissinel, E.B., *Femtosecond photolysis of HOCl(aq): Dissipation of fragment kinetic energy.* Journal of Physical Chemistry A, 2003. **107**(19): p. 3606-3611.

7. Harris, J.D., Oelkers, A.B., and Tyler, D.R., *Microviscosity and wavelength effects on radical cage pair recombination.* Journal of Organometallic Chemistry, 2007. **692**(15): p. 3261-3266.

8. Rossi, M., Glusker, J.P., Randaccio, L., Summers, M.F., Toscano, P.J., and Marzilli, L.G., *The Structure of a B-12 Coenzyme - Methylcobalamin Studies by X-Ray and Nmr Methods.* Journal of the American Chemical Society, 1985. **107**(6): p. 1729-1738.

9. Lenhert, P.G. and Hodgkin, D.C., *Structure of 5,6-Dimethylbenzimidazolylcobamide Coenzyme.* Nature, 1961. **192**(480): p. 937-&.

10. Chen, L.X., *Probing transient molecular structures in photochemical processes using laser-initiated time-resolved X-ray absorption spectroscopy.* Annual Review of Physical Chemistry, 2005. **56**: p. 221-254.

11. Shaw, G.B., Grant, C.D., Shirota, H., Castner, E.W., Meyer, G.J., and Chen, L.X., *Ultrafast structural rearrangements in the MLCT excited state for copper(I) bis-phenanthrolines in solution.* Journal of the American Chemical Society, 2007. **129**(7): p. 2147-2160.

12. Demas, J.N., *Excited State Lifetime Measurements*. 1983, New York, NY: Academic Press.

13. Lakowicz, J.R., *Principles of Flourescence Spectroscopy*. Third ed. 2006, New York, NY: Springer.

14. Okamoto, K., Kohdate, K., Nagai, K., Miyawaki, J., Kondoh, H., Yokoyama, T., Nojima, A., and Ohta, T., *Development of light-modulated XAFS spectroscopy*. Journal of Synchrotron Radiation, 2003. **10**: p. 242-247.

15. Penner-Hahn, J.P., R.J. Sension, Editor. 2008: Ann Arbor.

16. Malmberg, C.G. and Maryott, A.A., *Dielectric Constants of Aqueous Solutions of Dextrose and Sucrose.* Journal of Research of the National Bureau of Standards, 1950. **45**(4): p. 299-303.

Appendices

Appendix A

Noncollinear Parametric Amplification Crossing Angle

As stated in Chapter 2 (Equation 2.9), the noncollinear angle between the pump and seed beams in a noncollinear parametric amplifier (NOPA) can be approximated as [1]:

$$\Psi \approx \frac{\Omega}{\left(1+\dfrac{\lambda_{idler}}{\lambda_{signal}}\right)}, \qquad \begin{matrix}(A.1)\\(2.9)\end{matrix}$$

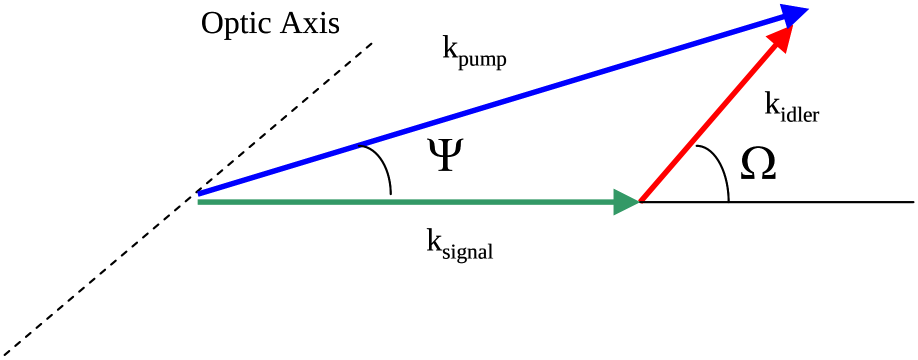

Figure A.1 (2.9). Wave vectors in noncollinear geometry [1].

where Ω is the angle between the idler and signal wave vectors and λ_{idler}, λ_{signal} are the wavelengths of the idler and signal, respectively. The approximation of Equation A.1 is in assuming that the group velocities of the signal and idler are nearly equal to each other and to the refractive index at the pump wavelength and polarization [1]. The exact expression is given by [2]

$$\Psi = \arcsin\left(\frac{1-\frac{v_{gs}^2}{v_{gi}^2}}{1+\frac{2v_{gs}n_s\lambda_i}{v_{gi}n_{is}\lambda_s}+\frac{n_s^2\lambda_i^2}{n_i^2\lambda_s^2}}\right)^{1/2} . \tag{A.2}$$

The subscript *s* refers to signal and *i* to idler. v_g is the group velocity, n_x the refractive index for beam *x*, and λ_x the wavelength for beam *x*.

Obtaining parameters for the refractive indices and group velocities from the SNLO program [3], Ψ is calculated to be ~3.5° for a central wavelength of 540nm. For these parameters, a BBO crystal cut at 28° was assumed as the nonlinear medium. As is evidenced in Figure A.2, this angle is excellent for broadband phase matching throughout much of the visible. Figure A.2 plots both the phase matching angle for Ψ = 3.5° and for the linear case, Ψ = 0°. These plots were constructed again with the SNLO nonlinear optics code [3].

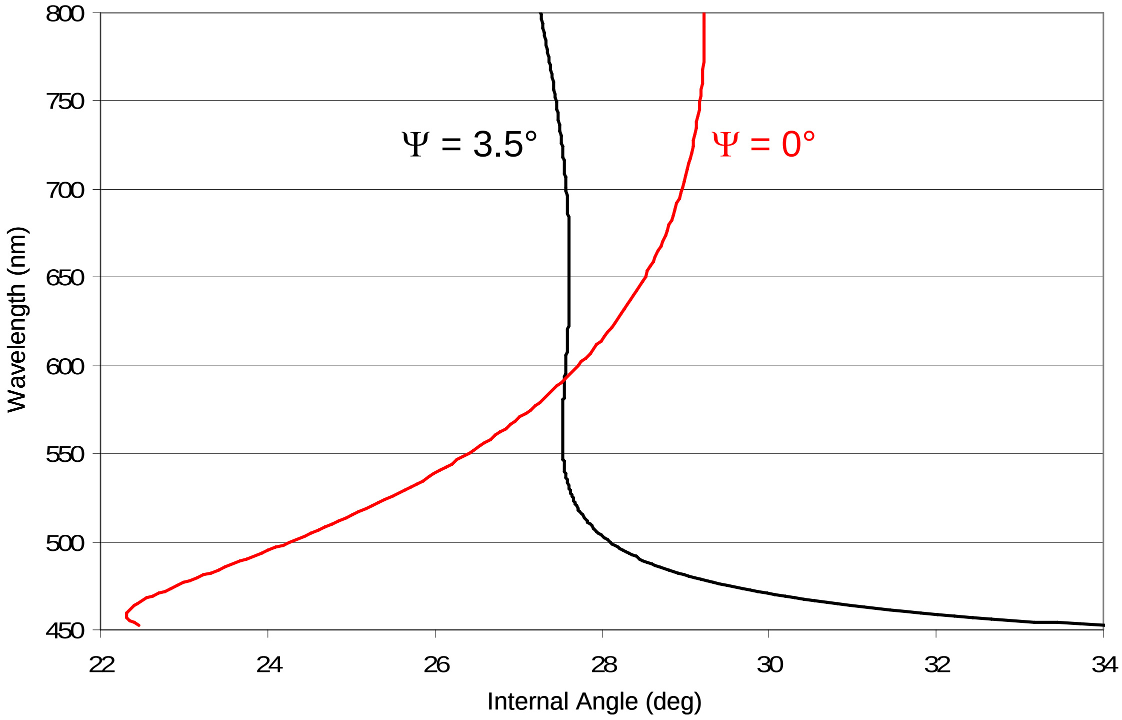

Figure A.2. Phase matching angle for the case of a linear geometry of the pump and seed wavelength (red) and for a noncollinear geometry (black). Angles calculated using the SNLO nonlinear optics code [3].

Figure A.2 shows that broadband phase matching is not possible in the collinear case but can be accomplished for the case of Ψ = 3.5° (the plot is nearly vertical throughout much of the visible wavelengths). For the experimental geometry used in these experiments, where the face of the BBO difference frequency generation crystal was near normal to the seed beam, the external crossing angle can be estimated at approximately ~5.9°. Once set near this angle, the crossing angle was normally scanned slightly to find the best beam quality.

A.1 Bibliography

1. Riedle, E., Beutter, M., Lochbrunner, S., Piel, J., Schenkl, S., Sporlein, S., and Zinth, W., *Generation of 10 to 50 fs pulses tunable through all of the visible and the NIR.* Applied Physics B-Lasers and Optics, 2000. **71**(3): p. 457-465.

2. Cerullo, G. and De Silvestri, S., *Ultrafast optical parametric amplifiers*. Review of Scientific Instruments, 2003. **74**(1): p. 1-18.

3. Smith, A.V., *SNLO nonlinear optics code available from A.V. Smith*. 2005: Sandia National Laboratories, Albuquerque, NM 87185-1423.

Appendix B

Beam Diameter as a Function of Distance from Focus

Although simple, the following expressions were of particular value during many different instances. It is included here in the hopes that is will prove worthwhile for future graduate students carrying on the research described in this thesis.

As included in Chapter 2, the beam diameter at the focus of a Gaussian beam can be calculated as [1]:

$$D = \frac{2w_0}{\left[1 + \left(\frac{z_0}{f}\right)^2\right]^{1/2}}, \qquad \begin{matrix}(B.1)\\(2.10)\end{matrix}$$

with D the focused diameter, w_0 the beam radius at the focusing lens, f the focus length, and z_0 the Rayleigh range of the input beam,

$$z_0 = \frac{2\pi w_0}{\lambda}. \qquad \begin{matrix}(B.2)\\(2.11)\end{matrix}$$

It is often convenient to know how the spot size changes as one moves away from the focus. For instance this is a handy parameter when determining focusing characteristics at the sample or when determining focusing characteristics at a nonlinear crystal. Selected portions of a MathCAD document making use of this expression are included below.

First the equations from above are defined in the MathCAD worksheet:

$$W_0 := \frac{D_0}{2} \quad [\mathrm{m}] \qquad\qquad z_0(\lambda, w_0) := \frac{\pi \cdot w_0^{2}}{\lambda} \quad [\mathrm{m}]$$

$$D(f, \lambda, w_0) := \frac{2w_0}{\sqrt{1 + \left(\frac{z_0(\lambda, w_0)}{f}\right)^2}} \cdot \frac{1}{1 \cdot 10^{-6}} \quad [\mu\mathrm{m}]$$

$$f := 0, .001 .. 1 \quad [\mathrm{m}]$$

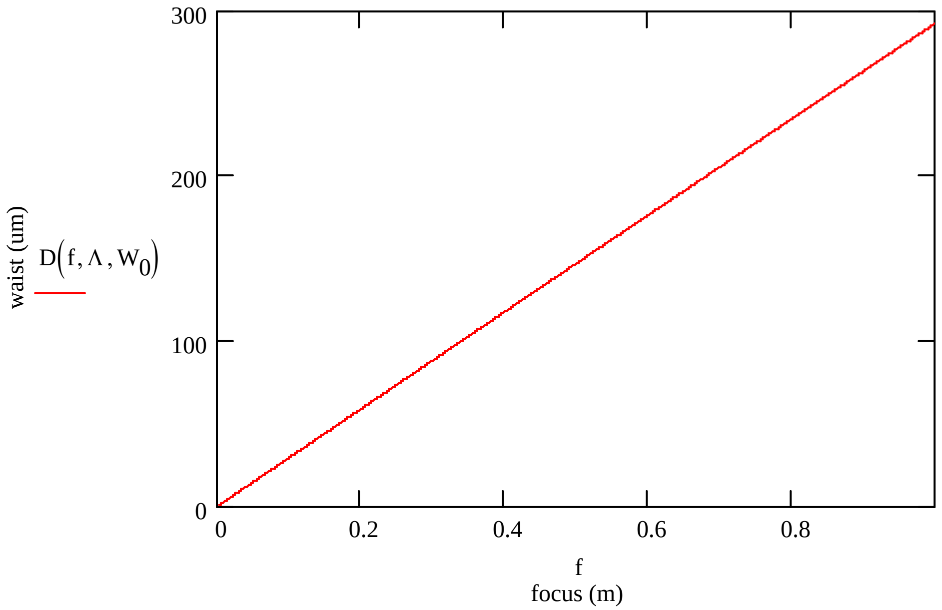

Figure B.1. Definition of equations presented above and in Chapter 2. Also included is a plot of the focus spot size for a range of focal length from 0 to 1 meter, a wavelength of Λ = 532nm, and an initial spot size of 2.3mm. Units are indicated in square brackets, i.e. meters is indicated by [m] in the equation expressions. Powers of ten are included to correct for units.

For reference, the focus location [1] is shown in Figure B.2;

$$z(f,\lambda,w_0) := \frac{f}{1+\left(\frac{f}{z_0(\lambda,w_0)}\right)^2} \quad [\mathrm{m}]$$

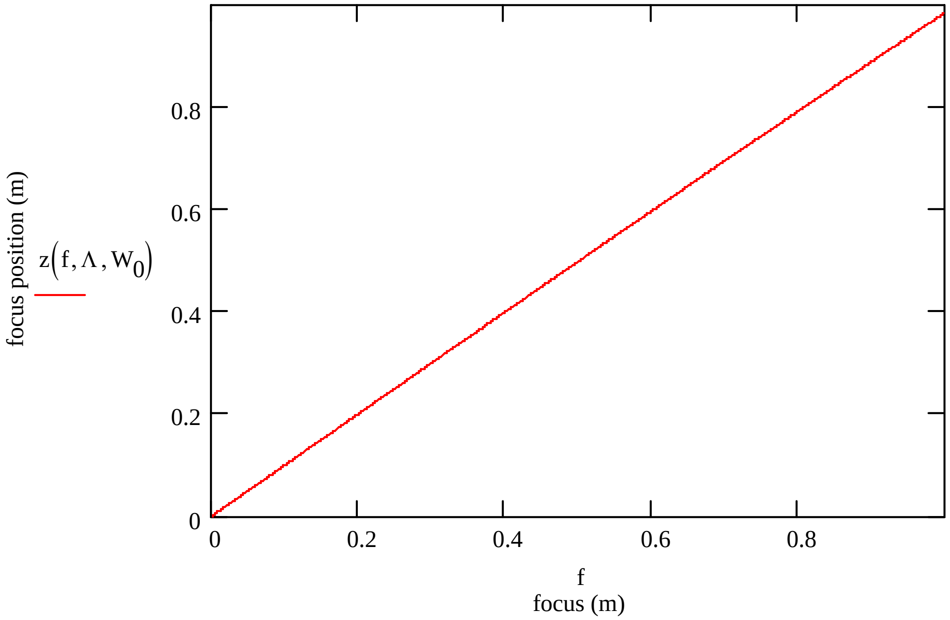

Figure B.2. Focus location for the same parameters as in Figure B.1 (focal lengths from 0 to 1 meter, wavelength of 532nm, and initial spot size of 2.3mm). The focus location is expressed as "z." Notice that at longer focal lengths the actual minimum spot location begins to deviate from the lens focal length value.

To determine the beam diameter $D(x)$ at some distance, x, from the focus the following expression [1] for a Gaussian can be used:

$$D(x) = 2w_0\left[1+\left(\frac{x}{z_0}\right)^2\right]^{1/2}. \tag{B.3}$$

All of the variables are as defined above for Equations B.1 and B.2. In Equation B.3 the focus location is located at $x = 0$. The Rayleigh range, z_0, will depend on the focused spot radius as described in Equation B.2. By using the beam radius calculated in Equation B.1 (D/2) in the expression for the Rayleigh range, the beam radius (or diameter) can easily be calculated as a function of distance from the focus.

$$z_1(f,\lambda,w_0) := \frac{\pi\cdot\left(\frac{D(f,\lambda,w_0)}{2}\cdot 1\cdot 10^{-6}\right)^2}{\lambda} \qquad [\mathrm{m}]$$

$$W_1(x,f,\lambda,w_0) := \frac{D(f,\lambda,w_0)}{2}\cdot\left[1+\left(\frac{x}{z_1(f,\lambda,w_0)}\right)^2\right]^{\frac{1}{2}} \qquad [\mu\mathrm{m}]$$

$$x := 0, .001 .. 0.3 \qquad [\mathrm{m}]$$

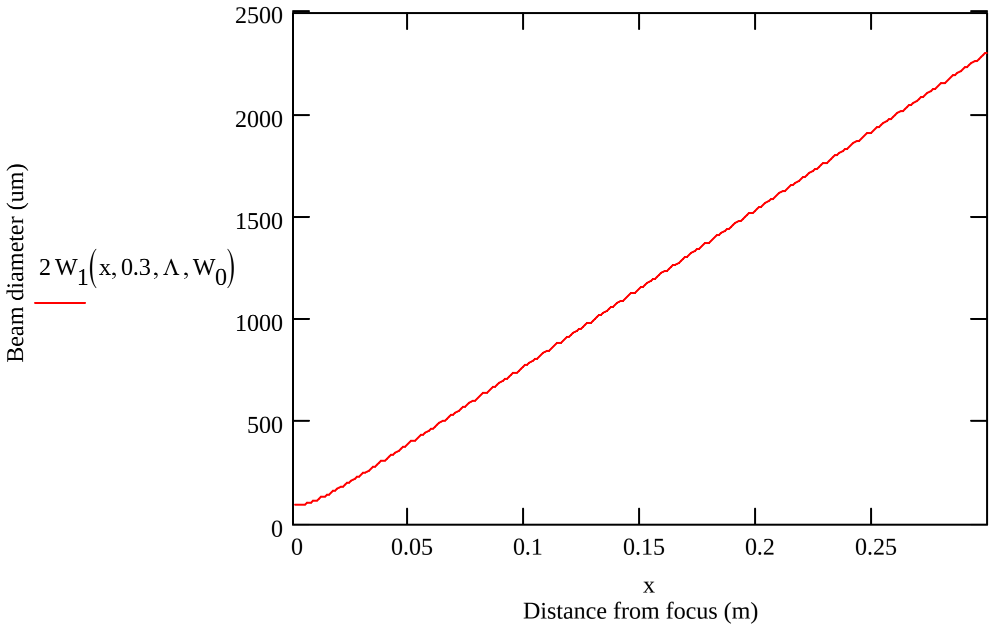

Figure B.3. Beam diameter as a function of distance from focus location. z_1 is the Rayleigh range with variable waist radius, calculated based on the focal length. W_1 is the beam radius as a function of distance from the focus location. Powers of ten are just for unit correction. The plot shown is for wavelength of 532nm and initial spot size of 2.3mm as above. This plot is for a lens focal length of 30cm. At x = 0 the minimum spot size ($2W_1$) is measured at the focus location. The beam then diverges away from the focus. At x = 2.3mm, the beam diameter reaches the input diameter of 2.3mm.

B.1 Bibliography

1. Saleh, B.E.A. and Teich, M.C., *Fundamentals of Photonics*. 1991, New York: Wiley-Interscience Publication.

Appendix C

Angle Mismatch between Compressor and Stretcher

As was mentioned in Chapter 2, the current stretcher and compressor design implemented can be used to simultaneously compensate both second and third order dispersion, including material dispersion, by employing angle mismatch between the stretcher and compressor [1]. The optimal angle in the compressor will be a function of material length. Since a multipass design is employed in the amplification system the material length is normally not adjusted and therefore this is reasonable constraint. A MathCAD worksheet is included below which follows the program of Kane and Squier [1] to determine the estimated optimal angle mismatch for the chirped pulse amplification setup used in these experiments.

For the MathCAD worksheet, the angle α is equal to θ_I in the stretcher and β is the diffracted angle. γ is the incident angle in the compressor and θ_{num} the diffracted angle. Otherwise parameters are as defined in Chapter 2. **Begin MathCAD document (boxed):**

Parameters for incident light, gratings, and stretcher incident angle (α):

$\lambda_0 := 0.8$ μm

$\alpha := 18.4166667$ deg

$c := 0.3$ μm/fs

$N := 1.2$ grooves/μm

$\omega(\lambda) := \dfrac{2\cdot\pi\cdot c}{\lambda}$

$b := 2.96\cdot 10^{5}$ μm

Calculation of the second and third order dispersion for all material in the amplifier: first write expressions for each type of material.

$\mathrm{Ti{:}Al_20_3}$ (Reference [2])

$\phi_{2TS}(l_{TS}) := 1020.99 l_{TS}$ SOD (λ=800nm) for $\mathrm{Ti{:}Al_2O_3}$, l in cm, SOD in fs ^{2}

$\phi_{3TS}(l_{TS}) := 753.32 l_{TS}$ TOD (λ=800nm) for $\mathrm{Ti{:}Al_2O_3}$, l in cm, TOD in fs ^{3}

BK7 (Reference [3], Table 2.1)

$n_{2BK7\lambda} := 0.050$ n''(λ=800nm) in μm^{-2}

$n_{3BK7\lambda} := -0.29$ n'''(λ=800nm) in μm^{-3}

$$\beta_{2BK7\lambda} := \frac{\lambda_0^{\,3}}{2\cdot\pi\cdot c^2}\cdot n_{2BK7\lambda} \qquad \frac{fs^2}{\mu m}$$

$$\beta_{3BK7\lambda} := -\frac{\lambda_0^{\,2}}{4\pi^2\cdot c^3}\left(3\lambda_0^{\,2}\cdot n_{2BK7\lambda} + \lambda_0^{\,3}\cdot n_{3BK7\lambda}\right) \qquad \frac{fs^3}{\mu m}$$

$\phi_{2BK7\lambda}(l_{BK7}) := \beta_{2BK7\lambda}\cdot l_{BK7}$ SOD for BK7 (fs^2), l in μm

$\phi_{3BK7\lambda}(l_{BK7}) := \beta_{3BK7\lambda}\cdot l_{BK7}$ TOD for BK7 (fs^3), l in μm

KD*P (Reference [4])

$$n_o(\lambda) := \sqrt{1.9575544 + \frac{0.2901391}{\left(\lambda^2 - 0.0281399\right)} - 0.02824391\lambda^2 + 0.004977826\lambda^4}$$

$$n_e(\lambda) := \sqrt{1.5005779 + \frac{0.6276034}{\left(\lambda^2 - 0.0131558\right)} - 0.01054063\lambda^2 + 0.002243821\lambda^4}$$

$$\beta_{2KDPo}(\lambda) := \frac{\lambda_0^{\,3}}{2\cdot\pi\cdot c^2}\cdot\frac{d^2}{d\lambda^2}n_o(\lambda)$$

$$\beta_{3KDPo}(\lambda) := -\frac{\lambda_0^{\,2}}{4\pi^2\cdot c^3}\left(3\lambda_0^{\,2}\cdot\frac{d^2}{d\lambda^2}n_o(\lambda) + \lambda_0^{\,3}\cdot\frac{d^3}{d\lambda^3}n_o(\lambda)\right)$$

$$\beta_{2KDPe}(\lambda) := \frac{\lambda_0^{\,3}}{2\cdot\pi\cdot c^2}\cdot\frac{d^2}{d\lambda^2}n_e(\lambda)$$

$$\beta_{3KDPe}(\lambda) := -\frac{\lambda_0^{\,2}}{4\pi^2\cdot c^3}\left(3\lambda_0^{\,2}\cdot\frac{d^2}{d\lambda^2}n_e(\lambda) + \lambda_0^{\,3}\cdot\frac{d^3}{d\lambda^3}n_e(\lambda)\right)$$

SOD for KDP (fs^2) o/e, l in μm

$$\phi_{2KDPo}\left(l_{KDP}\right) := \beta_{2KDPo}(.8)\cdot l_{KDP} \qquad \phi_{2KDPe}\left(l_{KDP}\right) := \beta_{2KDPe}(.8)\cdot l_{KDP}$$

TOD for KDP (fs^3) o/e, l in μm

$$\phi_{3KDPo}\left(l_{KDP}\right) := \beta_{3KDPo}(.8)\cdot l_{KDP} \qquad \phi_{3KDPe}\left(l_{KDP}\right) := \beta_{3KDPe}(.8)\cdot l_{KDP}$$

Calculate dispersion in the stretcher for given incidence angle and wavelength:

$\mathrm{sind}(x) := \sin(x \cdot \mathrm{deg})$ $\qquad$ $\mathrm{cosd}(x) := \cos(x \cdot \mathrm{deg})$

$\beta := \frac{180}{\pi} \cdot \mathrm{asin}\left(N \cdot \lambda_0 - \mathrm{sind}(\alpha)\right)$ Returns the diffracted angle in degrees; incident angle entered in degrees

$\phi_{2str} := -\frac{N^2 \cdot \lambda_0^{\,3} \cdot b}{\pi \cdot c^2 \cdot (\mathrm{cosd}(\beta))^2}$ fs^2

$\phi_{3str} := -\phi_{2str} \cdot \frac{3 \cdot \lambda_0}{2 \cdot \pi \cdot c} \cdot \left[1 + N \cdot \lambda_0 \cdot \frac{\mathrm{sind}(\beta)}{(\mathrm{cosd}(\beta))^2}\right]$ fs^3

$\phi_{2str} = -1.319 \times 10^6$ fs^2 $\qquad$ $\phi_{3str} = 3.454 \times 10^6$ fs^3

Calculate material dispersion for all material between stretcher and compressor:

$\phi_{2mat}(l_{TS}, l_{BK7}, l_{KDP}) := \phi_{2TS}(l_{TS}) + \phi_{2BK7\lambda}(l_{BK7}) + \phi_{2KDPo}(l_{KDP})$ fs^2

$\phi_{3mat}(l_{TS}, l_{BK7}, l_{KDP}) := \phi_{3TS}(l_{TS}) + \phi_{3BK7\lambda}(l_{BK7}) + \phi_{3KDPo}(l_{KDP})$ fs^3

Estimated total material traversal (8 passes through crystal, lenses, pockels cell, etc.)

Note: l_{TS} entered in cm, while l_{BK7} and l_{KDP} entered in μm

$L_{TS} := 4.8$ cm $\qquad$ $L_{BK7} := 1.27 \cdot 10^4$ μm $\qquad$ $L_{KDP} := 2.54 \cdot 10^4$ μm

Compressor Settings:

$$C\left(l_{TS}, l_{BK7}, l_{KDP}\right) := \frac{1}{N \cdot \lambda_0} \cdot \left[\frac{2 \cdot \pi \cdot c}{3 \cdot \lambda_0} \cdot \left(\frac{\left|\phi_{3str}\right| - \left|\phi_{3mat}\left(l_{TS}, l_{BK7}, l_{KDP}\right)\right|}{\left|\phi_{2str}\right| + \left|\phi_{2mat}\left(l_{TS}, l_{BK7}, l_{KDP}\right)\right|} \right) - 1 \right]$$

Guess Value

$$\theta := 1$$

Given

$$\frac{\sin(\theta)}{\left(\cos(\theta)\right)^2} = C\left(L_{TS}, L_{BK7}, L_{KDP}\right)$$

$$\theta_{num} := \text{Find}(\theta)$$

$$\theta_{num} = 0.676 \qquad \gamma := \frac{180}{\pi} \cdot \text{asin}\left(N \cdot \lambda_0 - \sin\left(\theta_{num}\right)\right)$$

$\boxed{\gamma = 19.541}$ This is the incident angle in degrees

$$b := \frac{\pi \cdot c^2 \cdot \left(\cos\left(\theta_{num}\right)\right)^2}{N^2 \cdot \lambda_0^{\,3}} \cdot \left(\left|\phi_{2str}\right| + \left|\phi_{2mat}\left(L_{TS}, L_{BK7}, L_{KDP}\right)\right|\right)$$

$\boxed{b \cdot 1 \cdot 10^{-4} = 31.71}$ This is the separation in cm (for diffracted angle θ)

End MathCad Document (boxed)

C.1 Bibliography

1. Kane, S. and Squier, J., *Grism-pair stretcher-compressor system for simultaneous second- and third-order dispersion compensation in chirped-pulse amplification.* Journal of the Optical Society of America B-Optical Physics, 1997. **14**(3): p. 661-665.

2. Norris, T., *Course Notes, EECS 546: Ultrafast Optics*. 2005, University of Michigan: Ann Arbor, MI.

3. Diels, J.C. and Rudolph, W., *Ultrashort Laser Pulse Phenomena*. 1996, San Diego, CA: Academic Press.

4. Roberts, D.A., *Dispersion equations for nonlinear optical crystals: KDP,* $AgGaSe_2$*, and* $AgGaS_2$*.* Applied Optics, 1996. **24**: p. 4677-4688.